

**PENELOPE – A Code System
for Monte Carlo Simulation of
Electron and Photon Transport**

**Workshop Proceedings
Issy-les-Moulineaux, France
7-10 July 2003**

**Francesc Salvat,
José M. Fernández-Varea,
Josep Sempau**
Facultat de Física (ECM), Universitat de Barcelona, Spain

© OECD 2003

NUCLEAR ENERGY AGENCY
ORGANISATION FOR ECONOMIC CO-OPERATION AND DEVELOPMENT

ORGANISATION FOR ECONOMIC CO-OPERATION AND DEVELOPMENT

Pursuant to Article 1 of the Convention signed in Paris on 14th December 1960, and which came into force on 30th September 1961, the Organisation for Economic Co-operation and Development (OECD) shall promote policies designed:

- to achieve the highest sustainable economic growth and employment and a rising standard of living in Member countries, while maintaining financial stability, and thus to contribute to the development of the world economy;
- to contribute to sound economic expansion in Member as well as non-member countries in the process of economic development; and
- to contribute to the expansion of world trade on a multilateral, non-discriminatory basis in accordance with international obligations.

The original Member countries of the OECD are Austria, Belgium, Canada, Denmark, France, Germany, Greece, Iceland, Ireland, Italy, Luxembourg, the Netherlands, Norway, Portugal, Spain, Sweden, Switzerland, Turkey, the United Kingdom and the United States. The following countries became Members subsequently through accession at the dates indicated hereafter: Japan (28th April 1964), Finland (28th January 1969), Australia (7th June 1971), New Zealand (29th May 1973), Mexico (18th May 1994), the Czech Republic (21st December 1995), Hungary (7th May 1996), Poland (22nd November 1996), Korea (12th December 1996) and the Slovak Republic (14 December 2000). The Commission of the European Communities takes part in the work of the OECD (Article 13 of the OECD Convention).

NUCLEAR ENERGY AGENCY

The OECD Nuclear Energy Agency (NEA) was established on 1st February 1958 under the name of the OEEC European Nuclear Energy Agency. It received its present designation on 20th April 1972, when Japan became its first non-European full Member. NEA membership today consists of 28 OECD Member countries: Australia, Austria, Belgium, Canada, Czech Republic, Denmark, Finland, France, Germany, Greece, Hungary, Iceland, Ireland, Italy, Japan, Luxembourg, Mexico, the Netherlands, Norway, Portugal, Republic of Korea, Slovak Republic, Spain, Sweden, Switzerland, Turkey, the United Kingdom and the United States. The Commission of the European Communities also takes part in the work of the Agency.

The mission of the NEA is:

- to assist its Member countries in maintaining and further developing, through international co-operation, the scientific, technological and legal bases required for a safe, environmentally friendly and economical use of nuclear energy for peaceful purposes, as well as
- to provide authoritative assessments and to forge common understandings on key issues, as input to government decisions on nuclear energy policy and to broader OECD policy analyses in areas such as energy and sustainable development.

Specific areas of competence of the NEA include safety and regulation of nuclear activities, radioactive waste management, radiological protection, nuclear science, economic and technical analyses of the nuclear fuel cycle, nuclear law and liability, and public information. The NEA Data Bank provides nuclear data and computer program services for participating countries.

In these and related tasks, the NEA works in close collaboration with the International Atomic Energy Agency in Vienna, with which it has a Co-operation Agreement, as well as with other international organisations in the nuclear field.

© OECD 2003

Permission to reproduce a portion of this work for non-commercial purposes or classroom use should be obtained through the Centre français d'exploitation du droit de copie (CCF), 20, rue des Grands-Augustins, 75006 Paris, France, Tel. (33-1) 44 07 47 70, Fax (33-1) 46 34 67 19, for every country except the United States. In the United States permission should be obtained through the Copyright Clearance Center, Customer Service, (508)750-8400, 222 Rosewood Drive, Danvers, MA 01923, USA, or CCC Online: <http://www.copyright.com/>. All other applications for permission to reproduce or translate all or part of this book should be made to OECD Publications, 2, rue André-Pascal, 75775 Paris Cedex 16, France.

FOREWORD

The OECD/NEA Data Bank was established to promote effective sharing of data and software developed in member countries in the field of nuclear technology and radiation physics applications. It operates a Computer Program Service (CPS) related to nuclear energy applications. The software library collects, compiles and verifies programs in an appropriate computer environment, ensuring that the computer program package is complete and adequately documented. Internationally agreed quality assurance methods are used in the verification process.

In order to obtain good results in modelling the behaviour of technological systems two conditions must be fulfilled:

1. Good quality and validated computer codes and associated basic data libraries should be used.
2. Modelling should be performed by a qualified user of such codes.

One subject to which special effort has been devoted in recent years is radiation transport. Workshops and training courses including the use of computer codes have been organised in the field of neutral particle transport for codes using both deterministic and stochastic methods. The area of charged particle transport, and in particular electron-photon transport, has received increased attention for a number of technological and medical applications. At the most recent Monte Carlo 2000 Conference, held on 23-26 October 2000 in Lisbon, Portugal, about half of the papers covered electron-photon transport and its application. The trend towards increased interest in electron-photon transport was confirmed at the 2002 International Conference on Radiation Protection and Shielding, held on 14-17 April 2002 in Santa Fe, New Mexico, USA. The Workshop on Computing Radiation Dosimetry, held in June 2002 at ITN Lisbon, presented the latest progress in this field, in particular concerning charged-particle radiation.

A new computer code was released to the NEA Data Bank for general distribution in 2001: "PENELOPE, A Code System for Monte Carlo Simulation of Electron and Photon Transport" developed by Francesc Salvat, José M. Fernández-Varea, Eduardo Acosta and Josep Sempau. A first workshop/tutorial was held at the NEA Data Bank in November 2001. This code began to be used very widely by radiation physicists and users requested that a second PENELOPE workshop with hands-on training be organised. The NEA Nuclear Science Committee endorsed this request while the authors agreed to teach a course covering the physics behind the code and to demonstrate, with corresponding exercises, how it can be used for practical applications. This course was held on 7-10 July 2003. A new version of the code, PENELOPE-2003, was presented containing improved physics models and algorithms.

These proceedings contain the corresponding manual and teaching notes of the PENELOPE-2003 workshop and training course.

Abstract

The computer code system PENELOPE (version 2003) performs Monte Carlo simulation of coupled electron-photon transport in arbitrary materials for a wide energy range, from a few hundred eV to about 1 GeV. Photon transport is simulated by means of the standard, detailed simulation scheme. Electron and positron histories are generated on the basis of a mixed procedure, which combines detailed simulation of hard events with condensed simulation of soft interactions. A geometry package called PENGEOm permits the generation of random electron-photon showers in material systems consisting of homogeneous bodies limited by quadric surfaces, i.e. planes, spheres, cylinders, etc. This report is intended not only to serve as a manual of the PENELOPE code system, but also to provide the user with the necessary information to understand the details of the Monte Carlo algorithm.

Keywords: *Radiation transport, electron-photon showers, Monte Carlo simulation, sampling algorithms, quadric geometry*

Symbols and numerical values of constants frequently used in the text (Mohr and Taylor, 2000)

Quantity	Symbol	Value
Avogadro's number	N_A	$6.02214199 \times 10^{23} \text{ mol}^{-1}$
Velocity of light in vacuum	c	$2.99792458 \times 10^8 \text{ m s}^{-1}$
Reduced Planck's constant	$\hbar = h/(2\pi)$	$6.58211889 \times 10^{-16} \text{ eV s}$
Electron charge	e	$1.602176462 \times 10^{-19} \text{ C}$
Electron mass	m_e	$9.10938188 \times 10^{-31} \text{ kg}$
Electron rest energy	$m_e c^2$	510.998902 keV
Classical electron radius	$r_e = e^2/(m_e c^2)$	$2.817940285 \times 10^{-15} \text{ m}$
Fine-structure constant	$\alpha = e^2/(\hbar c)$	$1/137.03599976$
Bohr radius	$a_0 = \hbar^2/(m_e e^2)$	$0.5291772083 \times 10^{-10} \text{ m}$
Hartree energy	$E_h = e^2/a_0$	27.2113834 eV

TABLE OF CONTENTS

Foreword	iii
Preface	ix
1. Monte Carlo simulation. Basic concepts.....	1
1.1 Elements of probability theory.....	2
1.1.1 Two-dimensional random variables.....	5
1.2 Random sampling methods.....	6
1.2.1 Random number generator	6
1.2.2 Inverse transform method	7
1.2.3 Discrete distributions	10
1.2.4 Rejection methods	13
1.2.5 Two-dimensional variables. Composition methods.....	15
1.3 Monte Carlo integration.....	18
1.4 Simulation of radiation transport	21
1.4.1 Scattering model and probability distributions.....	21
1.4.2 Generation of random tracks.....	24
1.4.3 Particle transport as a Markov process	26
1.5 Statistical averages and uncertainties.....	28
1.6 Variance reduction.....	30
1.6.1 Interaction forcing	31
1.6.2 Splitting and Russian roulette	32
1.6.3 Other methods.....	33
2. Photon interactions.....	35
2.1 Coherent (Rayleigh) scattering	36
2.1.1 Simulation of coherent scattering events	39
2.2 Photoelectric effect	40
2.2.1 Simulation of photoelectron emission	42

2.3	Incoherent (Compton) scattering	45
2.3.1	Analytical Compton profiles.....	51
2.3.2	Simulation of incoherent scattering events.....	52
2.4	Electron-positron pair production	55
2.4.1	Simulation of pair production events.....	60
2.5	Attenuation coefficients	63
2.6	Atomic relaxation.....	65
3.	Electron and positron interactions	69
3.1	Elastic collisions	70
3.1.1	The modified Wentzel (MW) model	75
3.1.2	Simulation of single elastic events with the MW model	80
3.2	Inelastic collisions.....	81
3.2.1	GOS model	85
3.2.2	Differential cross sections.....	88
3.2.3	Integrated cross sections	91
3.2.4	Stopping power of high-energy electrons and positrons.....	96
3.2.5	Simulation of hard inelastic collisions.....	98
3.2.6	Ionization of inner shells	103
3.3	Bremsstrahlung emission	106
3.3.1	The energy-loss scaled DCS	107
3.3.2	Integrated cross sections	110
3.3.3	Angular distribution of emitted photons.....	112
3.3.4	Simulation of hard radiative events	114
3.4	Positron annihilation	118
3.4.1	Generation of emitted photons.....	120
4.	Electron/positron transport mechanics	123
4.1	Elastic scattering	124
4.1.1	Multiple elastic scattering theory.....	124
4.1.2	Mixed simulation of elastic scattering	125
4.1.3	Simulating with the MW model.....	131
4.2	Soft energy losses	132
4.2.1	Energy dependence of the soft DCS	136

4.3	Combined scattering and energy loss.....	139
4.3.1	Variation of $\lambda_T^{(h)}$ with energy	141
4.3.2	Scattering by atomic electrons	144
4.3.3	Bielajew's alternate random hinge	146
4.4	Generation of random tracks	146
4.4.1	Stability of the simulation algorithm	149
5.	Constructive quadric geometry	153
5.1	Rotations and translations	155
5.2	Quadric surfaces.....	157
5.3	Constructive quadric geometry	160
5.4	Geometry definition file.....	163
5.5	The subroutine package PENGEOm	167
5.6	Debugging and viewing the geometry	170
5.7	A short tutorial	172
6.	Structure and operation of the code system	177
6.1	PENELOPE.....	178
6.1.1	Database and input material data file.....	179
6.1.2	Structure of the MAIN program	182
6.1.3	Variance reduction.....	190
6.2	Examples of MAIN programs.....	190
6.2.1	Program PENSLAB.....	191
6.2.2	Program PENCYL	192
6.2.3	Program PENDOSSES	194
6.2.4	Running the PENCYL program.....	194
6.3	Selecting the simulation parameters	200
6.4	The code SHOWER.....	204
6.5	Installation.....	205
A.	Collision kinematics.....	209
A.1	Two-body reactions	210
A.1.1	Elastic scattering.....	212
A.2	Inelastic collisions of charged particles	213

B. Numerical tools	217
B.1 Cubic spline interpolation	217
B.2 Numerical quadrature.....	221
B.2.1 Gauss integration	221
B.2.2 Adaptive bipartition	222
C. Electron/positron transport in electromagnetic fields.....	223
C.1 Tracking particles in vacuum.....	224
C.1.1 Uniform electric fields.....	226
C.1.2 Uniform magnetic fields.....	228
C.2 Exact tracking in homogeneous magnetic fields.....	229
Bibliography.....	233

PREFACE

Radiation transport in matter has been a subject of intense work since the beginning of the 20th century. Today, we know that high-energy photons, electrons and positrons penetrating matter suffer multiple interactions by which energy is transferred to the atoms and molecules of the material and secondary particles are produced.¹ By repeated interaction with the medium, a high-energy particle originates a cascade of particles which is usually referred to as a shower. After each interaction of a particle, its energy is reduced and further particles may be generated so that the evolution of the shower represents an effective degradation in energy. As time goes on, the initial energy is progressively deposited into the medium, while that remaining is shared by an increasingly larger number of particles.

A reliable description of shower evolution is required in a number of fields. Thus, knowledge of radiation transport properties is needed for quantitative analysis in surface electron spectroscopies (Jablonski, 1987; Tofterup, 1986), positron surface spectroscopy (Schultz and Lynn, 1988), electron microscopy (Reimer, 1985), electron energy loss spectroscopy (Reimer, *et al.*, 1992), electron probe microanalysis (Heinrich and Newbury, 1991), etc. Detailed information on shower evolution is also required for the design and quantitative use of radiation detectors (Titus, 1970; Berger and Seltzer, 1972). A field where radiation transport studies play an important sociological role is that of radiation dosimetry and radiotherapy (Andreo, 1991).

The study of radiation transport problems was initially attempted on the basis of the Boltzmann transport equation. However, this procedure comes up against considerable difficulties when applied to limited geometries, with the result that numerical methods based on the transport equation have only had a certain success in simple geometries, mainly for unlimited and semi-infinite media (see e.g. Zheng-Ming and Brahme, 1993). At the end of the 1950s, with the availability of computers, Monte Carlo simulation methods were developed as a powerful alternative to deal with transport problems. Basically, the evolution of an electron-photon shower is of a random nature, so that this is a process particularly amenable to Monte Carlo simulation. Detailed simulation, where all the interactions experienced by a particle are simulated in chronological succession, is exact, i.e. it yields the same results as the rigorous solution of the transport equation (apart from the inherent statistical uncertainties).

To our knowledge, the first numerical Monte Carlo simulation of photon transport is that of Hayward and Hubbell (1954) who generated 67 photon histories using a desk calculator. The simulation of photon transport is straightforward since the mean number of events in each history is fairly small. Indeed, the photon is effectively absorbed after a single photoelectric or pair-production interaction or after a few Compton interactions (say, of the order of 10). With present-day computational facilities, detailed simulation of photon transport is a simple routine task.

The simulation of electron and positron transport is much more difficult than that of photons. The main reason is that the average energy loss of an electron in a single interaction is very small (of the order of a few tens of eV). As a consequence, high-energy electrons suffer a large number of interactions before being effectively absorbed in the medium. In practice, detailed simulation is feasible

¹ In this report, the term particle will be used to designate either photons, electrons or positrons.

only when the average number of collisions per track is not too large (say, up to a few hundred). Experimental situations which are amenable to detailed simulation are those involving either electron sources with low initial kinetic energies (up to about 100 keV) or special geometries such as electron beams impinging on thin foils. For larger initial energies, and thick geometries, the average number of collisions experienced by an electron until it is effectively stopped becomes very large, and detailed simulation is very inefficient.

For high-energy electrons and positrons, most of the Monte Carlo codes currently available [e.g. ETRAN (Berger and Seltzer, 1988), ITS3 (Halbleib, *et al.*, 1992), EGS4 (Nelson, *et al.*, 1985), EGSnrc (Kawrakow and Rogers, 2000), GEANT3 (Brun, *et al.*, 1986), MCNP4b (Briesmeister, 1997), ...] have recourse to multiple scattering theories which allow the simulation of the global effect of a large number of events in a track segment of a given length (step). Following Berger (1963), these simulation procedures will be referred to as “condensed” Monte Carlo methods. The multiple scattering theories implemented in condensed simulation algorithms are only approximate and may lead to systematic errors, which can be made evident by the dependence of the simulation results on the adopted step length (Bielajew and Rogers, 1987). To analyse their magnitude, one can perform simulations of the same arrangement with different step lengths. The results are usually found to stabilise when the step length is reduced, while computation time increases rapidly, roughly in proportion to the inverse of the step length. Thus, for each particular problem, one must reach a certain compromise between available computer time and attainable accuracy. It is also worth noting that, owing to the nature of certain multiple scattering theories and/or to the particular way they are implemented in the simulation code, the use of very short step lengths may introduce spurious effects in the simulation results. For instance, the multiple elastic scattering theory of Molière (1948), which is the model used in EGS4-based codes, is not applicable to step lengths shorter than a few times the elastic mean free path (see e.g. Fernández-Varea, *et al.*, 1993b) and multiple elastic scattering has to be switched off when the step length becomes smaller than this value. As a consequence, stabilisation for short step lengths does not necessarily imply that simulation results are correct. Condensed schemes also have difficulties in generating particle tracks in the vicinity of an interface, i.e. a surface separating two media of different compositions. When the particle moves near an interface, the step length must be kept smaller than the minimum distance to the interface so as to make sure that the step is completely contained in the initial medium (Bielajew and Rogers, 1987). This may complicate the code considerably, even for relatively simple geometries.

In the present report, we describe the version 2003 of PENELOPE, a Monte Carlo algorithm and computer code for the simulation of coupled electron-photon transport. The name is an acronym that stands for PENetration and Energy LOSS of Positrons and Electrons (photon simulation was introduced later). The simulation algorithm is based on a scattering model that combines numerical databases with analytical cross section models for the different interaction mechanisms and is applicable to energies (kinetic energies in the case of electrons and positrons) from a few hundred eV to ~1 GeV. Photon transport is simulated by means of the conventional detailed method. The simulation of electron and positron transport is performed by means of a mixed procedure. Hard interactions, with scattering angle θ or energy loss W greater than pre-selected cut-off values θ_c and W_c , are simulated in detail. Soft interactions, with scattering angle or energy loss less than the corresponding cut-offs, are described by means of multiple scattering approaches. This simulation scheme handles lateral displacements and interface crossing appropriately and provides a consistent description of energy straggling. The simulation is stable under variations of the cut-offs θ_c , W_c and these can be made quite large, thus speeding up the calculation considerably, without altering the results. A characteristic feature of our code is that the most delicate parts of the simulation are handled internally; electrons, positrons and photons are simulated by calling the same subroutines. Thus, from the user’s point of view, PENELOPE makes the practical simulation of electrons and positrons as simple as that of photons (although simulating a charged particle may take a longer time).

The present version of PENELOPE is the result of continued evolution from the first version, which was released in 1996. The idea of developing a general-purpose Monte Carlo code, with better modelling than those available at that time, arose during a short course on radiation transport simulation given by F. Salvat at the Radiation Metrology Unit, CIEMAT (Madrid), in 1988. The present version 2003 contains substantial changes/improvements to the previous versions 1996, 2000 and 2001. As for the physics, the model for electron/positron elastic scattering has been revised, bremsstrahlung emission is now simulated using partial-wave data instead of analytical approximate formulae, photoelectric absorption in K and L shells is described from the corresponding partial cross sections, and fluorescence radiation from vacancies in K and L shells is now followed. Refinements have also been introduced in the electron/positron transport mechanics, mostly to account for the energy dependence of the mean free paths for hard events. Inner-shell ionisation by electron and positron impact is described as an independent mechanism by means of total cross sections obtained from an optical-data model. The simulation routines have been re-programmed in a more structured (and readable) way and new example MAIN programs have been written, with a more flexible input and expanded output.

We have recently published a set of benchmark comparisons of simulation results with experimental data (Sempau, *et al.*, 2003), which involves radiation transport in multiple materials and for a wide energy range. Overall, the agreement between PENELOPE results and experiment was found to be excellent. These calculations can be easily reproduced by using the example MAIN programs included in the distribution package.

This report is intended not only to serve as a manual of the simulation package, but also to provide the user with the necessary information to understand the details of the Monte Carlo algorithm. In Chapter 1 we give a brief survey of random sampling methods and an elementary introduction to Monte Carlo simulation of radiation transport. The cross sections adopted in PENELOPE to describe particle interactions, and the associated sampling techniques, are presented in Chapters 2 and 3.² Chapter 4 is devoted to mixed simulation methods for electron and positron transport. In Chapter 5, a relatively simple, but effective, method to handle simulation in quadric geometries is presented. The FORTRAN77 simulation package PENELOPE and other complementary programs, are described in Chapter 6, which also provides instructions to operate them. Information on relativistic kinematics and numerical methods is given in Appendices A and B. Finally, Appendix C is devoted to simulation of electron/positron transport under external, static electric and magnetic fields. The source files of PENELOPE, the auxiliary programs and the database are supplied on a ZIP-compressed file, which is distributed by the NEA Data Bank.³ The code is also available from the authors, but we would appreciate it if users did try to get the code from this institution.

In the course of our Monte Carlo research, we have had the fortune of getting much help from numerous friends and colleagues. Since the mid 1980s, we have benefited from discussions with D. Liljequist, which gave shape to our first algorithm for simulation of electrons and positrons. We are particularly grateful to A. Riveros for his enthusiastic and friendly support over the years, and for guiding us into the field of microanalysis and X-ray simulation. A. Sánchez-Reyes and E. García-Toraño were the first external users of the code system; they suffered the inconveniences of using continuously changing preliminary versions of the code without complaining too much. More recently, stimulating collaboration with A.F. Bielajew has led to substantial improvements in the electron transport mechanics and in the code organisation. We are deeply indebted to J.H. Hubbell and D.E. Cullen for kindly providing us with updated information on photon interaction and atomic relaxation data.

² In these chapters, and in other parts of the text, the CGS Gaussian system of units is adopted.

³ OECD Nuclear Energy Agency Data Bank. Le Seine St. Germain, 12 Bd. des Iles. 92130 Issy-les-Moulineaux, France. E-mail: nea@nea.fr; <http://www.nea.fr>

Thanks are also due to S.M. Seltzer for sending us his bremsstrahlung energy-loss database. L. Sorbier generously prepared most of the photoelectric and atomic relaxation database files and worked on the associated sampling algorithms. We are especially indebted to P. Andreo for comments and suggestions, which have been of much help to improve the present version of the code, and for providing a preliminary version of the tutorial. Our most sincere appreciation to the members of our research group; X. Llovet, M. Dingfelder, J. Asenjo and C. Campos. They did much more than chasing bugs through the programs and in this write-up.

Finally, we would like to thank the staff of the NEA Data Bank, particularly E. Sartori, for kindly organising the training courses on PENELOPE. Last but not least, we are also indebted to J. Baró and E. Acosta, who contributed to previous versions of the code system and documentation.

Partial support from the Fondo de Investigación Sanitaria (Ministerio de Sanidad y Consumo, Spain), project no. 01/0093, is gratefully acknowledged.

Barcelona, July 2003

Chapter 1

Monte Carlo simulation. Basic concepts

The name “Monte Carlo” was coined in the 1940s by scientists working on the nuclear weapon project in Los Alamos to designate a class of numerical methods based on the use of random numbers. Nowadays, Monte Carlo methods are widely used to solve complex physical and mathematical problems (James, 1980; Rubinstein, 1981; Kalos and Whitlock, 1986), particularly those involving multiple independent variables where more conventional numerical methods would demand formidable amounts of memory and computer time. The book by Kalos and Whitlock (1986) gives a readable survey of Monte Carlo techniques, including simple applications in radiation transport, statistical physics, and many-body quantum theory.

In Monte Carlo simulation of radiation transport, the history (track) of a particle is viewed as a random sequence of free flights that end with an interaction event where the particle changes its direction of movement, loses energy and, occasionally, produces secondary particles. The Monte Carlo simulation of a given experimental arrangement (e.g. an electron beam, coming from an accelerator and impinging on a water phantom) consists of the numerical generation of random histories. To simulate these histories we need an “interaction model”, i.e. a set of differential cross sections (DCS) for the relevant interaction mechanisms. The DCSs determine the probability distribution functions (PDF) of the random variables that characterize a track; 1) free path between successive interaction events, 2) kind of interaction taking place and 3) energy loss and angular deflection in a particular event (and initial state of emitted secondary particles, if any). Once these PDFs are known, random histories can be generated by using appropriate sampling methods. If the number of generated histories is large enough, quantitative information on the transport process may be obtained by simply averaging over the simulated histories.

The Monte Carlo method yields the same information as the solution of the Boltzmann transport equation, with the same interaction model, but is easier to implement (Berger, 1963). In particular, the simulation of radiation transport in finite samples is

straightforward, while even the simplest finite geometries (e.g. thin foils) are very difficult to be dealt with by the transport equation. The main drawback of the Monte Carlo method lies in its random nature: all the results are affected by statistical uncertainties, which can be reduced at the expense of increasing the sampled population and, hence, the computation time. Under special circumstances, the statistical uncertainties may be lowered by using variance-reduction techniques (Rubinstein, 1981; Bielajew and Rogers, 1988).

1.1 Elements of probability theory

The essential characteristic of Monte Carlo simulation is the use of random numbers and random variables. A random variable is a quantity that results from a repeatable process and whose actual values (realizations) cannot be predicted with certainty. In the real world, randomness originates either from uncontrolled factors (as occurs e.g. in games of chance) or from the quantum nature of microscopic systems and processes (e.g. nuclear disintegration and radiation interactions). As a familiar example, assume that we throw two dice in a box; the sum of points in their upper faces is a discrete random variable, which can take the values 2 to 12, while the distance x between the dice is a continuous random variable, which varies between zero (dice in contact) and a maximum value determined by the dimensions of the box. In the computer, random variables are generated by means of numerical transformations of random numbers (see below).

Let x be a continuous random variable that takes values in the interval $x_{\min} \leq x \leq x_{\max}$. To measure the likelihood of obtaining x in an interval (a, b) we use the probability $P\{x|a < x < b\}$, defined as the ratio n/N of the number n of values of x that fall within that interval and the total number N of generated x -values, in the limit $N \rightarrow \infty$. The probability of obtaining x in a differential interval of length dx about x_1 can be expressed as

$$P\{x|x_1 < x < x_1 + dx\} = p(x_1) dx, \quad (1.1)$$

where $p(x)$ is the PDF of x . Since 1) negative probabilities have no meaning and 2) the obtained value of x must be somewhere in (x_{\min}, x_{\max}) , the PDF must be definite positive and normalized to unity, i.e.

$$p(x) \geq 0 \quad \text{and} \quad \int_{x_{\min}}^{x_{\max}} p(x) dx = 1. \quad (1.2)$$

Any “function” that satisfies these two conditions can be interpreted as a PDF. In Monte Carlo simulation we shall frequently use the uniform distribution,

$$U_{x_{\min}, x_{\max}}(x) \equiv \begin{cases} 1/(x_{\max} - x_{\min}) & \text{if } x_{\min} < x < x_{\max}, \\ 0 & \text{otherwise,} \end{cases} \quad (1.3)$$

which is discontinuous. The definition (1.2) also includes singular distributions such as the Dirac delta, $\delta(x - x_0)$, which is defined by the property

$$\int_a^b f(x) \delta(x - x_0) dx = \begin{cases} f(x_0) & \text{if } a < x_0 < b, \\ 0 & \text{if } x_0 < a \text{ or } x_0 > b \end{cases} \quad (1.4)$$

for any function $f(x)$ that is continuous at x_0 . An equivalent, more intuitive definition is the following,

$$\delta(x - x_0) \equiv \lim_{\Delta \rightarrow 0} U_{x_0 - \Delta, x_0 + \Delta}(x), \quad (1.4')$$

which represents the delta distribution as the zero-width limit of a sequence of uniform distributions centred at the point x_0 . Hence, the Dirac distribution describes a single-valued discrete random variable (i.e. a constant). The PDF of a random variable x that takes the discrete values $x = x_1, x_2, \dots$ with point probabilities p_1, p_2, \dots can be expressed as a mixture of delta distributions,

$$p(x) = \sum_i p_i \delta(x - x_i). \quad (1.5)$$

Discrete distributions can thus be regarded as particular forms of continuous distributions.

Given a continuous random variable x , the cumulative distribution function of x is defined by

$$\mathcal{P}(x) \equiv \int_{x_{\min}}^x p(x') dx'. \quad (1.6)$$

This is a non-decreasing function of x that varies from $\mathcal{P}(x_{\min}) = 0$ to $\mathcal{P}(x_{\max}) = 1$. In the case of a discrete PDF of the form (1.5), $\mathcal{P}(x)$ is a step function. Notice that the probability $P\{x|a < x < b\}$ of having x in the interval (a, b) is

$$P\{x|a < x < b\} = \int_a^b p(x) dx = \mathcal{P}(b) - \mathcal{P}(a), \quad (1.7)$$

and that $p(x) = d\mathcal{P}(x)/dx$.

The n -th moment of $p(x)$ is defined as

$$\langle x^n \rangle = \int_{x_{\min}}^{x_{\max}} x^n p(x) dx. \quad (1.8)$$

The moment $\langle x^0 \rangle$ is simply the integral of $p(x)$, which is equal to unity, by definition. However, higher order moments may or may not exist. An example of a PDF that has no even-order moments is the Lorentz or Cauchy distribution,

$$p_L(x) \equiv \frac{1}{\pi} \frac{\gamma}{\gamma^2 + x^2}, \quad -\infty < x < \infty. \quad (1.9)$$

Its first moment, and other odd-order moments, can be assigned a finite value if they are defined as the “principal value” of the integrals, e.g.

$$\langle x \rangle_L = \lim_{a \rightarrow \infty} \int_{-a}^{+a} x \frac{1}{\pi} \frac{\gamma}{\gamma^2 + x^2} dx = 0, \quad (1.10)$$

but the second and higher even-order moments are infinite, irrespective of the way they are defined.

The first moment, when it exists, is called the mean or expected value of the random variable x ,

$$\langle x \rangle = \int x p(x) dx. \quad (1.11)$$

The expected value of a function $f(x)$ is defined in a similar way,

$$\langle f(x) \rangle \equiv \int f(x) p(x) dx. \quad (1.12)$$

Since $f(x)$ is a random variable, it has its own PDF, $\pi(f)$, which is such that the probability of having f in a certain interval of length df is equal to the probability of having x in the corresponding interval or intervals¹. Thus, if $f(x)$ is a monotonously increasing function of x (so that there is a one-to-one correspondence between the values of x and f), $p(x) dx = \pi(f) df$ and

$$\pi(f) = p(x) (df/dx)^{-1}. \quad (1.13)$$

It can be shown that the definitions (1.11) and (1.12) are equivalent. If $f(x)$ increases monotonously with x , the proof is trivial: we can start from the definition (1.11) and write

$$\langle f \rangle = \int f \pi(f) df = \int f(x) p(x) (dx/df) df = \int f(x) p(x) dx,$$

which agrees with (1.12). Notice that the expectation value is linear, i.e.

$$\langle a_1 f_1(x) + a_2 f_2(x) \rangle = a_1 \langle f_1(x) \rangle + a_2 \langle f_2(x) \rangle, \quad (1.14)$$

where a_1 and a_2 are arbitrary real constants.

If the first and second moments of the PDF $p(x)$ exist, we define the variance of x [or of $p(x)$] by

$$\text{var}(x) \equiv \langle (x - \langle x \rangle)^2 \rangle = \int (x - \langle x \rangle)^2 p(x) dx = \langle x^2 \rangle - \langle x \rangle^2. \quad (1.15)$$

The square root of the variance, $\sigma \equiv [\text{var}(x)]^{1/2}$, is called the “standard deviation” (and sometimes the “standard uncertainty”); it gives a measure of the dispersion of the random variable (i.e. of the width of the PDF). The Dirac delta is the only PDF that has zero variance. Similarly, the variance of a function $f(x)$ is defined as

$$\text{var}\{f(x)\} = \langle f^2(x) \rangle - \langle f(x) \rangle^2. \quad (1.16)$$

Thus, for a constant $f(x) = a$, $\langle f \rangle = a$ and $\text{var}\{f\} = 0$.

¹When $f(x)$ does not increase or decrease monotonously with x , there may be multiple values of x corresponding to a given value of f .

1.1.1 Two-dimensional random variables

Let us now consider the case of a two-dimensional random variable, (x, y) . The corresponding (joint) PDF $p(x, y)$ satisfies the conditions

$$p(x, y) \geq 0 \quad \text{and} \quad \int dx \int dy p(x, y) = 1. \quad (1.17)$$

The *marginal* PDFs of x and y are defined as

$$q(x) \equiv \int p(x, y) dy \quad \text{and} \quad q(y) \equiv \int p(x, y) dx, \quad (1.18)$$

i.e. $q(x)$ is the probability of obtaining the value x and *any* value of y . The joint PDF can be expressed as

$$p(x, y) = q(x) p(y|x) = q(y) p(x|y), \quad (1.19)$$

where

$$p(x|y) = \frac{p(x, y)}{q(y)} \quad \text{and} \quad p(y|x) = \frac{p(x, y)}{q(x)} \quad (1.20)$$

are the *conditional* PDFs of x and y , respectively. Notice that $p(x|y)$ is the normalized PDF of x for a fixed value of y .

The expectation value of a function $f(x, y)$ is

$$\langle f(x, y) \rangle = \int dx \int dy f(x, y) p(x, y). \quad (1.21)$$

The moments of the PDF are defined by

$$\langle x^n y^m \rangle = \int dx \int dy x^n y^m p(x, y). \quad (1.22)$$

In particular,

$$\langle x^n \rangle = \int dx \int dy x^n p(x, y) = \int x^n q(x) dx. \quad (1.23)$$

Again, the only moment that is necessarily defined is $\langle x^0 y^0 \rangle = 1$. When the corresponding moments exist, the variances of x and y are given by

$$\text{var}(x) = \langle x^2 \rangle - \langle x \rangle^2 \quad \text{and} \quad \text{var}(y) = \langle y^2 \rangle - \langle y \rangle^2. \quad (1.24)$$

The variance of $x + y$ is

$$\text{var}(x + y) = \langle (x + y)^2 \rangle - \langle x + y \rangle^2 = \text{var}(x) + \text{var}(y) + 2 \text{cov}(x, y), \quad (1.25)$$

where

$$\text{cov}(x, y) = \langle xy \rangle - \langle x \rangle \langle y \rangle \quad (1.26)$$

is the *covariance* of x and y , which can be positive or negative. A related quantity is the *correlation coefficient*,

$$\rho(x, y) = \frac{\text{cov}(x, y)}{\sqrt{\text{var}(x) \text{var}(y)}}, \quad (1.27)$$

which takes values from -1 to 1 . Notice that $\text{cov}(x, x) = \text{var}(x)$. When the variables x and y are independent, i.e. when $p(x, y) = p_x(x) p_y(y)$, we have

$$\text{cov}(x, y) = 0 \quad \text{and} \quad \text{var}(x + y) = \text{var}(x) + \text{var}(y). \quad (1.28)$$

Moreover, for independent variables,

$$\text{var}\{a_1 x + a_2 y\} = a_1^2 \text{var}(x) + a_2^2 \text{var}(y). \quad (1.29)$$

1.2 Random sampling methods

The first component of a Monte Carlo calculation is the numerical sampling of random variables with specified PDFs. In this section we describe different techniques to generate random values of a variable x distributed in the interval (x_{\min}, x_{\max}) according to a given PDF $p(x)$. We concentrate on the simple case of single-variable distributions, since random sampling from multivariate distributions can always be reduced to single-variable sampling (see below). A more detailed description of sampling methods can be found in the textbooks of Rubinstein (1981) and Kalos and Whitlock (1986).

1.2.1 Random number generator

In general, random sampling algorithms are based on the use of random numbers ξ uniformly distributed in the interval $(0,1)$. These random numbers can be easily generated on the computer (see e.g. Kalos and Whitlock, 1986; James, 1990). Among the “good” random number generators currently available, the simplest ones are the so-called multiplicative congruential generators (Press and Teukolsky, 1992). A popular example of this kind of generator is the following,

$$R_n = 7^5 R_{n-1} \pmod{2^{31} - 1}, \quad \xi_n = R_n / (2^{31} - 1), \quad (1.30)$$

which produces a sequence of random numbers ξ_n uniformly distributed in $(0,1)$ from a given “seed” R_0 ($< 2^{31} - 1$). Actually, the generated sequence is not truly random, since it is obtained from a deterministic algorithm (the term “pseudo-random” would be more appropriate), but it is very unlikely that the subtle correlations between the values in the sequence have an appreciable effect on the simulation results. The generator (1.30) is known to have good random properties (Press and Teukolsky, 1992). However, the sequence is periodic, with a period of the order of 10^9 . With present-day computational facilities, this value is not large enough to prevent re-initiation in a single simulation run. An excellent critical review of random number generators has been published by James (1990), where he recommends using algorithms that are more sophisticated than simple congruential ones. The generator implemented in the FORTRAN77 function **RAND** (table 1.1) is due to L’Ecuyer (1988); it produces 32-bit floating point numbers uniformly distributed in the *open* interval between zero and one. Its period is of the order of 10^{18} , which is virtually infinite for practical simulations.

Table 1.1: FORTRAN77 random number generator.

```

C *****
C               FUNCTION RAND
C *****
C               FUNCTION RAND(DUMMY)
C
C This is an adapted version of subroutine RANECU written by F. James
C (Comput. Phys. Commun. 60 (1990) 329-344), which has been modified to
C give a single random number at each call.
C
C The 'seeds' ISEED1 and ISEED2 must be initialized in the main program
C and transferred through the named common block /RSEED/.
C
C       IMPLICIT DOUBLE PRECISION (A-H,O-Z), INTEGER*4 (I-N)
C       PARAMETER (USCALE=1.0D0/2.0D0**31)
C       COMMON/RSEED/ISEED1, ISEED2
C
C       I1=ISEED1/53668
C       ISEED1=40014*(ISEED1-I1*53668)-I1*12211
C       IF(ISEED1.LT.0) ISEED1=ISEED1+2147483563
C
C       I2=ISEED2/52774
C       ISEED2=40692*(ISEED2-I2*52774)-I2*3791
C       IF(ISEED2.LT.0) ISEED2=ISEED2+2147483399
C
C       IZ=ISEED1-ISEED2
C       IF(IZ.LT.1) IZ=IZ+2147483562
C       RAND=IZ*USCALE
C
C       RETURN
C       END

```

1.2.2 Inverse transform method

The cumulative distribution function of $p(x)$, eq. (1.6), is a non-decreasing function of x and, therefore, it has an inverse function $\mathcal{P}^{-1}(\xi)$. The transformation $\xi = \mathcal{P}(x)$ defines a new random variable that takes values in the interval (0,1), see fig. 1.1. Owing to the correspondence between x and ξ values, the PDF of ξ , $p_\xi(\xi)$, and that of x , $p(x)$, are related by $p_\xi(\xi) d\xi = p(x) dx$. Hence,

$$p_\xi(\xi) = p(x) \left(\frac{d\xi}{dx} \right)^{-1} = p(x) \left(\frac{d\mathcal{P}(x)}{dx} \right)^{-1} = 1, \quad (1.31)$$

that is, ξ is distributed uniformly in the interval (0,1).

Now it is clear that if ξ is a random number, the variable x defined by $x = \mathcal{P}^{-1}(\xi)$ is randomly distributed in the interval (x_{\min}, x_{\max}) with PDF $p(x)$ (see fig. 1.1). This provides a practical method of generating random values of x using a generator of random numbers uniformly distributed in (0,1). The randomness of x is guaranteed by

that of ξ . Notice that x is the (unique) root of the equation

$$\xi = \int_{x_{\min}}^x p(x') dx', \quad (1.32)$$

which will be referred to as the *sampling equation* of the variable x . This procedure for random sampling is known as the *inverse transform method*; it is particularly adequate for PDFs $p(x)$ given by simple analytical expressions such that the sampling equation (1.32) can be solved analytically.

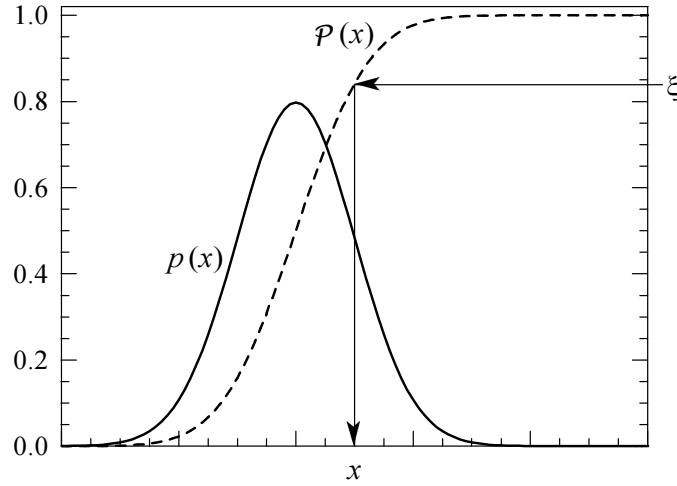


Figure 1.1: Random sampling from a distribution $p(x)$ using the inverse transform method.

Consider, for instance, the uniform distribution in the interval (a, b) ,

$$p(x) \equiv U_{a,b}(x) = \frac{1}{b-a}.$$

The sampling equation (1.32) then reads

$$\xi = \frac{x-a}{b-a}, \quad (1.33)$$

which leads to the well-known sampling formula

$$x = a + \xi(b-a). \quad (1.34)$$

As another familiar example, consider the exponential distribution

$$p(s) = \frac{1}{\lambda} \exp(-s/\lambda), \quad s > 0, \quad (1.35)$$

of the free path s of a particle between interaction events (see section 1.4.1). The parameter λ represents the mean free path. In this case, the sampling equation (1.32) is easily solved to give the sampling formula

$$s = -\lambda \ln(1-\xi) = -\lambda \ln \xi. \quad (1.36)$$

The last equality follows from the fact that $1-\xi$ is also a random number distributed in $(0,1)$.

Numerical inverse transform

The inverse transform method can also be efficiently used for random sampling from continuous distributions $p(x)$ that are given in numerical form, or that are too complicated to be sampled analytically. To apply this method, the cumulative distribution function $\mathcal{P}(x)$ has to be evaluated at the points x_i of a certain grid. The sampling equation $\mathcal{P}(x) = \xi$ can then be solved by inverse interpolation, i.e. by interpolating in the table (ξ_i, x_i) , where $\xi_i \equiv \mathcal{P}(x_i)$ (ξ is regarded as the independent variable). Care must be exercised to make sure that the numerical integration and interpolation do not introduce significant errors.

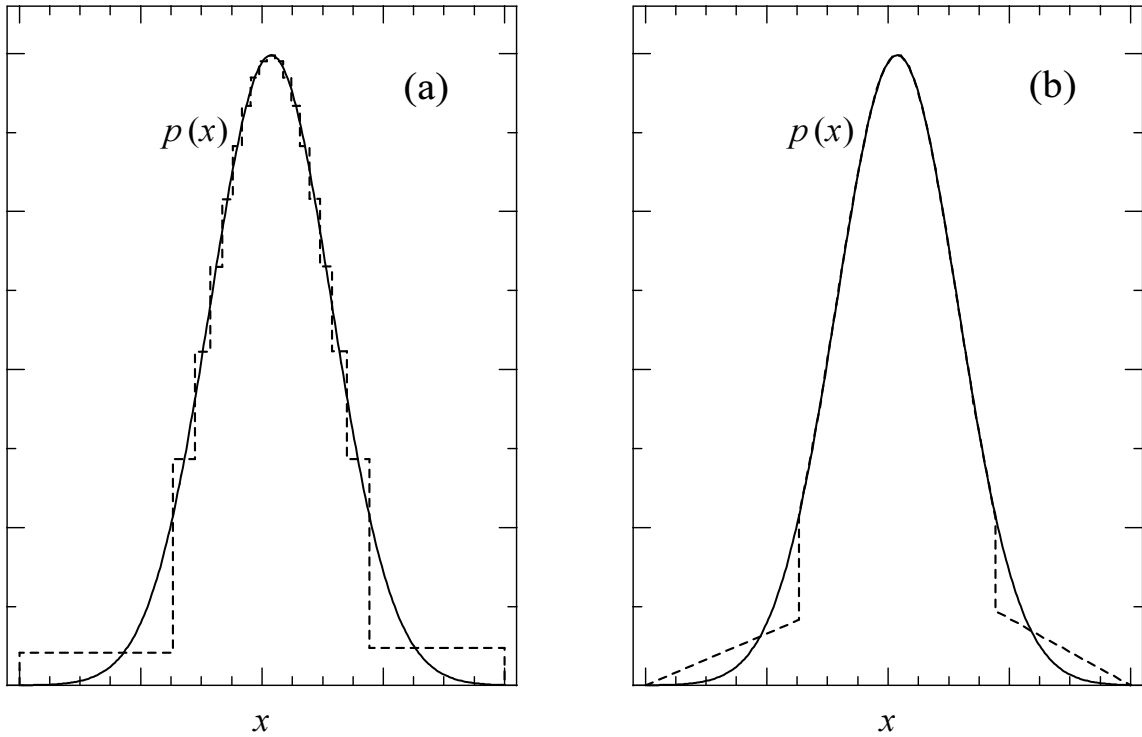


Figure 1.2: Random sampling from a continuous distribution $p(x)$ using the numerical inverse transform method with $N = 20$ intervals. a) Piecewise constant approximation. b) Piecewise linear approximation.

A simple, general, approximate method for numerical sampling from continuous distributions is the following. The values x_n ($n = 0, 1, \dots, N$) of x for which the cumulative distribution function has the values n/N ,

$$\mathcal{P}(x_n) = \int_{x_{\min}}^{x_n} p(x) dx = \frac{n}{N}, \quad (1.37)$$

are previously computed and stored in memory. Notice that the *exact* probability of having x in the interval (x_n, x_{n+1}) is $1/N$. We can now sample x by linear interpolation:

we generate a random number ξ and consider the quantity $y \equiv \xi N$, which takes values in the interval $(0, N)$. We set $n = [y]$, where the symbol $[y]$ denotes the integer part of y (i.e. the largest integer that is less than y). The value of x is obtained as

$$x = x_n + (x_{n+1} - x_n)u, \quad u \equiv y - n \in (0, 1). \quad (1.38)$$

This is equivalent to approximating the PDF by a piecewise constant function (see fig. 1.2a). Since the spacing between the points x_n (at which the cumulative distribution function is specified) is roughly proportional to $1/p(x_n)$, the approximation is more accurate in regions where $p(x)$ is large.

The algorithm can be improved by storing the values $p(x_n)$ of the PDF at the points x_n in memory and approximating the PDF in the interval (x_n, x_{n+1}) linearly,

$$p_{\text{la}}(x) \simeq C_n \left[p(x_n) + \frac{p(x_{n+1}) - p(x_n)}{x_{n+1} - x_n} (x - x_n) \right], \quad (1.39)$$

with a normalization constant C_n such that the integral of $p_{\text{la}}(x)$ over the interval (x_n, x_{n+1}) equals $1/N$. In general, this piecewise linear approximation is not continuous. Of course, $p_{\text{la}}(x)$ will differ from the exact PDF $p(x)$ when the latter is not linear in the interval, but the differences are smaller than for the piecewise constant approximation with the same number N of grid points (see fig. 1.2). Again, the approximation is better where $p(x)$ is larger. An exact algorithm for random sampling from the piecewise linear approximation (1.39) is the following,

- (i) Generate a random number ξ and set $y = \xi N$, $n = [y]$ and $u = y - n$.
- (ii) If $p(x_n) \neq 0$, set $r = p(x_{n+1})/p(x_n)$ and

$$t = \begin{cases} \frac{(1 - u + r^2 u)^{1/2} - 1}{r - 1} & \text{if } r \neq 1, \\ u & \text{if } r = 1. \end{cases} \quad (1.40)$$

- (iii) If $p(x_n) = 0$, set $t = u^{1/2}$.
- (iv) Deliver $x = x_n + (x_{n+1} - x_n)t$.

1.2.3 Discrete distributions

The inverse transform method can also be applied to discrete distributions. Consider that the random variable x can take the discrete values $x = 1, \dots, N$ with point probabilities p_1, \dots, p_N , respectively. The corresponding PDF can be expressed as

$$p(x) = \sum_{i=1}^N p_i \delta(x - i), \quad (1.41)$$

where $\delta(x)$ is the Dirac distribution. Here $p(x)$ is assumed to be defined in an interval (a, b) with $a < 1$ and $b > N$. The corresponding cumulative distribution function is

$$\mathcal{P}(x) = \sum_{i=1}^{[x]} p_i, \quad (1.42)$$

where $[x]$ stands for the integer part of x . Notice that $\mathcal{P}(x) = 0$ when $x < 1$. Then, eq. (1.32) leads to the sampling formula

$$\begin{aligned} x &= 1 && \text{if } \xi \leq p_1 \\ &= 2 && \text{if } p_1 < \xi \leq p_1 + p_2 \\ &\vdots \\ &= j && \text{if } \sum_{i=1}^{j-1} p_i < \xi \leq \sum_{i=1}^j p_i \\ &\vdots \end{aligned} \tag{1.43}$$

We can define the quantities

$$P_1 = 0, \quad P_2 = p_1, \quad P_3 = p_1 + p_2, \quad \dots, \quad P_{N+1} = \sum_{i=1}^N p_i = 1. \tag{1.44}$$

To sample x we generate a random number ξ and set x equal to the index i such that

$$P_i < \xi \leq P_{i+1}. \tag{1.45}$$

If the number N of x -values is large, this sampling algorithm may be quite slow because of the large number of comparisons needed to determine the sampled value. The easiest method to reduce the number of comparisons is to use binary search instead of sequential search. The algorithm for binary search, for a given value of ξ , proceeds as follows:

- (i) Set $i = 1$ and $j = N + 1$.
- (ii) Set $k = [(i + j)/2]$.
- (iii) If $P_k < \xi$, set $i = k$; otherwise set $j = k$.
- (iv) If $j - i > 1$, go to step (ii).
- (v) Deliver i .

When $2^n < N \leq 2^{n+1}$, i is obtained after $n+1$ comparisons. This number of comparisons is evidently much less than the number required when using purely sequential search.

Walker's aliasing method

Walker (1977) described an optimal sampling method for discrete distributions, which yields the sampled value with only one comparison. The idea underlying Walker's method can be easily understood by resorting to graphical arguments (Salvat, 1987). For this purpose, let us represent the PDF (1.41) as a histogram constructed with N bars of width $1/N$ and heights Np_i (see fig. 1.3). Now, the histogram bars can be cut off at convenient heights and the resulting pieces can be arranged to fill up the square of unit side in such a way that each vertical line crosses, at most, two different pieces. This arrangement can be performed systematically by selecting the lowest and the highest bars in the histogram, say the ℓ th and the j th, respectively, and by cutting the highest bar off to complete the lowest one, which subsequently is kept unaltered. In order to

keep track of the performed transformation, we label the added piece with the “alias” value $K_\ell = j$, giving its original position in the histogram, and introduce the “cutoff” value F_ℓ defined as the height of the lower piece in the ℓ th bar of the resulting square. This lower piece keeps the label ℓ . Evidently, iteration of this process eventually leads to the complete square (after $N - 1$ steps). Notice that the point probabilities p_i can be reconstructed from the alias and cutoff values. We have

$$Np_i = F_i + \sum_{j \neq i} (1 - F_j) \delta(i, K_j), \quad (1.46)$$

where $\delta(i, j)$ denotes the Kronecker delta ($= 1$ if $i = j$ and $= 0$ otherwise). Walker’s method for random sampling of x proceeds as follows: We sample two independent random numbers, say ξ_1 and ξ_2 , and define the random point (ξ_1, ξ_2) , which is uniformly distributed in the square. If (ξ_1, ξ_2) lies over a piece labelled with the index i , we take $x = i$ as the selected value. Obviously, the probability of obtaining i as a result of the sampling equals the fractional area of the pieces labelled with i , which coincides with p_i .

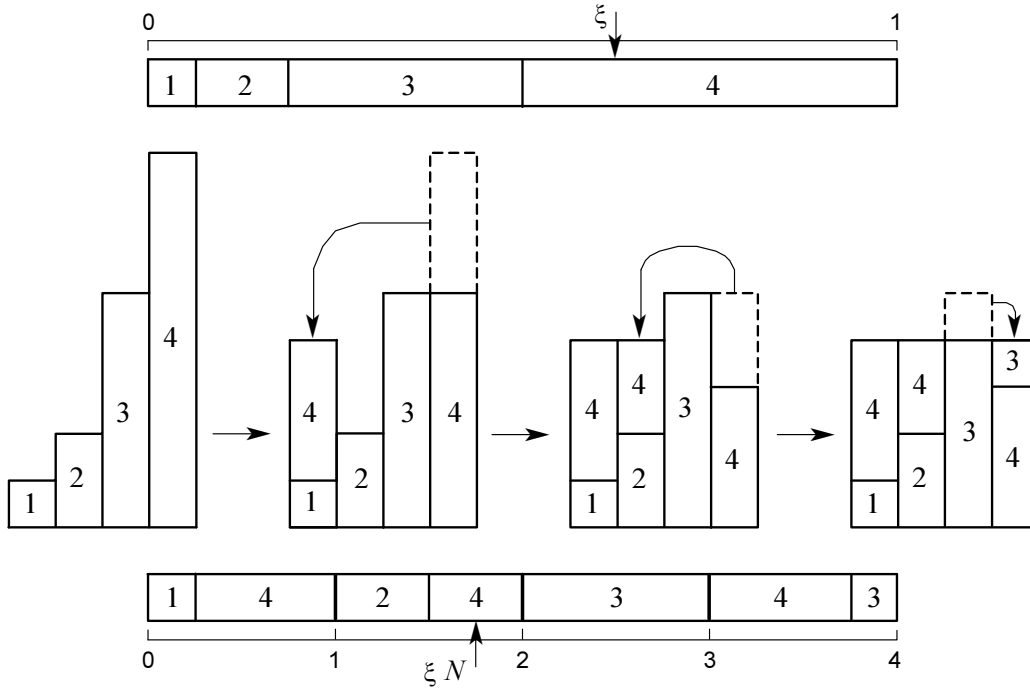


Figure 1.3: Graphical representation of the inverse transform method (top) and Walker’s aliasing method (bottom) for random sampling from a discrete distribution. In this example, the random variable can take the values $i = 1, 2, 3$ and 4 with relative probabilities 1, 2, 5 and 8, respectively.

As formulated above, Walker’s algorithm requires the generation of two random numbers for each sampled value of x . With the aid of the following trick, the x -value

can be generated from a single random number. Continuing with our graphical picture, assume that the N bars in the square are aligned consecutively to form a segment of length N (bottom of fig. 1.3). To sample x , we can generate a single random value ξN , which is uniformly distributed in $(0, N)$ and determines one of the segment pieces. The result of the sampling is the label of the selected piece. Explicitly, the sampling algorithm proceeds as follows:

- (i) Generate a random number ξ and set $R = \xi N + 1$.
- (ii) Set $i = [R]$ and $r = R - i$.
- (iii) If $r > F_i$, deliver $x = K_i$.
- (iv) Deliver $x = i$.

We see that the sampling of x involves only the generation of a random number and one comparison (irrespective of the number N of possible outcomes). The price we pay for this simplification reduces to doubling the number of memory locations that are needed: the two arrays K_i and F_i are used instead of the single array p_i (or P_i). Unfortunately, the calculation of alias and cutoff values is fairly involved and this limits the applicability of Walker's algorithm to distributions that remain constant during the course of the simulation.

1.2.4 Rejection methods

The inverse transform method for random sampling is based on a one-to-one correspondence between x and ξ values, which is expressed in terms of a single-valued function. There is another kind of sampling method, due to von Neumann, that consists of sampling a random variable from a certain distribution [different from $p(x)$] and subjecting it to a random test to determine whether it will be accepted for use or rejected. These rejection methods lead to very general techniques for sampling from any PDF.

The rejection algorithms can be understood in terms of simple graphical arguments (fig. 1.4). Consider that, by means of the inverse transform method or any other available sampling method, random values of x are generated from a PDF $\pi(x)$. For each sampled value of x we sample a random value y uniformly distributed in the interval $(0, C\pi(x))$, where C is a positive constant. Evidently, the points (x, y) , generated in this way, are uniformly distributed in the region A of the plane limited by the x -axis ($y = 0$) and the curve $y = C\pi(x)$. Conversely, if (by some means) we generate random points (x, y) uniformly distributed in A, their x -coordinate is a random variable distributed according to $\pi(x)$ (irrespective of the value of C). Now, consider that the distribution $\pi(x)$ is such that $C\pi(x) \geq p(x)$ for some $C > 0$ and that we generate random points (x, y) uniformly distributed in the region A as described above. If we reject the points with $y > p(x)$, the accepted ones (with $y \leq p(x)$) are uniformly distributed in the region between the x -axis and the curve $y = p(x)$ and hence, their x -coordinate is distributed according to $p(x)$.

A rejection method is thus completely specified by representing the PDF $p(x)$ as

$$p(x) = C\pi(x)r(x), \quad (1.47)$$

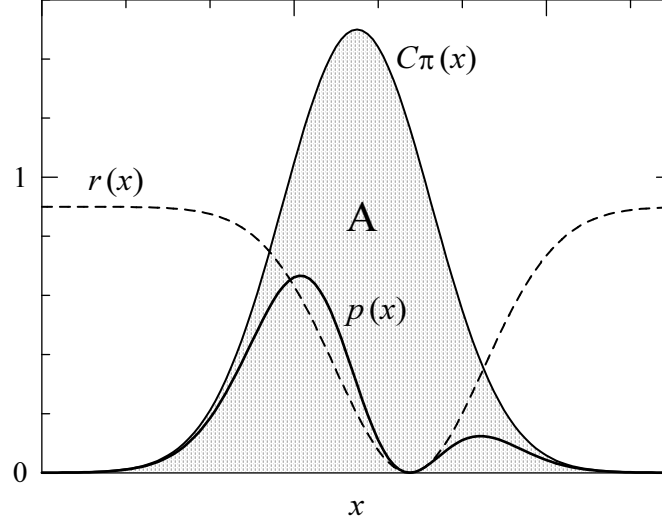


Figure 1.4: Random sampling from a distribution $p(x)$ using a rejection method.

where $\pi(x)$ is a PDF that can be easily sampled e.g. by the inverse transform method, C is a positive constant and the function $r(x)$ satisfies the conditions $0 < r(x) \leq 1$. The rejection algorithm for sampling from $p(x)$ proceeds as follows:

- (i) Generate a random value x from $\pi(x)$.
- (ii) Generate a random number ξ .
- (iii) If $\xi > r(x)$, go to step (i).
- (iv) Deliver x .

From the geometrical arguments given above, it is clear that the algorithm does yield x values distributed according to $p(x)$. The following is a more formal proof: Step (i) produces x -values in the interval $(x, x + dx)$ with probability $\pi(x) dx$, these values are accepted with probability $r(x) = p(x)/[C\pi(x)]$ and, therefore, (apart from a normalization constant) the probability of delivering a value in $(x, x + dx)$ is equal to $p(x) dx$ as required. It is important to realize that, as regards Monte Carlo, the normalization of the simulated PDF is guaranteed by the mere fact that the algorithm delivers some value of x .

The efficiency of the algorithm, i.e. the probability of accepting a generated x -value, is

$$\epsilon = \int_a^b r(x)\pi(x) dx = \frac{1}{C}. \quad (1.48)$$

Graphically, the efficiency equals the ratio of the areas under the curves $y = p(x)$ and $y = C\pi(x)$, which are 1 and C , respectively. For a given $\pi(x)$, since $r(x) \leq 1$, the constant C must satisfy the condition $C\pi(x) \geq p(x)$ for all x . The minimum value of C , with the requirement that $C\pi(x) = p(x)$ for some x , gives the optimum efficiency.

The PDF $\pi(x)$ in eq. (1.47) should be selected in such a way that the resulting sampling algorithm is as fast as possible. In particular, random sampling from $\pi(x)$

must be performed rapidly, by the inverse transform method or by the composition method (see below). High efficiency is also desirable, but not decisive. One hundred percent efficiency is obtained only with $\pi(x) = p(x)$ (but random sampling from this PDF is just the problem we want to solve); any other PDF gives a lower efficiency. The usefulness of the rejection method lies in the fact that a certain loss of efficiency can be largely compensated with the ease of sampling x from $\pi(x)$ instead of $p(x)$. A disadvantage of this method is that it requires the generation of several random numbers ξ to sample each x -value.

1.2.5 Two-dimensional variables. Composition methods

Let us consider a two-dimensional random variable (x, y) with joint probability distribution $p(x, y)$. Introducing the marginal PDF $q(y)$ and the conditional PDF $p(x|y)$ [see eqs. (1.18) and (1.20)],

$$q(y) \equiv \int p(x, y) dx, \quad p(x|y) = \frac{p(x, y)}{q(y)},$$

the two-variate distribution can be expressed as

$$p(x, y) = q(y) p(x|y). \quad (1.49)$$

It is now evident that to generate random points (x, y) from $p(x, y)$ we can first sample y from $q(y)$ and then x from $p(x|y)$. Hence, two-dimensional random variables can be generated by using single-variable sampling methods. This is also true for multivariate distributions, because an n -dimensional PDF can always be expressed as the product of a single-variable marginal distribution and an $(n - 1)$ -dimensional conditional PDF.

From the definition of the marginal PDF of x ,

$$q(x) \equiv \int p(x, y) dy = \int q(y) p(x|y) dy, \quad (1.50)$$

it is clear that if we sample y from $q(y)$ and, then, x from $p(x|y)$, the generated values of x are distributed according to $q(x)$. This idea is the basis of the *composition* methods, which are applicable when $p(x)$, the distribution to be simulated, is a probability mixture of several PDFs. More specifically, we consider that $p(x)$ can be expressed as

$$p(x) = \int w(y) p_y(x) dy, \quad (1.51)$$

where $w(y)$ is a continuous distribution and $p_y(x)$ is a family of one-parameter PDFs, where y is the parameter identifying a unique distribution. Notice that if the parameter y takes only integer values $y = i$ with point probabilities w_i , we would write

$$p(x) = \sum_i w_i p_i(x). \quad (1.52)$$

The composition method for random sampling from the PDF $p(x)$ is as follows. First, a value of y (or i) is drawn from the PDF $w(y)$ and then x is sampled from the PDF $p_y(x)$ for that chosen y .

This technique may be applied to generate random values from complex distributions obtained by combining simpler distributions that are themselves easily generated, by the inverse transform method or by rejection methods.

Devising fast, exact methods for random sampling from a given PDF is an interesting technical challenge. The ultimate criterion for the quality of a sampling algorithm is its speed in actual simulations: the best algorithm is the fastest. However, programming simplicity and elegance may justify the use of slower algorithms. For simple analytical distributions that have an analytical inverse cumulative distribution function, the inverse transform method is usually satisfactory. This is the case for a few elementary distributions (e.g. the uniform and exponential distributions considered above). The inverse transform method is also adequate for discrete distributions and for continuous PDFs given in numerical form. By combining the inverse transform, rejection and composition methods we can devise sampling algorithms for virtually any (single- or multivariate) PDF.

Example 1. Sampling from the normal distribution

Frequently, we need to generate random values from the normal (or Gaussian) distribution

$$p_G(x) = \frac{1}{\sqrt{2\pi}} \exp(-x^2/2). \quad (1.53)$$

Since the cumulative distribution function cannot be inverted analytically, the inverse transform method is not appropriate. The easiest (but not the fastest) method to sample from the normal distribution consists of generating two independent random variables at a time, as follows. Let x_1 and x_2 be two independent normal variables. They determine a random point in the plane with PDF

$$p_{2G}(x_1, x_2) = p_G(x_1) p_G(x_2) = \frac{1}{2\pi} \exp[-(x_1^2 + x_2^2)/2].$$

Introducing the polar coordinates r and ϕ ,

$$x_1 = r \cos \phi, \quad x_2 = r \sin \phi,$$

the PDF can be expressed as

$$p_{2G}(x_1, x_2) dx_1 dx_2 = \frac{1}{2\pi} \exp(-r^2/2) r dr d\phi = \left[\exp(-r^2/2) r dr \right] \left[\frac{1}{2\pi} d\phi \right].$$

We see that r and ϕ are independent random variables. The angle ϕ is distributed uniformly on $(0, 2\pi)$ and can be sampled as $\phi = 2\pi\xi$. The PDF of r is $\exp(-r^2/2) r$ and

the corresponding cumulative distribution function is $\mathcal{P}(r) = 1 - \exp(-r^2/2)$. Therefore, r can be generated by the inverse transform method as

$$r = \sqrt{-2 \ln(1 - \xi)} = \sqrt{-2 \ln \xi}.$$

The two independent normal random variables are given by

$$\begin{aligned} x_1 &= \sqrt{-2 \ln \xi_1} \cos(2\pi \xi_2), \\ x_2 &= \sqrt{-2 \ln \xi_1} \sin(2\pi \xi_2), \end{aligned} \quad (1.54)$$

where ξ_1 and ξ_2 are two independent random numbers. This procedure is known as the Box-Müller method. It has the advantages of being exact and easy to program (it can be coded as a single FORTRAN statement).

The mean and variance of the normal variable are $\langle x \rangle = 0$ and $\text{var}(x) = 1$. The linear transformation

$$X = m + \sigma x \quad (\sigma > 0) \quad (1.55)$$

defines a new random variable. From the properties (1.14) and (1.29), we have

$$\langle X \rangle = m \quad \text{and} \quad \text{var}(X) = \sigma^2. \quad (1.56)$$

The PDF of X is

$$p(X) = p_G(x) \frac{dx}{dX} = \frac{1}{\sigma \sqrt{2\pi}} \exp \left[-\frac{(X - m)^2}{2\sigma^2} \right], \quad (1.57)$$

i.e. X is normally distributed with mean m and variance σ^2 . Hence, to generate X we only have to sample x using the Box-Müller method and apply the transformation (1.55).

Example 2. Uniform distribution on the unit sphere

In radiation transport, the direction of motion of a particle is described by a unit vector $\hat{\mathbf{d}}$. Given a certain frame of reference, the direction $\hat{\mathbf{d}}$ can be specified by giving either its direction cosines (u, v, w) (i.e. the projections of $\hat{\mathbf{d}}$ on the directions of the coordinate axes) or the polar angle θ and the azimuthal angle ϕ , defined as in fig. 1.5,

$$\hat{\mathbf{d}} = (u, v, w) = (\sin \theta \cos \phi, \sin \theta \sin \phi, \cos \theta). \quad (1.58)$$

Notice that $\theta \in (0, \pi)$ and $\phi \in (0, 2\pi)$.

A direction vector can be regarded as a point on the surface of the unit sphere. Consider an isotropic source of particles, i.e. such that the initial direction (θ, ϕ) of emitted particles is a random point uniformly distributed on the surface of the sphere. The PDF is

$$p(\theta, \phi) d\theta d\phi = \frac{1}{4\pi} \sin \theta d\theta d\phi = \left[\frac{\sin \theta}{2} d\theta \right] \left[\frac{1}{2\pi} d\phi \right]. \quad (1.59)$$

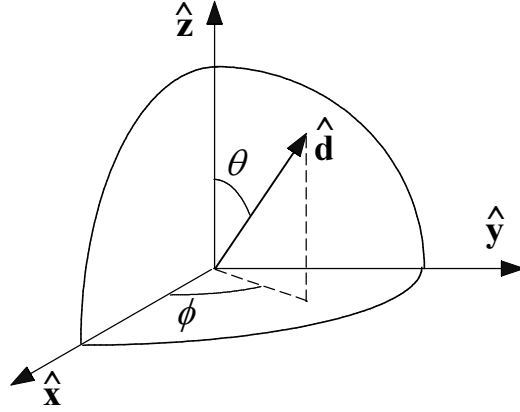


Figure 1.5: Polar and azimuthal angles of a direction vector.

That is, θ and ϕ are independent random variables with PDFs $p_\theta(\theta) = \sin \theta/2$ and $p_\phi(\phi) = 1/(2\pi)$, respectively. Therefore, the initial direction of a particle from an isotropic source can be generated by applying the inverse transform method to these PDFs,

$$\theta = \arccos(1 - 2\xi_1), \quad \phi = 2\pi\xi_2. \quad (1.60)$$

In some cases, it is convenient to replace the polar angle θ by the variable

$$\mu = (1 - \cos \theta)/2, \quad (1.61)$$

which varies from 0 ($\theta = 0$) to 1 ($\theta = \pi$). In the case of an isotropic distribution, the PDF of μ is

$$p_\mu(\mu) = p_\theta(\theta) \left(\frac{d\mu}{d\theta} \right)^{-1} = 1. \quad (1.62)$$

That is, a set of random points (μ, ϕ) uniformly distributed on the rectangle $(0, 1) \times (0, 2\pi)$ corresponds to a set of random directions (θ, ϕ) uniformly distributed on the unit sphere.

1.3 Monte Carlo integration

As pointed out by James (1980), at least in a formal sense, all Monte Carlo calculations are equivalent to integrations. This equivalence permits a formal theoretical foundation for Monte Carlo techniques. An important aspect of simulation is the evaluation of the statistical uncertainties of the calculated quantities. We shall derive the basic formulae by considering the simplest Monte Carlo calculation, namely, the evaluation of a unidimensional integral. Evidently, the results are also valid for multidimensional integrals.

Consider the integral

$$I = \int_a^b F(x) dx, \quad (1.63)$$

which we recast in the form of an expectation value,

$$I = \int f(x) p(x) dx \equiv \langle f \rangle, \quad (1.64)$$

by introducing an arbitrary PDF $p(x)$ and setting $f(x) = F(x)/p(x)$ [it is assumed that $p(x) > 0$ in (a, b) and $p(x) = 0$ outside this interval]. The Monte Carlo evaluation of the integral I is very simple: generate a large number N of random points x_i from the PDF $p(x)$ and accumulate the sum of values $f(x_i)$ in a counter. At the end of the calculation the expected value of f is estimated as

$$\bar{f} \equiv \frac{1}{N} \sum_{i=1}^N f(x_i). \quad (1.65)$$

The law of large numbers says that, as N becomes very large,

$$\bar{f} \rightarrow I \quad (\text{in probability}). \quad (1.66)$$

In statistical terminology, this means that \bar{f} , the Monte Carlo result, is a *consistent estimator* of the integral (1.63). This is valid for any function $f(x)$ that is finite and piecewise continuous, i.e. with a finite number of discontinuities.

The law of large numbers (1.66) can be restated as

$$\langle f \rangle = \lim_{N \rightarrow \infty} \frac{1}{N} \sum_{i=1}^N f(x_i). \quad (1.67)$$

By applying this law to the integral that defines the variance of $f(x)$ [cf. eq. (1.16)]

$$\text{var}\{f(x)\} = \int f^2(x) p(x) dx - \langle f \rangle^2, \quad (1.68)$$

we obtain

$$\text{var}\{f(x)\} = \lim_{N \rightarrow \infty} \left\{ \frac{1}{N} \sum_{i=1}^N [f(x_i)]^2 - \left[\frac{1}{N} \sum_{i=1}^N f(x_i) \right]^2 \right\}. \quad (1.69)$$

The expression in curly brackets is a consistent estimator of the variance of $f(x)$. It is advisable (see below) to accumulate the squared function values $[f(x_i)]^2$ in a counter and, at the end of the simulation, estimate $\text{var}\{f(x)\}$ according to eq. (1.69).

It is clear that different Monte Carlo runs [with different, independent sequences of N random numbers x_i from $p(x)$] will yield different estimates \bar{f} . This implies that the outcome of our Monte Carlo code is affected by statistical uncertainties, similar to those found in laboratory experiments, which need to be properly evaluated to determine the “accuracy” of the Monte Carlo result. For this purpose, we may consider \bar{f} as a random

variable, the PDF of which is, in principle, unknown. Its mean and variance are given by

$$\langle \bar{f} \rangle = \left\langle \frac{1}{N} \sum_{i=1}^N f(x_i) \right\rangle = \frac{1}{N} \sum_{i=1}^N \langle f \rangle = \langle f \rangle \quad (1.70)$$

and

$$\text{var}(\bar{f}) = \text{var} \left[\frac{1}{N} \sum_{i=1}^N f(x_i) \right] = \frac{1}{N^2} \sum_{i=1}^N \text{var}\{f(x)\} = \frac{1}{N} \text{var}\{f(x)\}, \quad (1.71)$$

where use has been made of properties of the expectation and variance operators. The standard deviation (or standard error) of \bar{f} ,

$$\sigma_f \equiv \sqrt{\text{var}(\bar{f})} = \sqrt{\frac{\text{var}\{f(x)\}}{N}}, \quad (1.72)$$

gives a measure of the statistical uncertainty of the Monte Carlo estimate \bar{f} . The result (1.72) has an important practical implication: in order to reduce the statistical uncertainty by a factor of 10, we have to increase the sample size N by a factor of 100. Evidently, this sets a limit to the accuracy that can be attained with the available computer power.

We can now invoke the central limit theorem (see e.g. James, 1980), which establishes that, in the limit $N \rightarrow \infty$, the PDF of \bar{f} is a normal (Gaussian) distribution with mean $\langle f \rangle$ and standard deviation σ_f ,

$$p(\bar{f}) = \frac{1}{\sigma_f \sqrt{2\pi}} \exp \left(-\frac{(\bar{f} - \langle f \rangle)^2}{2\sigma_f^2} \right). \quad (1.73)$$

It follows that, for sufficiently large values of N , for which the theorem is applicable, the interval $\bar{f} \pm n\sigma_f$ contains the exact value $\langle f \rangle$ with a probability of 68.3% if $n = 1$, 95.4% if $n = 2$ and 99.7% if $n = 3$ (3σ rule).

The central limit theorem is a very powerful tool, since it predicts that the generated values of \bar{f} follow a specific distribution, but it applies only asymptotically. The minimum number N of sampled values needed to apply the theorem with confidence depends on the problem under consideration. If, in the case of our problem, the third central moment of f ,

$$\mu_3 \equiv \int [f(x) - \langle f \rangle]^3 p(x) dx, \quad (1.74)$$

exists, the theorem is essentially satisfied when

$$|\mu_3| \ll \sigma_f^3 \sqrt{N}. \quad (1.75)$$

In general, it is advisable to study the distribution of the estimator to ascertain the applicability of the central limit theorem. In most Monte Carlo calculations, however, statistical errors are estimated by simply assuming that the theorem is satisfied, irrespective of the sample size. We shall adopt this practice and report Monte Carlo results in the form $\bar{f} \pm 3\sigma_f$. In simulations of radiation transport, this is empirically validated

by the fact that simulated continuous distributions do “look” continuous (i.e. the “error bars” define a smooth band).

Each possible $p(x)$ defines a Monte Carlo algorithm to calculate the integral I , eq. (1.63). The simplest algorithm (crude Monte Carlo) is obtained by using the uniform distribution $p(x) = 1/(b-a)$. Evidently, $p(x)$ determines not only the density of sampled points x_i , but also the magnitude of the variance $\text{var}\{f(x)\}$, eq. (1.68),

$$\text{var}\{f(x)\} = \int_a^b p(x) \left[\frac{F(x)}{p(x)} \right]^2 dx - I^2 = \int_a^b F(x) \left[\frac{F(x)}{p(x)} - I \right] dx. \quad (1.76)$$

As a measure of the effectiveness of a Monte Carlo algorithm, it is common to use the efficiency ϵ , which is defined by

$$\epsilon = 1/[\sigma_f^2 T], \quad (1.77)$$

where T is the computing time (or any other measure of the calculation effort) needed to get the simulation result. Since σ_f^2 and T are roughly proportional to N^{-1} and N , respectively, ϵ is a constant (i.e. it is independent of N), on average.

The so-called variance-reduction methods are techniques that aim to optimize the *efficiency* of the simulation through an adequate choice of the PDF $p(x)$. Improving the efficiency of the algorithms is an important, and delicate, part of the art of Monte Carlo simulation. The interested reader is addressed to the specialized bibliography (e.g. Rubinstein, 1981). Although of common use, the term “variance reduction” is somewhat misleading, since a reduction in variance does not necessarily lead to improved efficiency. To make this clear, consider that a Monte Carlo algorithm, based on a certain PDF $p(x)$, has a variance that is less than that of crude Monte Carlo (i.e. with the uniform distribution); if the generation of x -values from $p(x)$ takes a longer time than for the uniform distribution, the “variance-reduced” algorithm may be less efficient than crude Monte Carlo. Hence, one should avoid using PDFs that are too difficult to sample.

1.4 Simulation of radiation transport

In this section, we describe the essentials of Monte Carlo simulation of radiation transport. For the sake of simplicity, we limit our considerations to the detailed simulation method, where all the interaction events experienced by a particle are simulated in chronological succession, and we disregard the production of secondary particles, so that only one kind of particle is transported.

1.4.1 Scattering model and probability distributions

Consider a particle with energy E (kinetic energy, in the case of electrons and positrons) moving in a given medium. We limit our considerations to homogeneous “random scattering” media, such as gases, liquids and amorphous solids, where the “molecules”

are distributed at random with uniform density. The composition of the medium is specified by its stoichiometric formula, i.e. atomic number Z_i and number of atoms per molecule n_i of all the elements present. The stoichiometric indices n_i need not have integer values. In the case of alloys, for instance, they may be set equal to the percentage in number of each element and then a “molecule” is a group of 100 atoms with the appropriate proportion of each element. The “molecular weight” is $A_M = \sum n_i A_i$, where A_i is the atomic weight of the i -th element. The number of molecules per unit volume is given by

$$\mathcal{N} = N_A \frac{\rho}{A_M}, \quad (1.78)$$

where N_A is Avogadro’s number and ρ is the mass density of the material.

In each interaction, the particle may lose energy W and/or change its direction of movement. The angular deflection is determined by the polar scattering angle θ , i.e. the angle between the directions of the particle before and after the interaction, and the azimuthal angle ϕ . Let us assume that the particle can interact with the medium through two independent mechanisms, denoted as “A” and “B” (for instance, elastic and inelastic scattering, in the case of low-energy electrons). The scattering model is completely specified by the molecular differential cross sections (DCS)

$$\frac{d^2\sigma_A}{dWd\Omega}(E; W, \theta) \quad \text{and} \quad \frac{d^2\sigma_B}{dWd\Omega}(E; W, \theta), \quad (1.79)$$

where $d\Omega$ is a solid angle element in the direction (θ, ϕ) . We have made the parametric dependence of the DCSs on the particle energy E explicit. Considering that the molecules in the medium are oriented at random, the DCS is independent of the azimuthal scattering angle, i.e. the angular distribution of scattered particles is axially symmetrical around the direction of incidence. The total cross sections (per molecule) are

$$\sigma_{A,B}(E) = \int_0^E dW \int_0^\pi 2\pi \sin \theta d\theta \frac{d^2\sigma_{A,B}}{dWd\Omega}(E; W, \theta). \quad (1.80)$$

The PDFs of the energy loss and the polar scattering angle in individual scattering events are

$$p_{A,B}(E; W, \theta) = \frac{2\pi \sin \theta}{\sigma_{A,B}(E)} \frac{d^2\sigma_{A,B}}{dWd\Omega}(E; W, \theta). \quad (1.81)$$

Notice that $p_A(E; W, \theta)dWd\theta$ gives the (normalized) probability that, in a scattering event of type A, the particle loses energy in the interval $(W, W + dW)$ and is deflected into directions with polar angle (relative to the initial direction) in the interval $(\theta, \theta + d\theta)$. The azimuthal scattering angle in each collision is uniformly distributed in the interval $(0, 2\pi)$, i.e.

$$p(\phi) = \frac{1}{2\pi}. \quad (1.82)$$

The total interaction cross section is

$$\sigma_T(E) = \sigma_A(E) + \sigma_B(E). \quad (1.83)$$

When the particle interacts with the medium, the kind of interaction that occurs is a discrete random variable, that takes the values “A” and “B” with probabilities

$$p_A = \sigma_A/\sigma_T \quad \text{and} \quad p_B = \sigma_B/\sigma_T. \quad (1.84)$$

It is worth recalling that this kind of single scattering model is only valid when diffraction effects resulting from coherent scattering from several centres (e.g. Bragg diffraction, channelling of charged particles) are negligible. This means that the simulation is applicable only to amorphous media and, with some care, to polycrystalline solids.

To get an intuitive picture of the scattering process, we can imagine each molecule as a sphere of radius r_s such that the cross-sectional area πr_s^2 equals the total cross section σ_T . Now, assume that a particle impinges normally on a very thin material foil of thickness ds . What the particle sees in front of it is a uniform distribution of $\mathcal{N} ds$ spheres per unit surface. An interaction takes place when the particle strikes one of these spheres. Therefore, the probability of interaction within the foil equals the fractional area covered by the spheres, $\mathcal{N}\sigma_T ds$. In other words, $\mathcal{N}\sigma_T$ is the interaction probability per unit path length. Its inverse,

$$\lambda_T \equiv (\mathcal{N}\sigma_T)^{-1}, \quad (1.85)$$

is the (total) mean free path between interactions.

Let us now consider a particle that moves within an unbounded medium. The PDF $p(s)$ of the path length s of the particle from its current position to the site of the next interaction may be obtained as follows. The probability that the particle travels a path length s without interacting is

$$\mathcal{F}(s) = \int_s^\infty p(s') ds'. \quad (1.86)$$

The probability $p(s) ds$ of having the next interaction when the travelled length is in the interval $(s, s + ds)$ equals the product of $\mathcal{F}(s)$ (the probability of arrival at s without interacting) and $\lambda_T^{-1} ds$ (the probability of interacting within ds). It then follows that

$$p(s) = \lambda_T^{-1} \int_s^\infty p(s') ds'. \quad (1.87)$$

The solution of this integral equation, with the boundary condition $p(\infty) = 0$, is the familiar exponential distribution

$$p(s) = \lambda_T^{-1} \exp(-s/\lambda_T). \quad (1.88)$$

Notice that the mean free path λ_T coincides with the average path length between collisions:

$$\langle s \rangle = \int_0^\infty s p(s) ds = \lambda_T. \quad (1.89)$$

The differential inverse mean free path for the interaction process A is defined as

$$\frac{d^2 \lambda_A^{-1}}{dW d\Omega}(E; W, \theta) = \mathcal{N} \frac{d^2 \sigma_A}{dW d\Omega}(E; W, \theta). \quad (1.90)$$

Evidently, the integral of the differential inverse mean free path gives the inverse mean free path for the process,

$$\lambda_A^{-1} = \int dW \int 2\pi \sin \theta d\theta \frac{d^2 \lambda_A^{-1}}{dW d\Omega}(E; W, \theta) = \mathcal{N} \sigma_A. \quad (1.91)$$

In the literature, the product $\mathcal{N} \sigma_A$ is frequently called the *macroscopic cross section*, although this name is not appropriate for a quantity that has the dimensions of inverse length. Notice that the total inverse mean free path is the sum of the inverse mean free paths of the different active interaction mechanisms,

$$\lambda_T^{-1} = \lambda_A^{-1} + \lambda_B^{-1}. \quad (1.92)$$

1.4.2 Generation of random tracks

Each particle track starts off at a given position, with initial direction and energy in accordance with the characteristics of the source. The “state” of a particle immediately after an interaction (or after entering the sample or starting its trajectory) is defined by its position coordinates $\mathbf{r} = (x, y, z)$, energy E and direction cosines of the direction of flight, i.e. the components of the unit vector $\hat{\mathbf{d}} = (u, v, w)$, as seen from the laboratory reference frame. Each simulated track is thus characterized by a series of states $\mathbf{r}_n, E_n, \hat{\mathbf{d}}_n$, where \mathbf{r}_n is the position of the n -th scattering event and E_n and $\hat{\mathbf{d}}_n$ are the energy and direction cosines of the direction of movement just *after* that event.

The generation of random tracks proceeds as follows. Let us assume that a track has already been simulated up to a state $\mathbf{r}_n, E_n, \hat{\mathbf{d}}_n$. The length s of the free path to the next collision, the involved scattering mechanism, the change of direction and the energy loss in this collision are random variables that are sampled from the corresponding PDFs, using the methods described in section 1.2. Hereafter, ξ stands for a random number uniformly distributed in the interval $(0,1)$.

The length of the free flight is distributed according to the PDF given by eq. (1.88). Random values of s are generated by using the sampling formula [see eq. (1.36)]

$$s = -\lambda_T \ln \xi. \quad (1.93)$$

The following interaction occurs at the position

$$\mathbf{r}_{n+1} = \mathbf{r}_n + s \hat{\mathbf{d}}_n. \quad (1.94)$$

The type of this interaction (“A” or “B”) is selected from the point probabilities given by eq. (1.84) using the inverse transform method (section 1.2.2). The energy loss W and the polar scattering angle θ are sampled from the distribution $p_{A,B}(E; W, \theta)$, eq. (1.81), by using a suitable sampling technique. The azimuthal scattering angle is generated, according to the uniform distribution in $(0, 2\pi)$, as $\phi = 2\pi\xi$.

After sampling the values of W , θ and ϕ , the energy of the particle is reduced, $E_{n+1} = E_n - W$, and the direction of movement after the interaction $\hat{\mathbf{d}}_{n+1} = (u', v', w')$

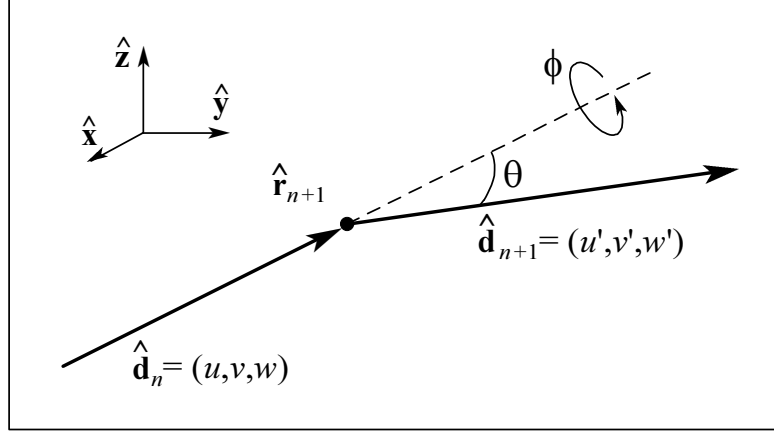


Figure 1.6: Angular deflections in single-scattering events.

is obtained by performing a rotation of $\hat{\mathbf{d}}_n = (u, v, w)$ (see fig. 1.6). The rotation matrix $R(\theta, \phi)$ is determined by the polar and azimuthal scattering angles. To explicitly obtain the direction vector $\hat{\mathbf{d}}_{n+1} = R(\theta, \phi)\hat{\mathbf{d}}_n$ after the interaction, we first note that, if the initial direction is along the z -axis, the direction after the collision is

$$\begin{pmatrix} \sin \theta \cos \phi \\ \sin \theta \sin \phi \\ \cos \theta \end{pmatrix} = R_z(\phi)R_y(\theta)\hat{\mathbf{z}}, \quad (1.95)$$

where $\hat{\mathbf{z}} = (0, 0, 1)$ and

$$R_y(\theta) = \begin{pmatrix} \cos \theta & 0 & \sin \theta \\ 0 & 1 & 0 \\ -\sin \theta & 0 & \cos \theta \end{pmatrix} \quad \text{and} \quad R_z(\phi) = \begin{pmatrix} \cos \phi & -\sin \phi & 0 \\ \sin \phi & \cos \phi & 0 \\ 0 & 0 & 1 \end{pmatrix} \quad (1.96)$$

are rotation matrices corresponding to active rotations of angles θ and ϕ about the y - and z -axes, respectively. On the other hand, if ϑ and φ are the polar and azimuthal angles of the initial direction

$$\hat{\mathbf{d}}_n = (\sin \vartheta \cos \varphi, \sin \vartheta \sin \varphi, \cos \vartheta), \quad (1.97)$$

the rotation $R_y(-\vartheta)R_z(-\varphi)$ transforms the vector $\hat{\mathbf{d}}_n$ into $\hat{\mathbf{z}}$. It is then clear that the final direction vector $\hat{\mathbf{d}}_{n+1}$ can be obtained by performing the following sequence of rotations of the initial direction vector: 1) $R_y(-\vartheta)R_z(-\varphi)$, which transforms $\hat{\mathbf{d}}_n$ into $\hat{\mathbf{z}}$; 2) $R_z(\phi)R_y(\theta)$, which rotates $\hat{\mathbf{z}}$ according to the sampled polar and azimuthal scattering angles; and 3) $R_z(\varphi)R_y(\vartheta)$, which inverts the rotation of the first step. Hence

$$R(\theta, \phi) = R_z(\varphi)R_y(\vartheta)R_z(\phi)R_y(\theta)R_y(-\vartheta)R_z(-\varphi). \quad (1.98)$$

The final direction vector is

$$\hat{\mathbf{d}}_{n+1} = R(\theta, \phi) \hat{\mathbf{d}}_n = R_z(\varphi) R_y(\vartheta) \begin{pmatrix} \sin \theta \cos \phi \\ \sin \theta \sin \phi \\ \cos \theta \end{pmatrix} \quad (1.99)$$

and its direction cosines are

$$\begin{aligned} u' &= u \cos \theta + \frac{\sin \theta}{\sqrt{1-w^2}} [uw \cos \phi - v \sin \phi], \\ v' &= v \cos \theta + \frac{\sin \theta}{\sqrt{1-w^2}} [vw \cos \phi + u \sin \phi], \\ w' &= w \cos \theta - \sqrt{1-w^2} \sin \theta \cos \phi. \end{aligned} \quad (1.100)$$

These equations are indeterminate when $w \simeq \pm 1$, i.e. when the initial direction is nearly parallel or antiparallel to the z -axis; in this case we can simply set

$$u = \pm \sin \theta \cos \phi, \quad v = \pm \sin \theta \sin \phi, \quad w = \pm \cos \theta. \quad (1.101)$$

Moreover, eqs. (1.100) are not very stable numerically and the normalization of $\hat{\mathbf{d}}_{n+1}$ tends to drift from 1 after repeated usage. This must be remedied by periodically renormalizing $\hat{\mathbf{d}}_{n+1}$. The change of direction expressed by eqs. (1.100) and (1.101) is performed by the subroutine **DIRECT** (see the **PENELOPE** source listing).

The simulation of the track then proceeds by repeating these steps. A track is finished either when it leaves the material system or when the energy becomes smaller than a given energy E_{abs} , which is the energy where particles are assumed to be effectively stopped and absorbed in the medium.

1.4.3 Particle transport as a Markov process

The foregoing concepts, definitions and simulation scheme rest on the assumption that particle transport can be modelled as a Markov process², i.e. “future values of a random variable (interaction event) are statistically determined by present events and depend only on the event immediately preceeding”. Owing to the Markovian character of the transport, we can stop the generation of a particle history at an arbitrary state (any point of the track) and resume the simulation from this state without introducing any bias in the results.

In mixed simulations of electron/positron transport, it is necessary to limit the length s of each “free jump” so that it does not exceed a given value s_{max} . To accomplish this, we still sample the free path length s to the next interaction from the exponential PDF

²The quoted definition is from the Webster’s Encyclopedic Unabridged Dictionary of the English Language (Portland House, New York, 1989).

(1.88), but when $s > s_{\max}$ we only let the particle advance a distance s_{\max} along the direction of motion. At the end of the truncated free jump we do nothing (i.e. the particle keeps its energy and direction of motion unaltered); however, for programming convenience, we shall say that the particle suffers a *delta interaction* (actually, a “non-interaction”). When the sampled value of s is less than s_{\max} , a real interaction is simulated. After the interaction (either real or delta), we sample a new free path s , move the particle a distance $s' = \min(s, s_{\max})$, etc. From the Markovian character of the transport, it is clear that the insertion of delta interactions keeps the simulation unbiased. If you do not see it so clearly, here comes a direct proof. First we note that the probability that a free jump ends with a delta interaction is

$$p_{\delta} = \int_{s_{\max}}^{\infty} p(s) ds = \exp(-s_{\max}/\lambda_T). \quad (1.102)$$

To obtain the probability $p(s)ds$ of having the first real interaction at a distance in the interval $(s, s + ds)$, we write $s = ns_{\max} + s'$ with $n = [s/s_{\max}]$ and, hence, $s' < s_{\max}$. The sought probability is then equal to the probability of having n successive delta interactions followed by a real interaction at a distance in $(s', s' + ds)$ from the last, n -th, delta interaction,

$$p(s) ds = p_{\delta}^n \lambda_T^{-1} \exp(-s'/\lambda_T) ds = \lambda_T^{-1} \exp(-s/\lambda_T) ds, \quad (1.103)$$

which is the correct value [cf. eq. (1.88)].

Up to this point, we have considered transport in a single homogeneous medium. In practical cases, however, the material structure where radiation is transported may consist of various regions with different compositions. We assume that the interfaces between contiguous media are sharp (i.e. there is no diffusion of chemical species across them) and passive (which amounts to neglecting e.g. surface plasmon excitation and transition radiation). In the simulation code, when a particle arrives at an interface, it is stopped there and the simulation is resumed with the interaction properties of the new medium. Obviously, this procedure is consistent with the Markovian property of the transport process.

Consider two homogeneous media, 1 and 2 (with corresponding mean free paths $\lambda_{T,1}$ and $\lambda_{T,2}$), separated by an interface, which is crossed by particles that move from the first medium to the second. The average path length between the last real interaction in medium 1 and the first real interaction in medium 2 is $\lambda_{T,1} + \lambda_{T,2}$, as can be easily verified by simulation. This result seemed paradoxical to some authors and induced confusion in the past. In fact, there is nothing odd here as you may easily verify (again by simulation) as follows. Assume particles being transported within a single homogeneous medium with an imaginary plane that acts as a “virtual” interface, splitting the medium into two halves. In the simulation, the particles do not see this interface, i.e. they do not stop when crossing. Every time a particle crosses the plane, we score the length s_{plane} of the track segment between the two real interactions immediately before and after the crossing. It is found that the average value of s_{plane} is $2\lambda_T$, in spite of the fact that the free path length between consecutive collisions was sampled from an exponential PDF

with the mean free path λ_T [yes, the scored values s_{plane} were generated from this PDF!]. The explanation of this result is that, as a consequence of the Markovian character, the average path length from the plane (an arbitrary *fixed* point in the track) back to the last collision (or up to the next collision) is λ_T .

1.5 Statistical averages and uncertainties

For the sake of being more specific, let us consider the simulation of a high-energy electron beam impinging on the surface of a semi-infinite water phantom. Each primary electron originates a shower of electrons and photons, which are individually tracked down to the corresponding absorption energy. Any quantity of interest Q is evaluated as the average score of a large number N of simulated random showers. Formally, Q can be expressed as an integral of the form (1.64),

$$Q = \int q p(q) dq, \quad (1.104)$$

where the PDF $p(q)$ is usually unknown. The simulation of individual showers provides a practical method to sample q from the “natural” PDF $p(q)$: from each generated shower we get a random value q_i distributed according to $p(q)$. The only difference to the case of Monte Carlo integration considered above is that now the PDF $p(q)$ describes a cascade of random interaction events, each with its characteristic PDF. The Monte Carlo estimate of Q is

$$\overline{Q} = \frac{1}{N} \sum_{i=1}^N q_i. \quad (1.105)$$

Thus, for instance, the average energy E_{dep} deposited within the water phantom per incident electron is obtained as

$$E_{\text{dep}} = \frac{1}{N} \sum_{i=1}^N e_i, \quad (1.106)$$

where e_i is the energy deposited by *all* the particles of the i -th shower. The statistical uncertainty (standard deviation) of the Monte Carlo estimate [eq. (1.72)] is

$$\sigma_Q = \sqrt{\frac{\text{var}(q)}{N}} = \sqrt{\frac{1}{N} \left[\frac{1}{N} \sum_{i=1}^N q_i^2 - \overline{Q}^2 \right]}. \quad (1.107)$$

As mentioned above, we shall usually express the simulation result in the form $\overline{Q} \pm 3\sigma_Q$, so that the interval $(\overline{Q} - 3\sigma_Q, \overline{Q} + 3\sigma_Q)$ contains the true value Q with 99.7% probability. Notice that to evaluate the standard deviation (1.107) we must score the squared contributions q_i^2 . In certain cases, the contributions q_i can only take the values 0 and 1, and the standard error can be determined without scoring the squares,

$$\sigma_Q = \sqrt{\frac{1}{N} \overline{Q}(1 - \overline{Q})}. \quad (1.108)$$

Simulation/scoring can also be used to compute continuous distributions. The simplest method is to “discretize” the distributions, by treating them as histograms, and to determine the “heights” of the different bars. To make the arguments clear, let us consider the depth-dose distribution $D(z)$, defined as the average energy deposited per unit depth and per incident electron within the water phantom. $D(z)dz$ is the average energy deposited at depths between z and $z+dz$ per incident electron, and the integral of $D(z)$ from 0 to ∞ is the average deposited energy E_{dep} (again, per incident electron). Since part of the energy is reflected back from the water phantom (through backscattered radiation), E_{dep} is less than the kinetic energy E_{inc} of the incident electrons. We are interested in determining $D(z)$ in a limited depth interval, say from $z = 0$ to $z = z_{\text{max}}$. The calculation proceeds as follows. First of all, we have to select a partition of the interval $(0, z_{\text{max}})$ into M different depth bins (z_{k-1}, z_k) , with $0 = z_0 < z_1 < \dots < z_M = z_{\text{max}}$. Let $e_{ij,k}$ denote the amount of energy deposited into the k -th bin by the j -th particle of the i -th shower (each incident electron may produce multiple secondary particles). The average energy deposited into the k -th bin (per incident electron) is obtained as

$$E_k = \frac{1}{N} \sum_{i=1}^N e_{i,k} \quad \text{with} \quad e_{i,k} \equiv \sum_j e_{ij,k}, \quad (1.109)$$

and is affected by a statistical uncertainty

$$\sigma_{Ek} = \sqrt{\frac{1}{N} \left[\frac{1}{N} \sum_{i=1}^N e_{i,k}^2 - E_k^2 \right]}. \quad (1.110)$$

The Monte Carlo depth-dose distribution $D_{\text{MC}}(z)$ is a stepwise constant function,

$$D_{\text{MC}}(z) = D_k \pm 3\sigma_{Dk} \quad \text{for } z_{k-1} < z < z_k \quad (1.111)$$

with

$$D_k \equiv \frac{1}{z_k - z_{k-1}} E_k, \quad \sigma_{Dk} \equiv \frac{1}{z_k - z_{k-1}} \sigma_{Ek}. \quad (1.112)$$

Notice that the bin average and standard deviation have to be divided by the bin width to obtain the final Monte Carlo distribution. Defined in this way, $D_{\text{MC}}(z)$ is an unbiased estimator of the *average* dose in each bin. The limitation here is that we are approximating the continuous distribution $D(z)$ as a histogram with finite bar widths. In principle, we could obtain a closer approximation by using narrower bins. However, care has to be taken in selecting the bin widths since statistical uncertainties may completely hide the information in narrow bins.

A few words regarding programming details are in order. To evaluate the average deposited energy and its standard deviation for each bin, eqs. (1.109) and (1.110), we must score the shower contributions $e_{i,k}$ and their squares $e_{i,k}^2$. There are cases in which the literal application of this recipe may take a large fraction of the simulation time. Consider, for instance, the simulation of the 3D dose distribution in the phantom, which may involve several thousand volume bins. For each bin, the energies $e_{ij,k}$ deposited by the individual particles of a shower must be accumulated in a partial counter to obtain

the shower contribution $e_{i,k}$ and, after completion of the whole shower, the value $e_{i,k}$ and its square must be added to the accumulated counters. As only a small fraction of the bins receive energy from a single shower, it is not practical to treat all bin counters on an equal footing. The fastest method is to transfer partial scores to the accumulated counters only when the partial counter is going to receive a contribution from a new shower. This can be easily implemented in a computer program as follows. For each quantity of interest, say Q , we define three real counters, Q , $Q2$ and QP , and an integer label LQ ; all these quantities are initially set to zero. The partial scores q_{ij} of the particles of a shower are accumulated in the partial counter QP , whereas the global shower contribution q_i and its square are accumulated in Q and $Q2$, respectively. Each shower is assigned a label, for instance its order number i , which is stored in LQ the first time that the shower contributes to QP . In the course of the simulation, the value of QP is transferred to the global counters Q and $Q2$ only when it is necessary to store a contribution q_{ij} from a new shower. Explicitly, the FORTRAN code for scoring Q is

```

      IF (i.NE.LQ) THEN
        Q=Q+QP
        Q2=Q2+QP**2
        QP=qij
        LQ=i
      ELSE
        QP=QP+qij
      ENDIF

```

At the end of the simulation, the residual contents of QP must be transferred to the global counters.

For some quantities (e.g. the mean number of scattering events per track, the depth-dose function, ...) almost all the simulated tracks contribute to the score and the inherent statistical uncertainties of the simulation results are comparatively small. Other quantities (e.g. angle and energy distributions of the particles transmitted through a thick foil) have considerable statistical uncertainties (i.e. large variances) because only a small fraction of the simulated tracks contribute to the partial scores.

1.6 Variance reduction

In principle, the statistical error of a quantity may be somewhat reduced (without increasing the computer simulation time) by using variance-reduction techniques. Unfortunately, these optimization techniques are extremely problem-dependent, and general recipes to minimize the variance cannot be given. On the other hand, the importance of variance reduction should not be overvalued. In many cases, analogue³ simulation does the work in a reasonable time. Spending manhours by complicating the program, to get a modest reduction in computing time may not be a good investment. It is

³We use the term “analogue” to refer to detailed, condensed or mixed simulations that do not incorporate variance-reduction procedures.

also important to realize that an efficient variance-reduction method usually lowers the statistical error of a given quantity Q at the expense of increasing the uncertainties of other quantities. Thus, variance-reduction techniques are not recommended when a global description of the transport process is sought. Here we give a brief description of those techniques which, with a modest programming effort, can be useful in improving the solution of some ill-conditioned problems. For the sake of generality, we consider that secondary particles can be generated in the interactions with the medium. A nice, and practically oriented, review of variance-reduction methods in radiation transport has been given by Bielajew and Rogers (1988).

1.6.1 Interaction forcing

Sometimes, a high variance results from an extremely low interaction probability. Consider, for instance, the simulation of the energy spectrum of bremsstrahlung photons emitted by medium energy (~ 100 keV) electrons in a thin foil of a certain material. As radiative events are much less probable than elastic and inelastic scattering, the uncertainty of the simulated photon spectrum will be relatively large. In such cases, an efficient variance-reduction method is to artificially increase the interaction probability of the process A of interest. Our practical implementation of interaction forcing consists of replacing the mean free path λ_A of the real process by a shorter one, $\lambda_{A,f}$, i.e. we force A interactions to occur more frequently than for the real process. We consider that the PDF for the energy loss, the angular deflections (and the directions of emitted secondary particles, if any) in the forced interactions is the same as for the real interactions. To sample the length of the free jump to the next interaction, we use the exponential distribution with the reduced mean free path $\lambda_{A,f}$. This is equivalent to increasing the interaction probability per unit path length of the process A by a factor

$$\mathcal{F} = \frac{\lambda_A}{\lambda_{A,f}} > 1. \quad (1.113)$$

To keep the simulation unbiased, we must correct for the introduced distortion as follows:

- (i) A weight $w_p^{(1)} = 1$ is associated with each primary particle. Secondary particles produced in forced interactions have an associated weight $w_p^{(2)} = w_p^{(1)}/\mathcal{F}$; the weights of successive generations of forced secondaries are $w_p^{(k)} = w_p^{(k-1)}/\mathcal{F}$. Secondary particles generated in non-forced interactions (i.e. of types other than A) are given a weight equal to that of their parent particle.
- (ii) Forced interactions are simulated to determine the energy loss and possible emission of secondary radiation, but the state variables of the interacting particle are altered only with probability $1/\mathcal{F}$. That is, the energy E and direction of movement $\hat{\mathbf{d}}$ of the projectile are varied only when the value ξ of a random number falls below $1/\mathcal{F}$, otherwise E and $\hat{\mathbf{d}}$ are kept unchanged.
- (iii) A weight $w_E^{(k)} = w_p^{(k)}/\mathcal{F}$ is given to the deposited energy⁴ (and to any other

⁴This option may effectively reduce the statistical uncertainties of simulated dose distributions in

alteration of the medium such as e.g. charge deposition) that results from forced interactions of a particle with weight $w_p^{(k)}$. For non-forced interactions $w_E^{(k)} = w_p^{(k)}$.

Of course, interaction forcing should be applied only to interactions that are dynamically allowed, i.e. for particles with energy above the corresponding “reaction” threshold.

Let w_{i1} and f_{i1} denote the weight and the contribution to the score of the i -th primary, and let w_{ij} and f_{ij} ($j > 1$) represent the weights and contributions of the j -th secondary particles generated by the i -th primary. The Monte Carlo estimate of F obtained from the N simulated histories is

$$\bar{F} = \frac{1}{N} \sum_{i,j} w_{ij} f_{ij}. \quad (1.114)$$

Evidently, the estimates \bar{F} obtained with interaction forcing and from an analogue simulation are equal (in the statistical sense, i.e. in the limit $N \rightarrow \infty$, their difference tends to zero). The standard deviation is given by

$$\sigma_F = \sqrt{\frac{1}{N} \left[\frac{1}{N} \sum_i \left(\sum_j w_{ij} f_{ij} \right)^2 - \bar{F}^2 \right]}. \quad (1.115)$$

Quantities directly related to the forced interactions will have a reduced statistical error, due to the increase in number of these interactions. However, for a given simulation time, other quantities may exhibit standard deviations larger than those of the analogue simulation, because of the time spent in simulating the forced interactions.

1.6.2 Splitting and Russian roulette

These two techniques, which are normally used in conjunction, are effective in problems where interest is focused on a localized spatial region. Typical examples are the calculation of dose functions in deep regions of irradiated objects and, in the case of collimated radiation beams, the evaluation of radial doses far from the beam axis. The basic idea of splitting and Russian roulette methods is to favour the flux of radiation towards the region of interest and inhibit the radiation that leaves that region. These techniques are also useful in other problems where only a partial description of the transport process is required. The “region of interest” may then be a limited volume in the space of state variables $(\mathbf{r}, E, \hat{\mathbf{d}})$. Thus, in studies of radiation backscattering, the region of interest may be selected as the spatial region of the sample close to the irradiated surface *and* the set of particle directions that point towards this surface.

As in the case of interaction forcing, variance reduction is accomplished by modifying the weights of the particles. It is assumed that primary particles start moving with unit

very thin media. However, it violates energy conservation (because the sum of energies deposited along a track differs from the energy lost by the projectile) and, therefore, yields energy deposition spectra that are biased.

weight and each secondary particle produced by a primary one is assigned an initial weight equal to that of the primary. Splitting consists of transforming a particle, with weight w_0 and in a certain state, into a number $\mathcal{S} > 1$ of identical particles with weights $w = w_0/\mathcal{S}$ in the same initial state. Splitting should be applied when the particle “approaches” the region of interest. The Russian roulette technique is, in a way, the reverse process: when a particle tends to move away from the region of interest it is “killed” with a certain probability, $\mathcal{K} < 1$, and, if it survives, its weight is increased by a factor $1/(1 - \mathcal{K})$. Here, killing means that the particle is just discarded (and does not contribute to the scores anymore). Evidently, splitting and killing leave the simulation unbiased. The mean and standard deviation of the calculated quantities are given by eqs. (1.114) and (1.115). The effectiveness of these methods relies on the adopted values of the parameters \mathcal{S} and \mathcal{K} , and on the strategy used to decide when splitting and killing are to be applied. These details can only be dictated by the user’s experience.

1.6.3 Other methods

Very frequently, an effective “reduction of variance” may be obtained by simply avoiding unnecessary calculations. This is usually true for simulation codes that incorporate “general-purpose” geometry packages. In the case of simple (e.g. planar, spherical, cylindrical) geometries the program may be substantially simplified and this may speed up the simulation appreciably. In general, the clever use of possible symmetries of the problem under consideration may lead to spectacular variance reductions. As a last example, we can quote the so-called “range rejection” method, which simply consists of absorbing a particle when it (and its possible secondaries) cannot leave (or reach) regions of interest. Range rejection is useful e.g. when computing the total energy deposition of electrons or positrons in a given spatial region. When the residual range of a particle (and its possible secondaries) is less than the distance to the nearest limiting surface of the region of interest, the particle will deposit all its energy inside or outside the considered region (depending of its current position) and the simulation of the track can be stopped. Range rejection is not adequate for photon transport simulation, since the concept of photon range is not well defined (or, to be more precise, photon path length fluctuations are very large).

Chapter 2

Photon interactions

In this chapter, we consider the interactions of unpolarized photons of energy E with atoms of atomic number Z . We limit our considerations to the energy range from 100 eV up to 1 GeV, where the dominant interaction processes are coherent (Rayleigh) scattering, incoherent (Compton) scattering, the photoelectric effect and electron-positron pair production. Other interactions, such as photonuclear absorption, occur with much smaller probability and can be disregarded for most practical purposes (see e.g. Hubbell et al., 1980).

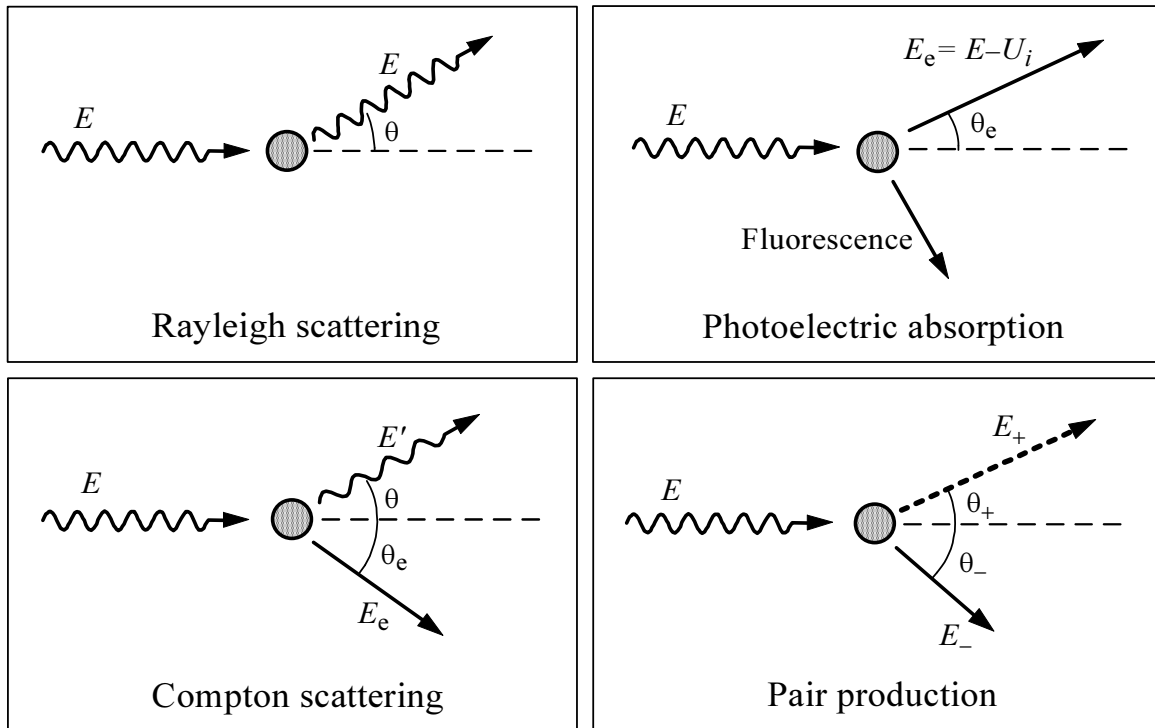


Figure 2.1: Basic interactions of photons with matter.

As long as the response of an atom is not appreciably distorted by molecular binding, the single-atom theory can be extended to molecules by using the additivity approximation, i.e. the molecular cross section for a process is approximated by the sum of the atomic cross sections of all the atoms in the molecule. The additivity approximation can also be applied to dense media whenever interference effects between waves scattered by different centres (which, for instance, give rise to Bragg diffraction in crystals) are small. We assume that these conditions are always satisfied.

The ability of Monte Carlo simulation methods to describe photon transport in complex geometries has been established from research during the last five decades (Hayward and Hubbell, 1954; Zerby, 1963; Berger and Seltzer, 1972; Chan and Doi, 1983; Ljungberg and Strand, 1989). The most accurate DCSs available are given in numerical form and, therefore, advanced Monte Carlo codes make use of extensive databases. To reduce the amount of required numerical information, in PENELOPE we use a combination of analytical DCSs and numerical tables. The adopted DCSs are defined by simple, but physically sound analytical forms. The corresponding total cross sections are obtained by a single numerical quadrature that is performed very quickly using the **SUMGA** external function described in appendix B. Moreover, the random sampling from these DCSs can be done analytically and, hence, exactly. Only coherent scattering requires a simple preparatory numerical step.

It may be argued that using analytical *approximate* DCSs, instead of more accurate tabulated DCSs implies a certain loss of accuracy. To minimize this loss, PENELOPE renormalizes the analytical DCSs so as to reproduce partial attenuation coefficients that are read from the input material data file. As a consequence, the free path between events and the kind of interaction are sampled using total cross sections that are nominally exact; approximations are introduced only in the description of individual interaction events.

In the following, κ stands for the photon energy in units of the electron rest energy, i.e.

$$\kappa \equiv \frac{E}{m_e c^2}. \quad (2.1)$$

2.1 Coherent (Rayleigh) scattering

Coherent or Rayleigh scattering is the process by which photons are scattered by bound atomic electrons without excitation of the target atom, i.e. the energies of the incident and scattered photons are the same. The scattering is qualified as “coherent” because it arises from the interference between secondary electromagnetic waves coming from different parts of the atomic charge distribution.

The atomic DCS per unit solid angle for coherent scattering is given approximately by (see e.g. Born, 1969)

$$\frac{d\sigma_{\text{Ra}}}{d\Omega} = \frac{d\sigma_{\text{T}}}{d\Omega} [F(q, Z)]^2, \quad (2.2)$$

where

$$\frac{d\sigma_T(\theta)}{d\Omega} = r_e^2 \frac{1 + \cos^2 \theta}{2} \quad (2.3)$$

is the classical Thomson DCS for scattering by a free electron at rest, θ is the polar scattering angle (see fig. 2.1) and $F(q, Z)$ is the atomic form factor. The quantity r_e is the classical electron radius and q is the magnitude of the momentum transfer given by

$$q = 2(E/c) \sin(\theta/2) = (E/c) [2(1 - \cos \theta)]^{1/2}. \quad (2.4)$$

In the literature on x-ray crystallography, the dimensionless variable

$$x \equiv \frac{q \cdot 10^{-8} \text{cm}}{4\pi\hbar} = 20.6074 \frac{q}{m_e c} \quad (2.5)$$

is normally used instead of q .

The atomic form factor can be expressed as the Fourier transform of the atomic electron density $\rho(\mathbf{r})$ which, for a spherically symmetrical atom, simplifies to

$$F(q, Z) = 4\pi \int_0^\infty \rho(r) \frac{\sin(qr/\hbar)}{qr/\hbar} r^2 dr. \quad (2.6)$$

$F(q, Z)$ is a monotonically decreasing function of q that varies from $F(0, Z) = Z$ to $F(\infty, Z) = 0$. The most accurate form factors are those obtained from Hartree-Fock or configuration-interaction atomic-structure calculations; here we adopt the non-relativistic atomic form factors tabulated by Hubbell et al. (1975). Although relativistic form factors are available (Doyle and Turner, 1968), Hubbell has pointed out that the non-relativistic form factors yield results in closer agreement with experiment (Cullen et al., 1997).

In the calculations, we use the following analytical approximation

$$F(q, Z) = \begin{cases} f(x, Z) \equiv Z \frac{1 + a_1 x^2 + a_2 x^3 + a_3 x^4}{(1 + a_4 x^2 + a_5 x^4)^2}, \\ \max \{f(x, Z), F_K(q, Z)\} & \text{if } Z > 10 \text{ and } f(x, Z) < 2, \end{cases} \quad (2.7)$$

where

$$F_K(q, Z) \equiv \frac{\sin(2b \arctan Q)}{bQ (1 + Q^2)^b}, \quad (2.8)$$

with

$$Q = \frac{q}{2m_e c a}, \quad b = \sqrt{1 - a^2}, \quad a \equiv \alpha(Z - 5/16), \quad (2.9)$$

where α is the fine-structure constant. The function $F_K(q, Z)$ is the contribution to the atomic form factor due to the two K-shell electrons (see e.g. Baró et al., 1994a). The parameters of expression $f(x, Z)$ for $Z = 1$ to 92, which have been determined by Baró et al. (1994a) by numerically fitting the atomic form factors tabulated by Hubbell et al. (1975), are included in the block data subprogram **PENDAT**. The average relative

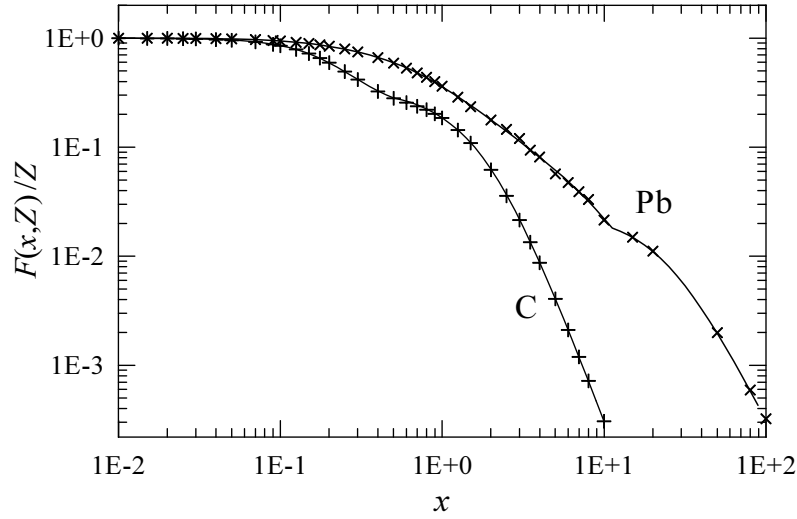


Figure 2.2: Atomic form factors for carbon and lead. Crosses are values from the tables of Hubbell et al. (1975), continuous curves represent the analytical approximation given by eq. (2.7).

difference between the analytical and tabulated form factors is less than 0.5% (see fig. 2.2).

The total coherent scattering cross section per atom is

$$\sigma_{\text{Ra}} = \int \frac{d\sigma_{\text{Ra}}}{d\Omega} d\Omega = \pi r_e^2 \int_{-1}^1 (1 + \cos^2 \theta) [F(q, Z)]^2 d(\cos \theta). \quad (2.10)$$

Introducing q , eq. (2.4), as a new integration variable, the asymptotic behaviour of the total cross section for small and large photon energies is made clear. For low photon energies, the form factor in the integrand does not depart appreciably from the value $F(0, Z) = Z$, i.e. coherent scattering reduces to pure Thomson scattering. Consequently, we have

$$\sigma_{\text{Ra}} \simeq \frac{8}{3} \pi r_e^2 Z^2. \quad (2.11)$$

In the high-energy limit, we get

$$\sigma_{\text{Ra}} \propto E^{-2}. \quad (2.12)$$

In practice, this limiting behaviour is attained for energies of the order of $Z/2$ MeV.

Strictly speaking, expression (2.2) is adequate only for photons with energy well above the K absorption edge. The low-energy behaviour given by eq. (2.11) is substantially altered when anomalous scattering factors are introduced (see e.g. Cullen et al., 1989; Kane et al., 1986). These factors lead to a general decrease of the coherent scattering cross section near the absorption edges and at low energies. Nevertheless, at the energies where anomalous scattering effects become significant, coherent scattering is much less probable than photoelectric absorption (see fig. 2.10 below), and the approximation given by eq. (2.2) is usually sufficient for simulation purposes.

2.1.1 Simulation of coherent scattering events

The PDF of the angular deflection, $\cos \theta$, can be written as [see eqs. (2.2) and (2.3); normalization is irrelevant here]

$$p_{\text{Ra}}(\cos \theta) = \frac{1 + \cos^2 \theta}{2} [F(x, Z)]^2, \quad (2.13)$$

where x , which is defined by eqs. (2.4) and (2.5), can take values in the interval from 0 to

$$x_{\text{max}} = 20.6074 \times 2\kappa. \quad (2.14)$$

This PDF can be factorized in the form

$$p_{\text{Ra}}(\cos \theta) = g(\cos \theta)\pi(x^2) \quad (2.15)$$

with

$$g(\cos \theta) \equiv \frac{1 + \cos^2 \theta}{2} \quad \text{and} \quad \pi(x^2) \equiv [F(x, Z)]^2. \quad (2.16)$$

Notice that, for a compound, $[F(x, Z)]^2$ has to be replaced by the sum of squared form factors of the atoms in the molecule.

The function $\pi(x^2)$ can be considered as the (unnormalized) PDF of the variable x^2 . Random values of x^2 distributed according to this PDF can be generated by the inverse transform method (section 1.2.2), i.e. from the sampling equation

$$\int_0^{x^2} \pi(x'^2) dx'^2 = \xi \int_0^{x_{\text{max}}^2} \pi(x'^2) dx'^2. \quad (2.17)$$

It is convenient to introduce the function

$$\Pi(x^2) = \int_0^{x^2} \pi(x'^2) dx'^2, \quad (2.18)$$

which increases monotonically with x^2 and saturates for high x^2 -values to a constant finite value. Then, the sampling equation (2.17) can be written in the form

$$\Pi(x^2) = \xi \Pi(x_{\text{max}}^2), \quad (2.19)$$

which is easy to solve numerically. To this end, we only need to have a table of values of the function $\Pi(x^2)$ stored in memory. For a given photon energy, $\Pi(x_{\text{max}}^2)$ can be evaluated by interpolation in this table. Linear log-log interpolation (extrapolation) in a table with about 240 points logarithmically distributed in the interval $(10^{-4}, 10^6)$ yields results which are accurate to within 0.01% (notice that in the interval from 0 to 10^{-4} , $F(x, Z) \simeq Z$ and, hence, $\Pi(x^2)$ is proportional to x^2 , i.e. extrapolation for $x^2 < 10^{-4}$ is exact). The value

$$x^2 = \Pi^{-1}(\xi \Pi(x_{\text{max}}^2)) \quad (2.20)$$

can then be obtained by inverse linear interpolation (or extrapolation) with a binary search.

The angular deflection $\cos\theta$ can now be sampled by the rejection method (section 1.2.4), since the function $g(\cos\theta)$ is a valid rejection function (i.e. it is positive and less than or equal to unity). The algorithm for sampling $\cos\theta$ proceeds as follows:

- (i) Compute $\Pi(x_{\max}^2)$.
- (ii) Generate a random number ξ and determine x^2 using eq. (2.20). Set

$$\cos\theta = 1 - \frac{1}{2} \frac{x^2}{(20.6074\kappa)^2}. \quad (2.21)$$

- (iii) Generate a new random number ξ .
- (iv) If $\xi > g(\cos\theta)$, go to step (ii).
- (v) Deliver $\cos\theta$.

Although numerical interpolation is necessary, it is performed on a single function that is independent of the photon energy and the errors introduced are negligible. It is worth noting that the sampling algorithm is essentially independent of the adopted form factor, and directly applicable to molecules. The advantage of using the analytical form factor, eq. (2.7), instead of a numerical database is that $\Pi(x^2)$ can be easily calculated to the desired accuracy, using the **SUMGA** integration function (appendix B).

The efficiency of the sampling method (i.e. the fraction of generated values of $\cos\theta$ that is accepted) increases with photon energy. At low energies, it equals 2/3 (exactly) for all elements. For $E = 100$ keV, the efficiencies for hydrogen and uranium are 100% and 86%, respectively.

2.2 Photoelectric effect

In the photoelectric effect, a photon of energy E is absorbed by the target atom, which makes a transition to an excited state. The photon beams found in radiation transport studies have relatively low photon densities and, as a consequence, only single-photon absorption is observed¹. To represent the atomic states, we can adopt an independent-electron model, such as the Dirac-Hartree-Fock-Slater self-consistent model (see e.g. Pratt et al., 1973), in which each electron occupies a single-particle orbital, with well-defined ionization energy. The set of orbitals with the same principal and total angular momentum quantum numbers and the same parity constitute a shell. Each shell i can accommodate a finite number of electrons, with characteristic ionization energy U_i . Notice that the shell ionization energies are positive, the quantity $-U_i$ represents the “binding” energy of each individual electron. Fig. 2.3 (left diagram) shows the various notations used to designate the innermost atomic electron shells (i.e. those with the

¹In intense low-energy photon beams, such as those from high-power lasers, simultaneous absorption of several photons is possible.

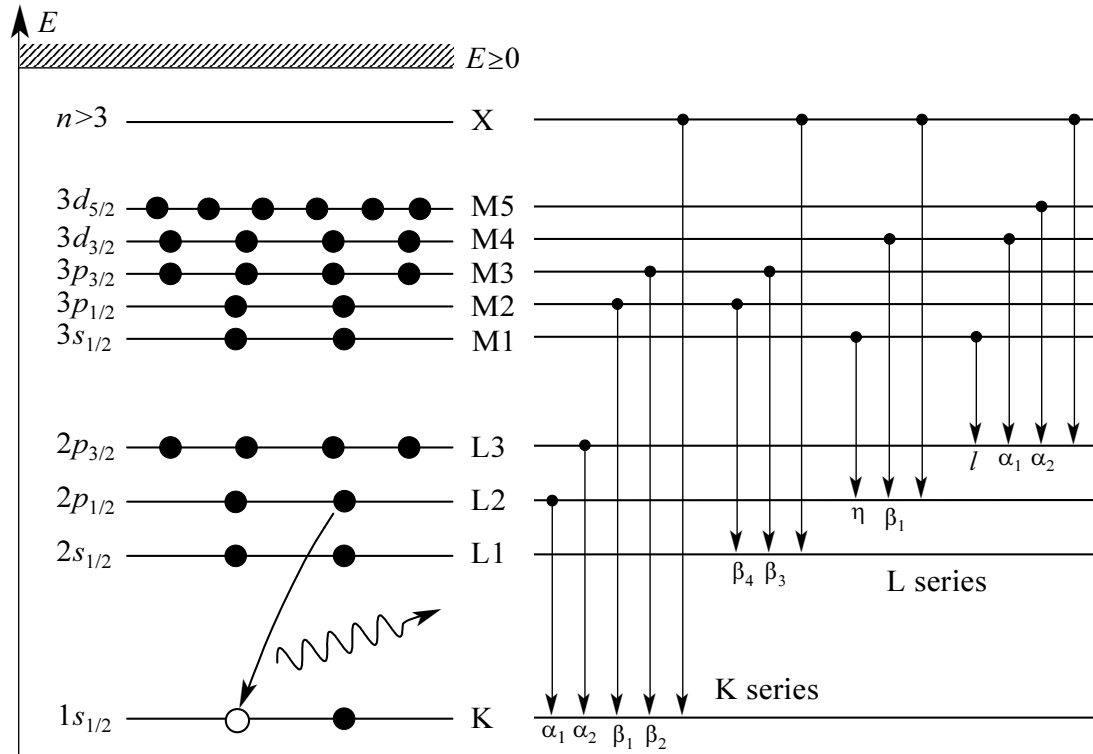


Figure 2.3: Various notations for inner atomic electron shells (left) and allowed radiative transitions (right) to these shells. Transitions different from the ones indicated in the diagram (e.g. K-M4) are also possible, but their transition probabilities are extremely small.

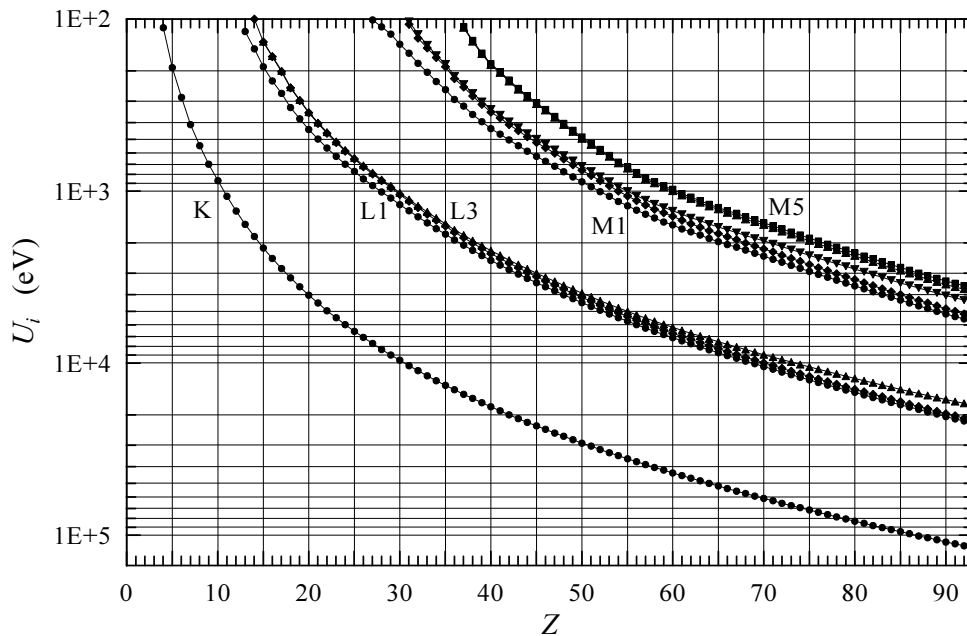


Figure 2.4: Ionization energies of the innermost shells of free atoms, as given by Lederer and Shirley (1978).

largest ionization energies) as well as their ordering in energy and allowed occupancies. In our simulations, we use the experimental ionization energies given by Lederer and Shirley (1978), which pertain to free, neutral atoms. Ionization energies of K-, L- and M-shells are displayed in fig. 2.4.

Considering the interaction with the photon field as a first-order perturbation (which is appropriate for fields with low photon densities) it follows that only one-electron transitions are allowed. That is, in the photoelectric effect, the photon is absorbed by an individual electron in the “active” shell i , which leaves the parent atom with kinetic energy $E_e = E - U_i$. Evidently, photoionization of a given shell is only possible when the photon energy exceeds the corresponding ionization energy; this gives rise to the characteristic absorption edges in the photoelectric cross section (see fig. 2.5).

The photoelectric cross sections used in PENELOPE are obtained by interpolation in a numerical table that was extracted from the LLNL Evaluated Photon Data Library (EPDL; Cullen et al., 1997). This library contains photoelectric cross sections for all shells of the elements $Z = 1 - 100$ and photon energies from 1 eV to 1000 GeV, derived from Scofield’s theoretical calculations of shell cross sections (Saloman et al., 1988) and Hubbell’s total cross sections (Hubbell et al., 1980; Berger and Hubbell, 1987). The PENELOPE database for photoelectric absorption (a subset of the EPDL) consists of tables of the total atomic cross section $\sigma_{\text{ph}}(E)$ and the cross sections for the K and L shells, $\sigma_{\text{ph},i}(E)$ ($i = \text{K, L1, L2 and L3}$) for the elements $Z = 1-92$, which span the energy range from 100 eV to 1000 GeV. These tables are estimated to be accurate to within a few percent for photon energies above 1 keV (Cullen et al., 1997). At lower energies, uncertainties in the data are much larger: 10–20% for $0.5 \text{ keV} < E < 1 \text{ keV}$ and 100–200% for $0.1 \text{ keV} < E < 0.5 \text{ keV}$. Notice that the cross sections in the EPDL are based on free-atom theoretical calculations and, therefore, near-edge absorption structures produced by molecular or crystalline ordering (e.g. extended x-ray absorption fine-structure) are ignored.

For compound materials (and also for mixtures) the molecular cross section $\sigma_{\text{ph}}(E)$ is evaluated by means of the additivity approximation, that is, as the sum of the atomic cross sections of the elements involved. In the energy range between successive absorption edges, the photoelectric cross section is a continuous function of the photon energy (see fig. 2.5). In PENELOPE, the molecular cross section is defined by means of a table of numerical values $\sigma_{\text{ph}}(E_i)$ for a logarithmic grid of energies E_i , which is stored in memory. Photon mean free paths are determined by linear log-log interpolation in this table. Knowledge of the atomic cross sections is needed, only when a photoabsorption event has effectively occurred, to select the element that has been ionized (whose probability is proportional to the atomic cross section).

2.2.1 Simulation of photoelectron emission

Let us consider that a photon with energy E is absorbed by an atom of the element Z . The “active” shell i that is ionized is considered as a discrete random variable with

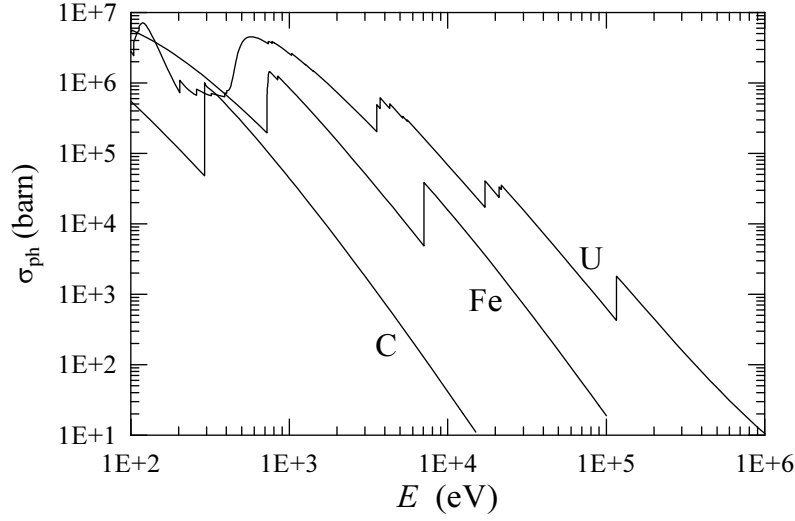


Figure 2.5: Atomic photoelectric cross sections for carbon, iron and uranium as functions of the photon energy E .

PDF

$$p_i = \sigma_{\text{ph},i}(Z, E) / \sigma_{\text{ph}}(Z, E), \quad (2.22)$$

where $\sigma_{\text{ph},i}(Z, E)$ is the cross section for ionization of shell i and $\sigma_{\text{ph}}(Z, E)$ is the total photoelectric cross section of the atom. PENELOPE incorporates a detailed description of photoabsorption in K- and L-shells (including the subsequent atomic relaxation). The ionization probabilities of these inner shells are determined from the corresponding partial cross sections. The probability of ionization in an outer shell is obtained as

$$p_{\text{outer}} = 1 - (p_K + p_{L1} + p_{L2} + p_{L3}). \quad (2.23)$$

When the ionization occurs in an inner K- or L-shell, the initial energy of the photoelectron is set equal to $E_e = E - U_i$; the residual atom, with a vacancy in the shell, subsequently relaxes to its ground state by emitting x rays and Auger electrons. If the ionization occurs in an outer shell, we assume that the photoelectron leaves the target atom with kinetic energy equal to the energy deposited by the photon, $E_e = E$, and we disregard the emission of subsidiary fluorescent radiation (see section 2.6).

Initial direction of photoelectrons

The direction of emission of the photoelectron, relative to that of the absorbed photon, is defined by the polar and azimuthal angles θ_e (fig. 2.1) and ϕ_e . We consider that the incident photon is not polarized and, hence, the angular distribution of photoelectrons is independent of ϕ_e , which is uniformly distributed in the interval $(0, 2\pi)$. The polar angle θ_e is sampled from the K-shell cross section derived by Sauter (1931) using K-shell

hydrogenic electron wave functions. The Sauter DCS (per electron) can be written as

$$\frac{d\sigma_{\text{ph}}}{d\Omega_e} = \alpha^4 r_e^2 \left(\frac{Z}{\kappa}\right)^5 \frac{\beta^3}{\gamma} \frac{\sin^2 \theta_e}{(1 - \beta \cos \theta_e)^4} \left[1 + \frac{1}{2} \gamma(\gamma - 1)(\gamma - 2)(1 - \beta \cos \theta_e)\right], \quad (2.24)$$

where α is the fine-structure constant, r_e is the classical electron radius, and

$$\gamma = 1 + E_e/(m_e c^2), \quad \beta = \frac{\sqrt{E_e(E_e + 2m_e c^2)}}{E_e + m_e c^2}. \quad (2.25)$$

Strictly speaking, the DCS (2.24) is adequate only for ionization of the K-shell by high-energy photons. Nevertheless, in many practical simulations no appreciable errors are introduced when Sauter's distribution is used to describe any photoionization event, irrespective of the atomic shell and the photon energy. The main reason is that the emitted photoelectron immediately starts to interact with the medium, and its direction of movement is strongly altered after travelling a path length much shorter than the photon mean free path. On the other hand, when the photon energy exceeds the K-edge, most of the ionizations occur in the K-shell and then the Sauter distribution represents a good approximation.

Introducing the variable $\nu = 1 - \cos \theta_e$, the angular distribution of photoelectrons can be expressed in the form

$$p(\nu) = (2 - \nu) \left[\frac{1}{A + \nu} + \frac{1}{2} \beta \gamma(\gamma - 1)(\gamma - 2) \right] \frac{\nu}{(A + \nu)^3}, \quad A = \frac{1}{\beta} - 1, \quad (2.26)$$

apart from a normalization constant. Random sampling of ν from this distribution can be performed analytically. To this end, $p(\nu)$ can be factorized in the form

$$p(\nu) = g(\nu)\pi(\nu) \quad (2.27)$$

with

$$g(\nu) = (2 - \nu) \left[\frac{1}{A + \nu} + \frac{1}{2} \beta \gamma(\gamma - 1)(\gamma - 2) \right] \quad (2.28)$$

and

$$\pi(\nu) = \frac{A(A + 2)^2}{2} \frac{\nu}{(A + \nu)^3}. \quad (2.29)$$

The variable ν takes values in the interval (0,2), where the function $g(\nu)$ is definite positive and attains its maximum value at $\nu = 0$, while the function $\pi(\nu)$ is positive and normalized to unity. Random values from the probability distribution $\pi(\nu)$ are generated by means of the sampling formula (inverse transform method, see section 1.2.2)

$$\int_0^\nu \pi(\nu') d\nu' = \xi, \quad (2.30)$$

which can be solved analytically to give

$$\nu = \frac{2A}{(A + 2)^2 - 4\xi} \left[2\xi + (A + 2)\xi^{1/2} \right]. \quad (2.31)$$

Therefore, random sampling from Sauter's distribution can be performed by the rejection method (see section 1.2.4) as follows:

- (i) Generate ν from $\pi(\nu)$ by using eq. (2.31).
- (ii) Generate a random number ξ .
- (iii) If $\xi g(0) > g(\nu)$, go to step (i).
- (iv) Deliver $\cos \theta_e = 1 - \nu$.

The efficiency of this algorithm is ~ 0.33 at low energies and increases slowly with E_e ; for $E_e = 1$ MeV, the efficiency is 0.4. As photoelectric absorption occurs at most once in each photon history, this small sampling efficiency does not slow down the simulation significantly.

2.3 Incoherent (Compton) scattering

In Compton scattering, a photon of energy E interacts with an atomic electron, which absorbs it and re-emits a secondary (Compton) photon of energy E' in the direction $\Omega = (\theta, \phi)$ relative to the direction of the original photon. In PENELOPE, Compton scattering events are described by means of the cross section obtained from the relativistic impulse approximation (Ribberfors, 1983). Contributions from different atomic electron shells are considered separately. After a Compton interaction with the i -th shell, the active target electron is ejected to a free state with kinetic energy $E_e = E - E' - U_i > 0$, where U_i is the ionization energy of the considered shell, and the residual atom is left in an excited state with a vacancy in the i -th shell.

In the case of scattering by free electrons at rest, the conservation of energy and momentum implies the following relation between the energy E' of the scattered (Compton) photon and the scattering angle θ [cf. eq. (A.19)]

$$E' \equiv \frac{E}{1 + \kappa(1 - \cos \theta)} \equiv E_C, \quad (2.32)$$

where $\kappa = E/m_e c^2$, as before. The DCS for Compton scattering by a free electron at rest is given by the familiar Klein-Nishina formula,

$$\frac{d\sigma_{\text{Co}}^{\text{KN}}}{d\Omega} = \frac{r_e^2}{2} \left(\frac{E_C}{E} \right)^2 \left(\frac{E_C}{E} + \frac{E}{E_C} - \sin^2 \theta \right). \quad (2.33)$$

Although this simple DCS was generally used in old Monte Carlo transport codes, it represents only a rough approximation for the Compton interactions of photons with atoms. In reality, atomic electrons are not at rest, but move with a certain momentum distribution, which gives rise to the so-called Doppler broadening of the Compton line. Moreover, transitions of bound electrons are allowed only if the energy transfer $E - E'$ is larger than the ionization energy U_i of the active shell (binding effect).

The impulse approximation accounts for Doppler broadening and binding effects in a natural, and relatively simple, way. The DCS is obtained by considering that

electrons in the i -th shell move with a momentum distribution $\rho_i(\mathbf{p})$. For an electron in an orbital $\psi_i(\mathbf{r})$, $\rho_i(\mathbf{p}) \equiv |\psi_i(\mathbf{p})|^2$, where $\psi_i(\mathbf{p})$ is the wave function in the momentum representation. The DCS for Compton scattering by an electron with momentum \mathbf{p} is derived from the Klein-Nishina formula by applying a Lorentz transformation with velocity \mathbf{v} equal to that of the moving target electron. The impulse approximation to the Compton DCS (per electron) of the considered shell is obtained by averaging over the momentum distribution $\rho_i(\mathbf{p})$.

After some manipulations, the Compton DCS of an electron in the i -th shell can be expressed as [eq. (21) in Brusa et al., 1996]

$$\frac{d^2\sigma_{\text{Co},i}}{dE'd\Omega} = \frac{r_e^2}{2} \left(\frac{E_C}{E}\right)^2 \left(\frac{E_C}{E} + \frac{E}{E_C} - \sin^2\theta\right) F(p_z) J_i(p_z) \frac{dp_z}{dE'}, \quad (2.34)$$

where r_e is the classical electron radius. E_C is the energy of the Compton line, defined by eq. (2.32), i.e. the energy of photons scattered in the direction θ by *free electrons at rest*. The momentum transfer vector is given by $\mathbf{q} \equiv \hbar\mathbf{k} - \hbar\mathbf{k}'$, where $\hbar\mathbf{k}$ and $\hbar\mathbf{k}'$ are the momenta of the incident and scattered photons; its magnitude is

$$q = \frac{1}{c} \sqrt{E^2 + E'^2 - 2EE' \cos\theta}. \quad (2.35)$$

The quantity p_z is the projection of the initial momentum \mathbf{p} of the electron on the direction of the scattering vector $\hbar\mathbf{k}' - \hbar\mathbf{k} = -\mathbf{q}$; it is given by²

$$p_z \equiv -\frac{\mathbf{p} \cdot \mathbf{q}}{q} = \frac{EE'(1 - \cos\theta) - m_e c^2(E - E')}{c^2 q} \quad (2.36)$$

or, equivalently,

$$\frac{p_z}{m_e c} = \frac{E(E' - E_C)}{E_C c q}. \quad (2.37)$$

Notice that $p_z = 0$ for $E' = E_C$. Moreover,

$$\frac{dp_z}{dE'} = \frac{m_e c}{c q} \left(\frac{E}{E_C} + \frac{E \cos\theta - E'}{c q} \frac{p_z}{m_e c} \right). \quad (2.38)$$

The function $J_i(p_z)$ in eq. (2.34) is the one-electron Compton profile of the active shell, which is defined as

$$J_i(p_z) \equiv \iint \rho_i(\mathbf{p}) dp_x dp_y, \quad (2.39)$$

where $\rho_i(\mathbf{p})$ is the electron momentum distribution. That is, $J_i(p_z) dp_z$ gives the probability that the component of the electron momentum in the z -direction is in the interval $(p_z, p_z + dp_z)$. Notice that the normalization

$$\int_{-\infty}^{\infty} J_i(p_z) dp_z = 1 \quad (2.40)$$

²The expression (2.36) contains an approximation, the exact relation is obtained by replacing the electron rest energy $m_e c^2$ in the numerator by the electron initial total energy, $\sqrt{(m_e c^2)^2 + (cp)^2}$.

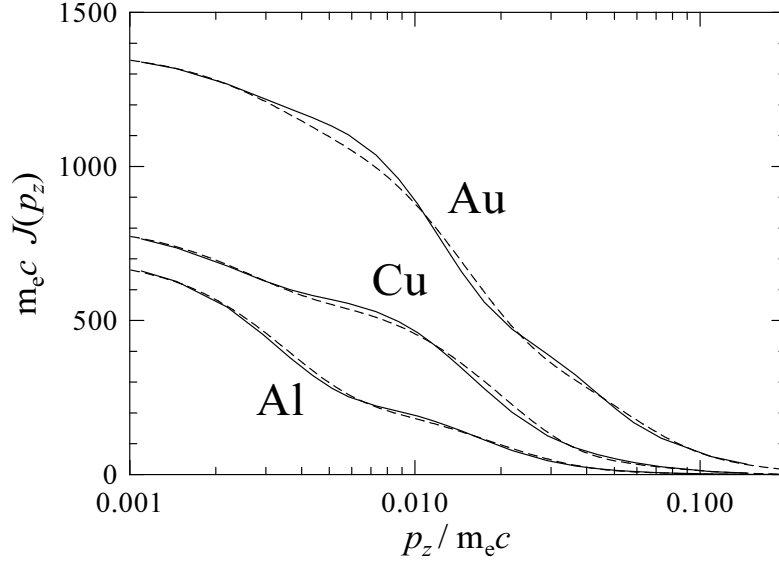


Figure 2.6: Atomic Compton profiles ($p_z > 0$) for aluminium, copper and gold. The continuous curves are numerical Hartree-Fock profiles tabulated by Biggs et al. (1975). The dashed curves represent the analytical profiles defined by eq. (2.57). (Adapted from Brusa et al., 1996.)

is assumed. In the Hartree-Fock approximation for closed-shell configurations, the momentum distribution of the electrons in an atomic shell, obtained by adding the contributions of the orbitals in that shell, is isotropic. For an isotropic distribution, expression (2.39) simplifies to

$$J_i(p_z) = 2\pi \int_{|p_z|}^{\infty} p \rho_i(p) dp. \quad (2.41)$$

The atomic Compton profile is given by

$$J(p_z) = \sum_i f_i J_i(p_z), \quad (2.42)$$

where f_i is the number of electrons in the i -th shell and $J_i(p_z)$ is the one-electron profile of this shell. The functions $J(p_z)$ and $J_i(p_z)$ are both bell-shaped and symmetrical about $p_z = 0$ (see fig. 2.6). Extensive tables of Hartree-Fock Compton profiles for the elements have been published by Biggs et al. (1975). These numerical profiles are adequate for bound electron shells. In the case of conductors, the one-electron Compton profile for conduction electrons may be estimated by assuming that these form a free-electron gas with ρ_e electrons per unit volume. The one-electron profile for this system is (see e.g. Cooper, 1971)

$$J_i^{\text{feg}}(p_z) = \frac{3}{4p_F} \left(1 - \frac{p_z^2}{p_F^2} \right) \Theta(p_F - |p_z|), \quad J_i^{\text{feg}}(0) = \frac{3}{4p_F}, \quad (2.43)$$

where $p_F \equiv \hbar(3\pi^2\rho_e)^{1/3}$ is the Fermi momentum. For scattering in a compound material,

the molecular Compton profile is obtained as the sum of atomic profiles of the atoms in a molecule (additivity rule).

The factor $F(p_z)$ in eq. (2.34) is approximately given by

$$F(p_z) \simeq 1 + \frac{cq_C}{E} \left(1 + \frac{E_C(E_C - E \cos \theta)}{(cq_C)^2} \right) \frac{p_z}{m_e c}, \quad (2.44)$$

where q_C is the momentum transfer associated with the energy $E' = E_C$ of the Compton line,

$$q_C \equiv \frac{1}{c} \sqrt{E^2 + E_C^2 - 2EE_C \cos \theta}. \quad (2.45)$$

Expression (2.44) is accurate only for small $|p_z|$ -values. For large $|p_z|$, $J_i(p_z)$ tends to zero and the factor $F(p_z)$ has no effect on the DCS. We use the values given by expression (2.44) only for $|p_z| < 0.2m_e c$ and take $F(\pm|p_z|) = F(\pm 0.2m_e c)$ for $|p_z| > 0.2m_e c$. Owing to the approximations introduced, negative values of F may be obtained for large $|p_z|$; in this case, we must set $F = 0$.

We can now introduce the effect of electron binding: Compton excitations are allowed only if the target electron is promoted to a free state, i.e. if the energy transfer $E - E'$ is larger than the ionization energy U_i of the active shell. Therefore the atomic DCS, including Doppler broadening and binding effects, is given by

$$\begin{aligned} \frac{d^2\sigma_{Co}}{dE'd\Omega} &= \frac{r_e^2}{2} \left(\frac{E_C}{E} \right)^2 \left(\frac{E_C}{E} + \frac{E}{E_C} - \sin^2 \theta \right) \\ &\times F(p_z) \left(\sum_i f_i J_i(p_z) \Theta(E - E' - U_i) \right) \frac{dp_z}{dE'}, \end{aligned} \quad (2.46)$$

where $\Theta(x)$ ($= 1$ if $x > 0$, $= 0$ otherwise) is the Heaviside step function. In the calculations we use the ionization energies U_i given by Lederer and Shirley (1978), fig. 2.4. The DCS for scattering of 10 keV photons by aluminium atoms is displayed in fig. 2.7, for $\theta = 60$ and 180 degrees, as a function of the fractional energy of the emerging photon. The DCS for a given scattering angle has a maximum at $E' = E_C$; its shape resembles that of the atomic Compton profile, except for the occurrence of edges at $E' = E - U_i$.

In the case of scattering by free electrons at rest we have $U_i = 0$ (no binding) and $J_i(p_z) = \delta(p_z)$ (no Doppler broadening). Moreover, from eq. (2.37) $E' = E_C$, so that photons scattered through an angle θ have energy E_C . Integration of the DCS, eq. (2.46), over E' then yields the familiar Klein-Nishina cross section,

$$\frac{d\sigma_{Co}^{KN}}{d\Omega} = Z \frac{r_e^2}{2} \left(\frac{E_C}{E} \right)^2 \left(\frac{E_C}{E} + \frac{E}{E_C} - \sin^2 \theta \right), \quad (2.47)$$

for the Z atomic electrons [cf. eq. (2.33)]. For energies of the order of a few MeV and larger, Doppler broadening and binding effects are relatively small and the free-electron theory yields results practically equivalent to those of the impulse approximation.

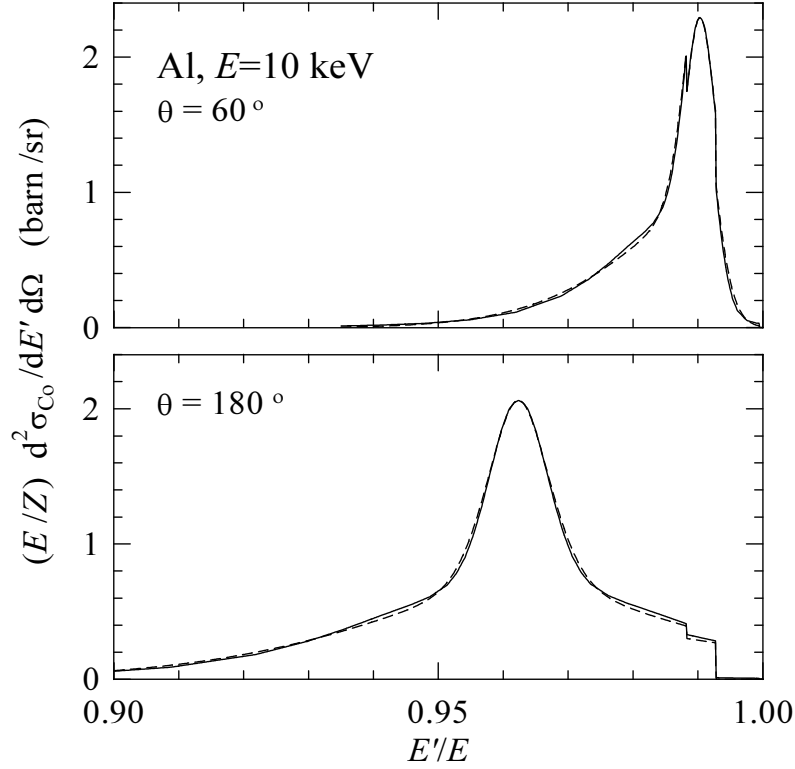


Figure 2.7: DCS for Compton scattering of 10 keV photons by aluminium atoms at the indicated scattering angles. The continuous curves represent the DCS (2.46) calculated using the Hartree-Fock Compton profile (Biggs et al., 1975). The dashed curves are results from eq. (2.46) with the analytical profiles given by eq. (2.57). (Adapted from Brusa et al., 1996.)

The angular distribution of scattered photons is given by the directional DCS,

$$\begin{aligned} \frac{d\sigma_{\text{Co}}}{d\Omega} &= \int \frac{d^2\sigma_{\text{Co}}}{dE' d\Omega} dE' = \frac{r_e^2}{2} \left(\frac{E_C}{E} \right)^2 \left(\frac{E_C}{E} + \frac{E}{E_C} - \sin^2 \theta \right) \\ &\times \sum_i f_i \Theta(E - U_i) \int_{-\infty}^{p_{i,\max}} F(p_z) J_i(p_z) dp_z, \end{aligned} \quad (2.48)$$

where $p_{i,\max}$ is the highest p_z -value for which an electron in the i -th shell can be excited. It is obtained from eq. (2.36) by setting $E' = E - U_i$,

$$p_{i,\max}(E, \theta) = \frac{E(E - U_i)(1 - \cos \theta) - m_e c^2 U_i}{c \sqrt{2E(E - U_i)(1 - \cos \theta) + U_i^2}}. \quad (2.49)$$

Except for energies just above the shell ionization threshold, the function $F(p_z)$ in the integral can be replaced by unity, since $p_z J_i(p_z)$ is an odd function and its integral is close to zero, i.e.

$$\int_{-\infty}^{p_{i,\max}} F(p_z) J_i(p_z) dp_z \simeq n_i(p_{i,\max}), \quad (2.50)$$

where

$$n_i(p_z) \equiv \int_{-\infty}^{p_z} J_i(p'_z) dp'_z. \quad (2.51)$$

Notice that $n_i(p_z)$ is a monotonously increasing function of p_z , which varies from 0 at $p_z = -\infty$ to unity at $p_z = \infty$; the quantity $n_i(p_{i,\max})$ represents the fraction of electrons in the i -th shell that can be effectively excited in a Compton interaction. We can then write

$$\frac{d\sigma_{\text{Co}}}{d\Omega} \simeq \frac{r_e^2}{2} \left(\frac{E_C}{E} \right)^2 \left(\frac{E_C}{E} + \frac{E}{E_C} - \sin^2 \theta \right) S(E, \theta). \quad (2.52)$$

The function

$$S(E, \theta) = \sum_i f_i \Theta(E - U_i) n_i(p_{i,\max}) \quad (2.53)$$

can be identified with the incoherent scattering function in the impulse approximation (see e.g. Ribberfors and Berggren, 1982). The total cross section can then be obtained as

$$\sigma_{\text{Co}} = 2\pi \int_{-1}^1 \frac{d\sigma_{\text{Co}}}{d\Omega} d(\cos \theta). \quad (2.54)$$

For comparison purposes, and also to calculate the energy deposition, it is useful to consider the cross section differential in only the energy of the scattered photon,

$$\frac{d\sigma_{\text{Co}}}{dE'} \equiv \int \frac{d^2\sigma_{\text{Co}}}{dE' d\Omega} d\Omega. \quad (2.55)$$

In the case of scattering by free electrons at rest, $E' = E_C$ and the Klein-Nishina formula (2.47) gives the following expression for the energy DCS,

$$\begin{aligned} \frac{d\sigma_{\text{Co}}^{\text{KN}}}{dE'} &= 2\pi \frac{d\sigma_{\text{Co}}^{\text{KN}}}{d\Omega} \frac{d(\cos \theta)}{dE_C} \\ &= \frac{\pi r_e^2}{E} \kappa^{-3} \left(\frac{E^2}{E'^2} + \frac{(\kappa^2 - 2\kappa - 2)E}{E'} + (2\kappa + 1) + \frac{\kappa^2 E'}{E} \right). \end{aligned} \quad (2.56)$$

Fig. 2.8 displays the energy DCSs obtained from this formula and from the impulse approximation for scattering of high-energy ($E > U_i$) photons by aluminium and gold atoms. These results show clearly the differences between the physics of the impulse approximation and the cruder free-electron approximation. The most conspicuous feature of the impulse approximation DCS is the absence of a threshold energy, which is a direct manifestation of the Doppler broadening. For relatively small energy transfers ($E' \sim E$) the Klein-Nishina DCS increases with the energy of the scattered photon, whereas the energy DCS obtained from the impulse approximation vanishes at $E' = E$ due to the effect of binding, which also causes the characteristic edge structure, similar to that of the photoelectric cross section (see fig. 2.8).

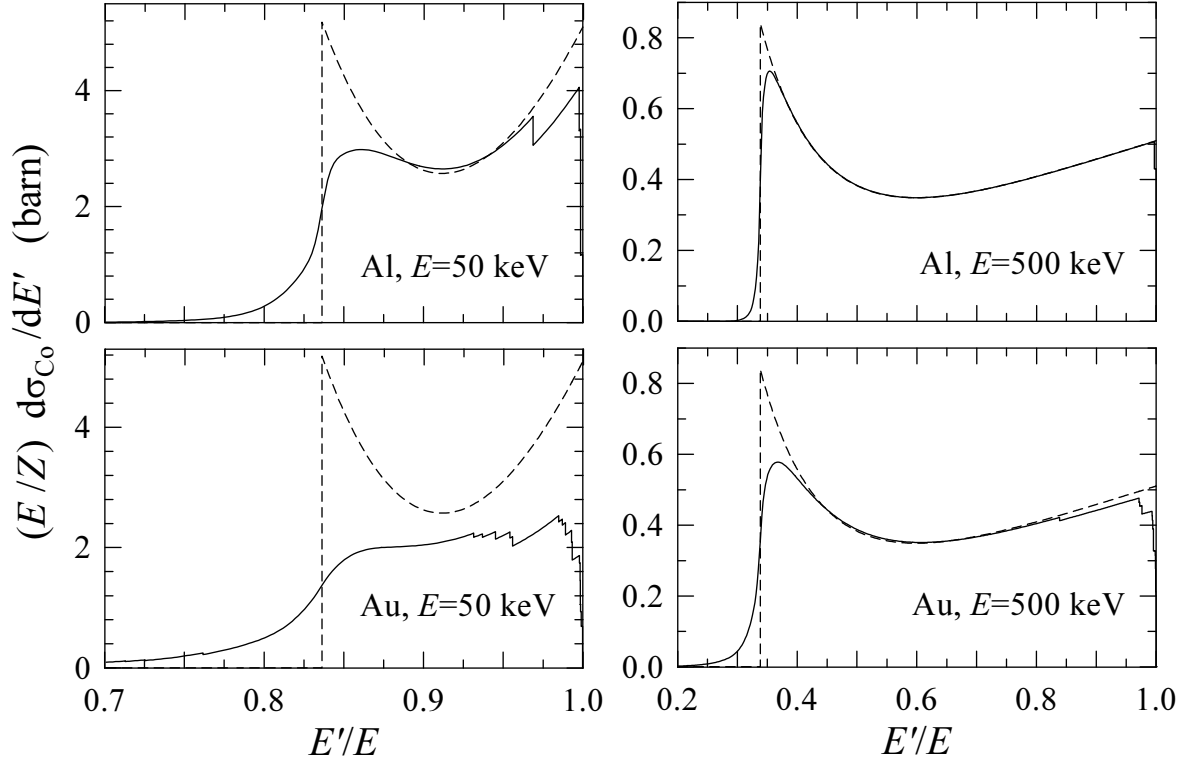


Figure 2.8: Energy DCSs for Compton scattering of 50 and 500 keV photons by aluminium and gold atoms. The continuous curves represent the DCS (2.55), computed using the analytical Compton profiles (2.57). The dashed curves are obtained from the Klein-Nishina formula (2.56), i.e. assuming that the atomic electrons are free and at rest.

2.3.1 Analytical Compton profiles

In order to minimize the required numerical information and to simplify the random sampling, we use approximate one-electron profiles of the form

$$J_i^A(p_z) = J_{i,0} \frac{nd_2}{2} \left(d_1 + d_2 J_{i,0} |p_z| \right)^{n-1} \exp \left[d_1^n - \left(d_1 + d_2 J_{i,0} |p_z| \right)^n \right] \quad (2.57)$$

with

$$n = 2, \quad d_1 = \left(\frac{n-1}{n} \right)^{1/n} = \sqrt{\frac{1}{2}}, \quad d_2 = \frac{2}{n} d_1^{1-n} = \sqrt{2}.$$

The quantity $J_{i,0} \equiv J_i(0)$ is the value of the profile at $p_z = 0$ obtained from the Hartree-Fock orbital (Biggs et al., 1975). $J_i(0)$ is tabulated in the file `PDATCONF.TAB` for all shells of the elements $Z = 1$ to 92. Notice that $J_i^A(p_z)$ is normalized according to eq. (2.40). With the profiles (2.57),

$$n_i^A(p_z) \equiv \int_{-p_z}^{p_z} J_i^A(p'_z) dp'_z = \begin{cases} \frac{1}{2} \exp \left[d_1^2 - \left(d_1 - d_2 J_{i,0} p_z \right)^2 \right] & \text{if } p_z < 0, \\ 1 - \frac{1}{2} \exp \left[d_1^2 - \left(d_1 + d_2 J_{i,0} p_z \right)^2 \right] & \text{if } p_z > 0. \end{cases} \quad (2.58)$$

Thus, the incoherent scattering function (2.53) can be expressed analytically and the integral (2.54) evaluated very quickly with the aid of function **SUMGA** (appendix B). On the other hand, the sampling equation $n_i^A(p_z) \equiv \xi n_i^A(p_{i,\max})$ (see section 1.2.2) can be solved analytically,

$$p_z = \begin{cases} \frac{1}{d_2 J_{i,0}} \left[d_1 - (d_1^2 - \ln 2A)^{1/2} \right] & \text{if } A < \frac{1}{2}, \\ \frac{1}{d_2 J_{i,0}} \left[(d_1^2 - \ln 2(1-A))^{1/2} - d_1 \right] & \text{if } A > \frac{1}{2}, \end{cases} \quad (2.59)$$

where $A \equiv \xi n_i^A(p_{i,\max})$. Atomic Compton profiles obtained from the approximation given by eq. (2.57) are accurate for small p_z and oscillate about the Hartree-Fock values for intermediate momenta (see fig. 2.6). The relative differences are normally less than 5%, except for large momenta for which $J(p_z)$ is very small. Similar differences are found between the DCS computed from Hartree-Fock and analytical Compton profiles (see fig. 2.7). For most applications (e.g. studies of detector response, dosimetry, radiotherapy, etc.), the effect of these differences on the simulation results is not important. The impulse approximation with the analytical one-electron profiles (2.57) then provides a conveniently simple method to introduce Doppler broadening and binding effects in the simulation of Compton scattering.

In PENELOPE, the maximum number of electron shells for each material is limited. For heavy elements, and also for compounds, the number of shells may be fairly large. In this case, outer shells with similar ionization energies are grouped together and replaced by a single shell with a $J_{i,0}$ value and an effective ionization energy equal to the corresponding averages of the grouped shells. This grouping does not alter the average effects of Doppler broadening and binding.

2.3.2 Simulation of incoherent scattering events

Compton events are simulated on the basis of the DCS given by eq. (2.46) with the analytical Compton profiles (2.57). The sampling algorithm adopted here is due to Brusa et al. (1996). It is similar to the one described by Namito et al. (1994), but has a higher efficiency.

The PDF of the polar deflection $\cos \theta$ and the energy E' of the scattered photon is given by (apart from normalization constants, which are irrelevant here)

$$P_{\text{Co}}(\cos \theta, E') = \left(\frac{E_C}{E} \right)^2 \left(\frac{E_C}{E} + \frac{E}{E_C} - \sin^2 \theta \right) \times F(p_z) \left(\sum_i f_i J_i(p_z) \Theta(E - E' - U_i) \right) \frac{dp_z}{dE'}. \quad (2.60)$$

Integration of expression (2.60) over E' , using the approximation (2.50), yields the PDF

of the polar deflection

$$P_\theta(\cos \theta) = \left(\frac{E_C}{E} \right)^2 \left(\frac{E_C}{E} + \frac{E}{E_C} - \sin^2 \theta \right) S(E, \theta), \quad (2.61)$$

where $S(E, \theta)$ is the incoherent scattering function, eq. (2.53).

Random values of $\cos \theta$ from the PDF (2.61) can be generated by using the following algorithm (Baró et al., 1994a). Let us introduce the quantity

$$\tau \equiv \frac{E_C}{E} = \frac{1}{1 + \kappa(1 - \cos \theta)}. \quad (2.62)$$

The minimum and maximum values of τ are

$$\tau_{\min} = \frac{1}{1 + 2\kappa} \quad \text{and} \quad \tau_{\max} = 1, \quad (2.63)$$

which correspond to backward ($\theta = \pi$) and forward ($\theta = 0$) scattering, respectively. The PDF of this variable is (again ignoring normalization constants)

$$P_\tau(\tau) = P_\theta(\cos \theta) \frac{d(\cos \theta)}{d\tau} = \left(\frac{1}{\tau^2} + \frac{\kappa^2 - 2\kappa - 2}{\tau} + (2\kappa + 1) + \kappa^2 \tau \right) S(E, \theta). \quad (2.64)$$

This distribution can be rewritten in the form (Nelson et al., 1985)

$$P_\tau(\tau) = [a_1 P_1(\tau) + a_2 P_2(\tau)] T(\cos \theta), \quad (2.65)$$

where

$$a_1 = \ln(1 + 2\kappa), \quad a_2 = \frac{2\kappa(1 + \kappa)}{(1 + 2\kappa)^2}, \quad (2.66)$$

$$P_1(\tau) = \frac{1}{\ln(1 + 2\kappa)} \frac{1}{\tau}, \quad P_2(\tau) = \frac{(1 + 2\kappa)^2}{2\kappa(1 + \kappa)} \tau \quad (2.67)$$

and

$$T(\cos \theta) = \left\{ 1 - \frac{(1 - \tau)[(2\kappa + 1)\tau - 1]}{\kappa^2 \tau(1 + \tau^2)} \right\} \frac{S(E, \theta)}{S(E, \theta = \pi)}. \quad (2.68)$$

The function in braces is positive, it equals 1 at the end points of the interval $(\tau_{\min}, 1)$, and is less than unity inside this interval. Moreover, the ratio of incoherent scattering functions is also less than unity for any value of $\theta < \pi$. Hence, the function $T(\cos \theta)$ is a valid rejection function. The functions $P_i(\tau)$ ($i = 1, 2$) are normalized PDFs in the interval $(\tau_{\min}, 1)$, which can be easily sampled by using the inverse transform method. The generation of random values of τ according to the PDF given by eq. (2.64) can then be performed by combining the composition and rejection methods (section 1.2). The algorithm to sample $\cos \theta$ proceeds as follows:

- (i) Sample a value of the integer i ($=1, 2$) according to the point probabilities

$$\pi(1) = \frac{a_1}{a_1 + a_2} \quad \text{and} \quad \pi(2) = \frac{a_2}{a_1 + a_2}. \quad (2.69)$$

(ii) Sample τ from $P_i(\tau)$ using the sampling formulae

$$\tau = \begin{cases} \tau_{\min}^{\xi} & \text{if } i = 1, \\ [\tau_{\min}^2 + \xi(1 - \tau_{\min}^2)]^{1/2} & \text{if } i = 2, \end{cases} \quad (2.70)$$

which can be easily derived by the inverse transform method (section 1.2.2).

(iii) Determine $\cos \theta$ using eq. (2.62),

$$\cos \theta = 1 - \frac{1 - \tau}{\kappa \tau}, \quad (2.71)$$

and compute the quantities $p_{i,\max}(E, \theta)$, eq. (2.49), and

$$S(E, \theta) = \sum_i f_i \Theta(E - U_i) n_i^A(p_{i,\max}). \quad (2.72)$$

(iv) Generate a new random number ξ .

(v) If $\xi > T(\cos \theta)$, go to step (i).

(vi) Deliver $\cos \theta$.

The efficiency of this algorithm, i.e. the probability of accepting a generated $\cos \theta$ -value, increases monotonically with photon energy and is nearly independent of Z ; typical values are 35%, 80% and 95% for $E = 1$ keV, 1 MeV and 10 MeV, respectively.

Once the direction of the emerging photon has been set, the active electron shell i is selected with relative probability equal to $Z_i \Theta(E - U_i) n_i^A(p_{i,\max}(E, \theta))$. A random value of p_z is generated from the analytical Compton profile (2.57) using the sampling formula (2.59). If p_z is less than $-m_e c$, it is rejected and a new shell and a p_z -value are sampled³. Finally, the factor $F(p_z)$ in the PDF (2.46) is accounted for by means of a rejection procedure. It should be noted that the approximation $F \simeq 1$ is valid only when the DCS is integrated over E' ; otherwise the complete expression (2.44) must be used. Let F_{\max} denote the maximum value of $F(p_z)$, which occurs at $p_z = 0.2m_e c$ or $-0.2m_e c$; a random number ξ is generated and the value p_z is accepted if $\xi F_{\max} < F(p_z)$, otherwise the process of selecting a shell and a p_z -value is reinitiated. The energy E' of the emerging photon is then calculated from eq. (2.36), which gives

$$E' = E \frac{\tau}{1 - t\tau^2} \left[(1 - t\tau \cos \theta) + \text{sign}(p_z) \sqrt{(1 - t\tau \cos \theta)^2 - (1 - t\tau^2)(1 - t)} \right], \quad (2.73)$$

where

$$t \equiv (p_z/m_e c)^2 \quad \text{and} \quad \text{sign}(p_z) \equiv p_z/|p_z|. \quad (2.74)$$

For photons with energy larger than 5 MeV, for which Doppler broadening is negligible, we set $E' = E_C$ (which amounts to assuming that $p_z = 0$). In this case, the active

³Notice that, due to the approximation introduced in eq. (2.36), a value $p_z < -m_e c$ would yield a negative energy for the scattered photon.

electron shell i is sampled with relative probability f_i and binding effects are accounted for by simply rejecting E' -values such that $E - E' < U_i$.

The azimuthal scattering angle ϕ of the photon is sampled uniformly in the interval $(0, 2\pi)$. We assume that the Compton electron is emitted with energy $E_e = E - E' - U_i$ in the direction of the momentum transfer vector $\mathbf{q} = \hbar\mathbf{k} - \hbar\mathbf{k}'$, with polar angle θ_e and azimuthal angle $\phi_e = \phi + \pi$, relative to the direction of the incident photon. $\cos\theta_e$ is given by

$$\cos\theta_e = \frac{E - E' \cos\theta}{\sqrt{E^2 + E'^2 - 2EE' \cos\theta}}. \quad (2.75)$$

When $E' = E_C$, this expression simplifies to

$$\cos\theta_e = \frac{E + m_e c^2}{E} \left(\frac{E - E_C}{2m_e c^2 + E - E_C} \right)^{1/2}, \quad (2.76)$$

which coincides with the result (A.20). Since the active electron shell is known, characteristic x rays and Auger electrons emitted in the de-excitation of the ionized atom can also be followed. This is important, for instance, to account for escape peaks in scintillation or solid state detectors

Table 2.1: Average number n_r of random numbers ξ needed to simulate a single incoherent scattering event for photons with energy E in aluminium, silver and gold.

E (eV)	Al	Ag	Au
10^3	16.6	11.9	13.4
10^4	11.0	11.4	11.5
10^5	9.5	9.8	10.0
10^6	8.2	8.2	8.3
10^7	7.5	7.5	7.5

As a measure of the efficiency of the sampling algorithm, we may consider the average number n_r of random numbers ξ required to simulate an incoherent scattering event. n_r is practically independent of the atomic number and decreases with photon energy (see table 2.1). The increase of n_r at low energies stems from the loss of efficiency of the algorithm used to sample $\cos\theta$. Although the simulation of incoherent events becomes more laborious as the photon energy decreases, this has only a small influence on the speed of practical photon transport simulations since low-energy photons interact predominantly via photoelectric absorption (see fig. 2.10 below).

2.4 Electron-positron pair production

Electron-positron pairs can be created by absorption of a photon in the vicinity of a massive particle, a nucleus or an electron, which absorbs energy and momentum so that

these two quantities are conserved. The threshold energy for pair production in the field of a nucleus (assumed of infinite mass) is $2m_e c^2$. When pair production occurs in the field of an electron, the target electron recoils after the event with appreciable kinetic energy; the process is known as “triplet production” because it causes three visible tracks when observed, e.g. in a cloud chamber. If the target electron is at rest, triplet production is only possible for photons with energy larger than $4m_e c^2$.

For the simulation of pair production events in the field of an atom of atomic number Z , we shall use the following semiempirical model (Baró et al., 1994a). Our starting point is the high-energy DCS for arbitrary screening, which was derived by Bethe and Heitler from the Born approximation (Motz et al., 1969; Tsai, 1974). The Bethe-Heitler DCS for a photon of energy E to create an electron-positron pair, in which the electron has a kinetic energy $E_- = \epsilon E - m_e c^2$, can be expressed as (Tsai, 1974)

$$\frac{d\sigma_{\text{pp}}^{(\text{BH})}}{d\epsilon} = r_e^2 \alpha Z [Z + \eta] \left\{ [\epsilon^2 + (1 - \epsilon)^2] (\Phi_1 - 4f_C) + \frac{2}{3} \epsilon (1 - \epsilon) (\Phi_2 - 4f_C) \right\}. \quad (2.77)$$

Notice that the “reduced energy” $\epsilon = (E_- + m_e c^2)/E$ is the fraction of the photon energy that is taken away by the electron. The screening functions Φ_1 and Φ_2 are given by integrals that involve the atomic form factor and, therefore, must be computed numerically when a realistic form factor is adopted (e.g. the analytical one described in section 2.1). To obtain approximate analytical expressions for these functions, we shall assume that the Coulomb field of the nucleus is exponentially screened by the atomic electrons (Schiff, 1968; Tsai, 1974), i.e. the electrostatic potential of the atom is assumed to be (Wentzel model)

$$\varphi_W(r) = \frac{Ze}{r} \exp(-r/R), \quad (2.78)$$

with the screening radius R considered as an adjustable parameter (see below). The corresponding atomic electron density is obtained from Poisson’s equation,

$$\rho_W(r) = \frac{1}{4\pi e} \nabla^2 \varphi(r) = \frac{1}{4\pi e} \frac{1}{r} \frac{d^2}{dr^2} [r\varphi(r)] = \frac{Z}{4\pi R^2 r} \exp(-r/R), \quad (2.79)$$

and the atomic form factor is

$$F_W(q, Z) = 4\pi \int_0^\infty \rho_W(r) \frac{\sin(qr/\hbar)}{qr/\hbar} r^2 dr = \frac{Z}{1 + (Rq/\hbar)^2}. \quad (2.80)$$

The screening functions for this particular form factor take the following analytical expressions (Tsai, 1974)

$$\begin{aligned} \Phi_1 &= 2 - 2 \ln(1 + b^2) - 4b \arctan(b^{-1}) + 4 \ln(Rm_e c/\hbar) \\ \Phi_2 &= \frac{4}{3} - 2 \ln(1 + b^2) + 2b^2 \left[4 - 4b \arctan(b^{-1}) - 3 \ln(1 + b^{-2}) \right] \\ &\quad + 4 \ln(Rm_e c/\hbar), \end{aligned} \quad (2.81)$$

where

$$b = \frac{Rm_e c}{\hbar} \frac{1}{2\kappa} \frac{1}{\epsilon(1 - \epsilon)}. \quad (2.82)$$

The quantity η in eq. (2.77) accounts for pair production in the field of the atomic electrons (triplet production), which is considered in detail by Hubbell et al. (1980) and Tsai (1974). In order to simplify the calculations, the dependence of the triplet cross section on the electron reduced energy, ϵ , is assumed to be the same as that of the pair cross section. The function f_C in (2.77) is the high-energy Coulomb correction of Davies, Bethe and Maximon (1954) given by

$$f_C(Z) = a^2 \left[(1 + a^2)^{-1} + 0.202059 - 0.03693a^2 + 0.00835a^4 - 0.00201a^6 + 0.00049a^8 - 0.00012a^{10} + 0.00003a^{12} \right], \quad (2.83)$$

with $a = \alpha Z$. The total atomic cross section for pair (and triplet) production is obtained as

$$\sigma_{\text{pp}}^{(\text{BH})} = \int_{\epsilon_{\text{min}}}^{\epsilon_{\text{max}}} \frac{d\sigma_{\text{pp}}^{(\text{BH})}}{d\epsilon} d\epsilon, \quad (2.84)$$

where

$$\epsilon_{\text{min}} = m_e c^2 / E = \kappa^{-1} \quad \text{and} \quad \epsilon_{\text{max}} = 1 - m_e c^2 / E = 1 - \kappa^{-1}. \quad (2.85)$$

Extensive tables of pair production total cross sections, evaluated by combining different theoretical approximations, have been published by Hubbell et al. (1980). These tables give the separate contributions of pair production in the field of the nucleus and in that of the atomic electrons for $Z = 1$ to 100 and for photon energies from threshold up to 10^5 MeV. Following Salvat and Fernández-Varea (1992), the screening radius R has been determined by requiring that eq. (2.77) with $\eta = 0$ exactly reproduces the total cross sections given by Hubbell et al. (1980) for pair production in the nuclear field by 10^5 MeV photons (after exclusion of radiative corrections, which only amount to $\sim 1\%$ of the total cross section). The screening radii for $Z = 1$ –92 obtained in this way are given in table 2.2.

Actually, the triplet contribution, η , varies with the photon energy. It increases monotonically from zero at $E \simeq 4m_e c^2$ and reaches a saturation value, η_∞ , at high energies. It can be obtained, for all elements and energies up to 10^5 MeV, as

$$\eta(E) = Z \sigma_{\text{triplet}}^{\text{HGO}}(E) / \sigma_{\text{pair}}^{\text{HGO}}(E), \quad (2.86)$$

where $\sigma_{\text{pair}}^{\text{HGO}}$ and $\sigma_{\text{triplet}}^{\text{HGO}}$ are the total pair and triplet production cross sections given by Hubbell et al. (1980). At 10^5 MeV, the high-energy limit is reached, i.e.

$$\eta_\infty \simeq Z \sigma_{\text{triplet}}^{\text{HGO}}(10^5 \text{ MeV}) / \sigma_{\text{pair}}^{\text{HGO}}(10^5 \text{ MeV}). \quad (2.87)$$

The values of η_∞ for the elements $Z = 1$ –92 are given in table 2.2. The average dependence of η on the photon energy is approximated by the following empirical expression

$$\eta = [1 - \exp(-v)] \eta_\infty, \quad (2.88)$$

Table 2.2: Reduced screening radius, $Rm_e c/\hbar$, and high-energy triplet contribution, η_∞ , for electron-positron pair production obtained from the tables of Hubbell et al. (1980) as described in the text. Notice that $\hbar/m_e c = 3.8616 \times 10^{-13}$ m is the Compton wavelength of the electron.

Z	$Rm_e c/\hbar$	η_∞	Z	$Rm_e c/\hbar$	η_∞	Z	$Rm_e c/\hbar$	η_∞
1	122.81	1.157	32	33.422	1.158	63	26.911	1.194
2	73.167	1.169	33	33.068	1.157	64	26.705	1.196
3	69.228	1.219	34	32.740	1.158	65	26.516	1.197
4	67.301	1.201	35	32.438	1.158	66	26.304	1.196
5	64.696	1.189	36	32.143	1.158	67	26.108	1.197
6	61.228	1.174	37	31.884	1.166	68	25.929	1.197
7	57.524	1.176	38	31.622	1.173	69	25.730	1.198
8	54.033	1.169	39	31.438	1.174	70	25.577	1.198
9	50.787	1.163	40	31.142	1.175	71	25.403	1.200
10	47.851	1.157	41	30.950	1.170	72	25.245	1.201
11	46.373	1.174	42	30.758	1.169	73	25.100	1.202
12	45.401	1.183	43	30.561	1.172	74	24.941	1.204
13	44.503	1.186	44	30.285	1.169	75	24.790	1.205
14	43.815	1.184	45	30.097	1.168	76	24.655	1.206
15	43.074	1.180	46	29.832	1.164	77	24.506	1.208
16	42.321	1.178	47	29.581	1.167	78	24.391	1.207
17	41.586	1.175	48	29.411	1.170	79	24.262	1.208
18	40.953	1.170	49	29.247	1.172	80	24.145	1.212
19	40.524	1.180	50	29.085	1.174	81	24.039	1.215
20	40.256	1.187	51	28.930	1.175	82	23.922	1.218
21	39.756	1.184	52	28.721	1.178	83	23.813	1.221
22	39.144	1.180	53	28.580	1.179	84	23.712	1.224
23	38.462	1.177	54	28.442	1.180	85	23.621	1.227
24	37.778	1.166	55	28.312	1.187	86	23.523	1.230
25	37.174	1.169	56	28.139	1.194	87	23.430	1.237
26	36.663	1.166	57	27.973	1.197	88	23.331	1.243
27	35.986	1.164	58	27.819	1.196	89	23.238	1.247
28	35.317	1.162	59	27.675	1.194	90	23.139	1.250
29	34.688	1.154	60	27.496	1.194	91	23.048	1.251
30	34.197	1.156	61	27.285	1.194	92	22.967	1.252
31	33.786	1.157	62	27.093	1.194			

where

$$v = (0.2840 - 0.1909a) \ln(4/\kappa) + (0.1095 + 0.2206a) \ln^2(4/\kappa) \\ + (0.02888 - 0.04269a) \ln^3(4/\kappa) + (0.002527 + 0.002623a) \ln^4(4/\kappa). \quad (2.89)$$

Then, the single quantity η_∞ characterizes the triplet production for each element.

The approximation given by eq. (2.77) with the fitted value of the screening radius, fails at low energies where it systematically underestimates the total cross section (it can even become negative). To compensate for this fact we introduce an empirical correcting term $F_0(\kappa, Z)$, which acts in a way similar to the Coulomb correction. To facilitate the random sampling, the Bethe-Heitler DCS, eq. (2.77), including this low-energy correction and a high-energy radiative correction, is written in the form

$$\frac{d\sigma_{pp}}{d\epsilon} = r_e^2 \alpha Z [Z + \eta] C_r \frac{2}{3} \left[2 \left(\frac{1}{2} - \epsilon \right)^2 \phi_1(\epsilon) + \phi_2(\epsilon) \right], \quad (2.90)$$

where

$$\begin{aligned} \phi_1(\epsilon) &= g_1(b) + g_0(\kappa) \\ \phi_2(\epsilon) &= g_2(b) + g_0(\kappa) \end{aligned} \quad (2.91)$$

with

$$\begin{aligned} g_1(b) &= \frac{1}{2}(3\Phi_1 - \Phi_2) - 4 \ln(Rm_e c / \hbar) = \frac{7}{3} - 2 \ln(1 + b^2) - 6b \arctan(b^{-1}) \\ &\quad - b^2 [4 - 4b \arctan(b^{-1}) - 3 \ln(1 + b^{-2})], \\ g_2(b) &= \frac{1}{4}(3\Phi_1 + \Phi_2) - 4 \ln(Rm_e c / \hbar) = \frac{11}{6} - 2 \ln(1 + b^2) - 3b \arctan(b^{-1}) \\ &\quad + \frac{1}{2} b^2 [4 - 4b \arctan(b^{-1}) - 3 \ln(1 + b^{-2})], \\ g_0(\kappa) &= 4 \ln(Rm_e c / \hbar) - 4f_C(Z) + F_0(\kappa, Z). \end{aligned} \quad (2.92)$$

$C_r = 1.0093$ is the high-energy limit of Mork and Olsen's radiative correction (Hubbell et al., 1980).

The correcting factor $F_0(\kappa, Z)$ has been determined by requiring that the total cross section for pair production obtained from the expression given in eq. (2.90) (with $\eta = 0$) coincides with the total cross sections for pair production in the field of the nucleus tabulated by Hubbell et al. (1980). By inspection and numerical fitting, we have obtained the following analytical approximation

$$\begin{aligned} F_0(\kappa, Z) &= (-0.1774 - 12.10a + 11.18a^2)(2/\kappa)^{1/2} \\ &\quad + (8.523 + 73.26a - 44.41a^2)(2/\kappa) \\ &\quad - (13.52 + 121.1a - 96.41a^2)(2/\kappa)^{3/2} \\ &\quad + (8.946 + 62.05a - 63.41a^2)(2/\kappa)^2. \end{aligned} \quad (2.93)$$

The functions ϕ_1 and ϕ_2 are now positive except for ϵ -values very near the endpoints of the allowed interval, given by eq. (2.85), for high atomic number elements. To avoid inconsistencies, these functions are set equal to zero when they take negative values.

The relative differences between the total atomic cross sections obtained from the DCS given by eq. (2.90) and the total cross sections tabulated by Hubbell et al. (1980) are appreciable near the threshold [actually, (2.90) shifts the threshold for pair production to values slightly larger than $2m_e c^2$], but decrease rapidly with increasing photon energy. At $E = 3$ MeV, the differences reduce to 4% and do not exceed 2% for energies larger than 6 MeV, for almost all the elements. Although these differences are not important, they may be larger than the uncertainties in the cross sections given by Hubbell et al. (1980). To avoid systematic errors, the mean free paths for pair production used in PENELOPE are obtained by interpolation in a table generated with the XCOM program (Berger and Hubbell, 1987). The Bethe-Heitler DCS is only used to sample the kinetic energies of the produced pair.

It is also worth noting that the Bethe-Heitler theory predicts that the pair-production DCS, considered as a function of the electron reduced energy ϵ , is symmetrical about $\epsilon = 1/2$ (see fig. 2.9). This dependence on ϵ is reasonably accurate only for photon energies larger than ~ 5 MeV. For lower photon energies, the effect of the electrostatic field of the atom (which slows down the electron and accelerates the positron) becomes increasingly important, with the result that the actual DCS becomes asymmetrical and the mean value of ϵ becomes less than $1/2$ (see e.g. Motz et al., 1969). At these relatively low energies, however, pair production is not dominant and, moreover, the produced particles have ranges that are much less than the mean free path of the absorbed photon. Therefore, no appreciable simulation errors are incurred by using the Bethe-Heitler DCS, eq. (2.90), for energies down to the threshold.

2.4.1 Simulation of pair production events

The Bethe-Heitler DCS, eq. (2.90), only depends on the kinetic energy $E_- = \epsilon E - m_e c^2$ of the produced electron, so that E_- can be directly sampled from eq. (2.90); the kinetic energy of the positron is obtained as $E_+ = E - E_- - 2m_e c^2$. Notice that, although the Bethe-Heitler total atomic cross section accounts for pair and triplet production, all the events are simulated as if they were pairs. This approximation is justified by the fact that, in triplet production, the recoiling electron has a range that is much smaller than the mean free path of the incident photon.

The electron reduced energy ϵ is distributed in the interval $(\kappa^{-1}, 1 - \kappa^{-1})$, see eq. (2.85), according to the PDF given by eq. (2.90) (normalization is again irrelevant)

$$p_{pp}(\epsilon) = 2 \left(\frac{1}{2} - \epsilon \right)^2 \phi_1(\epsilon) + \phi_2(\epsilon), \quad (2.94)$$

which is symmetrical about the point $\epsilon = 1/2$. Fig. 2.9 shows this PDF for lead and various photon energies. The following algorithm for sampling ϵ is based on the fact

that the functions $\phi_1(\epsilon)$ and $\phi_2(\epsilon)$ are non-negative and attain their maximum values at $\epsilon = 1/2$.

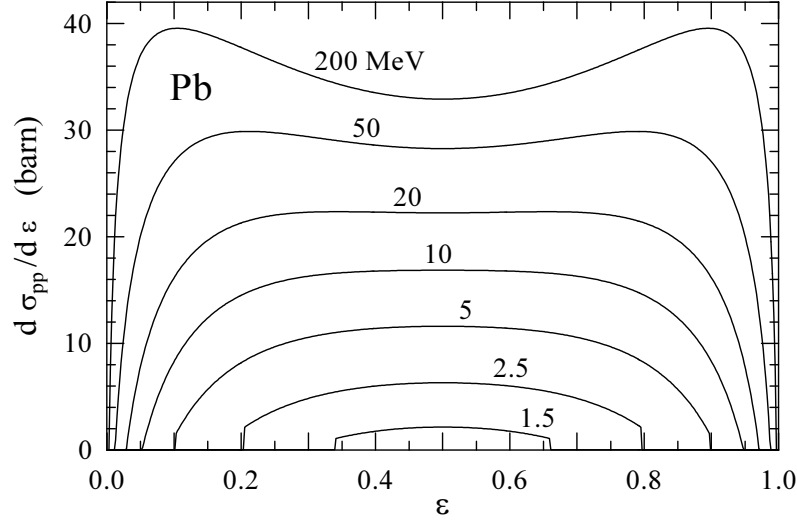


Figure 2.9: Pair production DCS in lead as a function of the electron reduced energy, $\epsilon = (E_- + m_e c^2)/E$. (Adapted from Baró et al., 1994a.)

Except for a normalization constant, the PDF (2.94) can be written in the form

$$p_{pp}(\epsilon) = u_1 U_1(\epsilon) \pi_1(\epsilon) + u_2 U_2(\epsilon) \pi_2(\epsilon) \quad (2.95)$$

with

$$u_1 = \frac{2}{3} \left(\frac{1}{2} - \frac{1}{\kappa} \right)^2 \phi_1(1/2), \quad u_2 = \phi_2(1/2), \quad (2.96)$$

$$\pi_1(\epsilon) = \frac{3}{2} \left(\frac{1}{2} - \frac{1}{\kappa} \right)^{-3} \left(\frac{1}{2} - \epsilon \right)^2, \quad \pi_2(\epsilon) = \frac{1}{2} \left(\frac{1}{2} - \frac{1}{\kappa} \right)^{-1} \quad (2.97)$$

and

$$U_1(\epsilon) = \phi_1(\epsilon)/\phi_1(1/2), \quad U_2(\epsilon) = \phi_2(\epsilon)/\phi_2(1/2). \quad (2.98)$$

The functions $\pi_i(\epsilon)$ are normalized PDFs in the interval $(\kappa^{-1}, 1 - \kappa^{-1})$, from which random values of ϵ can be easily sampled by using the inverse transform method. In this interval, the functions $U_i(\epsilon)$ are positive and less than unity, i.e. they are valid rejection functions. The generation of random values of ϵ from the distribution (2.95) can now be performed by combining the composition and rejection methods (see section 1.2) according to the following algorithm:

- (i) Sample a value of the integer i ($=1, 2$) according to the point probabilities

$$p(1) = \frac{u_1}{u_1 + u_2} \quad \text{and} \quad p(2) = \frac{u_2}{u_1 + u_2}. \quad (2.99)$$

- (ii) Sample ϵ from $\pi_i(\epsilon)$ using the sampling formulae (inverse transform method, see section 1.2.2)

$$\epsilon = \begin{cases} \frac{1}{2} + \left(\frac{1}{2} - \frac{1}{\kappa}\right) (2\xi - 1)^{1/3} & \text{if } i = 1, \\ \frac{1}{\kappa} + \left(\frac{1}{2} - \frac{1}{\kappa}\right) 2\xi & \text{if } i = 2. \end{cases} \quad (2.100)$$

- (iii) Generate a new random number ξ .

- (iv) If $\xi > U_i(\epsilon)$, go to step (i).

- (v) Deliver ϵ .

Notice that the quantity $2\xi - 1$ may be negative and, therefore, taking its cube root will lead to a computer error; provision of this fact must be made when programming the algorithm. The efficiency of the algorithm is greater than 70% for energies near the threshold, and increases with increasing photon energies. For $E = 1$ GeV it is of the order of 95% for all the elements in the periodic table.

Angular distribution of the produced particles

Actually, the complete DCS for pair production is a function of the directions of the pair of particles. As the final state involves three bodies (the nucleus and the produced pair), the directions of the produced particles cannot be obtained from only their kinetic energies. The polar angles of the directions of movement of the electron and positron (θ_- and θ_+ , fig. 2.1) relative to the direction of the incident photon are sampled from the leading term of the expression obtained from high-energy theory (Heitler, 1954; Motz et al., 1969)

$$p(\cos \theta_{\pm}) = a (1 - \beta_{\pm} \cos \theta_{\pm})^{-2}, \quad (2.101)$$

where a is a normalization constant and

$$\beta_{\pm} = \frac{\sqrt{E_{\pm}(E_{\pm} + 2m_e c^2)}}{E_{\pm} + m_e c^2} \quad (2.102)$$

is the particle velocity in units of the speed of light. Random values of $\cos \theta_{\pm}$ are obtained by using the inverse transform method (see section 1.2.2), which leads to the sampling formula

$$\cos \theta_{\pm} = \frac{2\xi - 1 + \beta_{\pm}}{(2\xi - 1)\beta_{\pm} + 1}. \quad (2.103)$$

As the directions of the produced particles and the incident photon are not necessarily coplanar, the azimuthal angles ϕ_- and ϕ_+ of the electron and the positron are sampled independently and uniformly in the interval $(0, 2\pi)$.

It is worth stressing the fact that the produced charged particles have ranges that are much smaller than the mean free path of the photons. Moreover, the charged particles immediately enter a multiple elastic scattering process which randomizes their

directions of movement. As a consequence, there should be little difference between simulation results obtained with the present method and with exact random sampling from a more accurate DCS, differential in the energies and directions of the generated particles.

Compound materials

Let us consider a compound X_xY_y , in which the molecules consist of x atoms of the element X and y atoms of the element Y . The number of electrons per molecule is $Z_M = xZ(X) + yZ(Y)$ and the molecular weight is $A_M = xA_w(X) + yA_w(Y)$, where $Z(X)$ and $A_w(X)$ stand for the atomic number and atomic weight of element X .

In the simulation of pair-production events, we could use the molecular DCSs obtained from the additivity rule. The simulation of each event would then consist of 1) sampling the atom which participates in the interaction and 2) generating a random value of the electron reduced energy ϵ from the corresponding atomic DCS. To save computer time, PENELOPE generates ϵ by considering an “equivalent” single element material of the same mass density ρ as the actual medium, atomic number Z_{eq} and atomic weight A_{eq} given by

$$Z_{eq}A_M = Z_MA_{eq} = xZ(X)A_w(X) + yZ(Y)A_w(Y), \quad (2.104)$$

i.e. its atomic number (weight) is the mass-average (Z -average) of the atomic numbers (weights) of the constituent atoms. The reduced energy is sampled from the DCS of the element with the atomic number closest to Z_{eq} . Usually, this approximation does not alter the simulation results appreciably and permits a considerable simplification of the program and a reduction of the simulation time.

2.5 Attenuation coefficients

The photon inverse mean free path for a given mechanism is known as the partial attenuation coefficient of that mechanism. Thus, the partial attenuation coefficient for photoelectric absorption is

$$\mu_{ph} = \mathcal{N}\sigma_{ph}, \quad (2.105)$$

where $\mathcal{N} = N_A\rho/A_M$ is the number of atoms or molecules per unit volume and σ_{ph} is the atomic or molecular photoelectric cross section. The photoelectric mass attenuation coefficient is defined as μ_{ph}/ρ and, therefore, is independent of the density of the material. Analogous definitions apply for the other interaction processes. The total mass attenuation coefficient is obtained as

$$\frac{\mu}{\rho} = \frac{N_A}{A_M} (\sigma_{Ra} + \sigma_{Co} + \sigma_{ph} + \sigma_{pp}). \quad (2.106)$$

As mentioned above, PENELOPE uses tables of total cross sections for photoelectric absorption and pair production obtained from the database EPDL (Cullen et al., 1997)

and the program *xcom* (Berger and Hubbell, 1987), respectively. Photoelectric cross sections for energies different from those in the tables are calculated by linear log-log interpolation. Total cross sections for pair production are evaluated by cubic spline log-log interpolation of the function $(1 - 2m_e c^2/E)^{-3} \sigma_{pp}$, which varies slowly with the photon energy.

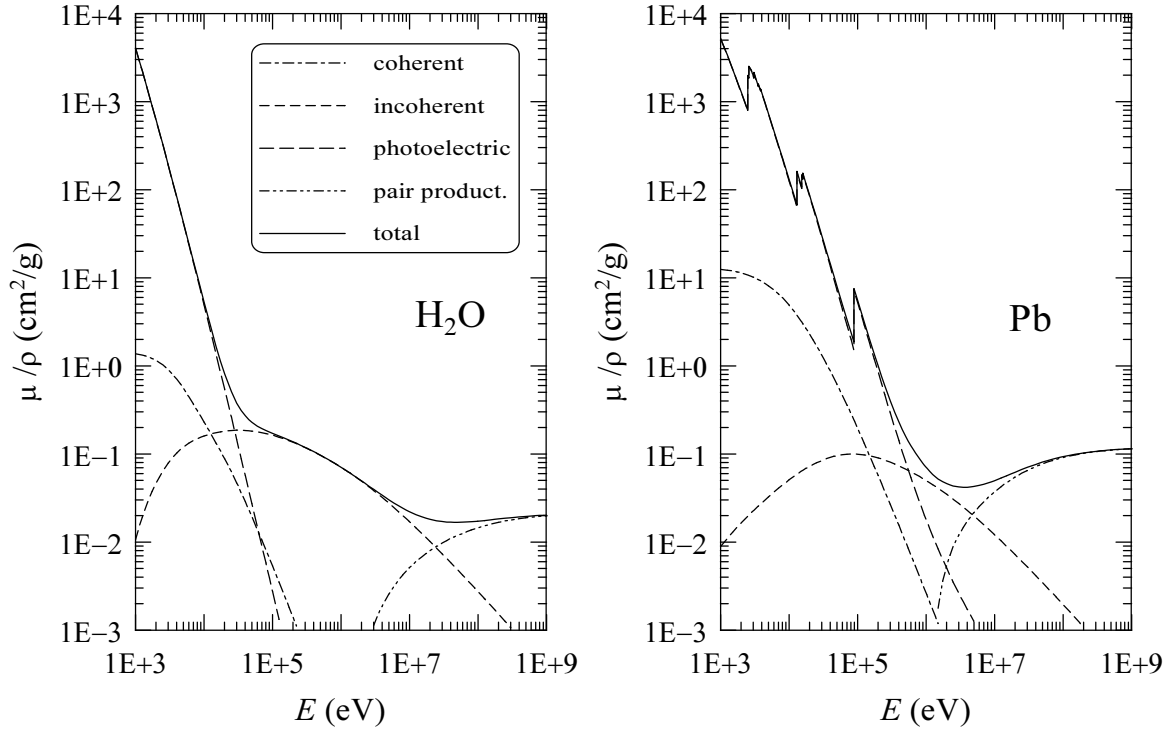


Figure 2.10: Partial and total mass attenuation coefficients of water and lead as functions of the photon energy.

Mean free paths for coherent and incoherent scattering are computed from the DCSs described in sections 2.1 and 2.3. The resulting values are virtually identical to those given by the *xcom* program for E greater than ~ 50 keV. At lower energies, our mean free paths for Compton scattering deviate from those given by *xcom*; these were calculated from a different theoretical model (Hubbell et al., 1975), which neglects Doppler broadening (see e.g. Brusa et al., 1996). The evaluation of the total atomic cross section for these processes [see eqs. (2.10) and (2.54)] involves a numerical quadrature, which is performed by using the function *SUMGA* (appendix B). Notice that for high-energy photons, the integrand in the coherent scattering cross section, eq. (2.10), is sharply peaked at $\theta = 0$. In such a case, the numerical integration method is not effective. For energies larger than $\sim Z/2$ MeV, we take advantage of the asymptotic behaviour shown by eq. (2.12) to avoid time-consuming integration. Partial and total mass attenuation coefficients for water and lead, as representatives of low- and high- Z materials, are displayed in fig. 2.10.

2.6 Atomic relaxation

Atoms are primarily ionized by photon interactions and by electron or positron impact. There is a fundamental difference between the ionizing effects of photons and of charged particles. A photon is only able to directly ionize a few atoms. In the case of photoabsorption, when the photon energy is larger than the K-shell binding energy, about 80% of photoabsorptions occur in the K shell, i.e. the resulting ion with a vacancy in the K shell is highly excited. Incoherent scattering is not as highly preferential, but still the probability that an inner shell is ionized is nearly proportional to the number of electrons in the shell. Conversely, fast electrons and positrons (and other charged particles) ionize many atoms along their paths; the ionizations occur preferentially in the less tightly bound atomic shells, or the conduction band in the case of metals (see section 3.2), so that most of the produced ions are only weakly excited.

Excited ions with a vacancy in an inner shell relax to their ground state through a sequence of radiative and non-radiative transitions. In a radiative transition, the vacancy is filled by an electron from an outer shell and an x ray with characteristic energy is emitted. In a non-radiative transition, the vacancy is filled by an outer electron and the excess energy is released through emission of an electron from a shell that is farther out (Auger effect). Each non-radiative transition generates an additional vacancy that, in turn, migrates “outwards”. The production of vacancies in inner shells and their subsequent relaxation must be simulated in detail, since the energetic x rays and/or electrons emitted during the process may transport energy quite a distance from the excited ion.

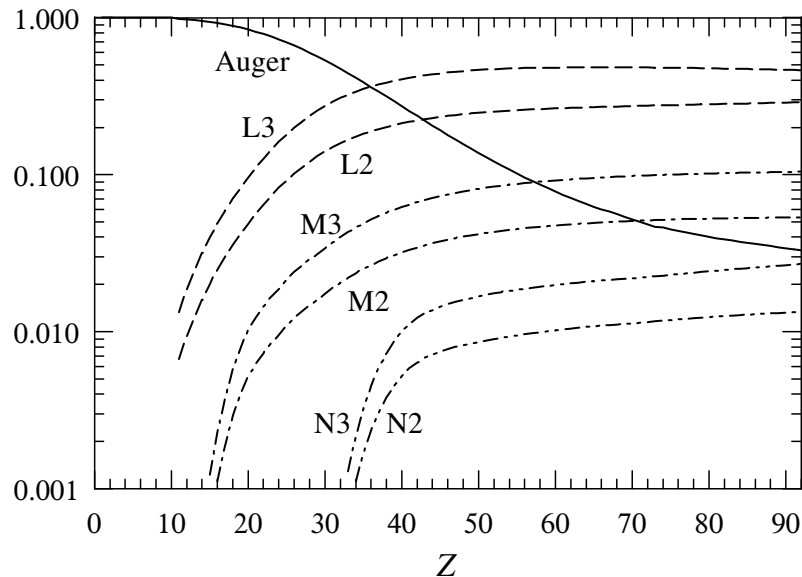


Figure 2.11: Relative probabilities for radiative and non-radiative (Auger) transitions that fill a vacancy in the K-shell of atoms.

PENELOPE simulates the emission of characteristic radiation and Auger electrons that result from vacancies produced in K shells and L subshells by photoelectric absorption, Compton scattering and electron/positron impact (see chapter 3). The relaxation of these vacancies is followed until the K and L shells are filled up, i.e. until the vacancies have migrated to M and outer shells. Vacancies in these outer shells originate much less energetic secondary radiation, whose main effect is to spread out the excitation energy of the ion within the surrounding material. To get a reliable description of the dose distribution, and other macroscopic transport characteristics, we only have to follow secondary radiation that is able to propagate to distances of the order of, say, 1% of the penetration distance (or range) of the primary radiation. Radiation with lower energy does not need to be followed, since its only effect is to blur the “primary” dose distribution on a small length scale.

To simplify the description of the ionization processes of outer shells (i.e. photoelectric absorption, Compton scattering and electron/positron impact), we simply assume that, when ionization occurs in M or outer shells, a secondary (delta) electron is emitted from the parent ion with a kinetic energy E_s equal to the energy deposited by the primary particle,

$$E_{\text{dep}} = \begin{cases} E - E' & \text{in Compton scattering,} \\ E & \text{in photoelectric absorption,} \\ W & \text{in electron/positron impact (see chapter 3).} \end{cases} \quad (2.107)$$

That is, the whole excitation energy of the ion is taken up by the ejected electron and no fluorescent radiation is simulated. In reality, the emitted electrons have energies less than the values (2.107) and can be followed by characteristic x rays, which have mean free paths that are usually much larger than the Bethe range of photoelectrons. By giving an artificially increased initial energy to the electron we allow it to transport energy farther from the ion so as to partially compensate for the neglect of other radiation emitted during the de-excitation cascade.

In the case of ionization of an inner shell i , i.e. a K shell or an L shell, we consider that the electron is ejected with kinetic energy

$$E_s = E_{\text{dep}} - U_i, \quad (2.108)$$

where U_i is the ionization energy of the active shell, and that the target atom is left with a vacancy in shell i . As mentioned above, we consider only characteristic x-rays and Auger electrons emitted in the first stages of the relaxation process. These secondary radiations are assumed to be emitted isotropically from the excited atom. We use the following notation to designate the possible transitions

- Radiative: S0-S1 (an electron from the S1 shell fills the vacancy in the S0 shell, leaving a hole in the S1 shell). The considered radiative transitions (for elements with $Z > 18$ with the M-shell filled) are shown in fig. 2.3.
- Non-radiative: S0-S1-S2 (an electron from the S1 shell fills the vacancy in the S0 shell, and the released energy is taken away by an electron in the S2 shell; this process leaves

two vacancies, in the S1 and S2 shells).

Non-radiative transitions of the type $LJ-LJ-Xq$, which involve an electron transition between two L-subshells and the ejection of an electron from an outer shell Xq are known as L-shell Coster-Kronig transitions.

The information furnished to PENELOPE for each element consists of a table of possible transitions, transition probabilities and energies of the emitted x-rays or electrons for ionized atoms with a single vacancy in the K-shell or in an L-subshell. These data are entered through the material definition file. The transition probabilities are extracted from the LLNL Evaluated Atomic Data Library (Perkins et al., 1991). Fig. 2.11 displays transition probabilities for the transitions that fill a vacancy in the K shell as functions of the atomic number Z ; the curve labelled “Auger” corresponds to the totality of non-radiative transitions. We see that for low- Z elements, the relaxation proceeds mostly through non-radiative transitions. It is worth noting that the ratio of probabilities of the radiative transitions K-S2 and K-S3 (where S stands for L, M or N) is approximately 1/2, as obtained from the dipole approximation (see e.g. Bransden and Joachain, 1983); radiative transitions K-S1 are strictly forbidden (to first order) within the dipole approximation.

The energies of x-rays emitted in radiative transitions are taken from Bearden’s (1967) review and reevaluation of experimental x-ray wavelengths. The energy of the electron emitted in the non-radiative transition S0-S1-S2 is set equal to

$$E_e = U_{S0} - U_{S1} - U_{S2}, \quad (2.109)$$

where U_{Si} is the binding energy of an electron in the shell Si of the neutral atom, which is taken from the PENELOPE database. These emission energies correspond to assuming that the presence of the vacancy (or vacancies) does not alter the ionization energies of the active electron shells, which is an approximation. It should be noted that these prescriptions are also used to determine the energies of the emitted radiation at any stage of the de-excitation cascade, which means that we neglect the possible relaxation of the ion (see e.g. Sevier, 1972). Therefore, our approach will not produce L_α and L_β x-ray satellite lines; these arise from the filling of a vacancy in a doubly-ionized L-shell (generated e.g. by a Coster-Kronig transition), which releases an energy that is slightly different from the energy liberated when the shell contains only a single vacancy. It is also worth recalling that the adopted transition probabilities are approximate. For K shells they are expected to be accurate to within one per cent or so, but for other shells they are subject to much larger uncertainties. Even the L-shell fluorescence yield (the sum of radiative transition probabilities for an L-shell vacancy) is uncertain by about 20% (see e.g. Hubbell, 1989; Perkins et al., 1991).

The simulation of the relaxation cascade is performed by subroutine RELAX. The transition that fills the initial vacancy is randomly selected according to the adopted transition probabilities, by using Walker’s aliasing method (section 1.2.3). This transition leaves the ion with one or two vacancies. If the energy of the emitted characteristic x ray or Auger electron is larger than the corresponding absorption energy, the state variables of the particle are stored in the secondary stack (which contains the initial

states of all particles produced during the current shower that have not yet been simulated). The generation of the cascade continues by repeating the process for each remaining vacancy. It ends either when the K shell and L subshells have been filled up or when there is not enough energy to produce “active” radiation (with energy larger than the absorption energy). The excitation energy of the residual ion is assumed to be deposited locally.

It is important to bear in mind that we are disregarding the emission and transport of soft x-rays and slow electrons. This sets a lower limit to the photon energies for which PENELOPE is applicable. In principle, simulation results are expected to be reliable only for photons with energies larger than the ionization energy of the M1 subshell of the heaviest element present (125 eV for copper, 720 eV for silver, 3.4 keV for gold and 5.5 keV for uranium).

Chapter 3

Electron and positron interactions

In this chapter we consider the interactions of fast electrons and positrons of kinetic energy E with matter. For the sake of simplicity, we start by assuming that the particles move in a single-element medium of atomic number Z and density ρ , with \mathcal{N} atoms per unit volume. The extension to compounds, and mixtures, is normally done on the basis of the additivity approximation, i.e. the molecular DCS is approximated as the *incoherent* sum of the atomic DCSs of all the atoms in a molecule.

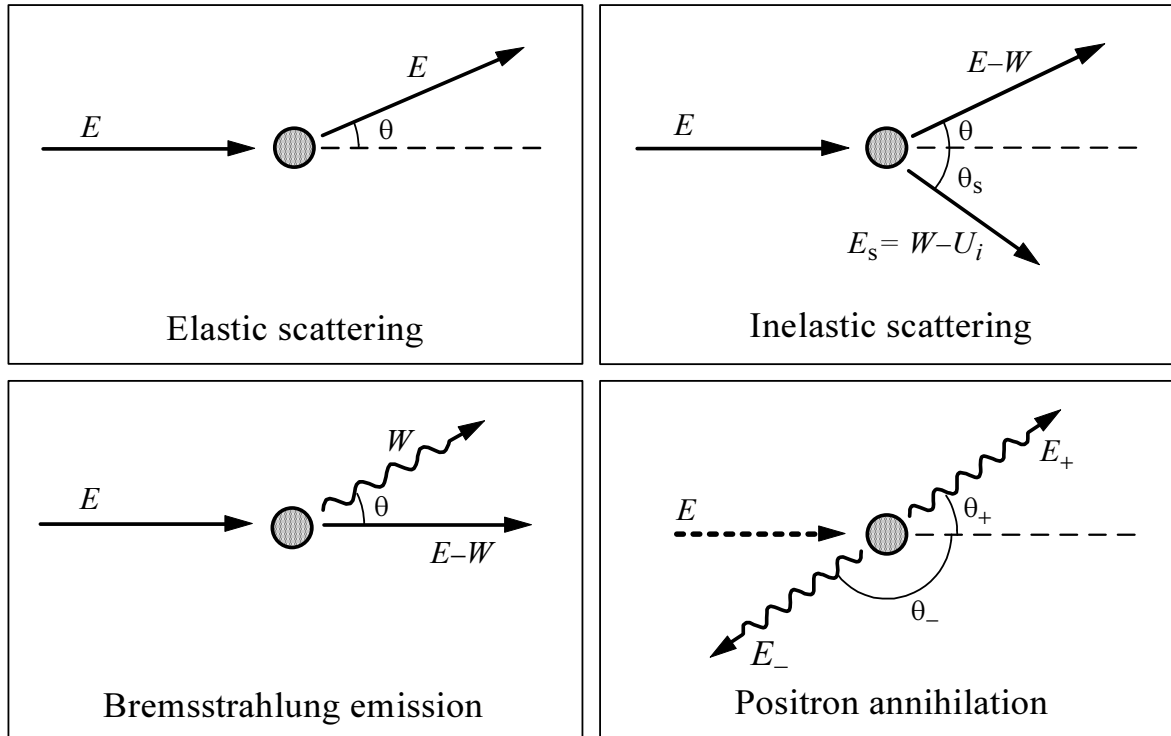


Figure 3.1: Basic interactions of electrons and positrons with matter.

The possible interactions of electrons and positrons with the medium are elastic scattering, inelastic collisions and bremsstrahlung emission; positrons can also undergo annihilation, either in flight or at rest. The atomic DCSs adopted in PENELOPE are defined either as analytical functions or by means of numerical tables, or as a combination of both. These DCSs, which are sufficiently accurate for most practical simulation purposes, allow fast and accurate random sampling of the individual interactions. It is worth pointing out that multiple scattering distributions are quite insensitive to the fine details of the single scattering DCSs. If the adopted DCSs have a physically reasonable shape, only the values of a few integrals of the DCS have a direct influence on the simulation results (Liljequist, 1987; Fernández-Varea et al., 1993b). As a consequence, a general-purpose simulation procedure can be made fairly simple by using approximate DCSs with the proviso that they exactly reproduce the correct values of the relevant integrals. The DCSs described below represent a compromise between reliability and simplicity; they are simple enough to allow the use of fast sampling methods and, at the same time, they are flexible enough to account for the relevant features of the interactions.

Owing to the large number of interactions suffered by a fast electron or positron before coming to rest, detailed simulation is unfeasible at high energies. In PENELOPE we overcome this practical difficulty by using a mixed simulation procedure (see chapter 4) instead of the habitual condensed simulation schemes adopted in other high-energy simulation codes —e.g. ETRAN (Berger and Seltzer, 1988), ITS3 (Halbleib et al., 1992), EGS4 (Nelson et al., 1985), GEANT3 (Brun et al., 1986). The formulation of mixed simulation is complicated by the fact that the sampling of hard interactions is done from restricted DCSs, with cutoffs that vary with the particle energy during the evolution of a track. This limits the complexity of the DCSs that can be efficiently used in a simulation code.

3.1 Elastic collisions

In this section we consider the theoretical description of elastic collisions of electrons and positrons with isolated neutral atoms of atomic number Z at rest. By definition, elastic interactions are those in which the initial and final quantum states of the target atom are the same, normally the ground state. The angular deflections of electron trajectories in matter are mainly (but not completely) due to elastic scattering. Notice that there is a certain energy transfer from the projectile to the target, which causes the recoil of the latter (see section A.1.1). Because of the large mass of the target ($\sim 3600Zm_e$), the average energy lost by the projectile is a very small fraction of its initial energy (a few meV for scattering of 30 keV electron by aluminium atoms) and is usually neglected, which is equivalent to assuming that the target has an infinite mass and does not recoil.

For a wide energy range (say from a few hundred eV to ~ 1 GeV), elastic interactions can be described as scattering of the projectile by the electrostatic field of the target (Mott and Massey, 1965). The charge distribution of the target atom consists of the

nucleus and the electron cloud. The density of atomic electrons $\rho(\mathbf{r})$ can be calculated by using available Hartree-Fock codes (e.g. the one of Desclaux, 1975). For atoms with closed shell configurations, the electron distribution is spherically symmetrical; for atoms with open shells, we assume that an average over directions is performed to give a spherical density $\rho(r)$. To account for the effect of the finite size of the nucleus on the elastic DCS (which is appreciable only for projectiles with energy E larger than a few MeV), we can represent the nucleus as a uniformly charged sphere of radius

$$R_{\text{nuc}} = 1.05 \times 10^{-15} A_w^{1/3} \text{ m}, \quad (3.1)$$

where A_w is the atomic mass (in g/mol). The electrostatic potential of the target atom is

$$\varphi(r) = \varphi_{\text{nuc}}(r) - e 4\pi \left[\frac{1}{r} \int_0^r \rho(r') r'^2 dr' + \int_r^\infty \rho(r') r' dr' \right], \quad (3.2)$$

where

$$\varphi_{\text{nuc}}(r) = \begin{cases} \frac{1}{2} \frac{Ze}{R_{\text{nuc}}} \left[3 - \left(\frac{r}{R_{\text{nuc}}} \right)^2 \right] & \text{if } r \leq R_{\text{nuc}}, \\ \frac{Ze}{r} & \text{if } r > R_{\text{nuc}} \end{cases} \quad (3.3)$$

is the potential of the nucleus.

Within the static-field approximation (Mott and Massey, 1965; Walker, 1971), the DCS for elastic scattering of electrons or positrons is obtained by solving the partial-wave expanded Dirac equation for the motion of the projectile in the field of the target atom. The interaction energy is given by

$$V(r) = z_0 e \varphi(r) + V_{\text{ex}}(r), \quad (3.4)$$

where z_0 is the charge of the projectile in units of e (-1 for electrons, $+1$ for positrons). The term $V_{\text{ex}}(r)$, which applies only for electrons, represents a local approximation to the exchange interaction between the projectile and the atomic electrons (see e.g. Salvat, 1998). We shall limit our considerations to the case of spin unpolarized projectiles, i.e. their spin is randomly oriented. Then, the effect of elastic interactions can be described as a deflection of the projectile trajectory, characterized by the polar and azimuthal scattering angles θ and ϕ . For a central field, the angular distribution of singly scattered electrons is axially symmetric about the direction of incidence, i.e. independent of ϕ . The DCS (per unit solid angle) for elastic scattering of a projectile with kinetic energy E into the solid angle element $d\Omega$ about the direction (θ, ϕ) is given by (Walker, 1971)

$$\frac{d\sigma_{\text{el}}}{d\Omega} = |f(\theta)|^2 + |g(\theta)|^2, \quad (3.5)$$

where

$$\begin{aligned} f(\theta) &= \frac{1}{2ik} \sum_{\ell=0}^{\infty} \{(\ell+1) [\exp(2i\delta_{\ell+}) - 1] + \ell [\exp(2i\delta_{\ell-}) - 1]\} P_{\ell}(\cos \theta), \\ g(\theta) &= \frac{1}{2ik} \sum_{\ell=0}^{\infty} \{\exp(2i\delta_{\ell-}) - \exp(2i\delta_{\ell+})\} P_{\ell}^1(\cos \theta) \end{aligned} \quad (3.6)$$

are the direct and spin-flip scattering amplitudes, respectively.

$$k \equiv \frac{p}{\hbar} = \frac{1}{\hbar c} [E(E + 2m_e c^2)]^{1/2} \quad (3.7)$$

is the wave number of the projectile, $P_\ell(\cos \theta)$ are Legendre polynomials, $P_\ell^1(\cos \theta)$ are associated Legendre functions and $\delta_{\ell\pm}$ are the phase shifts. These are determined from the asymptotic behaviour of the Dirac radial functions for large r (Walker, 1971). Thus, to determine each phase shift we must solve the radial Dirac equations for the potential $V(r)$. The convergence of the partial-wave series (3.6) slows down when the energy of the projectile increases. This makes the calculation difficult for energies larger than a few MeV (in the case of scattering by gold atoms, about 10,000 phase shifts are required at $E = 10$ MeV). The partial-wave DCS, eq. (3.5), rigourously accounts for spin and other relativistic effects, as well as finite nuclear size effects. A computer code to calculate elastic scattering cross sections by this method has been written by Salvat (2000).

Single elastic collisions are determined by the values of the polar and azimuthal scattering angles, θ and ϕ , respectively. Owing to the assumed spherical symmetry of the scattering centres, single and multiple scattering angular distributions are axially symmetrical about the direction of incidence, i.e. they are independent of the azimuthal scattering angle ϕ . For simulation purposes, it is convenient to measure polar angular deflections produced by single scattering events in terms of the variable [see eq. (1.61)]

$$\mu = (1 - \cos \theta)/2 \quad (3.8)$$

instead of the scattering angle θ . Notice that μ varies from 0 (forward scattering) to 1 (backward scattering). The DCS per unit angular deflection is

$$\frac{d\sigma_{\text{el}}}{d\mu} = 4\pi \frac{d\sigma_{\text{el}}}{d\Omega}. \quad (3.9)$$

Fig. 3.2 displays DCSs for elastic scattering of electrons and positrons of various energies by aluminium and gold atoms. These numerical results illustrate the variation of the DCS with the atomic number Z , the charge of the projectile and the energy E . Since the interaction $V(r)$ is attractive for electrons and repulsive for positrons, the scattering is more intense for electrons (which can fall deeply into the potential well of the atom) than for positrons (which are repelled from the nucleus and cannot “see” the inner part of the atom). The DCS for low-energy electrons exhibits a diffraction-like structure, while the DCS for positrons decreases monotonously with the deflection μ . The Born approximation (see e.g. Mott and Massey, 1965) predicts a structureless DCS that decreases with μ and is proportional to the squared charge of the projectile (i.e. the same for electrons and positrons). This approximation considers the scattering field as a perturbation (to first order) and, hence, it is valid only for weak fields (low- Z elements). The difference between the (partial wave) DCSs for electrons and positrons gives a clear indication of the applicability of the Born approximation.

The total elastic cross section is given by

$$\sigma_{\text{el}} = \int \frac{d\sigma_{\text{el}}}{d\Omega} d\Omega = \int \frac{d\sigma_{\text{el}}}{d\mu} d\mu. \quad (3.10)$$

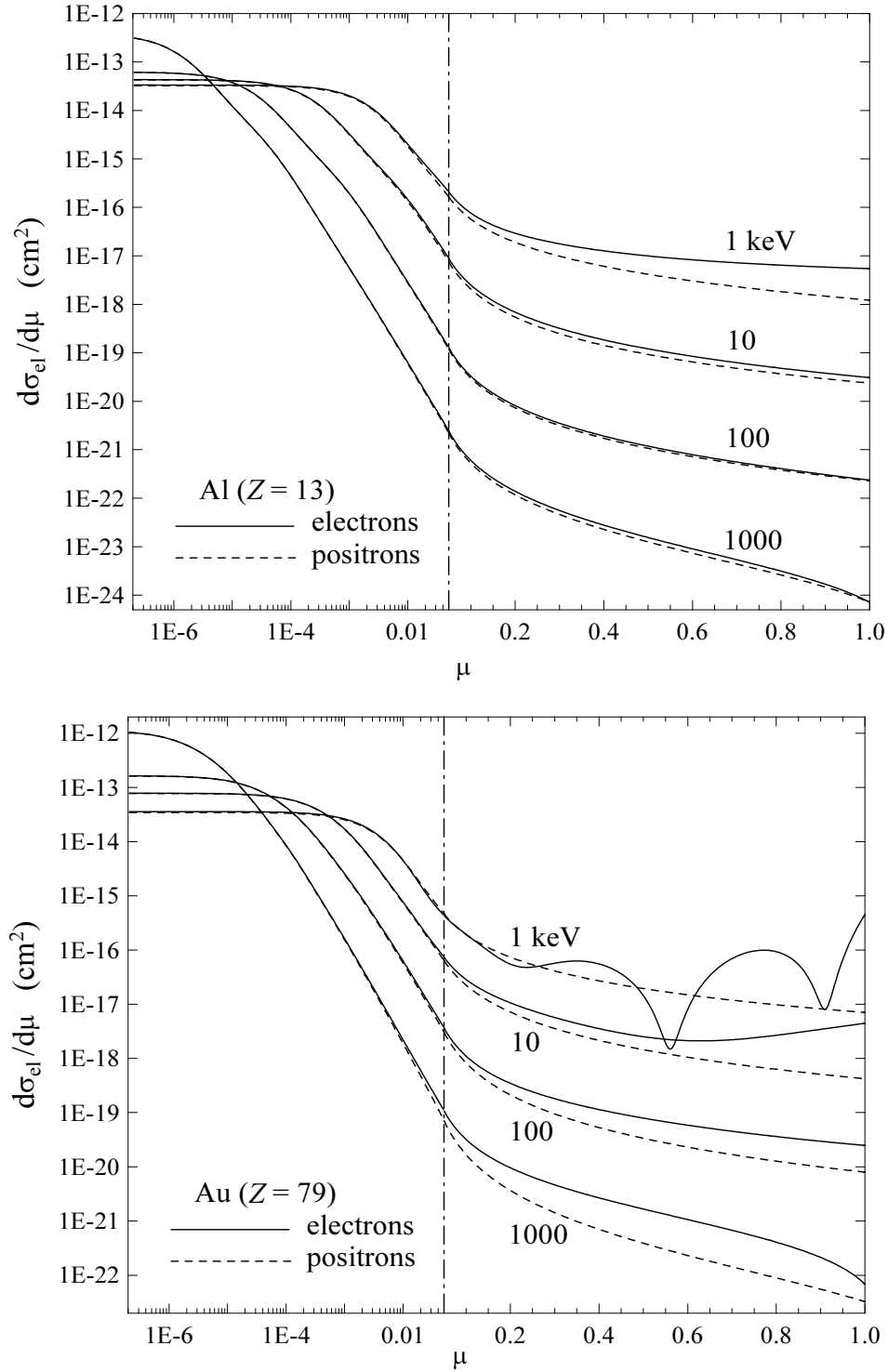


Figure 3.2: DCS for elastic scattering of electrons and positrons by aluminium and gold atoms as a function of the deflection $\mu = (1 - \cos \theta)/2$. Notice the change from logarithmic to linear scale at $\mu = 0.05$.

Notice that we can write

$$\frac{d\sigma_{\text{el}}}{d\mu} = \sigma_{\text{el}} p_{\text{el}}(\mu), \quad (3.11)$$

where $p_{\text{el}}(\mu)$ is the normalized PDF of μ in a single collision. The mean free path between consecutive elastic events in a homogeneous single-element medium is

$$\lambda_{\text{el}} = 1/(\mathcal{N}\sigma_{\text{el}}), \quad (3.12)$$

where \mathcal{N} is the number of atoms per unit volume.

Other important quantities (see section 4.1) are the transport cross sections¹

$$\sigma_{\text{el},\ell} \equiv \int [1 - P_{\ell}(\cos \theta)] \frac{d\sigma_{\text{el}}}{d\Omega} d\Omega. \quad (3.13)$$

The ℓ -th transport mean free path is defined by

$$\lambda_{\text{el},\ell} \equiv 1/(\mathcal{N}\sigma_{\text{el},\ell}). \quad (3.14)$$

The first and second transport cross sections, $\sigma_{\text{el},1}$ and $\sigma_{\text{el},2}$, are given by

$$\sigma_{\text{el},1} = \int (1 - \cos \theta) \frac{d\sigma_{\text{el}}}{d\Omega} d\Omega = 2\sigma_{\text{el}} \int_0^1 \mu p_{\text{el}}(\mu) d\mu = 2\sigma_{\text{el}} \langle \mu \rangle \quad (3.15)$$

and

$$\sigma_{\text{el},2} = \int \frac{3}{2}(1 - \cos^2 \theta) \frac{d\sigma_{\text{el}}}{d\Omega} d\Omega = 6\sigma_{\text{el}} \int_0^1 (\mu - \mu^2) p_{\text{el}}(\mu) d\mu = 6\sigma_{\text{el}} (\langle \mu \rangle - \langle \mu^2 \rangle), \quad (3.16)$$

where $\langle \dots \rangle$ indicates the average value in a single collision. The quantities $\lambda_{\text{el},1}$ and $\lambda_{\text{el},2}$, eq. (3.14), determine the first and second moments of the multiple scattering distributions (see section 4.1). The inverse of the first transport mean free path,

$$\lambda_{\text{el},1}^{-1} = \mathcal{N}\sigma_{\text{el},1} = \frac{2}{\lambda_{\text{el}}} \langle \mu \rangle, \quad (3.17)$$

gives a measure of the average angular deflection per unit path length. By analogy with the “stopping power”, which is defined as the mean energy loss per unit path length (see section 3.2.3), the quantity $2\lambda_{\text{el},1}^{-1}$ is sometimes called the “scattering power”².

Fig. 3.3 shows elastic mean free paths and transport mean free paths for electrons in aluminium and gold. At low energies, the differences between the DCS of the two elements (see fig. 3.2) produce very visible differences between the transport mean free

¹The Legendre polynomials of lowest orders are

$$P_0(x) = 1, \quad P_1(x) = x, \quad P_2(x) = \frac{1}{2}(3x^2 - 1).$$

²At high energies, where the scattering is concentrated at very small angles, $\langle \mu \rangle \simeq \langle \theta^2 \rangle / 4$ and $\lambda_{\text{el},1}^{-1} \simeq \langle \theta^2 \rangle / (2\lambda_{\text{el}})$.

paths. When E increases, the DCS becomes strongly peaked in the forward direction and $\langle\mu^2\rangle$ becomes much smaller than $\langle\mu\rangle$. In the high-energy limit, $\sigma_{\text{el},2} \simeq 3\sigma_{\text{el},1}$ ($\lambda_{\text{el},2} \simeq \lambda_{\text{el},1}/3$). The total cross section, $\propto 1/(\rho\lambda_{\text{el}})$, decreases monotonously with E to reach a constant value at high energies. This saturation is a relativistic effect: the total cross section measures the interaction probability, which is proportional to the time spent by the projectile within the region where the scattering field is appreciable. This time is determined by the speed of the projectile, which approaches c from below when the projectile energy increases. In the non-relativistic theory, the speed $v_{\text{n.r.}} = (2E/m_e)^{1/2}$ increases without limit with E and the calculated non-relativistic total cross section tends to zero at high energies.

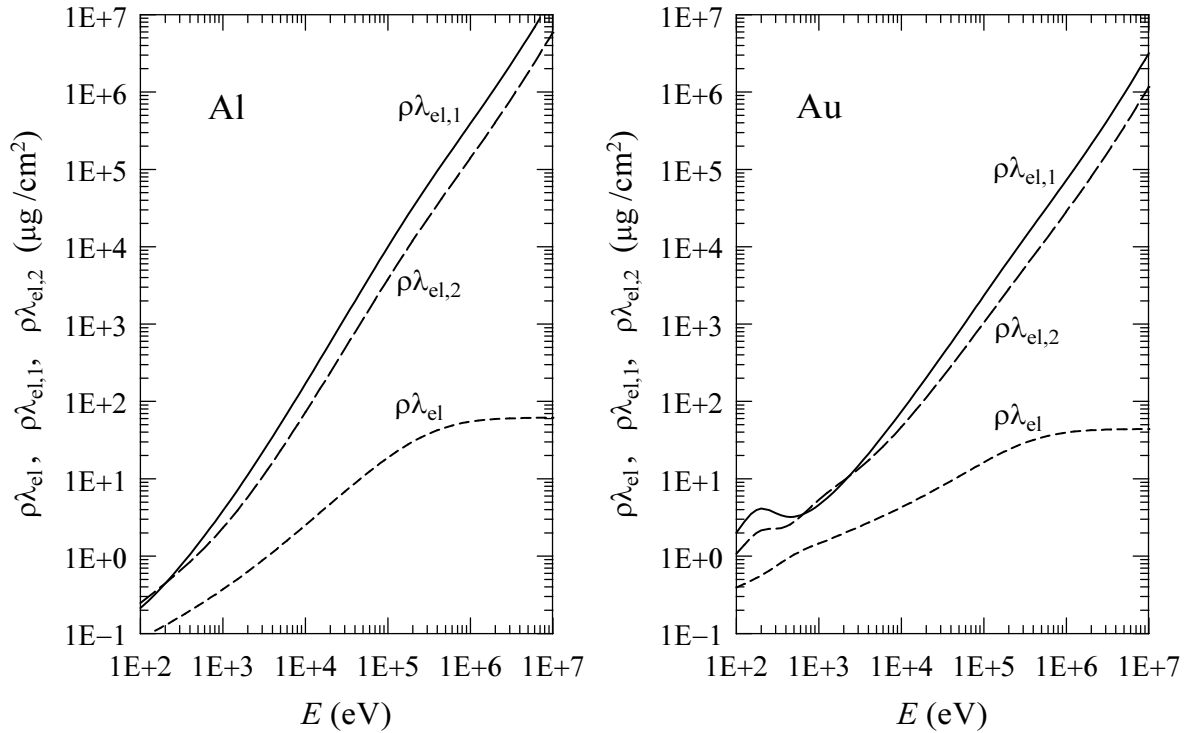


Figure 3.3: Elastic mean free path, λ_{el} , and first and second transport mean free paths, $\lambda_{\text{el},1}$ and $\lambda_{\text{el},2}$, for electrons scattered in aluminium and gold as functions of the kinetic energy of the projectile.

3.1.1 The modified Wentzel (MW) model

Although it is possible to do Monte Carlo simulation of electron and positron transport using numerical partial-wave DCSs (Benedito et al., 2001), this procedure is too laborious to be adopted as the basis of a simulation code for general purposes (mostly because of the large volume of required numerical information). It is more convenient to use suitable analytical approximate DCSs that may differ in detail from the partial-wave

DCSs but lead to nearly the same multiple scattering distributions. In PENELOPE we use a model in which the DCS is expressed as

$$\frac{d\sigma_{\text{el}}^{(\text{MW})}}{d\mu} = \sigma_{\text{el}} p_{\text{MW}}(\mu). \quad (3.18)$$

The single scattering distribution $p_{\text{MW}}(\mu)$ is defined by a simple analytical expression, with a physically plausible form, depending on two adjustable parameters. These parameters are determined in such a way that the values of $\langle\mu\rangle$ and $\langle\mu^2\rangle$ obtained from $p_{\text{MW}}(\mu)$ are equal to those of the actual (partial-wave) DCS:

$$\langle\mu\rangle_{\text{MW}} \equiv \int_0^1 \mu p_{\text{MW}}(\mu) d\mu = \langle\mu\rangle = \frac{1}{2} \frac{\sigma_{\text{el},1}}{\sigma_{\text{el}}} \quad (3.19)$$

and

$$\langle\mu^2\rangle_{\text{MW}} \equiv \int_0^1 \mu^2 p_{\text{MW}}(\mu) d\mu = \langle\mu^2\rangle = \frac{1}{2} \frac{\sigma_{\text{el},1}}{\sigma_{\text{el}}} - \frac{1}{6} \frac{\sigma_{\text{el},2}}{\sigma_{\text{el}}}. \quad (3.20)$$

Thus, the MW model will give the same mean free path and the same first and second transport mean free paths as the partial-wave DCS. As a consequence (see chapter 4), detailed simulations using this model will yield multiple scattering distributions that do not differ significantly from those obtained from the partial wave DCS, quite irrespectively of other details of the “artificial” distribution $p_{\text{MW}}(\mu)$.

To set the distribution $p_{\text{MW}}(\mu)$, we start from the Wentzel (1927) angular distribution,

$$p_{\text{W},A_0}(\mu) \equiv \frac{A_0(1+A_0)}{(\mu+A_0)^2}, \quad (A_0 > 0) \quad (3.21)$$

which describes the scattering by an exponentially screened Coulomb field within the Born approximation (see e.g. Mott and Massey, 1965), that is, it provides a physically plausible angular distribution, at least for light elements or high-energy projectiles. It is also worth mentioning that the multiple scattering theory of Molière (1947, 1948) can be derived by assuming that electrons scatter according to the Wentzel distribution (see Fernández-Varea et al., 1993b). The first moments of the Wentzel distribution are

$$\langle\mu\rangle_{\text{W},A_0} = \int_0^1 \mu \frac{A_0(1+A_0)}{(\mu+A_0)^2} d\mu = A_0 \left[(1+A_0) \ln \left(\frac{1+A_0}{A_0} \right) - 1 \right] \quad (3.22)$$

and

$$\langle\mu^2\rangle_{\text{W},A_0} = \int_0^1 \mu^2 \frac{A_0(1+A_0)}{(\mu+A_0)^2} d\mu = A_0 [1 - 2\langle\mu\rangle_{\text{W},A_0}]. \quad (3.23)$$

Let us define the value of the screening constant A_0 so that $\langle\mu\rangle_{\text{W},A_0} = \langle\mu\rangle$. The value of A_0 can be easily calculated by solving eq. (3.22) numerically, e.g. by the Newton-Raphson method. Usually, we shall have $\langle\mu^2\rangle_{\text{W},A_0} \neq \langle\mu^2\rangle$. At low energies, the Wentzel distribution that gives the correct average deflection is too “narrow” [$\langle\mu^2\rangle_{\text{W},A_0} < \langle\mu^2\rangle$ for both electrons and positrons and for all the elements]. At high energies, the angular distribution is strongly peaked in the forward direction and the Wentzel distribution

becomes too “wide”. This suggests using a modified Wentzel (MW) model obtained by combining a Wentzel distribution with a simple distribution, which takes different forms in these two cases,

- Case I. If $\langle \mu^2 \rangle_{W,A_0} > \langle \mu^2 \rangle$ (the Wentzel distribution is too wide), we take $p_{MW}(\mu)$ as a statistical admixture of the Wentzel distribution and a delta distribution (a zero-width, fixed scattering angle process)

$$p_{MW,I}(\mu) = (1 - B) p_{W,A}(\mu) + B \delta(\mu - \langle \mu \rangle) \quad (3.24)$$

with

$$A = A_0 \quad \text{and} \quad B = \frac{\langle \mu^2 \rangle_{W,A} - \langle \mu^2 \rangle}{\langle \mu^2 \rangle_{W,A} - \langle \mu \rangle^2}. \quad (3.25)$$

Notice that in this case we usually have $\langle \mu \rangle \ll 1$, so that the delta distribution is at very small angles. Although we have introduced a discrete peak in the DCS, its effect is smeared out by the successive collisions and not visible in the multiple scattering angular distributions.

- Case II. If $\langle \mu^2 \rangle_{W,A_0} < \langle \mu^2 \rangle$ (the Wentzel distribution is too narrow), we express $p_{MW}(\mu)$ as a statistical admixture of a Wentzel distribution (with A not necessarily equal to A_0) and a triangle distribution in the interval $(1/2, 1)$,

$$p_{MW,II}(\mu) = (1 - B) p_{W,A}(\mu) + B 8 (\mu - 1/2) \Theta(\mu - 1/2). \quad (3.26)$$

The parameters A and B are obtained from the conditions (3.19) and (3.20), which give

$$\begin{aligned} (1 - B) \langle \mu \rangle_{W,A} + B \frac{5}{6} &= \langle \mu \rangle \\ (1 - B) \langle \mu^2 \rangle_{W,A} + B \frac{17}{24} &= \langle \mu^2 \rangle. \end{aligned} \quad (3.27)$$

From the first of these equations,

$$B = \frac{\langle \mu \rangle - \langle \mu \rangle_{W,A}}{(5/6) - \langle \mu \rangle_{W,A}}. \quad (3.28)$$

Inserting this value in the second of eqs. (3.27), we obtain

$$\left(\frac{17}{24} - \langle \mu^2 \rangle \right) \langle \mu \rangle_{W,A} - \left(\frac{5}{6} - \langle \mu \rangle \right) \langle \mu^2 \rangle_{W,A} = \frac{17}{24} \langle \mu \rangle - \frac{5}{6} \langle \mu^2 \rangle. \quad (3.29)$$

For all situations of interest, this equation has a single root A in the interval $(0, A_0)$ and can be easily solved by means of a bipartition procedure. The value of B given by eq. (3.28) is then positive and less than unity, as required.

In fig. 3.4 we compare partial-wave DCSs and MW model DCSs for elastic scattering of electrons of various energies by gold atoms. The considered energies correspond to the case-II MW model [so that the distribution $p_{MW}(\mu)$ is continuous]. We see that the MW model does imitate the partial wave DCSs, but the differences are significant.

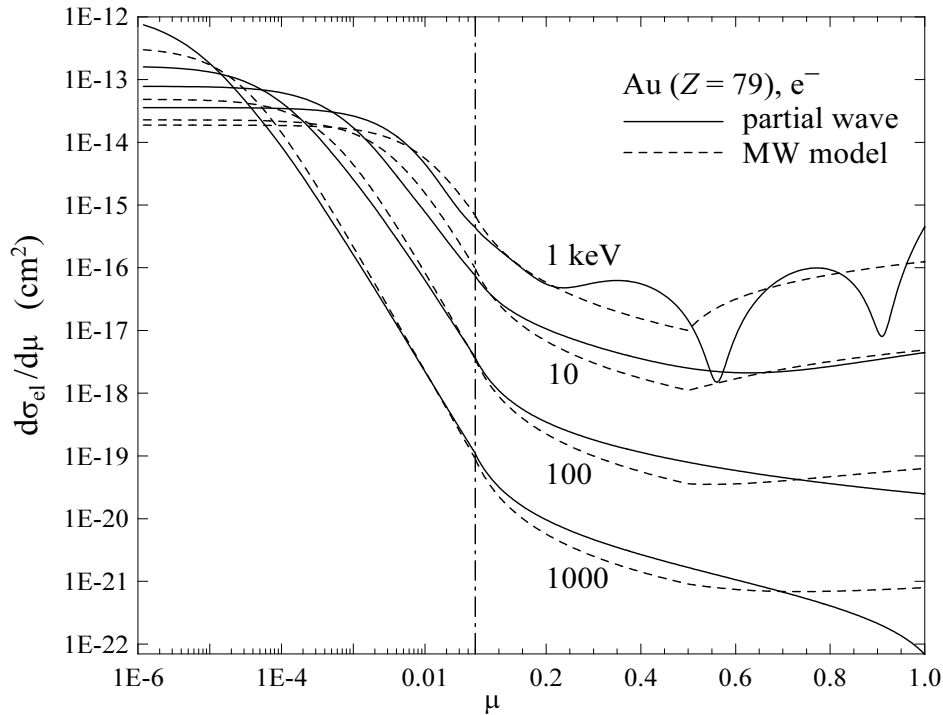


Figure 3.4: Partial-wave and MW model DCSs for elastic scattering of electrons by gold atoms.

Nevertheless, the important fact here is that both DCSs give exactly the same values of σ_{el} , $\langle\mu\rangle$ and $\langle\mu^2\rangle$.

The information needed to determine the parameters of the MW model reduces to the characteristic functions $\sigma_{\text{el}}(E)$, $\sigma_{\text{el},1}(E)$ and $\sigma_{\text{el},2}(E)$. PENELOPE reads these functions from a precalculated database for electrons and positrons, for the elements $Z = 1$ –92 and for a grid of energies that is dense enough to permit accurate cubic spline log-log interpolation. This elastic scattering database was generated by using the partial-wave code of Salvat (2000); the atomic electron densities were obtained from the Dirac-Hartree-Fock code of Desclaux (1975), which correspond to free atoms. Before starting the simulation, PENELOPE evaluates a table of the parameters A and B , and stores it in the computer memory. Instead of B , PENELOPE tabulates the quantity $B' = +B$ (case I) and $B' = -B$ (case II); this avoids the need to specify the case, which can be inferred from the sign of B' . It is worth noting that A and B' are continuous functions of energy and, therefore, can be rapidly evaluated, for any energy, by interpolation in the stored table. In case I, $\langle\mu\rangle$ coincides with $\langle\mu\rangle_{\text{W},A}$, which is determined by A , eq. (3.22). Fig. 3.5 displays the MW model parameters for aluminium and gold, as representative of low- and high- Z elements. Notice that at high energies, where the case I model applies, the strength of the delta contribution increases rapidly with energy, indicating that the partial-wave DCS is much narrower than the Wentzel distribution.

The MW model is directly applicable to compounds (and mixtures) by using the

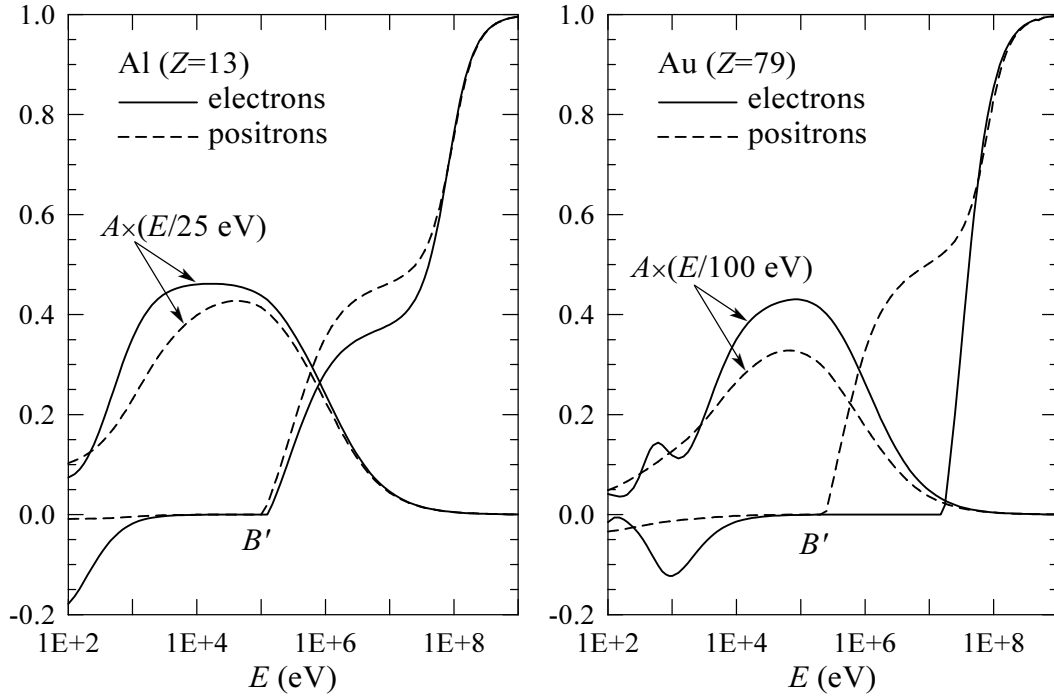


Figure 3.5: Parameters of the MW model for scattering of electrons and positrons by aluminium and gold atoms. The scale of the energy axes is logarithmic.

appropriate values of the total cross section and the first and second transport cross sections. In PENELOPE, these are calculated from atomic total and transport cross sections by means of the additivity approximation (incoherent sum of scattered intensities). This amounts to neglecting chemical binding effects. A more accurate approach, which yields a good estimate of these effects, is provided by the following independent-atom approximation (Walker, 1968; Yates, 1968). Assume that the interaction of the projectile with each atom is still given by the free-atom static potential (3.4). The molecular DCS may then be evaluated by adding the waves (not the currents) scattered from the various atoms in the molecule and averaging over molecular orientations. The resulting DCS is given by

$$\frac{d\sigma_{\text{el}}}{d\Omega} = \sum_{i,j} \frac{\sin(qa_{ij}/\hbar)}{qa_{ij}/\hbar} [f_i(\theta)f_j^*(\theta) + g_i(\theta)g_j^*(\theta)], \quad (3.30)$$

where $q = 2\hbar k \sin(\theta/2)$ is the momentum transfer, a_{ij} is the distance between the atoms i and j and f_i , g_i are the scattering amplitudes, eq. (3.6), for the atom i . It has been claimed that DCSs obtained from this formulation agree with experiments to within $\sim 2\%$ (Walker, 1968; Yates, 1968). DCSs for scattering of 100 eV and 2.5 keV electrons in water vapour, obtained from the simple additivity rule and computed from eq. (3.30), are compared in fig. 3.6. It is seen that, for energies above a few keV, chemical binding causes a slight distortion of the DCS at small angles, and a slight rippling for intermediate angles. Therefore, the use of the additivity approximation (i.e. neglecting

chemical binding effects) in Monte Carlo simulation at these energies is justified.

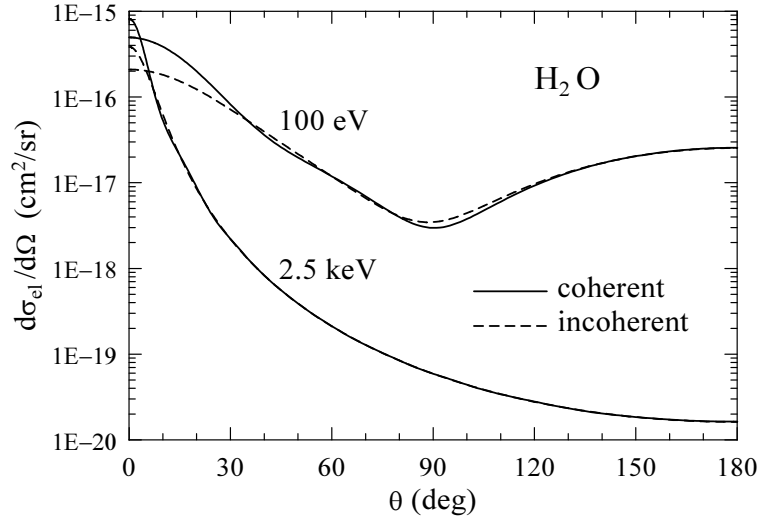


Figure 3.6: DCSs for elastic scattering of electrons by water molecules, calculated as the coherent sum of scattered waves, eq. (3.30), and from the additivity approximation (incoherent sum).

3.1.2 Simulation of single elastic events with the MW model

As mentioned above, the angular distribution in single elastic events is axially symmetrical about the direction of incidence. Hence, the azimuthal scattering angle ϕ is sampled uniformly in the interval $(0, 2\pi)$ using the sampling formula $\phi = 2\pi\xi$. In detailed simulations, μ is sampled in the whole interval $(0, 1)$. However, we shall also make use of the MW model for mixed simulation (see chapter 4), in which only hard events, with deflection μ larger than a given cutoff value μ_c , are sampled individually. In this section we describe analytical (i.e. exact) methods for random sampling of μ in the restricted interval $(\mu_c, 1)$.

- Case I. The cumulative distribution function of $p_{\text{MW,I}}(\mu)$ is

$$\mathcal{P}_{\text{MW,I}}(\mu) \equiv \int_0^\mu p_{\text{MW,I}}(\mu') d\mu' = \begin{cases} (1-B) \frac{(1+A)\mu}{A+\mu} & \text{if } 0 \leq \mu < \langle \mu \rangle, \\ B + (1-B) \frac{(1+A)\mu}{A+\mu} & \text{if } \langle \mu \rangle \leq \mu \leq 1. \end{cases} \quad (3.31)$$

Owing to the analytical simplicity of this function, the random sampling of μ can be performed by using the inverse transform method (section 1.2.2). The sampling equation for μ in $(0, 1)$ reads

$$\mu = \mathcal{P}_{\text{MW,I}}^{-1}(\xi), \quad (3.32)$$

where $\mathcal{P}_{\text{MW,I}}^{-1}(\xi)$ is the inverse of the cumulative distribution function, which is given by

$$\mathcal{P}_{\text{MW,I}}^{-1}(\xi) = \begin{cases} \frac{\xi A}{(1-B)(1+A) - \xi} & \text{if } 0 \leq \xi < \xi_0, \\ \langle \mu \rangle & \text{if } \xi_0 \leq \xi < \xi_0 + B, \\ \frac{(\xi - B)A}{(1-B)(1+A) - (\xi - B)} & \text{if } \xi_0 + B \leq \xi \leq 1, \end{cases} \quad (3.33)$$

with

$$\xi_0 = (1-B) \frac{(1+A)\langle \mu \rangle}{A + \langle \mu \rangle}. \quad (3.34)$$

To sample μ in the restricted interval $(\mu_c, 1)$, we can still use the inverse transform method, eq. (3.32), but with the random number ξ sampled uniformly in the interval $(\xi_c, 1)$ with

$$\xi_c = \mathcal{P}_{\text{MW,I}}(\mu_c). \quad (3.35)$$

- Case II. The cumulative distribution function is

$$\begin{aligned} \mathcal{P}_{\text{MW,II}}(\mu) &\equiv \int_0^\mu p_{\text{MW,II}}(\mu') d\mu' \\ &= \begin{cases} (1-B) \frac{(1+A)\mu}{A + \mu} & \text{if } 0 \leq \mu < \frac{1}{2}, \\ (1-B) \frac{(1+A)\mu}{A + \mu} + B \left[\mu^2 - \mu + \frac{1}{4} \right] & \text{if } \frac{1}{2} \leq \mu \leq 1. \end{cases} \end{aligned} \quad (3.36)$$

In principle, to sample μ in $(0, 1)$, we can adopt the inverse transform method. The sampling equation

$$\xi = \mathcal{P}_{\text{MW,II}}(\mu) \quad (3.37)$$

can be cast in the form of a cubic equation. This equation can be solved either by using the analytical solution formulas for the cubic equation, which are somewhat complicated, or numerically, e.g. by the Newton-Raphson method. We employ this last procedure to determine the cutoff deflection (see section 4.1) for mixed simulation. To sample μ in the restricted interval $(\mu_c, 1)$ we use the composition method, which is easier than solving eq. (3.37). Notice that the sampling from the (restricted) Wentzel and from the triangle distributions can be performed analytically by the inverse transform method.

3.2 Inelastic collisions

The dominant energy loss mechanisms for electrons and positrons with intermediate and low energies are inelastic collisions, i.e. interactions that produce electronic excitations and ionizations in the medium. The quantum theory of inelastic collisions of charged particles with individual atoms and molecules was first formulated by Bethe (1930, 1932)

on the basis of the first-order (plane-wave) Born approximation. The extension of the theory to inelastic collisions in condensed materials has been discussed by Fano (1963). The formal aspects of the quantum theory for condensed matter are quite complicated. Fortunately, the results are essentially equivalent to those from classical dielectric theory.

The effect of individual inelastic collisions *on the projectile* is completely specified by giving the energy loss W and the polar and azimuthal scattering angles θ and ϕ , respectively. For amorphous media with randomly oriented atoms (or molecules), the DCS for inelastic collisions is independent of the azimuthal scattering angle ϕ . Instead of the polar scattering angle θ , it is convenient to use the recoil energy Q [see eqs. (A.29) and (A.30)], defined by

$$Q(Q + 2m_e c^2) = (cq)^2. \quad (3.38)$$

The quantity q is the magnitude of the momentum transfer $\mathbf{q} \equiv \mathbf{p} - \mathbf{p}'$, where \mathbf{p} and \mathbf{p}' are the linear momenta of the projectile before and after the collision. Notice that Q is the kinetic energy of an electron that moves with a linear momentum equal to q .

Let us first consider the inelastic interactions of electrons or positrons ($z_0^2 = 1$) with an isolated atom (or molecule) containing Z electrons in its ground state. The DCS for collisions with energy loss W and recoil energy Q , obtained from the first Born approximation, can be written in the form (Fano, 1963)

$$\frac{d^2\sigma_{\text{in}}}{dW dQ} = \frac{2\pi z_0^2 e^4}{m_e v^2} \left(\frac{2m_e c^2}{WQ(Q + 2m_e c^2)} + \frac{\beta^2 \sin^2 \theta_r W 2m_e c^2}{[Q(Q + 2m_e c^2) - W^2]^2} \right) \frac{df(Q, W)}{dW}, \quad (3.39)$$

where $v = \beta c$ is the velocity of the projectile. θ_r is the angle between the initial momentum of the projectile and the momentum transfer, which is given by eq. (A.42),

$$\cos^2 \theta_r = \frac{W^2/\beta^2}{Q(Q + 2m_e c^2)} \left(1 + \frac{Q(Q + 2m_e c^2) - W^2}{2W(E + m_e c^2)} \right)^2. \quad (3.40)$$

The result (3.39) is obtained in the Coulomb gauge (Fano, 1963); the two terms on the right-hand side are the contributions from interactions through the instantaneous (longitudinal) Coulomb field and through the exchange of virtual photons (transverse field), respectively. The factor $df(Q, W)/dW$ is the atomic generalized oscillator strength (GOS), which completely determines the effect of inelastic interactions *on the projectile*, within the Born approximation. Notice, however, that knowledge of the GOS does not suffice to describe the energy spectrum and angular distribution of secondary knock-on electrons (delta rays).

The GOS can be represented as a surface over the (Q, W) plane, which is called the Bethe surface (see Inokuti, 1971; Inokuti et al., 1978). Unfortunately, the GOS is known in analytical form only for two simple systems, namely, the (non-relativistic) hydrogenic ions (see fig. 3.7) and the free-electron gas. Even in these cases, the analytical expressions of the GOSs are too complicated for simulation purposes. For ionization of inner shells, the GOS can be computed numerically from first principles (see e.g. Manson, 1972), but using GOSs defined through extensive numerical tables is impractical for Monte Carlo simulation. Fortunately, the physics of inelastic collisions is largely determined by a few

global features of the Bethe surface. Relatively simple GOS models can be devised that are consistent with these features and, therefore, lead to a fairly realistic description of inelastic interactions (see e.g. Salvat and Fernández-Varea, 1992).

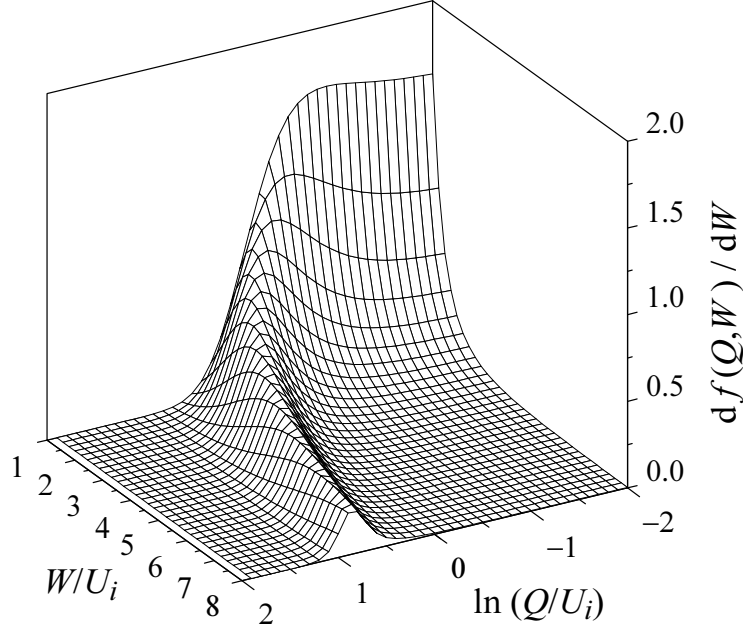


Figure 3.7: The GOS for ionization of the hydrogen atom ($Z = 1$) in the ground state. All energies are in units of the ionization energy $U_i = 13.6$ eV. The GOS for ionization of (non-relativistic) hydrogenic ions is independent of Z if energies are expressed in units of the ionization energy.

As mentioned above, the “atomic” DCS for inelastic interactions in dense media can be obtained from a semiclassical treatment in which the medium is considered as a dielectric, characterized by a complex dielectric function $\epsilon(k, \omega)$, which depends on the wave number k and the frequency ω . In the classical picture, the (external) electric field of the projectile polarizes the medium producing an induced electric field that causes the slowing down of the projectile. The dielectric function relates the Fourier components of the total (external+induced) and the external electric potentials. It is convenient to interpret the quantities $q = \hbar k$ and $W = \hbar \omega$ as the momentum and energy transfers and consider that the dielectric function depends on the variables Q [defined by eq. (3.38)] and W . The DCSs obtained from the dielectric and quantum treatments are consistent (i.e. the former reduces to the latter for a low-density medium) if one assumes the identity

$$\frac{df(Q, W)}{dW} \equiv W \frac{Q + m_e c^2}{m_e c^2} \frac{2Z}{\pi \Omega_p^2} \text{Im} \left(\frac{-1}{\epsilon(Q, W)} \right), \quad (3.41)$$

where Ω_p is the plasma energy of a free-electron gas with the electron density of the

medium, given by

$$\Omega_p^2 = 4\pi\mathcal{N}Z\hbar^2e^2/m_e. \quad (3.42)$$

Eq. (3.41) establishes the connection between the atomic GOS (a property of individual atoms) and the dielectric function (a macroscopic concept). The DCS for the condensed medium can be expressed in the form [cf. eq. (3.39)],

$$\begin{aligned} \frac{d^2\sigma_{\text{in}}}{dW dQ} = & \frac{2\pi z_0^2 e^4}{m_e v^2} \frac{df(Q, W)}{dW} \left(\frac{2m_e c^2}{WQ(Q + 2m_e c^2)} \right. \\ & \left. + \left\{ \frac{\beta^2 \sin^2 \theta_r W 2m_e c^2}{[Q(Q + 2m_e c^2) - W^2]^2} - \mathcal{D}(Q, W) \right\} \right), \end{aligned} \quad (3.43)$$

where the term $\mathcal{D}(Q, W)$, which is appreciable only for small Q , accounts for the so-called density-effect correction (Sternheimer, 1952). The origin of this term is the polarizability of the medium, which “screens” the distant transverse interaction causing a net reduction of its contribution to the stopping power. The density-effect correction $\mathcal{D}(Q, W)$ is determined by the dielectric function that, in turn, is related to the GOS. Thus, the GOS contains all the information needed to compute the DCS for electron/positron inelastic interactions in condensed media.

In the limit of very large recoil energies, the binding and momentum distribution of the target electrons have a small effect on the interaction. Therefore, in the large- Q region, the target electrons behave as if they were essentially free and at rest and, consequently, the GOS reduces to a ridge along the line $W = Q$, which was named the Bethe ridge by Inokuti (1971). In the case of hydrogenic ions in the ground state, fig. 3.7, the Bethe ridge becomes clearly visible at relatively small recoil energies, of the order of the ionization energy U_i . For smaller Q 's, the structure of the Bethe surface is characteristic of the material. In the limit $Q \rightarrow 0$, the GOS reduces to the optical oscillator strength (OOS),

$$\frac{df(W)}{dW} \equiv \frac{df(Q=0, W)}{dW}, \quad (3.44)$$

which is closely related to the (dipole) photoelectric cross section for photons of energy W (Fano, 1963). Experimental information on the OOS is provided by measurements of either photoelectric cross sections or dielectric functions (see e.g. Fernández-Varea et al., 1993a). The GOS satisfies the Bethe sum rule (Inokuti, 1971)

$$\int_0^\infty \frac{df(Q, W)}{dW} dW = Z \quad \text{for any } Q. \quad (3.45)$$

This sum rule, which is a result from non-relativistic theory (see e.g. Mott and Massey, 1965), is assumed to be generally satisfied. It leads to the interpretation of the GOS as the effective number of electrons per unit energy transfer that participate in interactions with given recoil energy Q . The mean excitation energy I , defined by (Fano, 1963; Inokuti, 1971)

$$Z \ln I = \int_0^\infty \ln W \frac{df(W)}{dW} dW, \quad (3.46)$$

plays a central role in the Bethe stopping power formula [eq. (3.103) below]. This quantity has been determined empirically for a large number of materials (see Berger and Seltzer, 1982, and references therein) from measurements of the stopping power of heavy charged particles and/or from experimental optical dielectric functions. In the following, we shall assume that the mean excitation energy of the stopping medium is known.

3.2.1 GOS model

The simulation of inelastic collisions of electrons and positrons in PENELOPE is performed on the basis of the following GOS model, which is tailored to allow fast random sampling of W and Q . We assume that the GOS splits into contributions from the different atomic electron shells. Each atomic shell k is characterized by the number Z_k of electrons in the shell and the ionization energy U_k . To model the contribution of a shell to the GOS, we refer to the example of the hydrogen atom (fig. 3.7) and observe that for $Q > U_k$ the GOS reduces to the Bethe ridge, whereas for $Q < U_k$ it is nearly constant with Q and decreases rapidly with W ; a large fraction of the OOS concentrates in a relatively narrow W -interval. Consideration of other well-known systems, such as inner shells of heavy atoms (Manson, 1972) and the free-electron gas (Lindhard and Winther, 1964), shows that these gross features of the GOS are universal. Liljequist (1983) proposed modelling the GOS of each atomic electron shell as a single “ δ -oscillator”, which is an entity with a simple GOS given by (see fig. 3.8)

$$F(W_k; Q, W) = \delta(W - W_k)\Theta(W_k - Q) + \delta(W - Q)\Theta(Q - W_k), \quad (3.47)$$

where $\delta(x)$ is the Dirac delta function and $\Theta(x)$ is the step function. The first term represents resonant low- Q (distant) interactions, which are described as a single resonance at the energy W_k . The second term corresponds to large- Q (close) interactions, in which the target electrons react as if they were free and at rest ($W = Q$). Notice that the oscillator GOS satisfies the sum rule

$$\int_0^\infty F(W_k; Q, W) dW = 1 \quad \text{for any } Q \quad (3.48)$$

and, consequently, a δ -oscillator corresponds to one electron in the target. The Liljequist GOS model for the whole atom is given by

$$\frac{df(Q, W)}{dW} = \sum_k f_k [\delta(W - W_k)\Theta(W_k - Q) + \delta(W - Q)\Theta(Q - W_k)]. \quad (3.49)$$

where the summation in k extends over all bound electron shells (and the conduction band, in the case of conductors) and the partial oscillator strength f_k is identified with the number of electrons in the k -th shell, i.e. $f_k = Z_k$. The corresponding OOS reduces to

$$\frac{df(W)}{dW} = \sum_k f_k \delta(W - W_k), \quad (3.50)$$

which has the same form (a superposition of resonances) as the OOS used by Sternheimer (1952) in his calculations of the density effect correction. In order to reproduce the high-energy stopping power given by the Bethe formula (Berger and Seltzer, 1982), the oscillator strengths must satisfy the Bethe sum rule (3.45),

$$\sum_k f_k = Z, \quad (3.51)$$

and the excitation energies must be defined in such a way that the GOS model leads, through eq. (3.46), to the accepted value of the mean excitation energy I ,

$$\sum_k f_k \ln W_k = Z \ln I. \quad (3.52)$$

As the partial oscillator strength f_k has been set equal to the number of electrons in the k -th shell, the Bethe sum rule is automatically satisfied.

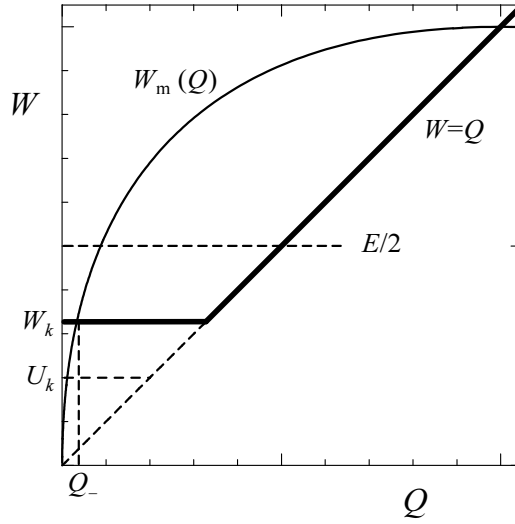


Figure 3.8: Oscillator model for the GOS of an inner shell with $U_k = 2$ keV. The continuous curve represents the maximum allowed energy loss as a function of the recoil energy, $W_m(Q)$, for electrons/positrons with $E = 10$ keV. For distant interactions the possible recoil energies lie in the interval from Q_- to W_k . Recoil energies larger than W_k correspond to close interactions. The largest allowed energy loss W_{\max} is $E/2$ for electrons and E for positrons (see text).

The largest contribution to the total cross section arises from low- W (soft) excitations. Therefore, the total cross section is mostly determined by the OOS of weakly bound electrons, which is strongly dependent on the state of aggregation. In the case of conductors and semiconductors, electrons in the outermost shells form the conduction band (cb). These electrons can move quite freely through the medium and, hence, their binding energy is set to zero, $U_{cb} = 0$. Excitations of the conduction band will be described by a single oscillator, with oscillator strength f_{cb} and resonance energy W_{cb} . These parameters should be identified with the effective number of electrons (per atom or molecule) that participate in plasmon excitations and the plasmon energy, respectively. They can be estimated e.g. from electron energy-loss spectra or from measured

optical data. When this information is not available, we will simply fix the value of f_{cb} (as the number of electrons with ionization energies less than, say, 15 eV) and set the resonance energy W_{cb} equal to the plasmon energy of a free-electron gas with the same density as that of conduction electrons,

$$W_{\text{cb}} = \sqrt{4\pi\mathcal{N}f_{\text{cb}}\hbar^2 e^2/m_e} = \sqrt{\frac{f_{\text{cb}}}{Z}} \Omega_{\text{p}}. \quad (3.53)$$

This gives a fairly realistic model for free-electron-like metals (such as aluminium), because the resonance energy is set equal to the plasmon energy of the free-electron gas (see e.g. Kittel, 1976). A similar prescription, with f_{cb} set equal to the lowest chemical valence of an element, was adopted by Sternheimer et al. (1982, 1984) in their calculations of the density effect correction for single-element metals.

Following Sternheimer (1952), the resonance energy of a bound-shell oscillator is expressed as

$$W_j = \sqrt{(aU_j)^2 + \frac{2}{3} \frac{f_j}{Z} \Omega_{\text{p}}^2}, \quad (3.54)$$

where U_j is the ionization energy and Ω_{p} is the plasma energy corresponding to the total electron density in the material, eq. (3.42). The term $2f_j\Omega_{\text{p}}^2/3Z$ under the square root accounts for the Lorentz-Lorenz correction (the resonance energies of a condensed medium differ from those of a free atom/molecule. The empirical adjustment factor a in eq. (3.54) (the same for all bound shells) is determined from the condition (3.52), i.e. from

$$Z \ln I = f_{\text{cb}} \ln W_{\text{cb}} + \sum_j f_j \ln \sqrt{(aU_j)^2 + \frac{2}{3} \frac{f_j}{Z} \Omega_{\text{p}}^2}. \quad (3.55)$$

For a one-shell system, such as the hydrogen atom, relations (3.51) and (3.52) imply that the resonance energy W_i is equal to I . Considering the $\sim W^{-3}$ dependence of the hydrogenic OOS, it is concluded that a should be of the order of $\exp(1/2) = 1.65$ (Sternheimer et al., 1982). It is worth noting that the Sternheimer adjustment factor a is a characteristic of the considered medium; therefore, the DCSs for ionization of a shell of a given element in two different compounds may be slightly different.

It should be mentioned that the oscillator model gives a Bethe ridge with zero width, i.e. the broadening caused by the momentum distribution of the target electrons is neglected. This is not a serious drawback for light projectiles (electrons and positrons), but it can introduce sizeable errors in the computed cross sections for slow heavy projectiles with $m \gg m_e$. The oscillator model also disregards the fact that, for low- Q interactions, there is a transfer of oscillator strength from inner to outer shells (see e.g. Shiles et al., 1980). As a consequence, the shell ionization cross sections obtained from this GOS model are only roughly approximate. Their use in a Monte Carlo code is permissible only because the ionization of inner shells is a low-probability process (see fig. 3.9 below) that has a very weak effect on the global transport properties.

In mixed (class II) simulations, only hard collisions, with energy loss larger than a specified cutoff value W_{cc} , are simulated (see chapter 4). The effect of soft interactions

(with $W < W_{cc}$) is described by means of a multiple scattering approximation, which does not require detailed knowledge of the shell DCSs. Hard collisions may produce ionizations in deep electron shells, which leave the target atom in a highly excited state (with a vacancy in an inner shell) that decays by emission of energetic x-rays and Auger electrons. In PENELOPE we use the GOS model only to describe the effect of the interactions on the projectile and the emission of knock-on secondary electrons. K and L shells with ionization energy U_j larger than $\max(200 \text{ eV}, W_{cc})$ will be referred to as “inner” shells. The production of vacancies in these inner shells is simulated by means of more accurate ionization cross sections (see section 3.2.6). Electron shells other than K and L shells, or with $U_j < \max(200 \text{ eV}, W_{cc})$, will be referred to as “outer” shells.

The present theory is directly applicable to compounds (and mixtures), since the oscillators may pertain either to atoms or molecules. When the value of the mean excitation energy of the compound is not known, it may be estimated from Bragg’s additivity rule as follows. Consider a compound X_xY_y , in which the molecules consist of x atoms of the element X and y atoms of the element Y. The number of electrons per molecule is $Z_M = xZ_X + yZ_Y$, where Z_X stands for the atomic number of element X. According to the additivity rule, the GOS of the compound is approximated as the sum of the atomic GOSs of the atoms so that

$$Z_M \ln I = xZ_X \ln I_X + yZ_Y \ln I_Y, \quad (3.56)$$

where I_X denotes the mean excitation energy of element X.

For heavy elements, and also for compounds and mixtures with several elements, the number of electron shells may be fairly large (of the order of sixty for an alloy of two heavy metals). In these cases, it would be impractical to treat all shells with the same detail/accuracy. In fact, the description of the outer shells can be simplified without sacrificing the reliability of the simulation results. In PENELOPE, the maximum number of oscillators for each material is limited. When the number of actual shells is too large, oscillators with similar resonance energies are grouped together and replaced by a single oscillator with oscillator strength equal to the sum of strengths of the original oscillators. The resonance energy of the group oscillator is set by requiring that the contribution to the mean excitation energy I equals the sum of contributions of the grouped oscillators; this ensures that grouping will not alter the stopping power of fast particles (with E substantially greater than the ionization energy of the grouped oscillators).

3.2.2 Differential cross sections

The DCS for inelastic collisions obtained from our GOS model can be split into contributions from distant longitudinal, distant transverse and close interactions,

$$\frac{d^2\sigma_{in}}{dW dQ} = \frac{d^2\sigma_{dis,l}}{dW dQ} + \frac{d^2\sigma_{dis,t}}{dW dQ} + \frac{d^2\sigma_{clo}}{dW dQ}. \quad (3.57)$$

The DCS for distant longitudinal interactions is given by the first term in eq. (3.43),

$$\frac{d^2\sigma_{\text{dis,l}}}{dW dQ} = \frac{2\pi e^4}{m_e v^2} \sum_k f_k \frac{1}{W} \frac{2m_e c^2}{Q(Q + 2m_e c^2)} \delta(W - W_k) \Theta(W_k - Q). \quad (3.58)$$

As mentioned above, the DCS for distant transverse interactions has a complicated expression. To simplify it, we shall ignore the (very small) angular deflections of the projectile in these interactions and replace the expression in curly brackets in eq. (3.43) by an averaged W -independent value that gives the exact contribution of the distant transverse interactions to the high-energy stopping power (Salvat and Fernández-Varea, 1992). This yields the following approximate expression for the DCS of distant transverse interactions,

$$\begin{aligned} \frac{d^2\sigma_{\text{dis,t}}}{dW dQ} &= \frac{2\pi e^4}{m_e v^2} \sum_k f_k \frac{1}{W} \left\{ \ln \left(\frac{1}{1 - \beta^2} \right) - \beta^2 - \delta_F \right\} \\ &\times \delta(W - W_k) \Theta(W_k - Q) \delta(Q - Q_-), \end{aligned} \quad (3.59)$$

where Q_- is the minimum recoil energy³ for the energy transfer W , eq. (A.31), and δ_F is the Fermi density effect correction on the stopping power, which has been studied extensively in the past (Sternheimer, 1952; Fano, 1963). δ_F can be computed as (Fano, 1963)

$$\delta_F \equiv \frac{1}{Z} \int_0^\infty \frac{df(Q=0, W)}{dW} \ln \left(1 + \frac{L^2}{W^2} \right) dW - \frac{L^2}{\Omega_p^2} (1 - \beta^2), \quad (3.60)$$

where L is a real-valued function of β^2 defined as the positive root of the following equation (Inokuti and Smith, 1982):

$$\mathcal{F}(L) \equiv \frac{1}{Z} \Omega_p^2 \int_0^\infty \frac{1}{W^2 + L^2} \frac{df(Q=0, W)}{dW} dW = 1 - \beta^2. \quad (3.61)$$

The function $\mathcal{F}(L)$ decreases monotonically with L , and hence, the root $L(\beta^2)$ exists only when $1 - \beta^2 < \mathcal{F}(0)$; otherwise it is $\delta_F = 0$. Therefore, the function $L(\beta^2)$ starts with zero at $\beta^2 = 1 - \mathcal{F}(0)$ and grows monotonically with increasing β^2 . With the OOS, given by eq. (3.50), we have

$$\mathcal{F}(L) = \frac{1}{Z} \Omega_p^2 \sum_k \frac{f_k}{W_k^2 + L^2} \quad (3.62)$$

and

$$\delta_F \equiv \frac{1}{Z} \sum_k f_k \ln \left(1 + \frac{L^2}{W_k^2} \right) - \frac{L^2}{\Omega_p^2} (1 - \beta^2). \quad (3.63)$$

In the high-energy limit ($\beta \rightarrow 1$), the L value resulting from eq. (3.61) is large ($L \gg W_k$) and can be approximated as $L^2 = \Omega_p^2 / (1 - \beta^2)$. Then, using the Bethe sum rule

³The recoil energy Q_- corresponds to $\theta = 0$, i.e. we consider that the projectile is not deflected by distant transverse interactions.

($\sum f_k = Z$) and the relation (3.52), we obtain

$$\delta_F \simeq \ln \left(\frac{\Omega_p^2}{(1 - \beta^2)I^2} \right) - 1, \quad \text{when } \beta \rightarrow 1. \quad (3.64)$$

The DCS for close collisions is given by

$$\frac{d^2\sigma_{\text{clo}}}{dW dQ} = \frac{2\pi e^4}{m_e v^2} \sum_k f_k \frac{1}{W} \left(\frac{2m_e c^2}{W(W + 2m_e c^2)} + \frac{\beta^2 \sin^2 \theta_{\text{clo}}}{2m_e c^2} \right) \delta(W - Q) \Theta(W - W_k),$$

where θ_{clo} is the recoil angle, defined by eq. (3.40) with $Q = W$,

$$\cos^2 \theta_{\text{clo}} = \frac{W}{E} \frac{E + 2m_e c^2}{W + 2m_e c^2}. \quad (3.65)$$

We have

$$\frac{d^2\sigma_{\text{clo}}}{dW dQ} = \frac{2\pi e^4}{m_e v^2} \sum_k f_k \frac{1}{W^2} \left(1 + \frac{\beta^2(E - W)W - EW}{E(W + 2m_e c^2)} \right) \delta(W - Q) \Theta(W - W_k). \quad (3.66)$$

DCS for close collisions of electrons

When the projectile is an electron, the DCS must be corrected to account for the indistinguishability of the projectile and the target electrons. For distant interactions, the effect of this correction is small (much smaller than the distortion introduced by our modelling of the GOS) and will be neglected. The energy loss DCS for binary collisions of electrons with free electrons at rest, obtained from the Born approximation with proper account of exchange, is given by the Møller (1932) formula,

$$\begin{aligned} \frac{d^2\sigma_M}{dW dQ} &= \frac{2\pi e^4}{m_e v^2} \frac{1}{W^2} \left[1 + \left(\frac{W}{E - W} \right)^2 - \frac{W}{E - W} \right. \\ &\quad \left. + a \left(\frac{W}{E - W} + \frac{W^2}{E^2} \right) \right] \delta(W - Q), \end{aligned} \quad (3.67)$$

where

$$a = \left(\frac{E}{E + m_e c^2} \right)^2 = \left(\frac{\gamma - 1}{\gamma} \right)^2. \quad (3.68)$$

To introduce exchange effects in the DCS for close interactions of electrons, we replace the factor in parenthesis in eq. (3.66) by the analogous factor in Møller's formula, i.e. we take

$$\frac{d^2\sigma_{\text{clo}}^{(-)}}{dW dQ} = \frac{2\pi e^4}{m_e v^2} \sum_k f_k \frac{1}{W^2} F^{(-)}(E, W) \delta(W - Q) \Theta(W - W_k), \quad (3.69)$$

with

$$F^{(-)}(E, W) \equiv 1 + \left(\frac{W}{E - W} \right)^2 - \frac{W}{E - W} + a \left(\frac{W}{E - W} + \frac{W^2}{E^2} \right). \quad (3.70)$$

In the final state we have two indistinguishable free electrons, and it is natural to consider the fastest one as the “primary”. Accordingly, the maximum allowed energy transfer in close collisions is

$$W_{\max} = E/2. \quad (3.71)$$

DCS for close collisions of positrons

Positrons in matter are unstable particles that annihilate with electrons giving photons (see section 3.4). On the other hand, electron-positron pairs can be created if enough electromagnetic energy ($> 2m_e c^2$) is available (either from real or virtual photons). A positron does not interact with matter as a usual (stable) positively charged particle, since the competing process of annihilation followed by re-creation can cause the same transitions as “direct” scattering (see e.g. Sakurai, 1967). The DCS for binary collisions of positrons with free electrons at rest, obtained from the first Born approximation including the “annihilation/creation” mechanism, is given by the Bhabha (1936) formula,

$$\frac{d^2\sigma_B}{dW dQ} = \frac{2\pi e^4}{m_e v^2} \frac{1}{W^2} \left[1 - b_1 \frac{W}{E} + b_2 \left(\frac{W}{E} \right)^2 - b_3 \left(\frac{W}{E} \right)^3 + b_4 \left(\frac{W}{E} \right)^4 \right] \delta(W - Q), \quad (3.72)$$

where

$$\begin{aligned} b_1 &= \left(\frac{\gamma - 1}{\gamma} \right)^2 \frac{2(\gamma + 1)^2 - 1}{\gamma^2 - 1}, & b_2 &= \left(\frac{\gamma - 1}{\gamma} \right)^2 \frac{3(\gamma + 1)^2 + 1}{(\gamma + 1)^2}, \\ b_3 &= \left(\frac{\gamma - 1}{\gamma} \right)^2 \frac{2\gamma(\gamma - 1)}{(\gamma + 1)^2}, & b_4 &= \left(\frac{\gamma - 1}{\gamma} \right)^2 \frac{(\gamma - 1)^2}{(\gamma + 1)^2}. \end{aligned} \quad (3.73)$$

To account approximately for the effect of annihilation/creation on the DCS for close inelastic interactions of positrons, we shall use the expression (3.66), with the factor in parenthesis replaced by the Bhabha factor,

$$F^{(+)}(E, W) = 1 - b_1 \frac{W}{E} + b_2 \left(\frac{W}{E} \right)^2 - b_3 \left(\frac{W}{E} \right)^3 + b_4 \left(\frac{W}{E} \right)^4. \quad (3.74)$$

That is,

$$\frac{d^2\sigma_{\text{clo}}^{(+)}}{dW dQ} = \frac{2\pi e^4}{m_e v^2} \sum_k f_k \frac{1}{W^2} F^{(+)}(E, W) \delta(W - Q) \Theta(W - W_k). \quad (3.75)$$

Notice that the maximum energy loss in collisions of positrons with energy E is $W_{\max} = E$.

3.2.3 Integrated cross sections

The energy-loss DCS is defined as

$$\frac{d\sigma_{\text{in}}}{dW} \equiv \int_{Q_-}^{Q_+} \frac{d^2\sigma_{\text{in}}}{dW dQ} dQ = \frac{d\sigma_{\text{dis,l}}}{dW} + \frac{d\sigma_{\text{dis,t}}}{dW} + \frac{d\sigma_{\text{clo}}}{dW}, \quad (3.76)$$

where Q_- and Q_+ are the minimum and maximum kinematically allowed recoil energies given by eq. (A.31). The contributions from distant longitudinal and transverse interactions are

$$\frac{d\sigma_{\text{dis,l}}}{dW} = \frac{2\pi e^4}{m_e v^2} \sum_k f_k \frac{1}{W_k} \ln \left(\frac{W_k Q_- + 2m_e c^2}{Q_- W_k + 2m_e c^2} \right) \delta(W - W_k) \Theta(W_k - Q_-) \quad (3.77)$$

and

$$\frac{d\sigma_{\text{dis,t}}}{dW} = \frac{2\pi e^4}{m_e v^2} \sum_k f_k \frac{1}{W_k} \left\{ \ln \left(\frac{1}{1 - \beta^2} \right) - \beta^2 - \delta_F \right\} \delta(W - W_k) \Theta(W_k - Q_-), \quad (3.78)$$

respectively. The energy-loss DCS for close collisions is

$$\frac{d\sigma_{\text{clo}}^{(\pm)}}{dW} = \frac{2\pi e^4}{m_e v^2} \sum_k f_k \frac{1}{W^2} F^{(\pm)}(E, W) \Theta(W - W_k). \quad (3.79)$$

Our analytical GOS model provides quite an accurate *average* description of inelastic collisions (see below). However, the continuous energy loss spectrum associated with single distant excitations of a given atomic electron shell is approximated here as a single resonance (a δ -distribution). As a consequence, the simulated energy loss spectra show unphysically narrow peaks at energy losses that are multiples of the resonance energies. These spurious peaks are automatically smoothed out after multiple inelastic collisions and also when the bin width used to tally the energy loss distributions is larger than the difference between resonance energies of neighbouring oscillators.

The PDF of the energy loss in a single inelastic collision is given by

$$p_{\text{in}}(W) = \frac{1}{\sigma_{\text{in}}} \frac{d\sigma_{\text{in}}}{dW}, \quad (3.80)$$

where

$$\sigma_{\text{in}} = \int_0^{W_{\text{max}}} \frac{d\sigma_{\text{in}}}{dW} dW \quad (3.81)$$

is the total cross section for inelastic interactions. It is convenient to introduce the quantities

$$\sigma_{\text{in}}^{(n)} \equiv \int_0^{W_{\text{max}}} W^n \frac{d\sigma_{\text{in}}}{dW} dW = \sigma_{\text{in}} \int_0^{W_{\text{max}}} W^n p_{\text{in}}(W) dW = \sigma_{\text{in}} \langle W^n \rangle, \quad (3.82)$$

where $\langle W^n \rangle$ denotes the n -th moment of the energy loss in a single collision (notice that $\sigma_{\text{in}}^{(0)} = \sigma_{\text{in}}$). $\sigma_{\text{in}}^{(1)}$ and $\sigma_{\text{in}}^{(2)}$ are known as the stopping cross section and the energy straggling cross section (for inelastic collisions), respectively.

The mean free path λ_{in} for inelastic collisions is

$$\lambda_{\text{in}}^{-1} = \mathcal{N} \sigma_{\text{in}}, \quad (3.83)$$

where \mathcal{N} is the number of scattering centres (atoms or molecules) per unit volume. The stopping power S_{in} and the energy straggling parameter Ω_{in}^2 are defined by

$$S_{\text{in}} = \mathcal{N} \sigma_{\text{in}}^{(1)} = \frac{\langle W \rangle}{\lambda_{\text{in}}} \quad (3.84)$$

and

$$\Omega_{\text{in}}^2 = \mathcal{N} \sigma_{\text{in}}^{(2)} = \frac{\langle W^2 \rangle}{\lambda_{\text{in}}}. \quad (3.85)$$

Notice that the stopping power gives the average energy loss per unit path length⁴. The physical meaning of the straggling parameter is less direct. Consider a monoenergetic electron (or positron) beam of energy E that impinges normally on a foil of material of (small) thickness ds , and assume that the electrons do not scatter (i.e. they are not deflected) in the foil. The product $\Omega_{\text{in}}^2 ds$ then gives the variance of the energy distribution of the beam after traversing the foil (see also section 4.2).

The integrated cross sections $\sigma_{\text{in}}^{(n)}$ can be calculated as

$$\sigma_{\text{in}}^{(n)} = \sigma_{\text{dis,l}}^{(n)} + \sigma_{\text{dis,t}}^{(n)} + \sigma_{\text{clo}}^{(n)}. \quad (3.86)$$

The contributions from distant longitudinal and transverse interactions are

$$\sigma_{\text{dis,l}}^{(n)} = \frac{2\pi e^4}{m_e v^2} \sum_k f_k W_k^{n-1} \ln \left(\frac{W_k Q_- + 2m_e c^2}{Q_- W_k + 2m_e c^2} \right) \Theta(W_{\text{max}} - W_k) \quad (3.87)$$

and

$$\sigma_{\text{dis,t}}^{(n)} = \frac{2\pi e^4}{m_e v^2} \sum_k f_k W_k^{n-1} \left\{ \ln \left(\frac{1}{1 - \beta^2} \right) - \beta^2 - \delta_F \right\} \Theta(W_{\text{max}} - W_k), \quad (3.88)$$

respectively. Notice that for distant interactions $W_{\text{max}} = E$, for both electrons and positrons.

The integrated cross sections for close collisions are

$$\sigma_{\text{clo}}^{(n)} = \frac{2\pi e^4}{m_e v^2} \sum_k f_k \int_{W_k}^{W_{\text{max}}} W^{n-2} F^{(\pm)}(E, W) dW. \quad (3.89)$$

In the case of electrons, the integrals in this formula are of the form

$$J_n^{(-)} = \int W^{n-2} \left[1 + \left(\frac{W}{E - W} \right)^2 - \frac{(1 - a)W}{E - W} + \frac{aW^2}{E^2} \right] dW \quad (3.90)$$

and can be calculated analytically. For the orders 0, 1 and 2 we have

$$J_0^{(-)} = -\frac{1}{W} + \frac{1}{E - W} + \frac{1 - a}{E} \ln \left(\frac{E - W}{W} \right) + \frac{aW}{E^2}, \quad (3.91)$$

⁴The term “stopping power” is somewhat misleading; in fact, S_{in} has the dimensions of force.

$$J_1^{(-)} = \ln W + \frac{E}{E-W} + (2-a) \ln(E-W) + \frac{aW^2}{2E^2} \quad (3.92)$$

and

$$J_2^{(-)} = (2-a)W + \frac{2E^2 - W^2}{E-W} + (3-a)E \ln(E-W) + \frac{aW^3}{3E^2}. \quad (3.93)$$

For positrons, the integrals in (3.89),

$$J_n^{(+)} \equiv \int W^{n-2} \left[1 - b_1 \frac{W}{E} + b_2 \left(\frac{W}{E} \right)^2 - b_3 \left(\frac{W}{E} \right)^3 + b_4 \left(\frac{W}{E} \right)^4 \right] dW, \quad (3.94)$$

can also be evaluated analytically as

$$J_0^{(+)} = -\frac{1}{W} - b_1 \frac{\ln W}{E} + b_2 \frac{W}{E^2} - b_3 \frac{W^2}{2E^3} + b_4 \frac{W^3}{3E^4}, \quad (3.95)$$

$$J_1^{(+)} = \ln W - b_1 \frac{W}{E} + b_2 \frac{W^2}{2E^2} - b_3 \frac{W^3}{3E^3} + b_4 \frac{W^4}{4E^4} \quad (3.96)$$

and

$$J_2^{(+)} = W - b_1 \frac{W^2}{2E} + b_2 \frac{W^3}{3E^2} - b_3 \frac{W^4}{4E^3} + b_4 \frac{W^5}{5E^4}. \quad (3.97)$$

Fig. 3.9 displays total inelastic cross sections for electrons in aluminium and gold, as well as contributions from various groups of shells, as functions of the kinetic energy of the projectile. The curves labelled “K” and “L1+...” represent cross sections for ionization in these shells. The cross section for ionization in a bound shell decreases rapidly with the shell ionization energy U_i (since energy transfers less than U_i , which would promote the target electron to occupied states, are forbidden). As a consequence, collisions occur preferentially with electrons in the conduction band and in outer bound shells. Inner-shell ionization by electron/positron impact is a relatively unlikely process. It should be noted that our GOS model is too crude to provide an accurate description of inner-shell ionization. To illustrate this, fig. 3.9 includes K- and L-shell ionization cross sections obtained from the optical-data model described in section 3.2.6, which are known to agree reasonably well with experimental data (Mayol and Salvat, 1990). We see that there are significant differences between the cross sections from the optical-data model and the predictions of our simple GOS model, which is designed to yield accurate stopping powers only. To get a realistic picture of inner-shell ionization, we have to rely on much more elaborate physical schemes. In fact, even the Born approximation ceases to be appropriate for projectiles with kinetic energies near the ionization threshold.

Collision stopping powers for electrons in aluminium, silver and gold obtained from the present analytical model are compared with sample values from the ICRU37 (1984) stopping power tables [given also in Berger and Seltzer (1982)] for $E \geq 10$ keV in fig. 3.10. Our results practically coincide with the values in the tables of reference. In fig. 3.11, inelastic mean free paths and stopping powers for low-energy electrons ($E = 100$ eV to 100 keV) in aluminium and gold obtained from the present model are compared with experimental data from several authors. We see that the theory predicts the

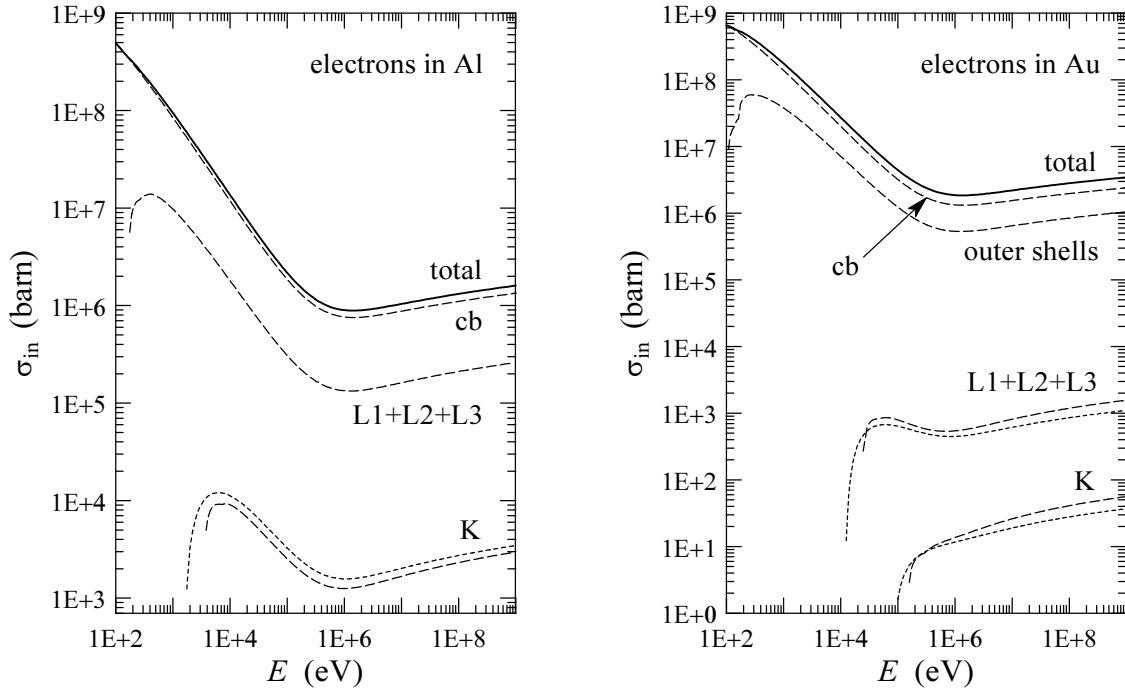


Figure 3.9: Total inelastic cross sections for electrons in aluminium and gold and contributions from the K shell, L shell, conduction band (cb) and outer shells, calculated from our model GOS ignoring density effect corrections (i.e. with $\delta_F = 0$). The short-dashed curves represent K- and L-shell ionization cross sections calculated from the optical-data model described in section 3.2.6, which yields results in close agreement with experimental data. Note: 1 barn = 10^{-24} cm².

energy variation of total integrated cross sections down to relatively low energies. It should be noted that the adopted value of W_{cb} , the resonance energy of conduction band electrons, has a strong effect on the calculated mean free paths. In the case of free-electron-like materials such as aluminium, W_{cb} can be identified with the energy of plasmon excitations (which is the dominant energy-loss mechanism). For other solids, the outermost electrons have a broad energy loss spectrum and there is no simple way of predicting this parameter. Fortunately, the stopping power (and, hence, the global stopping process) is practically independent of the adopted value of W_{cb} . To generate the data for aluminium, fig. 3.11, we have set $W_{cb} = 15$ eV, which is the measured energy of volume plasmons in the metal [eq. (3.53) with $f_{cb} = 3$ conduction electrons per atom gives $W_{cb} = 15.8$ eV]; in this case, the calculated mean free paths are seen to agree fairly well with measured data. In the case of gold, eq. (3.53) with $f_{cb} = 11$ conduction electrons per atom gives $W_{cb} = 30$ eV. Fig. 3.11 shows stopping powers and mean free paths for electrons in gold obtained with $W_{cb} = 30$ and 40 eV. We see that, as indicated above, the mean free path varies strongly with this parameter, but the stopping power is practically insensitive to it.

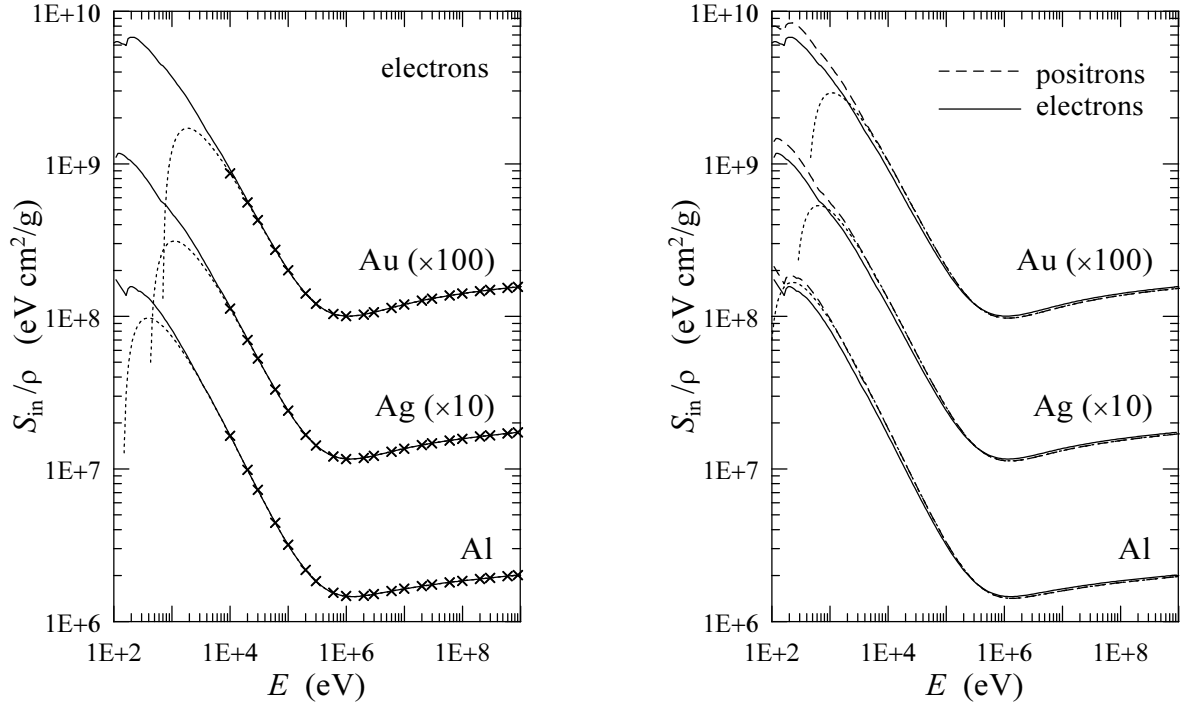


Figure 3.10: Collision stopping power S_{in}/ρ for electrons and positrons in aluminium, silver ($\times 10$) and gold ($\times 100$) as a function of the kinetic energy. Continuous and dashed curves are results from the present model. Crosses are data from the ICRU37 tables (1984) [also, Berger and Seltzer, 1982)]. The dotted curves are predictions from the Bethe formula (3.103), for electrons and positrons.

3.2.4 Stopping power of high-energy electrons and positrons

It is of interest to evaluate explicitly the stopping power for projectiles with high energies ($E \gg U_k$). We shall assume that $U_k \ll 2m_e c^2$ (for the most unfavourable case of the K shell of heavy elements, U_k is of the order of $2m_e c^2/10$). Under these circumstances, $Q_- \ll 2m_e c^2$ and we can use the approximation [see eq. (A.35)]

$$Q_- \simeq W_k^2 / (2m_e c^2 \beta^2). \quad (3.98)$$

The contribution from distant (longitudinal and transverse) interactions to the stopping cross section is then [see eqs. (3.77) and (3.78)]

$$\sigma_{\text{dis}}^{(1)} \simeq \frac{2\pi e^4}{m_e v^2} \sum_k f_k \left\{ \ln \left(\frac{2m_e c^2}{W_k} \right) + \ln \left(\frac{1}{1 - \beta^2} \right) - \beta^2 - \delta_F \right\}. \quad (3.99)$$

The contribution of close interactions is given by

$$\sigma_{\text{clo}}^{(1)} = \frac{2\pi e^4}{m_e v^2} \sum_k f_k \int_{W_k}^{W_{\text{max}}} W^{-1} F^{(\pm)}(E, W) dW. \quad (3.100)$$

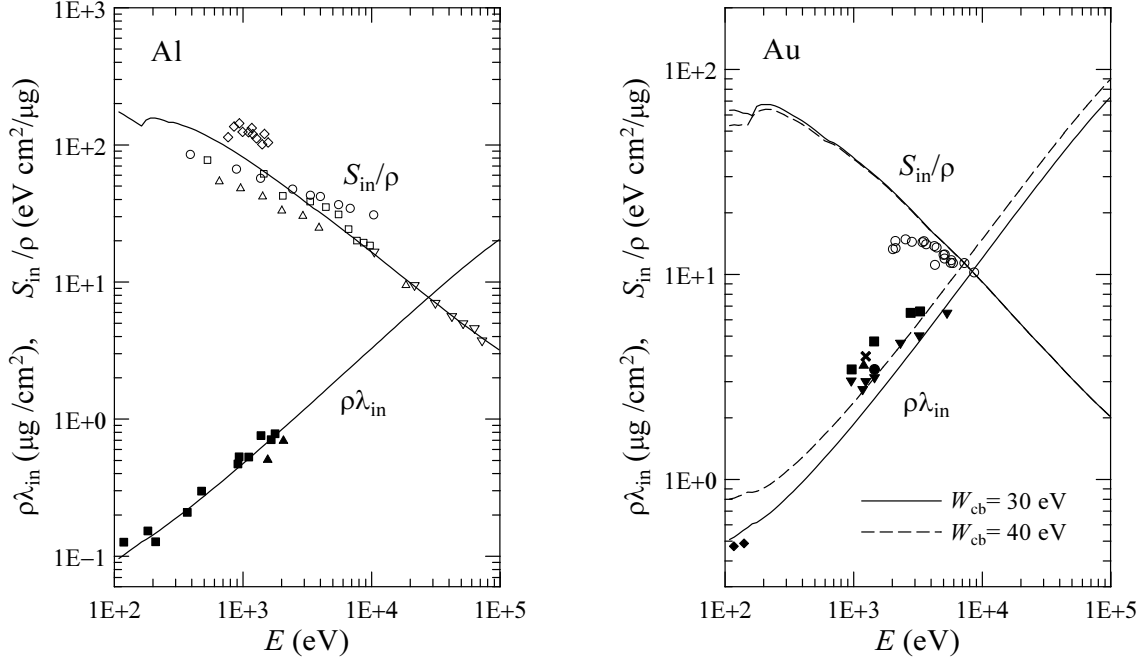


Figure 3.11: Collision mean free path and stopping power for low-energy electrons in aluminium and gold. The plotted quantities are $\rho\lambda_{\text{in}}$ and S_{in}/ρ . Special symbols are experimental data from different sources (see Fernández-Varea et al., 1993a); closed symbols for mean free paths and open symbols for stopping powers.

Recalling that $E \gg U_k$, we have

$$\begin{aligned} \sigma_{\text{clo}}^{(1)} \simeq & \frac{2\pi e^4}{m_e v^2} \sum_k f_k \left\{ \ln \left(\frac{E}{W_k} \right) + 1 - \left[1 + \beta^2 + 2\sqrt{1 - \beta^2} \right] \ln 2 \right. \\ & \left. + \frac{1}{8} \left(1 - \sqrt{1 - \beta^2} \right)^2 \right\} \end{aligned} \quad (3.101)$$

for electrons and

$$\sigma_{\text{clo}}^{(1)} \simeq \frac{2\pi e^4}{m_e v^2} \sum_k f_k \left\{ \ln \left(\frac{E}{W_k} \right) - b_1 + \frac{b_2}{2} - \frac{b_3}{3} + \frac{b_4}{4} \right\} \quad (3.102)$$

for positrons. Adding the distant and close stopping cross sections, and using the relation (3.52), we arrive at the familiar Bethe formula for the stopping power,

$$S_{\text{in}} \equiv \mathcal{N} \left(\sigma_{\text{dis}}^{(1)} + \sigma_{\text{clo}}^{(1)} \right) = \mathcal{N} \frac{2\pi e^4}{m_e v^2} Z \left\{ \ln \left(\frac{E^2}{I^2} \frac{\gamma + 1}{2} \right) + f^{(\pm)}(\gamma) - \delta_F \right\}, \quad (3.103)$$

where

$$f^{(-)}(\gamma) = 1 - \beta^2 - \frac{2\gamma - 1}{\gamma^2} \ln 2 + \frac{1}{8} \left(\frac{\gamma - 1}{\gamma} \right)^2 \quad (3.104)$$

and

$$f^{(+)}(\gamma) = 2 \ln 2 - \frac{\beta^2}{12} \left[23 + \frac{14}{\gamma + 1} + \frac{10}{(\gamma + 1)^2} + \frac{4}{(\gamma + 1)^3} \right] \quad (3.105)$$

for electrons and positrons, respectively. This formula can be derived from very general arguments that do not require knowing the fine details of the GOS; the only information needed is contained in the Bethe sum rule (3.45) and in the definition (3.46) of the mean excitation energy (see e.g. Fano, 1963). Since our approximate analytical GOS model is physically motivated, it satisfies the sum rule and reproduces the adopted value of the mean ionization energy, it yields (at high energies) the exact Bethe formula.

It is striking that the “asymptotic” Bethe formula is in fact valid down to fairly small energies, of the order of 10 keV for high- Z materials (see fig. 3.10). It also accounts for the differences between the stopping powers of electrons and positrons (to the same degree as our GOS model approximation).

For ultrarelativistic projectiles, for which the approximation (3.64) holds, the Bethe formula simplifies to

$$S_{\text{in}} \simeq \mathcal{N} \frac{2\pi e^4}{m_e v^2} Z \left\{ \ln \left(\frac{E^2}{\Omega_p^2} \frac{\gamma + 1}{2\gamma^2} \right) + f^{(\pm)}(\gamma) + 1 \right\}. \quad (3.106)$$

The mean excitation energy I has disappeared from this formula, showing that at very high energies the stopping power depends only on the electron density $\mathcal{N}Z$ of the medium.

3.2.5 Simulation of hard inelastic collisions

The DCSs given by expressions (3.76)-(3.79) permit the random sampling of the energy loss W and the angular deflection θ by using purely analytical methods. In the following we consider the case of mixed (class II) simulation, in which only hard collisions, with energy loss larger than a specified cutoff value W_{cc} , are simulated (see chapter 4). As the value of the cutoff energy loss can be selected arbitrarily, the sampling algorithm can also be used in detailed (interaction-by-interaction) simulations ($W_{\text{cc}} = 0$).

The first stage of the simulation is the selection of the active oscillator, for which we need to know the restricted total cross section,

$$\begin{aligned} \sigma(W_{\text{cc}}) &\equiv \int_{W_{\text{cc}}}^{W_{\text{max}}} \frac{d\sigma_{\text{in}}}{dW} dW = \sigma_{\text{dis,l}}(W_{\text{cc}}) + \sigma_{\text{dis,t}}(W_{\text{cc}}) + \sigma_{\text{clo}}(W_{\text{cc}}) \\ &= \sum_k \sigma_k(W_{\text{cc}}), \end{aligned} \quad (3.107)$$

as well as the contribution of each oscillator, $\sigma_k(W_{\text{cc}})$. The active oscillator is sampled from the point probabilities $p_k = \sigma_k(W_{\text{cc}})/\sigma(W_{\text{cc}})$. Since these probabilities are calculated analytically, the sampling algorithm is relatively slow. In mixed simulations, the algorithm can be sped up by using a larger cutoff energy loss W_{cc} , which eliminates all the oscillators with $W_k < W_{\text{cc}}$ from the sum.

After selecting the active oscillator, the oscillator branch (distant or close) is determined and, finally, the variables W and Q (or $\cos\theta$) are sampled from the associated DCS. For close collisions, $Q = W$ and, therefore, the scattering angle is obtained directly from the energy loss.

Hard distant interactions

In distant interactions with the k -th oscillator, $W = W_k$. The contributions of transverse and longitudinal interactions to the restricted cross section define the relative probabilities of these interaction modes. If the interaction is (distant) transverse, the angular deflection of the projectile is neglected, i.e. $\cos\theta = 1$. For distant longitudinal collisions, the (unnormalized) PDF of Q is given by [see eq. (3.58)]

$$P_{dk}(Q) = \begin{cases} \frac{1}{Q [1 + Q/(2m_e c^2)]} & \text{if } Q_- < Q < W_k, \\ 0 & \text{otherwise,} \end{cases} \quad (3.108)$$

where Q_- is the minimum recoil energy, eq. (A.31). Random sampling from this PDF can be performed by the inverse transform method, which gives the sampling formula

$$Q = Q_s \left\{ \left[\frac{Q_s}{W_k} \left(1 + \frac{W_k}{2m_e c^2} \right) \right]^\xi - \frac{Q_s}{2m_e c^2} \right\}^{-1}, \quad (3.109)$$

where

$$Q_s \equiv \frac{Q_-}{1 + Q_-/(2m_e c^2)}. \quad (3.110)$$

Once the energy loss and the recoil energy have been sampled, the polar scattering angle θ is determined from eq. (A.40),

$$\cos\theta = \frac{E(E + 2m_e c^2) + (E - W)(E - W + 2m_e c^2) - Q(Q + 2m_e c^2)}{2\sqrt{E(E + 2m_e c^2)(E - W)(E - W + 2m_e c^2)}}. \quad (3.111)$$

The azimuthal scattering angle ϕ is sampled uniformly in the interval $(0, 2\pi)$.

Hard close collisions of electrons

For the formulation of the sampling algorithm, it is convenient to introduce the reduced energy loss $\kappa \equiv W/E$. The PDF of κ in close collisions of electrons with the k -th oscillator is given by [see eqs. (3.69) and (3.70)]

$$P_k^{(-)}(\kappa) \equiv \kappa^{-2} F^{(-)}(E, W) \Theta(\kappa - \kappa_c) \Theta\left(\frac{1}{2} - \kappa\right) = \left[\frac{1}{\kappa^2} + \frac{1}{(1 - \kappa)^2} - \frac{1}{\kappa(1 - \kappa)} + a \left(1 + \frac{1}{\kappa(1 - \kappa)} \right) \right] \Theta(\kappa - \kappa_c) \Theta\left(\frac{1}{2} - \kappa\right), \quad (3.112)$$

with $\kappa_c \equiv \max(W_k, W_{cc})/E$. Notice that the maximum allowed value of κ is $1/2$. Here, normalization is irrelevant.

We introduce the distribution

$$\Phi^{(-)}(\kappa) \equiv (\kappa^{-2} + 5a) \Theta(\kappa - \kappa_c) \Theta\left(\frac{1}{2} - \kappa\right), \quad a \equiv \left(\frac{\gamma - 1}{\gamma}\right)^2. \quad (3.113)$$

It may be shown that $\Phi^{(-)} > P_k^{(-)}$ in the interval $(\kappa_c, \frac{1}{2})$. Therefore, we can sample the reduced energy loss κ from the PDF (3.112) by using the rejection method (see section 1.2.4) with trial values sampled from the distribution (3.113) and acceptance probability $P_k^{(-)}/\Phi^{(-)}$.

Random sampling from the PDF (3.113), can be performed by using the composition method (section 1.2.5). We consider the following decomposition of the (normalized) PDF given by eq. (3.113):

$$\Phi_{\text{norm}}^{(-)}(\kappa) = \frac{1}{1 + 5a\kappa_c/2} [p_1(\kappa) + (5a\kappa_c/2)p_2(\kappa)], \quad (3.114)$$

where

$$p_1(\kappa) = \frac{\kappa_c}{1 - 2\kappa_c} \kappa^{-2}, \quad p_2(\kappa) = \frac{2}{1 - 2\kappa_c} \quad (3.115)$$

are normalized PDFs in the interval $(\kappa_c, \frac{1}{2})$. Random values of κ from the PDF (3.113) can be generated by using the following algorithm:

- (i) Generate ξ .
- (ii) Set $\zeta = (1 + 5a\kappa_c/2)\xi$.
- (iii) If $\zeta < 1$, deliver the value $\kappa = \kappa_c/[1 - \zeta(1 - 2\kappa_c)]$.
- (iv) If $\zeta > 1$, deliver the value $\kappa = \kappa_c + (\zeta - 1)(1 - 2\kappa_c)/(5a\kappa_c)$.

The rejection algorithm for random sampling of κ from the PDF (3.112) proceeds as follows:

- (i) Sample κ from the distribution given by eq. (3.113).
- (ii) Generate a random number ξ .
- (iii) If $\xi(1 + 5a\kappa^2) < \kappa^2 P_k^{(-)}(\kappa)$, deliver κ .
- (iv) Go to step (i).

Notice that in the third step we accept the κ value with probability $P_k^{(-)}/\Phi^{(-)}$, which approaches unity when κ is small.

The efficiency of this sampling method depends on the values of the energy E and the cutoff reduced energy loss κ_c , as shown in table 3.1. For a given energy and for W_{cc} values which are not too large, the efficiency increases when W_{cc} decreases.

Table 3.1: Efficiency (%) of the random sampling algorithm of the energy loss in close collisions of electrons and positrons for different values of the energy E and the cutoff energy loss κ_c .

E (eV)	κ_c				
	0.001	0.01	0.1	0.25	0.4
10^3	99.9	99.9	99.8	99.7	99.6
10^5	99.7	98	87	77	70
10^7	99	93	70	59	59
10^9	99	93	71	62	63

After sampling the energy loss $W = \kappa E$, the polar scattering angle θ is obtained from eq. (A.40) with $Q = W$. This yields

$$\cos^2 \theta = \frac{E - W}{E} \frac{E + 2m_e c^2}{E - W + 2m_e c^2}, \quad (3.116)$$

which agrees with eq. (A.17). The azimuthal scattering angle ϕ is sampled uniformly in the interval $(0, 2\pi)$.

Hard close collisions of positrons

The PDF of the reduced energy loss $\kappa \equiv W/E$ in positron close collisions with the k -th oscillator is given by [see eqs. (3.74) and (3.75)]

$$\begin{aligned} P_k^{(+)}(\kappa) &= \kappa^{-2} F_k^{(+)}(E, W) \Theta(\kappa - \kappa_c) \Theta(1 - \kappa) \\ &= \left[\frac{1}{\kappa^2} - \frac{b_1}{\kappa} + b_2 - b_3 \kappa + b_4 \kappa^2 \right] \Theta(\kappa - \kappa_c) \Theta(1 - \kappa) \end{aligned} \quad (3.117)$$

with $\kappa_c \equiv \max(W_k, W_{cc})/E$. The maximum allowed reduced energy loss is 1. Again, normalization is not important.

Consider the distribution

$$\Phi^{(+)}(\kappa) \equiv \kappa^{-2} \Theta(\kappa - \kappa_c) \Theta(1 - \kappa). \quad (3.118)$$

It is easy to see that $\Phi^{(+)} > P_k^{(+)}$ in the interval $(\kappa_c, 1)$. Therefore, we can generate κ from the PDF, eq. (3.117), by using the rejection method with trial values sampled from the distribution of eq. (3.118) and acceptance probability $P_k^{(+)}/\Phi^{(+)}$. Sampling from the PDF $\Phi^{(+)}$ can easily be performed with the inverse transform method.

The algorithm for random sampling from the PDF (3.117), is:

- (i) Sample κ from the PDF (3.118), as $\kappa = \kappa_c/[1 - \xi(1 - \kappa_c)]$.
- (ii) Generate a new random number ξ .
- (iii) If $\xi < \kappa^2 P_k^{(+)}(\kappa)$, deliver κ .
- (iv) Go to step (i).

The efficiency of this algorithm, for given values of the kinetic energy and the cutoff reduced energy loss κ_c , practically coincides with that of the algorithm for electron collisions described above (see table 3.1).

Secondary electron emission

According to our GOS model, each oscillator W_k corresponds to a shell with f_k electrons and ionization energy U_k . After a hard collision with an inner-shell electron, the primary electron/positron has kinetic energy $E - W$, the “secondary” electron (delta ray) is ejected with kinetic energy $E_s = W - U_i$, and the residual ion is left in an excited state, with a vacancy in shell i , which corresponds to an excitation energy equal to U_i . This energy is eventually released by emission of energetic x rays and Auger electrons. However, in PENELOPE the relaxation of ions produced in hard collisions is not followed. The production of vacancies in inner shells and their relaxation is simulated by an independent, more accurate, scheme (see section 3.2.6) that is free from the crude approximations involved in our GOS model. To avoid double counting, the excitation energy U_i of the residual ion is deposited locally. On the other hand, when the impact ionization occurs in an outer shell or in the conduction band, the initial energy of the secondary electron is set equal to W and no fluorescent radiation from the ionized atom is followed by the simulation program. This is equivalent to assuming that the secondary electron carries away the excitation energy of the target atom.

To set the initial direction of the delta ray, we assume that the target electron was initially at rest, i.e. the delta ray is emitted in the direction of the momentum transfer \mathbf{q} . This implies that the polar emission angle θ_s (see fig. 3.1) coincides with the recoil angle θ_r [which is given by eq. (A.42)],

$$\cos^2 \theta_s = \frac{W^2/\beta^2}{Q(Q + 2m_e c^2)} \left(1 + \frac{Q(Q + 2m_e c^2) - W^2}{2W(E + m_e c^2)} \right)^2. \quad (3.119)$$

In the case of close collisions ($Q = W$), this expression simplifies to

$$\cos \theta_s (Q = W) = \left(\frac{W}{E} \frac{E + 2m_e c^2}{W + 2m_e c^2} \right)^{1/2}, \quad (3.120)$$

which agrees with the result for binary collisions with free electrons at rest, see eq. (A.18). Since the momentum transfer lies on the scattering plane (i.e. on the plane formed by the initial and final momenta of the projectile), the azimuthal emission angle is $\phi_s = \pi + \phi$.

In reality, the target electrons are not at rest and, therefore, the angular distribution of emitted delta rays is broad. Since the average momentum of bound electrons is zero, the average direction of delta rays coincides with the direction of \mathbf{q} . Thus, our simple emission model correctly predicts the average initial direction of delta rays, but disregards the “Doppler broadening” of the angular distribution. This is not a serious drawback, because secondary electrons are usually emitted with initial kinetic energies that are much smaller than the initial energy of the projectile. This means that the direction of motion of the delta ray is randomized, by elastic and inelastic collisions, after a relatively short path length (much shorter than the transport mean free path of the projectile).

3.2.6 Ionization of inner shells

As indicated above, the theory presented in sections 3.2.1 and 3.2.2 does not give realistic values of the cross sections for ionization of inner shells. Hence, it is not appropriate to simulate inner-shell ionization by electron and positron impact and the subsequent emission of fluorescent radiation, i.e. Auger electrons and characteristic x rays. Nevertheless, the GOS model does provide an appropriate description of the average (stopping and scattering) effect of inelastic collisions on the projectile.

A consistent model for the simulation of inner-shell ionization and relaxation must account for the following features of the process: 1) space distribution of inner-shell ionizations along the projectile’s track, 2) relative probabilities of ionizing various atomic electron shells and 3) energies and emission probabilities of the electrons and x rays released through the de-excitation cascade of the ionized atom. The correlation between energy loss/scattering of the projectile and ionization events is of minor importance and may be neglected (it is observable only in single-scattering experiments where the inelastically scattered electrons and the emitted x rays or Auger electrons are observed in coincidence). Consequently, we shall consider inner-shell ionization as an independent interaction process that has no effect on the state of the projectile. Accordingly, in the simulation of inelastic collisions the projectile is assumed to cause only the ejection of knock-on electrons (delta rays); in these collisions the target atom is considered to remain unaltered to avoid double counting of ionizations. Thus, to determine the location of ionizing events and the atomic shell that is ionized we only need to consider cross sections for ionization of individual inner shells, which can be obtained from elaborate theoretical models. The relaxation of the vacancies produced by inner-shell ionizations is simulated as described in section 2.6. This kind of simulation scheme is trivial to implement, but it may cause artifacts (in the form of small negative doses) in space regions where the simulated dose distributions have large relative statistical uncertainties. The reason is that simulated Auger electrons and x rays remove energy from their site (volume bin) of birth, in quantities that may exceed the actual energy deposited by the projectile.

To simulate the ionization of K shells and L subshells (with ionization energies larger than 200 eV) by electron and positron impact, PENELOPE uses total ionization

cross sections obtained from an optical-data model of the GOS (Mayol and Salvat, 1990). This model assumes the following relationship between the optical oscillator strength (OOS) of the i -th inner shell, $df_i(W)/dW$, and the photoelectric cross section $\sigma_{\text{ph},i}(Z, W)$ for absorption of a photon with energy W ,

$$\frac{df_i(W)}{dW} = \frac{m_e c}{2\pi^2 e^2 \hbar} \sigma_{\text{ph},i}(Z, W). \quad (3.121)$$

This equality holds when the dipole approximation is applicable, i.e. when the wavelength of the photon is much larger than the “size” of the active electron shell. In the calculations we use the photoelectric cross sections from the PENELOPE database, which were extracted from the EPDL (Cullen et al., 1997). The GOS is modelled as a continuous superposition of δ -oscillators weighted by the OOS,

$$\frac{df_i(Q, W)}{dW} = \int_{U_i}^{\infty} \frac{df_i(W')}{dW'} F(W'; Q, W) dW' + Z_r \delta(W - Q) \Theta(W - U_i) \quad (3.122)$$

with

$$Z_r = Z_i - \int_{U_i}^{\infty} \frac{df_i(W')}{dW'} dW'. \quad (3.123)$$

This GOS model satisfies the Bethe sum rule

$$\int_{U_i}^{\infty} \frac{df_i(Q, W)}{dW} dW = Z_i \quad \text{if } Q > U_i. \quad (3.124)$$

For $Q < U_i$ the integral of the GOS over W is less than the number Z_i of electrons in the active shell (because there is a transfer of oscillator strength to outer shells). As shown by Mayol and Salvat (1990), this model is formally equivalent to the Weizsäcker-Williams method of virtual quanta (see e.g. Jackson, 1975).

To compute the inner-shell ionization (“si”) cross section for electrons or positrons of energy E we first consider the energy-loss DCS, which is given by

$$\begin{aligned} \frac{d\sigma_{\text{si},i}^{(\pm)}(E)}{dW} = & \frac{2\pi e^4}{m_e v^2} \left\{ \frac{df_i(W)}{dW} \frac{1}{W} \left[\ln \left(\frac{W}{Q_-} \frac{Q_- + 2m_e c^2}{W + 2m_e c^2} \right) + \ln \left(\frac{1}{1 - \beta^2} \right) - \beta^2 \right] \right. \\ & \left. + \left(Z_r + \int_{U_i}^W \frac{df_i(W')}{dW'} dW' \right) \frac{1}{W^2} F^{(\pm)}(E, W) \right\} \Theta(W - U_i) \Theta(W_{\text{max}} - U_i), \end{aligned} \quad (3.125)$$

where Q_- is the minimum recoil energy for the energy loss W , eq. (A.31), and $F^{(\pm)}(E, W)$ are the Møller (−) and Bhabha (+) factors, eqs. (3.70) and (3.74).

It is well known that the Born approximation overestimates the ionization cross sections for incident electrons with kinetic energies near the ionization threshold. This is mainly due to the distortion of the projectile wave function by the electrostatic field of the target atom. This field produces an increase in the effective kinetic energy of the projectile, which is expected to be important in close collisions. To account for this

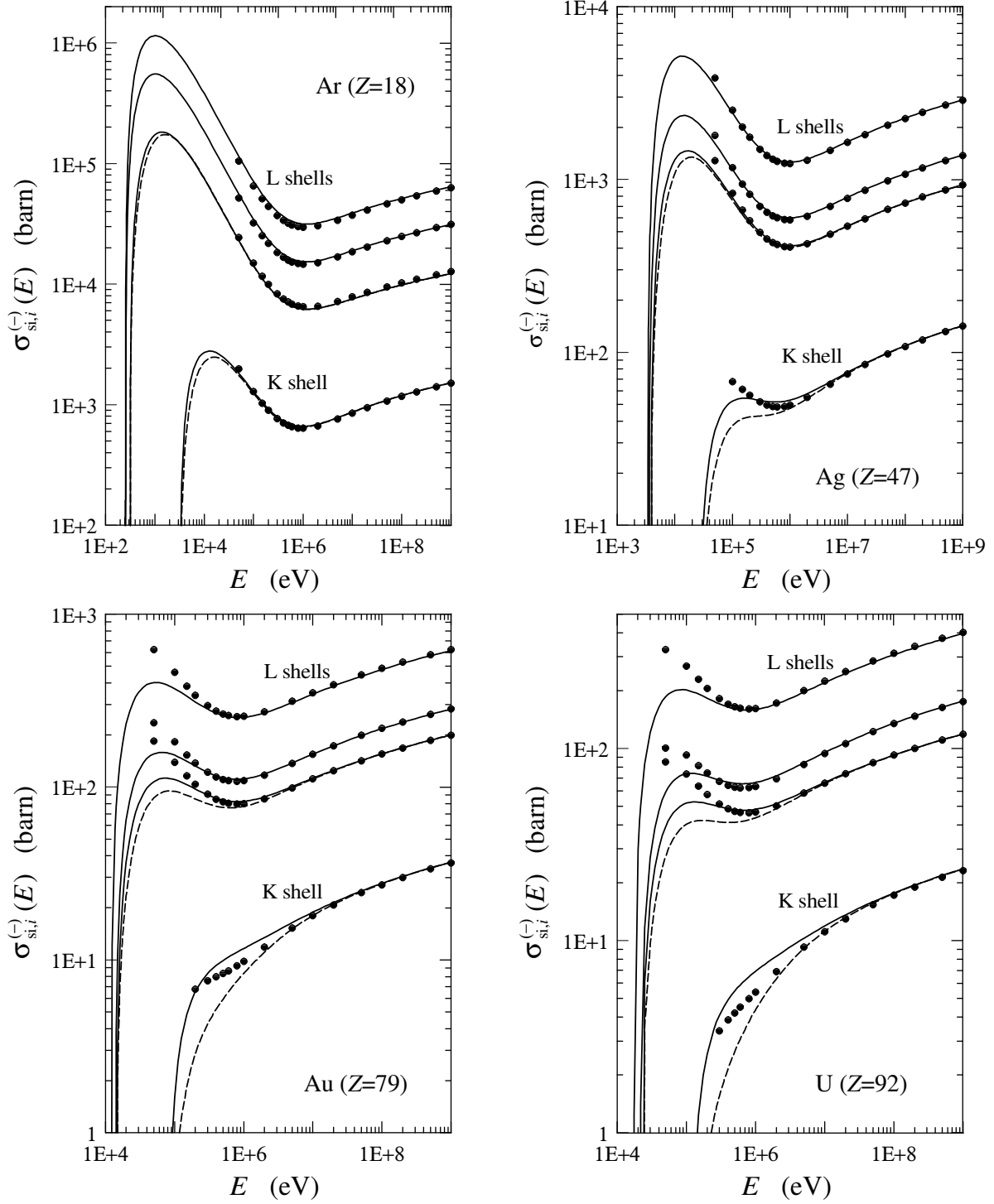


Figure 3.12: Cross sections for ionization of the K shell and the L subshells of argon, silver, gold and uranium atoms by electron impact as functions of the kinetic energy of the projectiles. Solid curves are results from the present optical data model. Circles represent cross-section values calculated by Scofield (1978) using the relativistic plane-wave Born approximation. The dashed curves are cross sections for ionization by impact of positrons calculated from eq. (3.126b).

effect we assume that the incident electron gains a kinetic energy⁵ $2U_i$ before it interacts with a target electron, which is bound with binding energy U_i . The maximum energy loss is assumed to be $W_{\max} = (E + U_i)/2$, because the final energies of the projectile ($E - W$) and the knock-on secondary electron ($W - U_i$) are equal when W equals that value. With this “Coulomb” correction, the ionization cross section for electrons is

$$\sigma_{\text{si},i}^{(-)}(E) = \int_{U_i}^{(E+U_i)/2} \frac{d\sigma_{\text{si},i}^{(-)}(E + 2U_i)}{dW} dW. \quad (3.126a)$$

The Coulomb correction reduces the ionization cross section near the threshold and yields values in better agreement with experimental data. For positrons the effect of the Coulomb distortion is introduced empirically by simply multiplying the ionization cross section by a global factor $(1 + U_i/E)^{-3}$. That is,

$$\sigma_{\text{si},i}^{(+)}(E) = \left(\frac{E}{E + U_i}\right)^3 \int_{U_i}^E \frac{d\sigma_{\text{si},i}^{(+)}(E)}{dW} dW. \quad (3.126b)$$

This correction gives positron ionization cross sections that are smaller than those of electrons near the ionization threshold, in qualitative agreement with available experimental data (see e.g. Hippler, 1990; Schneider et al., 1993). Fig. 3.12 displays cross sections for ionization of K shells and L subshells of atoms of the elements argon, silver, gold and uranium by impact of electrons obtained from the present optical-data model, eq. (3.126a), together with results from the relativistic plane-wave first Born approximation (Scofield, 1978). The differences at relatively low energies are mostly due to exchange and Coulomb corrections, which were not included in Scofield’s calculations. The dashed curves in fig. 3.12 represent cross sections for ionization by positron impact, eq. (3.126b). The relative differences between the cross sections for electrons and positrons are seen to increase with the binding energy of the active shell. It is worth mentioning that the present optical-data model disregards the influence of the polarizability of the medium (density effect) on inner-shell ionization. This effect causes a reduction of the ionization cross sections for projectiles with very high energies, which decreases with the binding energy of the knock-on electron.

The molecular cross section for ionization of inner shells is evaluated as (additivity approximation)

$$\sigma_{\text{si,mol}}^{(\pm)}(E) = \sum_i \sigma_{\text{si},i}^{(\pm)}(E), \quad (3.127)$$

where the summation extends over all inner shells of the atoms in the molecule.

3.3 Bremsstrahlung emission

As a result of the acceleration caused by the electrostatic field of atoms, swift electrons (or positrons) emit bremsstrahlung (braking radiation). In each bremsstrahlung event,

⁵For one-electron atoms and ions, the virial theorem implies that the average potential energy of the bound electron is equal to $2U_i$. In close collisions, for which the projectile reaches the position of the target electron, the gain in kinetic energy should be of the order of $2U_i$.

an electron with kinetic energy E generates a photon of energy W , which takes values in the interval from 0 to E . The process is described by an atomic DCS, differential in the energy loss W , the final direction of the projectile and the direction of the emitted photon (Koch and Motz, 1959; Tsai, 1974). The habitual practice in Monte Carlo simulation is to sample the energy loss from the single-variable distribution obtained by integrating the DCS over the other variables. This permits the generation of W easily, but information on the angular distributions is completely lost and has to be regained from suitable approximations. Angular deflections of the projectile are considered to be accounted for by the elastic scattering DCS and, consequently, the direction of movement of the projectile is kept unaltered in the simulation of radiative events.

3.3.1 The energy-loss scaled DCS

A simple description of the bremsstrahlung DCS is provided by the Bethe-Heitler formula with screening, which is derived within the Born approximation (Bethe and Heitler, 1934; Tsai, 1974). Although this formula is valid only when the kinetic energy of the electron before and after photon emission is much larger than its rest energy $m_e c^2$, it accounts for the most relevant features of the emission process. Within the Born approximation, bremsstrahlung emission is closely related to electron-positron pair production. In particular, the Bethe-Heitler DCS formulae for pair production and bremsstrahlung emission involve the same screening functions. Considering the exponential screening model (2.78), the Bethe-Heitler DCS for bremsstrahlung emission by electrons in the field of an atom of atomic number Z and screening radius R can be expressed as (Salvat and Fernández-Varea, 1992)

$$\frac{d\sigma_{\text{br}}^{(\text{BH})}}{dW} = r_e^2 \alpha Z(Z + \eta) \frac{1}{W} \left[\epsilon^2 \varphi_1(b) + \frac{4}{3}(1 - \epsilon) \varphi_2(b) \right], \quad (3.128)$$

where α is the fine-structure constant, r_e is the classical electron radius,

$$\epsilon = \frac{W}{E + m_e c^2} = \frac{W}{\gamma m_e c^2}, \quad b = \frac{R m_e c}{\hbar} \frac{1}{2\gamma} \frac{\epsilon}{1 - \epsilon}, \quad (3.129)$$

and

$$\begin{aligned} \varphi_1(b) &= 4 \ln(R m_e c / \hbar) + 2 - 2 \ln(1 + b^2) - 4b \arctan(b^{-1}), \\ \varphi_2(b) &= 4 \ln(R m_e c / \hbar) + \frac{7}{3} - 2 \ln(1 + b^2) - 6b \arctan(b^{-1}) \\ &\quad - b^2 \left[4 - 4b \arctan(b^{-1}) - 3 \ln(1 + b^{-2}) \right]. \end{aligned} \quad (3.130)$$

The quantity η in eq. (3.128) accounts for the production of bremsstrahlung in the field of the atomic electrons (see e.g. Seltzer and Berger, 1985); in the high-energy limit $\eta \simeq 1.2$.

The Bethe-Heitler formula indicates that, for a given value of Z , the quantity $W d\sigma_{\text{br}}/dW$ varies smoothly with E and W . It is therefore customary to express the DCS for bremsstrahlung emission by electrons in the form

$$\frac{d\sigma_{\text{br}}}{dW} = \frac{Z^2}{\beta^2} \frac{1}{W} \chi(Z, E, \kappa), \quad (3.131)$$

where W is the energy of the emitted photon, κ is the reduced photon energy, defined as

$$\kappa \equiv W/E, \quad (3.132)$$

which takes values between 0 and 1. The quantity

$$\chi(Z, E, \kappa) = (\beta^2/Z^2) W \frac{d\sigma_{\text{br}}}{dW} \quad (3.133)$$

is known as the “scaled” bremsstrahlung DCS; for a given element Z , it varies smoothly with E and κ . Seltzer and Berger (1985, 1986) produced extensive tables of the scaled DCS for all the elements ($Z = 1-92$) and for electron energies from 1 keV to 10 GeV. They tabulated the scaled DCSs for emission in the (screened) field of the nucleus (electron-nucleus bremsstrahlung) and in the field of atomic electrons (electron-electron bremsstrahlung) separately, as well as their sum, the total scaled DCS. The electron-nucleus bremsstrahlung DCS was calculated by combining analytical high-energy theories with results from partial-wave calculations by Pratt et al. (1977) for bremsstrahlung emission in screened atomic fields and energies below 2 MeV. The scaled DCS for electron-electron bremsstrahlung was obtained from the theory of Haug (1975) combined with a screening correction that involves Hartree-Fock incoherent scattering functions. Seltzer and Berger’s scaled DCS tables constitute the most reliable theoretical representation of bremsstrahlung energy spectra available at present.

The PENELOPE database of scaled bremsstrahlung DCSs consists of 92 files, one for each element from hydrogen to uranium, which were generated from the original database of Seltzer and Berger. The file of the element Z contains the values of $\chi(Z, E_i, \kappa_j)$ for a set of electron kinetic energies E_i , which covers the range from 1 keV to 10 GeV and is suitably spaced to allow accurate natural cubic spline interpolation in $\ln E$. For each energy E_i in this grid, the table contains the values of the scaled DCS for a given set of 32 reduced photon energies κ_j (the same for all elements), which span the interval (0,1), with a higher density at the upper end of this interval to reproduce the structure of the bremsstrahlung “tip” (see fig. 3.13). The spacing of the κ -grid is dense enough to allow linear interpolation of $\chi(Z, E_i, \kappa_j)$ in κ .

In the case of compounds (or mixtures) we use the additivity rule and compute the molecular DCS as the sum of the DCSs of all the atoms in a molecule. Consider a compound $X_x Y_y$, whose molecules consist of x atoms of the element X and y atoms of the element Y . The molecular DCS is

$$\frac{d\sigma_{\text{br,mol}}}{dW} = x \frac{Z_X^2}{\beta^2} \frac{1}{W} \chi(Z_X, E, \kappa) + y \frac{Z_Y^2}{\beta^2} \frac{1}{W} \chi(Z_Y, E, \kappa). \quad (3.134)$$

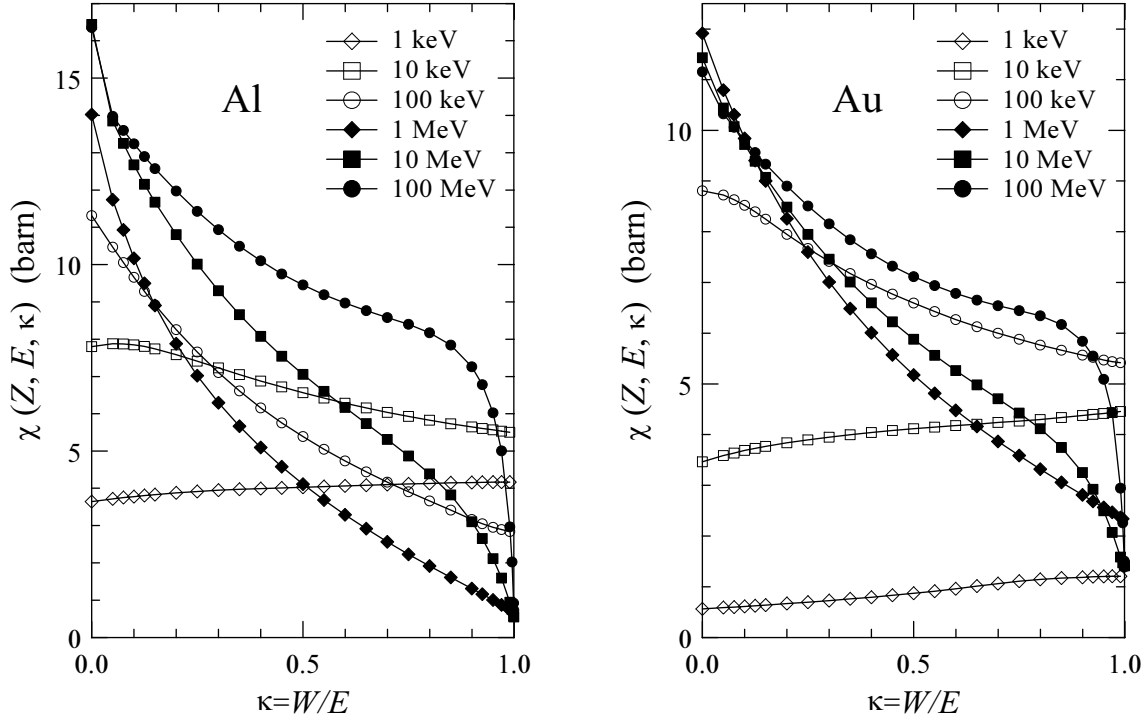


Figure 3.13: Numerical scaled bremsstrahlung energy-loss DCSs of aluminium and gold for electrons with the indicated energies (Seltzer and Berger, 1986).

To simulate each radiative event in a compound, we should first select the element (X or Y) where the emission occurs and then sample the photon energy and direction from the corresponding atomic DCS. This is a lengthy process and requires storing the scaled DCSs for all the elements present. To simplify the simulation, we shall express the molecular DCS in the same form as the atomic DCS, eq. (3.131),

$$\frac{d\sigma_{\text{br,mol}}}{dW} = \frac{Z_{\text{eq}}^2}{\beta^2} \frac{1}{W} \chi_{\text{mol}}(Z_{\text{eq}}, E, \kappa), \quad (3.135)$$

where

$$Z_{\text{eq}}^2 \equiv \frac{1}{x + y} (xZ_X^2 + yZ_Y^2) \quad (3.136)$$

is the “equivalent” atomic number Z_{eq} and

$$\chi_{\text{mol}}(Z_{\text{eq}}, E, \kappa) = \frac{xZ_X^2}{Z_{\text{eq}}^2} \chi(Z_X, E, \kappa) + \frac{yZ_Y^2}{Z_{\text{eq}}^2} \chi(Z_Y, E, \kappa) \quad (3.137)$$

is the molecular scaled DCS. Radiative events will be sampled directly from the molecular DCS (3.135). This method may introduce slight inconsistencies in the angular distribution of the emitted photons (see below), which usually have a negligible effect on the simulation results.

The radiative DCS for positrons reduces to that of electrons in the high-energy limit but is smaller for intermediate and low energies. Owing to the lack of more accurate calculations, the DCS for positrons is obtained by multiplying the electron DCS by a κ -independent factor, i.e.

$$\frac{d\sigma_{\text{br}}^{(+)}}{dW} = F_p(Z, E) \frac{d\sigma_{\text{br}}^{(-)}}{dW}. \quad (3.138)$$

The factor $F_p(Z, E)$ is set equal to the ratio of the radiative stopping powers for positrons and electrons, which has been calculated by Kim et al. (1986) (cf. Berger and Seltzer, 1982). In the calculations we use the following analytical approximation

$$\begin{aligned} F_p(Z, E) = & 1 - \exp(-1.2359 \times 10^{-1} t + 6.1274 \times 10^{-2} t^2 - 3.1516 \times 10^{-2} t^3 \\ & + 7.7446 \times 10^{-3} t^4 - 1.0595 \times 10^{-3} t^5 + 7.0568 \times 10^{-5} t^6 \\ & - 1.8080 \times 10^{-6} t^7), \end{aligned} \quad (3.139)$$

where

$$t = \ln \left(1 + \frac{10^6}{Z^2} \frac{E}{m_e c^2} \right). \quad (3.140)$$

Expression (3.139) reproduces the values of $F_p(Z, E)$ tabulated by Kim et al. (1986) to an accuracy of about 0.5%.

3.3.2 Integrated cross sections

The total cross section for bremsstrahlung emission is infinite due to the divergence of the DCS (3.131) for small reduced photon energies. Nevertheless, the cross section for emission of photons with reduced energy larger than a given cutoff value W_{cr} is finite. The corresponding mean free path is

$$\lambda_{\text{br}}^{-1}(E; W_{\text{cr}}) \equiv \mathcal{N} \int_{W_{\text{cr}}}^E \frac{d\sigma_{\text{br}}}{dW} dW = \mathcal{N} \frac{Z^2}{\beta^2} \int_{\kappa_{\text{cr}}}^1 \frac{1}{\kappa} \chi(Z, E, \kappa) d\kappa, \quad (3.141)$$

where $\kappa_{\text{cr}} = W_{\text{cr}}/E$. The radiative stopping power and the radiative energy straggling parameter, defined by

$$S_{\text{br}}(E) \equiv \mathcal{N} \int_0^E W \frac{d\sigma_{\text{br}}}{dW} dW = \mathcal{N} \frac{Z^2}{\beta^2} E \int_0^1 \chi(Z, E, \kappa) d\kappa \quad (3.142)$$

and

$$\Omega_{\text{br}}^2(E) \equiv \mathcal{N} \int_0^E W^2 \frac{d\sigma_{\text{br}}}{dW} dW = \mathcal{N} \frac{Z^2}{\beta^2} E^2 \int_0^1 \kappa \chi(Z, E, \kappa) d\kappa, \quad (3.143)$$

are both finite. For the kinetic energies E_i of the grid, these quantities are easily calculated from the tabulated scaled DCS by using linear interpolation in κ . For positrons, the definitions (3.141)-(3.143) must be multiplied by the factor $F_p(Z, E)$ [eq. (3.139)].

Radiative stopping powers of aluminium, silver and gold for electrons and positrons are shown as functions of the kinetic energy in fig. 3.14. The stopping powers computed

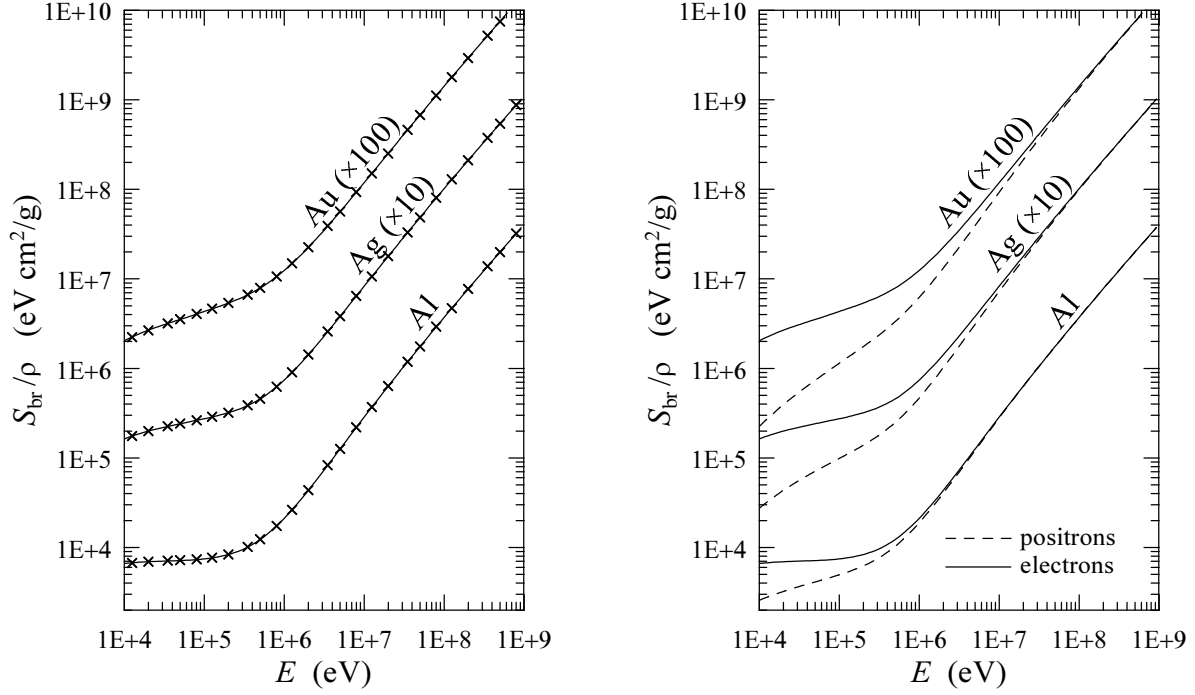


Figure 3.14: Radiative stopping power S_{br}/ρ for electrons and positrons in aluminium, silver ($\times 10$) and gold ($\times 100$) as a function of the kinetic energy. Solid and dashed curves are results from the present model. Crosses are data from the ICRU37 report (1984) (also in Berger and Seltzer, 1982).

from the DCS given by eq. (3.131) practically coincide with ICRU37 (1984) values (also Berger and Seltzer, 1982). To leave room for future improvements, PENELOPE reads the radiative stopping power for electrons from the input material data file, and renormalizes the DCS, eq. (3.131), (i.e. multiplies it by a κ -independent factor) so as to exactly reproduce the input radiative stopping power.

CSDA range

As mentioned above, the stopping power gives the average energy loss per unit path length. Thus, when an electron/positron with kinetic energy E advances a small distance ds within a medium, it loses an (average) energy $dE = -S(E)ds$, where

$$S(E) = S_{\text{in}}(E) + S_{\text{br}}(E) = -\frac{dE}{ds} \quad (3.144)$$

is the total (collisional+radiative) stopping power. Many electron transport calculations and old Monte Carlo simulations are based on the so-called continuous slowing down approximation (CSDA), which assumes that particles lose energy in a continuous way and at a rate equal to the stopping power. Evidently, the CSDA disregards energy-loss fluctuations and, therefore, it should be used with caution.

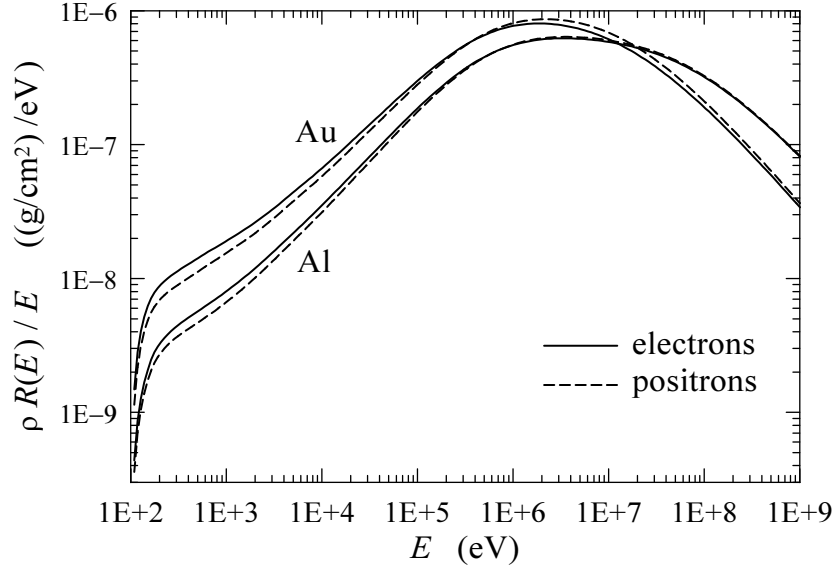


Figure 3.15: CSDA ranges for electrons and positrons in aluminium and gold as functions of the kinetic energy of the particle.

A parameter of practical importance is the so-called CSDA range (or Bethe range), which is defined as the path length travelled by a particle (in an infinite medium) before being absorbed and is given by

$$R(E) = \int_{E_{\text{abs}}}^E \frac{dE'}{S(E')}, \quad (3.145)$$

where we have considered that particles are effectively absorbed when they reach the energy E_{abs} . Notice that the CSDA range gives the *average* path length, actual (or Monte Carlo generated) path lengths fluctuate about the mean $R(E)$; the distribution of ranges has been studied by Lewis (1952). Fig. 3.15 displays CSDA ranges for electrons and positrons in aluminium and gold, this information is useful e.g. in estimating the maximum penetration depth of a beam and for range rejection (a variance-reduction method). Compare fig. 3.15 with figs. 3.10 and 3.14 (right plots only) to get a feeling of how differences in stopping power between electrons and positrons are reflected on the CSDA ranges of these particles.

3.3.3 Angular distribution of emitted photons

The direction of the emitted bremsstrahlung photon is defined by the polar angle θ (see fig. 3.1) and the azimuthal angle ϕ . For isotropic media, with randomly oriented atoms or molecules, the bremsstrahlung DCS is independent of ϕ and can be expressed as

$$\frac{d^2\sigma_{\text{br}}}{dW d(\cos\theta)} = \frac{d\sigma_{\text{br}}}{dW} p(Z, E, \kappa; \cos\theta) = \frac{Z^2}{\beta^2} \frac{1}{W} \chi(Z, E, \kappa) p(Z, E, \kappa; \cos\theta), \quad (3.146)$$

where $p(Z, E, \kappa; \cos \theta)$ is the PDF of $\cos \theta$.

Numerical values of the “shape function” $p(Z, E, \kappa; \cos \theta)$, calculated by partial-wave methods, have been published by Kissel et al. (1983) for the following benchmark cases: $Z = 2, 8, 13, 47, 79, 92$; $E = 1, 5, 10, 50, 100, 500$ keV and $\kappa = 0, 0.6, 0.8, 0.95$. These authors also gave a parameterization of the shape function in terms of Legendre polynomials. Unfortunately, their analytical form is not suited for random sampling of the photon direction. In PENELOPE we use a different parameterization that allows the random sampling of $\cos \theta$ in a simple way. Owing to the lack of numerical data for positrons, it is assumed that the shape function for positrons is the same as for electrons.

In previous simulation studies of x-ray emission from solids bombarded by electron beams (Acosta et al., 1998), the angular distribution of bremsstrahlung photons was described by means of the semiempirical analytical formulae derived by Kirkpatrick and Wiedmann (1945) [and subsequently modified by Statham (1976)]. These formulae were obtained by fitting the bremsstrahlung DCS derived from Sommerfeld’s theory. The shape function obtained from the Kirkpatrick-Wiedmann-Statham fit reads

$$p^{(\text{KWS})}(Z, E, \kappa; \cos \theta) = \frac{\sigma_x(1 - \cos^2 \theta) + \sigma_y(1 + \cos^2 \theta)}{(1 - \beta \cos \theta)^2}, \quad (3.147)$$

where the quantities σ_x and σ_y are independent of θ . Although this simple formula predicts the global trends of the partial-wave shape functions of Kissel et al. (1983) in certain energy and atomic number ranges, its accuracy is not sufficient for general-purpose simulations. In a preliminary analysis, we tried to improve this formula and determined the parameters σ_x and σ_y by direct fitting to the numerical partial-wave shape functions, but the improvement was not substantial. However, this analysis confirmed that the analytical form (3.147) is flexible enough to approximate the “true” (partial-wave) shape.

The analytical form (3.147) is plausible even for projectiles with relatively high energies, say E larger than 1 MeV, for which the angular distribution of emitted photons is peaked at forward directions. This can be understood by means of the following classical argument (see e.g. Jackson, 1975). Assume that the incident electron is moving in the direction of the z -axis of a reference frame K at rest with respect to the laboratory frame. Let (θ', ϕ') denote the polar and azimuthal angles of the direction of the emitted photon in a reference frame K' that moves with the electron and whose axes are parallel to those of K . In K' , we expect that the angular distribution of the emitted photons will not depart much from the isotropic distribution. To be more specific, we consider the following ansatz (modified dipole distribution) for the shape function in K' ,

$$p_d(\cos \theta') = A \frac{3}{8} (1 + \cos^2 \theta') + (1 - A) \frac{3}{4} (1 - \cos^2 \theta'), \quad (0 \leq A \leq 1), \quad (3.148)$$

which is motivated by the relative success of the Kirkpatrick-Wiedmann-Statham formula at low energies (note that the projectile is at rest in K'). The direction of emission (θ, ϕ) in K is obtained by means of the Lorentz transformation

$$\cos \theta = \frac{\cos \theta' + \beta}{1 + \beta \cos \theta'}, \quad \phi = \phi'. \quad (3.149)$$

Thus, the angular distribution in K reads

$$\begin{aligned}
 p(\cos \theta) &= p_d(\cos \theta') \frac{d(\cos \theta')}{d(\cos \theta)} \\
 &= A \frac{3}{8} \left[1 + \left(\frac{\cos \theta - \beta}{1 - \beta \cos \theta} \right)^2 \right] \frac{1 - \beta^2}{(1 - \beta \cos \theta)^2} \\
 &\quad + (1 - A) \frac{3}{4} \left[1 - \left(\frac{\cos \theta - \beta}{1 - \beta \cos \theta} \right)^2 \right] \frac{1 - \beta^2}{(1 - \beta \cos \theta)^2}. \tag{3.150}
 \end{aligned}$$

Now, it is clear that when β tends to unity, the shape function concentrates at forward directions.

We found that the benchmark partial-wave shape functions of Kissel et al. (1983) can be closely approximated by the analytical form (3.150) if one considers A and β as adjustable parameters. Explicitly, we write

$$\begin{aligned}
 p_{\text{fit}}(\cos \theta) &= A \frac{3}{8} \left[1 + \left(\frac{\cos \theta - \beta'}{1 - \beta' \cos \theta} \right)^2 \right] \frac{1 - \beta'^2}{(1 - \beta' \cos \theta)^2} \\
 &\quad + (1 - A) \frac{3}{4} \left[1 - \left(\frac{\cos \theta - \beta'}{1 - \beta' \cos \theta} \right)^2 \right] \frac{1 - \beta'^2}{(1 - \beta' \cos \theta)^2}, \tag{3.151}
 \end{aligned}$$

with $\beta' = \beta(1 + B)$. The parameters A and B have been determined, by least squares fitting, for the 144 combinations of atomic number, electron energy and reduced photon energy corresponding to the benchmark shape functions tabulated by Kissel et al. (1983). Results of this fit are compared with the original partial-wave shape functions in fig. 3.16. The largest differences between the fits and the data were found for the higher atomic numbers, but even then the fits are very accurate, as shown in fig. 3.16. The quantities $\ln(AZ\beta)$ and $B\beta$ vary smoothly with Z , β and κ and can be obtained by cubic spline interpolation of their values for the benchmark cases. This permits the fast evaluation of the shape function for any combination of Z , β and κ . Moreover, the random sampling of the photon direction, i.e. of $\cos \theta$, can be performed by means of a simple, fast analytical algorithm (see below). For electrons with kinetic energies larger than 500 keV, the shape function is approximated by the classical dipole distribution, i.e. by the analytical form (3.151) with $A = 1$ and $\beta' = \beta$.

3.3.4 Simulation of hard radiative events

Let us now consider the simulation of hard radiative events ($W > W_{\text{cr}}$) from the DCS defined by eqs. (3.146) and (3.151). PENELOPE reads the scaled bremsstrahlung DCS from the database files and, by natural cubic spline interpolation/extrapolation in $\ln E$, produces a table for a denser logarithmic grid of 200 energies (and for the “standard” mesh of 32 κ ’s), which is stored in memory. This energy grid spans the full energy range

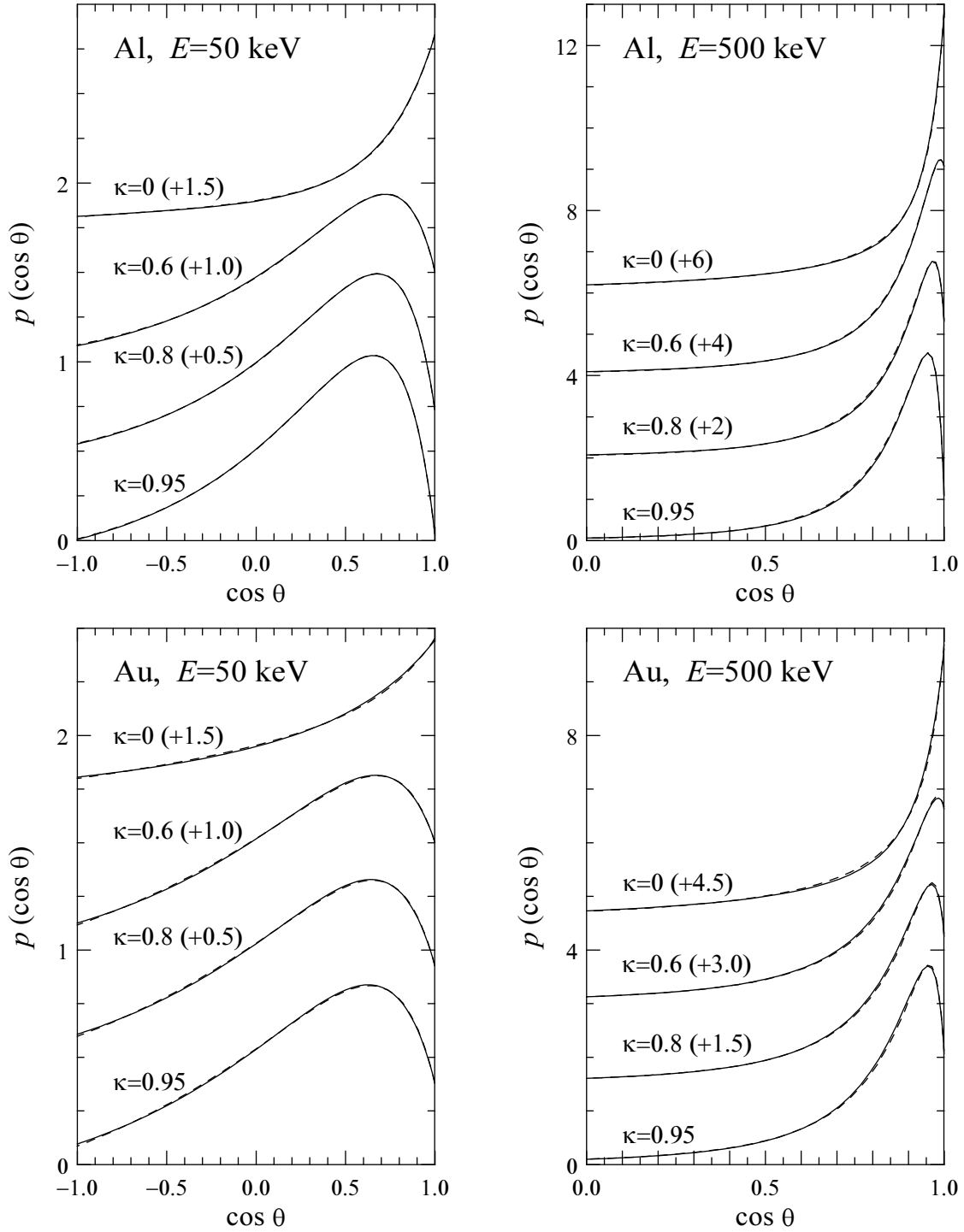


Figure 3.16: Shape functions (angular distributions) for bremsstrahlung emission by electrons of the indicated energies in the fields of aluminium and gold atoms. Dashed curves are partial-wave shape functions of Kissel et al. (1983). Continuous curves are the present analytical fits, eq. (3.151). For visual aid, some curves have been shifted upwards in the amounts indicated in parentheses.

considered in the simulation and allows accurate (and fast) linear interpolation of the scaled DCS in the variable $\ln E$, which is more adequate than E when interpolation over a wide energy interval is required.

Notice that in the Monte Carlo simulation the kinetic energy of the transported electron (or positron) varies in a random way and may take arbitrary values within a certain domain. Hence, we must be able to simulate bremsstrahlung emission by electrons with energies E not included in the grid.

Sampling of the photon energy

The PDF for the reduced photon energy, $\kappa = W/E$, is given by [see eq. (3.131)]

$$p(E, \kappa) = \frac{1}{\kappa} \chi(Z, E, \kappa) \Theta(\kappa - \kappa_{\text{cr}}) \Theta(1 - \kappa), \quad (3.152)$$

where $\kappa_{\text{cr}} = W_{\text{cr}}/E$ and $\chi(Z, E, \kappa)$ is calculated by linear interpolation, in both $\ln E$ and κ , in the stored table. That is, $\chi(Z, E, \kappa)$ is considered to be a piecewise linear function of κ . To sample κ from the PDF (3.152) for an energy E_i in the grid, we express the interpolated scaled DCS as

$$\chi(Z, E_i, \kappa) = a_j + b_j \kappa \quad \text{if } \kappa_j \leq \kappa \leq \kappa_{j+1}, \quad (3.153)$$

and introduce the cumulative distribution function,

$$\mathcal{P}_j = \int_{\kappa_{\text{cr}}}^{\kappa_j} p(E_i, \kappa) d\kappa, \quad (3.154)$$

which, for a piecewise linear χ , can be computed exactly. We also define

$$\chi_{\text{max},j} = \max \left\{ \chi(Z, E, \kappa), \kappa \in (\kappa_j, \kappa_{j+1}) \right\} \quad j = 1, \dots, 32. \quad (3.155)$$

With all this we can formulate the following sampling algorithm, which combines a numerical inverse transform and a rejection,

- (i) Generate a random number ξ and determine the index j for which $\mathcal{P}_j \leq \xi \mathcal{P}_{32} \leq \mathcal{P}_{j+1}$ using the binary search method.
- (ii) Sample κ from the distribution κ^{-1} in the interval (κ_j, κ_{j+1}) , i.e.

$$\kappa = \kappa_j (\kappa_{j+1}/\kappa_j)^\xi. \quad (3.156)$$

- (iii) Generate a new random number ξ . If $\xi \chi_{\text{max},j} < a_j + b_j \kappa$, deliver κ .
- (iv) Go to step (i).

This sampling algorithm is exact and very fast [notice that the binary search in step (i) requires at most 5 comparisons], but is only applicable for the energies in the grid where χ is tabulated.

To simulate bremsstrahlung emission by electrons with energies E not included in the grid, we should first obtain the PDF $p(E, \kappa)$ by interpolation along the energy axis and then perform the random sampling of κ from this PDF using the algorithm described above. This procedure is too time consuming. A faster method consists of assuming that the grid of energies is dense enough so that linear interpolation in $\ln E$ is sufficiently accurate. If $E_i < E < E_{i+1}$, we can express the interpolated PDF as

$$p_{\text{int}}(E, \kappa) = \pi_i p(E_i, \kappa) + \pi_{i+1} p(E_{i+1}, \kappa) \quad (3.157)$$

with

$$\pi_i = \frac{\ln E_{i+1} - \ln E}{\ln E_{i+1} - \ln E_i}, \quad \pi_{i+1} = \frac{\ln E - \ln E_i}{\ln E_{i+1} - \ln E_i}. \quad (3.158)$$

These “interpolation weights” are positive and add to unity, i.e. they can be interpreted as point probabilities. Therefore, to perform the random sampling of κ from $p_{\text{int}}(E, \kappa)$ we can employ the composition method (section 1.2.5), which leads to the following algorithm:

- (i) Sample the integer variable I , which can take the values i or $i + 1$ with point probabilities π_i and π_{i+1} , respectively.
- (ii) Sample κ from the distribution $p_{\text{int}}(E_I, \kappa)$.

With this “interpolation by weight” method we only need to sample κ from the tabulated PDFs, i.e. for the energies E_i of the grid.

Angular distribution of emitted photons

The random sampling of $\cos \theta$ is simplified by noting that the PDF given by eq. (3.151) results from a Lorentz transformation, with speed β' , of the PDF (3.148). This means that we can sample the photon direction $\cos \theta'$ in the reference frame K' from the PDF (3.148) and then apply the transformation (3.149) (with β' instead of β) to get the direction $\cos \theta$ in the laboratory frame.

To generate random values of $\cos \theta$ from (3.151) we use the following algorithm, which combines the composition and rejection methods,

- (i) Sample a random number ξ_1 .
- (ii) If $\xi_1 < A$, then
 - 1) Sample a random number ξ and set $\cos \theta' = -1 + 2\xi$.
 - 2) Sample a random number ξ .
 - 3) If $2\xi > 1 + \cos^2 \theta'$, go to 1).

- (iii) If $\xi_1 \geq A$, then
- 4) Sample a random number ξ and set $\cos \theta' = -1 + 2\xi$.
 - 5) Sample a random number ξ .
 - 6) If $\xi > 1 - \cos^2 \theta'$, go to 4).
- (iv) Deliver $\cos \theta = \frac{\cos \theta' + \beta'}{1 + \beta' \cos \theta'}$.

The efficiencies of the rejections in steps (ii) and (iii) are both equal to 0.66. That is, on average, we need 4 random numbers to generate each value of $\cos \theta$.

3.4 Positron annihilation

Following Nelson et al. (1985), we consider that positrons penetrating a medium of atomic number Z with kinetic energy E can annihilate with the electrons in the medium by emission of two photons. We assume that the target electrons are free and at rest, thus disregarding electron binding effects, which enable one-photon annihilation (Heitler, 1954). When annihilation occurs in flight, i.e. when the kinetic energy E of the positron is larger than the “absorption” energy, the two photons may have different energies, say E_- and E_+ , which add to $E + 2m_e c^2$. In what follows, quantities referring to the photon with the lowest energy will be denoted by the subscript “-”. Each annihilation event is then completely characterized by the quantity

$$\zeta \equiv \frac{E_-}{E + 2m_e c^2}. \quad (3.159)$$

Assuming that the positron moves initially in the direction of the z -axis, from conservation of energy and momentum it follows that the two photons are emitted in directions with polar angles [see eqs. (A.21) and (A.22) in appendix A]

$$\cos \theta_- = (\gamma^2 - 1)^{-1/2}(\gamma + 1 - 1/\zeta) \quad (3.160)$$

and

$$\cos \theta_+ = (\gamma^2 - 1)^{-1/2}[\gamma + 1 - 1/(1 - \zeta)], \quad (3.161)$$

and azimuthal angles ϕ_- and $\phi_+ = \phi_- + \pi$. The quantity $\gamma = 1 + E/(m_e c^2)$ is the total energy of the positron in units of its rest energy.

The maximum value of ζ is 1/2, its minimum value is found when $\cos \theta_- = -1$ and is given by

$$\zeta_{\min} = \frac{1}{\gamma + 1 + (\gamma^2 - 1)^{1/2}}. \quad (3.162)$$

The DCS (per electron) for two-photon annihilation, as observed in the centre-of-mass system of the positron and the electron, is given by Heitler (1954). Nelson et al.

(1985) transformed this DCS to the laboratory system (where the electron is at rest), their result can be written as

$$\frac{d\sigma_{\text{an}}}{d\zeta} = \frac{\pi r_e^2}{(\gamma + 1)(\gamma^2 - 1)} [S(\zeta) + S(1 - \zeta)], \quad (3.163)$$

where

$$S(\zeta) = -(\gamma + 1)^2 + (\gamma^2 + 4\gamma + 1)\frac{1}{\zeta} - \frac{1}{\zeta^2}. \quad (3.164)$$

Owing to the axial symmetry of the process, the DCS is independent of the azimuthal angle ϕ_- , which is uniformly distributed on the interval $(0, 2\pi)$. For fast positrons, annihilation photons are emitted preferentially at forward directions. When the kinetic energy of the positron decreases, the angular distribution of the generated photons becomes more isotropical (see fig. 3.17).

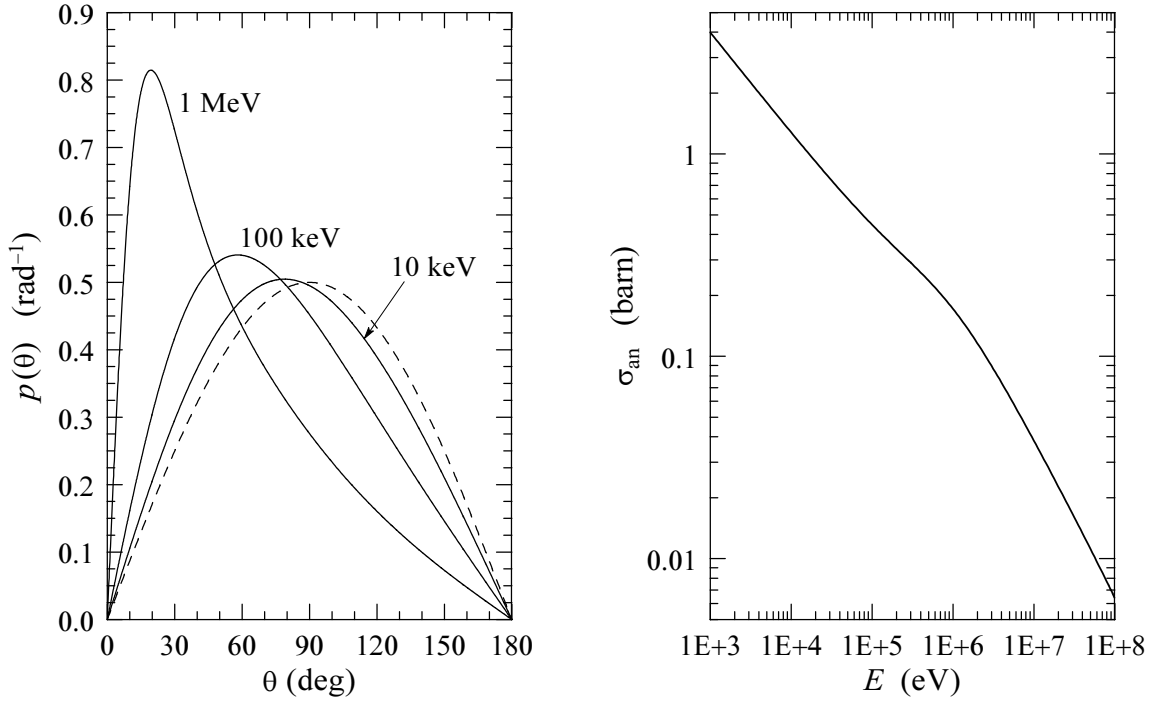


Figure 3.17: Left: angular distributions of photons produced by annihilation in flight of positrons with the indicated kinetic energies. The dashed line represents the isotropic distribution. Right: Annihilation cross section per target electron as a function of the kinetic energy of the positron.

The cross section (per target electron) for two-photon annihilation is

$$\begin{aligned} \sigma_{\text{an}} &= \int_{\zeta_{\text{min}}}^{1/2} \frac{d\sigma_{\text{an}}}{d\zeta} d\zeta = \frac{\pi r_e^2}{(\gamma + 1)(\gamma^2 - 1)} \\ &\times \left\{ (\gamma^2 + 4\gamma + 1) \ln \left[\gamma + (\gamma^2 - 1)^{1/2} \right] - (3 + \gamma) (\gamma^2 - 1)^{1/2} \right\}. \end{aligned} \quad (3.165)$$

The annihilation mean free path is given by

$$\lambda_{\text{an}}^{-1} = \mathcal{N}Z\sigma_{\text{an}}, \quad (3.166)$$

where $\mathcal{N}Z$ is the density of electrons in the medium. The annihilation cross section is displayed in fig. 3.17. The cross section decreases with the kinetic energy and, therefore, high-energy positrons can travel path lengths of the order of the CSDA range before annihilating.

3.4.1 Generation of emitted photons

The PDF of ζ is given by (normalization is irrelevant here)

$$p_{\text{an}}(\zeta) = S(\zeta) + S(1 - \zeta), \quad \zeta_{\text{min}} \leq \zeta \leq 1/2. \quad (3.167)$$

To sample ζ , we may take advantage of the symmetry of this expression under the exchange of the two photons, which corresponds to exchanging ζ and $1 - \zeta$. We first consider the distribution

$$P(v) \equiv S(v), \quad \zeta_{\text{min}} \leq v \leq 1 - \zeta_{\text{min}} \quad (3.168)$$

and write it in the form

$$P(v) = \pi(v)g(v) \quad (3.169)$$

with

$$\pi(v) = \left[\ln \left(\frac{1 - \zeta_{\text{min}}}{\zeta_{\text{min}}} \right) \right]^{-1} \frac{1}{v} \quad (3.170)$$

and

$$g(v) = \left[-(\gamma + 1)^2 v + (\gamma^2 + 4\gamma + 1) - \frac{1}{v} \right]. \quad (3.171)$$

$\pi(v)$ is a proper PDF (i.e. it is definite positive and normalized to unity) and $g(v)$ is a monotonically decreasing function. Random values of v from the distribution $P(v)$ can be generated by using the following algorithm (rejection method):

- (i) Sample a value v from the distribution $\pi(v)$. This is easily done with the inverse transform method, which yields the following sampling equation

$$v = \zeta_{\text{min}} \left(\frac{1 - \zeta_{\text{min}}}{\zeta_{\text{min}}} \right)^{\xi}. \quad (3.172)$$

- (ii) Generate a new random number ξ .
- (iii) If $\xi g(\zeta_{\text{min}}) > g(v)$, go to step (i).
- (iv) Deliver v .

It is clear that the random value

$$\zeta = \min(v, 1 - v) \quad (3.173)$$

follows the distribution given by eq. (3.167) when v is sampled from the distribution $P(v)$. The efficiency of this sampling algorithm practically equals 100% for positrons with kinetic energy E less than 10 keV, decreases when E increases to reach a minimum value of $\sim 80\%$ at $E \sim 10$ MeV and increases monotonically for larger energies.

As the result of annihilation, two photons with energies $E_- = \zeta(E + 2m_e c^2)$ and $E_+ = (1 - \zeta)(E + 2m_e c^2)$ are emitted in the directions given by eqs. (3.160) and (3.161).

Chapter 4

Electron/positron transport mechanics

In principle, the scattering model and sampling techniques described in chapter 3 allows the detailed Monte Carlo simulation of electron and positron transport in matter. However, detailed simulation is feasible only when the mean number of interactions per track is small (a few hundred at most). This occurs for electrons with low initial kinetic energies or for thin geometries. The number of interactions experienced by an electron or positron before being effectively stopped increases with its initial energy and, therefore, detailed simulation becomes impractical at high energies.

PENELOPE implements a “mixed” simulation scheme (Berger, 1963; Reimer and Krefting, 1976; Andreo and Brahme, 1984), which combines the detailed simulation of hard events (i.e. events with polar angular deflection θ or energy loss W larger than previously selected cutoff values θ_c and W_c) with condensed simulation of soft events, in which $\theta < \theta_c$ or $W < W_c$. Owing to the fact that for high-energy electrons the DCSs for the various interaction processes decrease rapidly with the polar scattering angle and the energy loss, cutoff values can be selected such that the mean number of hard events per electron track is sufficiently small to permit their detailed simulation. In general, this is accomplished by using relatively small cutoff values, so that each soft interaction has only a slight effect on the simulated track. The global effect of the (usually many) soft interactions that take place between each pair of consecutive hard events can then be simulated accurately by using a multiple scattering approach. Hard events occur much less frequently than soft events, but they have severe effects on the track evolution (i.e. they cause large angular deflections and lateral displacements or considerable energy losses), which can only be properly reproduced by detailed simulation. The computer time needed to simulate each track diminishes rapidly when the cutoff values for the angular deflection and the energy loss are increased. Mixed simulation algorithms are usually very stable under variations of the adopted cutoff values, whenever these are kept below some reasonable limits. Mixed simulation is then preferable to condensed simulation because 1) spatial distributions are simulated more accurately, 2) tracks in the vicinity of interfaces are properly handled, and 3) possible dependence of the results on user-defined parameters is largely reduced.

4.1 Elastic scattering

Let us start by considering electrons (or positrons) with kinetic energy E moving in a hypothetical infinite homogeneous medium, with \mathcal{N} scattering centres per unit volume, in which they experience only pure elastic collisions (i.e. with no energy loss).

4.1.1 Multiple elastic scattering theory

Assume that an electron starts off from a certain position, which we select as the origin of our reference frame, moving in the direction of the z -axis. Let $f(s; \mathbf{r}, \hat{\mathbf{d}})$ denote the probability density of finding the electron at the position $\mathbf{r} = (x, y, z)$, moving in the direction given by the unit vector $\hat{\mathbf{d}}$ after having travelled a path length s . The diffusion equation for this problem is (Lewis, 1950)

$$\frac{\partial f}{\partial s} + \hat{\mathbf{d}} \cdot \nabla f = \mathcal{N} \int [f(s; \mathbf{r}, \hat{\mathbf{d}}') - f(s; \mathbf{r}, \hat{\mathbf{d}})] \frac{d\sigma_{\text{el}}(\theta)}{d\Omega} d\Omega, \quad (4.1)$$

where $\theta \equiv \arccos(\hat{\mathbf{d}} \cdot \hat{\mathbf{d}}')$ is the scattering angle corresponding to the angular deflection $\hat{\mathbf{d}}' \rightarrow \hat{\mathbf{d}}$. This equation has to be solved with the boundary condition $f(0; \mathbf{r}, \hat{\mathbf{d}}) = (1/\pi)\delta(\mathbf{r})\delta(1 - \cos\chi)$, where χ is the polar angle of the direction $\hat{\mathbf{d}}$. By expanding $f(s; \mathbf{r}, \hat{\mathbf{d}})$ in spherical harmonics, Lewis (1950) obtained exact expressions for the angular distribution and for the first moments of the spatial distribution after a given path length s . The probability density $F(s; \chi)$ of having a final direction in the solid angle element $d\Omega$ around a direction defined by the polar angle χ is given by

$$F(s; \chi) = \int f(s; \mathbf{r}, \hat{\mathbf{d}}) d\mathbf{r} = \sum_{\ell=0}^{\infty} \frac{2\ell+1}{4\pi} \exp(-s/\lambda_{\text{el},\ell}) P_{\ell}(\cos\chi), \quad (4.2)$$

where $P_{\ell}(\cos\chi)$ are Legendre polynomials and $\lambda_{\text{el},\ell} = 1/(\mathcal{N}\sigma_{\text{el},\ell})$ is the ℓ -th transport mean free path defined by eq. (3.14). The result given by eq. (4.2) coincides with the multiple scattering distribution obtained by Goudsmit and Saunderson (1940a, 1940b). Evidently, the distribution $F(s; \chi)$ is symmetric about the z -axis, i.e. independent of the azimuthal angle of the final direction.

From the orthogonality of the Legendre polynomials, it follows that

$$\langle P_{\ell}(\cos\chi) \rangle \equiv 2\pi \int_{-1}^1 P_{\ell}(\cos\chi) F(s; \chi) d(\cos\chi) = \exp(-s/\lambda_{\text{el},\ell}). \quad (4.3)$$

In particular, we have

$$\langle \cos\chi \rangle = \exp(-s/\lambda_{\text{el},1}) \quad (4.4)$$

and

$$\langle \cos^2\chi \rangle = \frac{1}{3} [1 + 2 \exp(-s/\lambda_{\text{el},2})]. \quad (4.5)$$

Lewis (1950) also derived analytical formulae for the first moments of the spatial distribution and the correlation function of z and $\cos \chi$. Neglecting energy losses, the results explicitly given in Lewis' paper simplify to

$$\langle z \rangle \equiv 2\pi \int z f(s; \mathbf{r}, \hat{\mathbf{d}}) d(\cos \chi) d\mathbf{r} = \lambda_{\text{el},1} [1 - \exp(-s/\lambda_{\text{el},1})], \quad (4.6)$$

$$\begin{aligned} \langle x^2 + y^2 \rangle &\equiv 2\pi \int (x^2 + y^2) f(s; \mathbf{r}, \hat{\mathbf{d}}) d(\cos \chi) d\mathbf{r} \\ &= \frac{4}{3} \int_0^s dt \exp(-t/\lambda_{\text{el},1}) \int_0^t [1 - \exp(-u/\lambda_{\text{el},2})] \exp(u/\lambda_{\text{el},1}) du, \end{aligned} \quad (4.7)$$

$$\begin{aligned} \langle z \cos \chi \rangle &\equiv 2\pi \int z \cos \chi f(s; \mathbf{r}, \hat{\mathbf{d}}) d(\cos \chi) d\mathbf{r} \\ &= \exp(-s/\lambda_{\text{el},1}) \int_0^s [1 + 2 \exp(-t/\lambda_{\text{el},2})] \exp(t/\lambda_{\text{el},1}) dt. \end{aligned} \quad (4.8)$$

It is worth observing that the quantities (4.4)–(4.8) are completely determined by the values of the transport mean free paths $\lambda_{\text{el},1}$ and $\lambda_{\text{el},2}$; they are independent of the elastic mean free path λ_{el} .

4.1.2 Mixed simulation of elastic scattering

At high energies, where detailed simulation becomes impractical, $\lambda_{\text{el},1} \gg \lambda_{\text{el}}$ (see fig. 3.3) so that the average angular deflection in each collision is small. In other words, the great majority of elastic collisions of fast electrons are soft collisions with very small deflections. We shall consider mixed simulation procedures (see Fernández-Varea et al., 1993b; Baró et al., 1994b) in which hard collisions, with scattering angle θ larger than a certain value θ_c , are individually simulated and soft collisions (with $\theta < \theta_c$) are described by means of a multiple scattering approach.

In practice, the mixed algorithm will be defined by specifying the mean free path $\lambda_{\text{el}}^{(\text{h})}$ between hard elastic events, defined by [see eqs. (3.10) and (3.12)]

$$\frac{1}{\lambda_{\text{el}}^{(\text{h})}} = \mathcal{N} 2\pi \int_{\theta_c}^{\pi} \frac{d\sigma_{\text{el}}(\theta)}{d\Omega} \sin \theta d\theta. \quad (4.9)$$

This equation determines the cutoff angle θ_c as a function of $\lambda_{\text{el}}^{(\text{h})}$. A convenient recipe to set the mean free path $\lambda_{\text{el}}^{(\text{h})}$ is

$$\lambda_{\text{el}}^{(\text{h})}(E) = \max \{ \lambda_{\text{el}}(E), C_1 \lambda_{\text{el},1}(E) \}, \quad (4.10)$$

where C_1 is a pre-selected small constant (say, less than ~ 0.1). For increasing energies, λ_{el} attains a constant value and $\lambda_{\text{el},1}$ increases steadily (see fig. 3.3) so that the formula (4.10) gives a mean free path for hard collisions that increases with energy, i.e. hard collisions are less frequent when the scattering effect is weaker. The recipe (4.10) also ensures that $\lambda_{\text{el}}^{(\text{h})}$ will reduce to the actual mean free path λ_{el} for low energies. In this case,

soft collisions cease to occur ($\theta_c = 0$) and mixed simulation becomes purely detailed. It is worth noticing that, when mixed simulation is effective (i.e. when $\lambda_{\text{el}}^{(\text{h})} > \lambda_{\text{el}}$), the mean angular deflection in a path length $\lambda_{\text{el}}^{(\text{h})}$ is [see eq. (4.4)]

$$1 - \langle \cos \chi \rangle = 1 - \exp(-\lambda_{\text{el}}^{(\text{h})}/\lambda_{\text{el},1}) \simeq C_1. \quad (4.11)$$

Hence, when using the prescription (4.10), the average angular deflection due to all elastic collisions occurring along a path length $\lambda_{\text{el}}^{(\text{h})}$ equals C_1 .

The PDF of the step length s between two successive hard collisions is

$$p(s) = \frac{1}{\lambda_{\text{el}}^{(\text{h})}} \exp(-s/\lambda_{\text{el}}^{(\text{h})}), \quad (4.12)$$

and random values of s can be generated by means of the sampling formula, eq. (1.36)

$$s = -\lambda_{\text{el}}^{(\text{h})} \ln \xi. \quad (4.13)$$

The (unnormalized) PDF of the polar deflection θ in single hard collisions is

$$p^{(\text{h})}(\theta) = \frac{d\sigma_{\text{el}}(\theta)}{d\Omega} \sin \theta \Theta(\theta - \theta_c), \quad (4.14)$$

where $\Theta(x)$ stands for the step function.

The inverse transport mean free paths $\lambda_{\text{el},\ell}^{-1}$, see eq. (3.14), for the actual scattering process can be split into contributions from soft and hard collisions, i.e.

$$\frac{1}{\lambda_{\text{el},\ell}} = \frac{1}{\lambda_{\text{el},\ell}^{(\text{s})}} + \frac{1}{\lambda_{\text{el},\ell}^{(\text{h})}}, \quad (4.15)$$

where

$$\frac{1}{\lambda_{\text{el},\ell}^{(\text{s})}} = \mathcal{N} 2\pi \int_0^{\theta_c} [1 - P_\ell(\cos \theta)] \frac{d\sigma_{\text{el}}(\theta)}{d\Omega} \sin \theta d\theta \quad (4.16a)$$

and

$$\frac{1}{\lambda_{\text{el},\ell}^{(\text{h})}} = \mathcal{N} 2\pi \int_{\theta_c}^{\pi} [1 - P_\ell(\cos \theta)] \frac{d\sigma_{\text{el}}(\theta)}{d\Omega} \sin \theta d\theta. \quad (4.16b)$$

Let us assume that an electron starts off from the origin of coordinates moving in the direction of the z -axis and undergoes the first hard collision after travelling a path length s . The exact angular distribution produced by the soft collisions along this step is

$$F^{(\text{s})}(s; \chi) = \sum_{\ell=0}^{\infty} \frac{2\ell+1}{4\pi} \exp(-s/\lambda_{\text{el},\ell}^{(\text{s})}) P_\ell(\cos \chi). \quad (4.17)$$

The exact average longitudinal and transverse displacements at the end of the step are given by [see eqs. (4.6) and (4.7)]

$$\langle z \rangle^{(\text{s})} = \lambda_{\text{el},1}^{(\text{s})} [1 - \exp(-s/\lambda_{\text{el},1}^{(\text{s})})] = s \left[1 - \frac{1}{2} \left(\frac{s}{\lambda_{\text{el},1}^{(\text{s})}} \right) + \frac{1}{6} \left(\frac{s}{\lambda_{\text{el},1}^{(\text{s})}} \right)^2 - \dots \right], \quad (4.18)$$

$$\langle x^2 + y^2 \rangle^{(s)} = \frac{2}{9} \frac{s^3}{\lambda_{\text{el},2}^{(s)}} \left[1 - \frac{1}{4} \left(1 + \frac{\lambda_{\text{el},1}^{(s)}}{\lambda_{\text{el},2}^{(s)}} \right) \left(\frac{s}{\lambda_{\text{el},1}^{(s)}} \right) + \dots \right], \quad (4.19)$$

where $\lambda_{\text{el},1}^{(s)}$, the first transport mean free path for soft collisions, is larger than $\lambda_{\text{el},1}$. As the mean free path between hard collisions is normally much less than $\lambda_{\text{el},1}^{(s)}$ (depending on the value of C_1), the value $s/\lambda_{\text{el},1}^{(s)}$ is, on average, much less than unity (note that $\langle s \rangle = \lambda_{\text{el}}^{(h)}$). Therefore, the global effect of the soft collisions in the step, i.e. the change in direction of movement *and* the lateral displacement, is very small (part of the deflection is caused by the hard interaction at the end of the step).

In PENELOPE, the angular deflection and the lateral displacement due to the multiple soft collisions in a step of length s are simulated by means of the random hinge method¹ (Fernández-Varea et al., 1993b). The associated algorithm can be formulated as follows (see fig. 4.1),

- (i) The electron first moves a random distance τ , which is sampled uniformly in the interval $(0, s)$, in the initial direction.
- (ii) Then a single artificial soft scattering event (a hinge) takes place, in which the electron changes its direction of movement according to the multiple scattering distribution $F^{(s)}(s; \chi)$.
- (iii) Finally, the electron moves a distance $s - \tau$ in the new direction.

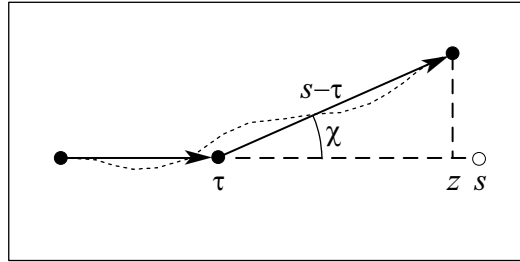


Figure 4.1: Simulation of the global effect of soft collisions between two consecutive hard collisions by the random hinge method.

Obviously, this algorithm leads to the exact angular distribution at the end of the step. The average longitudinal displacement at the end of the simulated step is

$$\langle z \rangle_{\text{sim}}^{(s)} = \frac{s}{2} + \frac{s}{2} \langle \cos \chi \rangle^{(s)} = s \left[1 - \frac{1}{2} \left(\frac{s}{\lambda_{\text{el},1}^{(s)}} \right) + \frac{1}{4} \left(\frac{s}{\lambda_{\text{el},1}^{(s)}} \right)^2 - \dots \right], \quad (4.20)$$

which agrees closely with the exact result given by eq. (4.18). Moreover, the average simulated transverse displacement is

$$\langle x^2 + y^2 \rangle_{\text{sim}}^{(s)} = \langle (s - \tau)^2 \sin^2 \chi \rangle_{\text{sim}}^{(s)} = \frac{1}{3} s^2 (1 - \langle \cos^2 \chi \rangle^{(s)})$$

¹The name was coined by Ron Kensek.

$$= \frac{2}{9} \frac{s^3}{\lambda_{\text{el},2}^{(s)}} \left[1 - \frac{1}{2} \frac{\lambda_{\text{el},1}^{(s)}}{\lambda_{\text{el},2}^{(s)}} \left(\frac{s}{\lambda_{\text{el},1}^{(s)}} \right) + \dots \right], \quad (4.21)$$

which does not differ much from the exact value given by eq. (4.19). From these facts, we may conclude that the random hinge method provides a faithful description of the transport when the step length s is much shorter than the first transport mean free path $\lambda_{\text{el},1}$, so that the global angular deflection and lateral displacement are small. Surprisingly, it does work well also in condensed (class I) simulations, where this requirement is not met. In spite of its simplicity, the random hinge method competes in accuracy and speed with other, much more sophisticated transport algorithms (see Bielajew and Salvat, 2001, and references therein). It seems that the randomness of the hinge position τ leads to correlations between the angular deflection and the displacement that are close to the actual correlations.

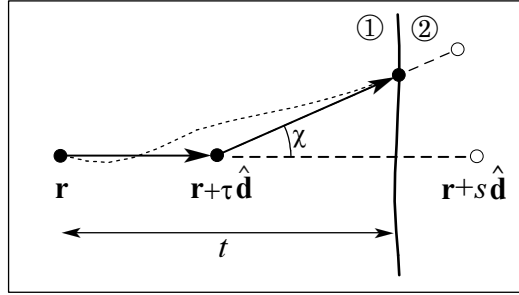


Figure 4.2: Simulation of a track near the crossing of an interface.

The random hinge algorithm can be readily adapted to simulate multiple elastic scattering processes in limited material structures, which may consist of several regions of different compositions separated by well-defined surfaces (interfaces). In these geometries, when the track crosses an interface, we simply stop it at the crossing point, and resume the simulation in the new material. In spite of its simplicity, this recipe gives a fairly accurate description of interface crossing. To see this, consider that a hard collision has occurred at the position \mathbf{r} in region “1” and assume that the following hard collision occurs in region “2”. The step length s between these two hard collisions is larger than the distance t from \mathbf{r} to the interface (see fig. 4.2). If the artificial soft elastic collision occurs in region “1”, the angular deflection in this collision is sampled from the distribution $F^{(s)}(s; \chi)$. Otherwise, the electron reaches the interface without changing its direction of movement. Assuming $s \ll \lambda_{\text{el},1}^{(s)}$, the mean angular deflection due to soft collisions is

$$1 - \langle \cos \chi \rangle^{(s)} = 1 - \exp(-s/\lambda_{\text{el},1}^{(s)}) \simeq \frac{s}{\lambda_{\text{el},1}^{(s)}}. \quad (4.22)$$

Moreover, when this assumption is valid, lateral displacements due to soft collisions are small and can be neglected to a first approximation. As the probability for the soft collision to occur within region “1” equals t/s , the average angular deflection of the

simulated electron track when it reaches the interface is

$$1 - \langle \cos \chi \rangle = \frac{t}{s} \left(1 - \langle \cos \chi \rangle^{(s)} \right) \simeq \frac{t}{\lambda_{\text{el},1}^{(s)}}, \quad (4.23)$$

which practically coincides with the exact mean deviation after the path length t within region “1”, as required. Thus, by sampling the position of the soft collision uniformly in the segment $(0, s)$ we make sure that the electron reaches the interface with the correct average direction of movement.

Angular deflections in soft scattering events

In the random hinge method, the global effect of the soft collisions experienced by the particle along a path segment of length s between two consecutive hard events is simulated as a single artificial soft scattering event. The angular deflection follows the multiple scattering distribution $F^{(s)}(s; \chi)$. Unfortunately, the exact Legendre expansion, eq. (4.17), is not appropriate for Monte Carlo simulation, since this expansion converges very slowly (because the associated single scattering DCS is not continuous) and the sum varies rapidly with the path length s .

Whenever the cutoff angle θ_c is small, the distribution $F^{(s)}(s; \chi)$ may be calculated by using the small angle approximation (see e.g. Lewis, 1950). Notice that θ_c can be made as small as desired by selecting a small enough value of C_1 , see eqs. (4.9) and (4.10). Introducing the limiting form of the Legendre polynomials

$$P_\ell(\cos \theta) \simeq 1 - \frac{1}{4} \ell(\ell + 1) \theta^2 \quad (4.24)$$

into eq. (4.16a) we get

$$\frac{1}{\lambda_{\text{el},\ell}^{(s)}} = \mathcal{N} 2\pi \frac{\ell(\ell + 1)}{4} \int_0^{\theta_c} \theta^2 \frac{d\sigma_{\text{el}}(\theta)}{d\Omega} \sin \theta d\theta = \frac{\ell(\ell + 1)}{2} \frac{1}{\lambda_{\text{el},1}^{(s)}}, \quad (4.25)$$

i.e. the transport mean free paths $\lambda_{\text{el},\ell}^{(s)}$ are completely determined by the single value $\lambda_{\text{el},1}^{(s)}$. The angular distribution $F^{(s)}$ then simplifies to

$$F^{(s)}(s; \chi) = \sum_{\ell=0}^{\infty} \frac{2\ell + 1}{4\pi} \exp \left[-\frac{\ell(\ell + 1)}{2} \frac{s}{\lambda_{\text{el},1}^{(s)}} \right] P_\ell(\cos \chi). \quad (4.26)$$

This expression can be evaluated by using the Molière (1948) approximation for the Legendre polynomials, we obtain (see Fernández-Varea et al., 1993b)

$$F^{(s)}(s; \chi) = \frac{1}{2\pi} \left(\frac{\chi}{\sin \chi} \right)^{1/2} \frac{\lambda_{\text{el},1}^{(s)}}{s} \exp \left[\frac{s}{8\lambda_{\text{el},1}^{(s)}} - \frac{\lambda_{\text{el},1}^{(s)}}{2s} \chi^2 \right], \quad (4.27)$$

which does not differ significantly from the Gaussian distribution with variance $s/\lambda_{\text{el},1}^{(s)}$. This result is accurate whenever $s \ll \lambda_{\text{el},1}^{(s)}$ and $\theta_c \ll 1$. It offers a possible method

of generating the angular deflection in artificial soft events. When the result given by eq. (4.27) is applicable, the single parameter $\lambda_{\text{el},1}^{(s)}$ completely determines the multiple scattering distribution due to soft collisions, i.e. other details of the DCS for scattering angles less than θ_c are irrelevant. However, in actual Monte Carlo simulations, the small-angle approximation is seldom applicable.

In most practical cases the number of hard collisions per electron track can be made relatively large by simply using a small value of the parameter C_1 [see eq. (4.10)]. When the number of steps is large enough, say larger than ~ 10 , it is not necessary to use the exact distribution $F^{(s)}(s; \chi)$ to sample the angular deflection in artificial soft collisions. Instead, we may use a simpler distribution, $F_a(s; \chi)$, with the same mean and variance, without appreciably distorting the simulation results. This is so because the details of the adopted distribution are washed out after a sufficiently large number of steps and will not be seen in the simulated distributions. Notice that, within the small angle approximation, it is necessary to keep only the proper value of the first moment to get the correct final distributions. However, if the cutoff angle θ_c is not small enough, the angular distribution $F^{(s)}(s; \chi)$ may become sensitive to higher-order moments of the soft single scattering distribution. Thus, by also keeping the proper value of the variance, the range of validity of the simulation algorithm is extended, i.e. we can speed up the simulation by using larger values of C_1 (or of $\lambda_{\text{el}}^{(h)}$) and still obtain the correct distributions.

We now return to the notation of section 3.1, and use the variable $\mu \equiv (1 - \cos \chi)/2$ to describe angular deflections in soft scattering events. The exact first and second moments of the multiple scattering distribution $F^{(s)}(s; \mu)$ are

$$\langle \mu \rangle^{(s)} \equiv \int_0^1 \mu F_a(s; \mu) d\mu = \frac{1}{2} [1 - \exp(-s/\lambda_{\text{el},1}^{(s)})] \quad (4.28)$$

and

$$\langle \mu^2 \rangle^{(s)} \equiv \int_0^1 \mu^2 F_a(s; \mu) d\mu = \langle \mu \rangle^{(s)} - \frac{1}{6} [1 - \exp(-s/\lambda_{\text{el},2}^{(s)})]. \quad (4.29)$$

The angular deflection in soft scattering events will be generated from a distribution $F_a(s; \mu)$, which is required to satisfy eqs. (4.28) and (4.29), but is otherwise arbitrary. PENELOPE uses the following,

$$F_a(s; \mu) = aU_{0,b}(\mu) + (1 - a)U_{b,1}(\mu), \quad (4.30)$$

where $U_{u,v}(x)$ denotes the normalized uniform distribution in the interval (u, v) ,

$$U_{u,v}(x) = \begin{cases} 1/(v - u) & \text{if } u \leq x \leq v, \\ 0 & \text{otherwise.} \end{cases} \quad (4.31)$$

The parameters a and b , obtained from the conditions (4.28) and (4.29), are

$$b = \frac{2\langle \mu \rangle^{(s)} - 3\langle \mu^2 \rangle^{(s)}}{1 - 2\langle \mu \rangle^{(s)}}, \quad a = 1 - 2\langle \mu \rangle^{(s)} + b. \quad (4.32)$$

The simple distribution (4.30) is flexible enough to reproduce the combinations of first and second moments encountered in the simulations [notice that $\langle \mu \rangle^{(s)}$, eq. (4.28), is always less than $1/2$] and allows fast random sampling of μ .

4.1.3 Simulating with the MW model

PENELOPE simulates elastic scattering by using the MW model (see section 3.1), which allows the formulation of the mixed simulation algorithm in closed analytical form.

The mean free path $\lambda_{\text{el}}^{(h)}$ between hard elastic events and the cutoff deflection $\mu_c = (1 - \cos \theta_c)/2$ are related through [see eqs. (3.18) and (4.9)]

$$\frac{1}{\lambda_{\text{el}}^{(h)}} = \frac{1}{\lambda_{\text{el}}} \int_{\mu_c}^1 p_{\text{MW}}(\mu) d\mu. \quad (4.33)$$

This equation can be easily inverted to give

$$\mu_c = \mathcal{P}_{\text{MW}}^{-1}(\xi_c), \quad (4.34)$$

where

$$\xi_c \equiv 1 - \frac{\lambda_{\text{el}}}{\lambda_{\text{el}}^{(h)}} \quad (4.35)$$

and $\mathcal{P}_{\text{MW}}^{-1}$ is the inverse of the single scattering cumulative distribution function given by eqs. (3.31) and (3.36).

In the following, we assume that the MW distribution is that of case I, eq. (3.24); the formulae for case II can be derived in a similar way. The random sampling of the angular deflection μ in hard collisions is performed by the inverse transform method (section 1.2.2); random values of μ are obtained from the sampling equation

$$\int_{\mu_c}^{\mu} p_{\text{MW}}(\mu') d\mu' = \xi \int_{\mu_c}^1 p_{\text{MW}}(\mu') d\mu'. \quad (4.36)$$

With the MW distribution, eq. (3.24), this equation can be solved analytically to give

$$\mu = \mathcal{P}_{\text{MW}}^{-1} \left(1 - \frac{\lambda_{\text{el}}}{\lambda_{\text{el}}^{(h)}} (1 - \xi) \right). \quad (4.37)$$

To determine the angular distribution of soft events $F_a(s; \mu)$, eq. (4.30), we need the first and second transport mean free paths for soft collisions, which are given by

$$\left(\lambda_{\text{el},1}^{(s)} \right)^{-1} = \frac{2}{\lambda_{\text{el}}} T_1(\mu_c) \quad \text{and} \quad \left(\lambda_{\text{el},2}^{(s)} \right)^{-1} = \frac{6}{\lambda_{\text{el}}} [T_1(\mu_c) - T_2(\mu_c)] \quad (4.38)$$

with

$$T_1(\mu_c) = \int_0^{\mu_c} \mu p_{\text{MW}}(\mu) d\mu \quad \text{and} \quad T_2(\mu_c) = \int_0^{\mu_c} \mu^2 p_{\text{MW}}(\mu) d\mu. \quad (4.39)$$

These latter quantities can be computed analytically as

$$T_1(\mu_c) = \begin{cases} (1-B)I_1(\mu_c) & \text{if } 0 \leq \xi_c < \xi_0 \\ (1-B)I_1(\mu_0) + (\xi_c - \xi_0)\mu_0 & \text{if } \xi_0 \leq \xi_c < \xi_0 + B \\ (1-B)I_1(\mu_c) + B\mu_0 & \text{if } \xi_0 + B \leq \xi_c \leq 1 \end{cases} \quad (4.40)$$

and

$$T_2(\mu_c) = \begin{cases} (1-B)I_2(\mu_c) & \text{if } 0 \leq \xi_c < \xi_0 \\ (1-B)I_2(\mu_0) + (\xi_c - \xi_0)\mu_0^2 & \text{if } \xi_0 \leq \xi_c < \xi_0 + B \\ (1-B)I_2(\mu_c) + B\mu_0^2 & \text{if } \xi_0 + B \leq \xi_c \leq 1 \end{cases} \quad (4.41)$$

with

$$I_1(\mu) \equiv A \left[(1+A) \ln \left(\frac{A+\mu}{A} \right) - \frac{(1+A)\mu}{A+\mu} \right] \quad (4.42)$$

and

$$I_2(\mu) \equiv A \left[\frac{(1+A)\mu^2}{A+\mu} - 2I_1(\mu) \right]. \quad (4.43)$$

The quantities ξ_0 and ξ_c are defined by eqs. (3.34) and (4.35), respectively.

4.2 Soft energy losses

The high-energy codes currently available implement different approximate methods to simulate inelastic collisions. Thus, ETRAN and ITS3 make use of the multiple scattering theories of Landau (1944) and Blunck and Leisegang (1950) to obtain the energy loss distribution due to inelastic collisions after a given path length; the production of secondary electrons is simulated by means of the Møller (1932) and Bhabha (1936) DCSs, which neglect binding effects. This approach accounts for the whole energy straggling, within the accuracy of the multiple scattering theory, but disregards the correlation between delta ray emission and energy loss in each track segment. As a consequence, energetic delta rays can be generated in a track segment where the energy lost by the primary particle is smaller than the energy of the emitted delta rays. EGS4 uses a mixed procedure to simulate collision energy losses: hard inelastic collisions are simulated from the Møller and Bhabha DCSs, thus neglecting binding effects, and soft inelastic collisions are described by means of the continuous slowing down approximation (CSDA), i.e. energy straggling due to soft inelastic collisions is ignored. As regards bremsstrahlung emission, EGS4 implements a mixed procedure in which hard radiative events are simulated in detail and use is made of the CSDA to simulate the effect of soft photon emission; ETRAN uses strictly detailed simulation.

To make the arguments more precise, we introduce the cutoff values W_{cc} and W_{cr} , and consider inelastic collisions with energy loss $W < W_{cc}$ and emission of bremsstrahlung photons with $W < W_{cr}$ as soft stopping interactions. The use of the CSDA to describe

soft interactions is well justified when the energy straggling due to these interactions is negligible, as happens when the cutoff energies W_{cc} and W_{cr} are both small, so that the fraction of the stopping power due to soft interactions is also small. To improve the description of energy straggling one should reduce the cutoff energies, but this enlarges the number of hard inelastic and radiative events to be simulated along each track and hence the simulation time. Our purpose is to go beyond the CSDA by introducing energy straggling in the description of soft stopping interactions. It is clear that, by proceeding in this way, we will be able to use larger values of the cutoff energies W_{cc} and W_{cr} , and hence speed up the simulation, without distorting the energy distributions.

In previous versions of PENELOPE, soft energy losses were simulated by using the mixed simulation algorithm described by Baró et al. (1995). The quantities that define the algorithm are the mean free paths $\lambda_{in}^{(h)}$ and $\lambda_{br}^{(h)}$ between hard collisions and hard radiative events, the stopping power S_s and the energy straggling parameter Ω_s^2 associated with soft interactions. These quantities are given by

$$\lambda_{in}^{(h)}(E) = \left(\mathcal{N} \int_{W_{cc}}^E \frac{d\sigma_{in}}{dW} dW \right)^{-1}, \quad (4.44)$$

$$\lambda_{br}^{(h)}(E) = \left(\mathcal{N} \int_{W_{cr}}^E \frac{d\sigma_{br}}{dW} dW \right)^{-1}, \quad (4.45)$$

$$S_s(E) = \mathcal{N} \int_0^{W_{cc}} W \frac{d\sigma_{in}}{dW} dW + \mathcal{N} \int_0^{W_{cr}} W \frac{d\sigma_{br}}{dW} dW \quad (4.46)$$

and

$$\Omega_s^2(E) = \mathcal{N} \int_0^{W_{cc}} W^2 \frac{d\sigma_{in}}{dW} dW + \mathcal{N} \int_0^{W_{cr}} W^2 \frac{d\sigma_{br}}{dW} dW. \quad (4.47)$$

To prevent $\lambda_{br}^{(h)}(E)$ from vanishing (infrared divergence), in PENELOPE the radiative cutoff energy W_{cr} is required to be larger than or equal to 10 eV.

Let us consider that a particle, electron or positron, travels a step of length s between two consecutive hard events of any kind (i.e. hard elastic or inelastic collisions, hard bremsstrahlung emissions, and annihilation in the case of positrons). Along this step, the particle is assumed to interact only through soft inelastic collisions and soft bremsstrahlung emission. We consider that the average energy loss in this path length, $S_s(E)s$, is much less than the initial energy E so that the DCSs can be assumed to stay essentially constant along the step. Let $G(s; \omega)$ denote the PDF of the energy loss ω along the path length s ; this distribution satisfies the transport equation (Landau, 1944)

$$\frac{\partial G(s; \omega)}{\partial s} = \mathcal{N} \int_0^\infty [G(s; \omega - W) - G(s; \omega)] \sigma_s(E; W) dW \quad (4.48)$$

with the initial value $G(0; \omega) = \delta(\omega)$. Here, $\sigma_s(E; W)$ stands for the DCS for soft stopping interactions, i.e.

$$\sigma_s(E; W) \equiv \frac{d\sigma_s}{dW} = \frac{d\sigma_{in}}{dW} \Theta(W_{cc} - W) + \frac{d\sigma_{br}}{dW} \Theta(W_{cr} - W), \quad (4.49)$$

where $\Theta(x)$ is the step function. A closed formal solution of the integral equation (4.48) may be obtained by considering its Fourier, or Laplace, transform with respect to ω (see e.g. Landau, 1944, Blunck and Leisegang, 1950). For our purposes it is only necessary to know the first moments of the energy loss distribution after the path length s ,

$$\langle \omega^n \rangle \equiv \int_0^\infty \omega^n G(s; \omega) d\omega. \quad (4.50)$$

From eq. (4.48) it follows that

$$\begin{aligned} \frac{d}{ds} \langle \omega^n \rangle &= \mathcal{N} \int_0^\infty d\omega \int_0^\infty dW \omega^n [G(s; \omega - W) - G(s; \omega)] \sigma_s(E; W) \\ &= \mathcal{N} \left(\int_0^\infty d\omega' \int_0^\infty dW (\omega' + W)^n G(s; \omega') \sigma_s(E; W) - \langle \omega^n \rangle \int_0^\infty \sigma_s(E; W) dW \right) \\ &= \sum_{k=1}^n \frac{n!}{k!(n-k)!} \langle \omega^{n-k} \rangle \mathcal{N} \int_0^\infty W^k \sigma_s(E; W) dW, \end{aligned} \quad (4.51)$$

where use has been made of the fact that $\sigma_s(E; W)$ vanishes when $W < 0$. In particular, we have

$$\frac{d}{ds} \langle \omega \rangle = \mathcal{N} \int_0^\infty W \sigma_s(E; W) dW = S_s, \quad (4.52)$$

$$\begin{aligned} \frac{d}{ds} \langle \omega^2 \rangle &= 2 \langle \omega \rangle \mathcal{N} \int_0^\infty W \sigma_s(E; W) dW + \mathcal{N} \int_0^\infty W^2 \sigma_s(E; W) dW \\ &= 2 \langle \omega \rangle S_s + \Omega_s^2 \end{aligned} \quad (4.53)$$

and, hence,

$$\langle \omega \rangle = S_s s, \quad (4.54)$$

$$\langle \omega^2 \rangle = (S_s s)^2 + \Omega_s^2 s. \quad (4.55)$$

The variance of the energy loss distribution is

$$\text{var}(\omega) = \langle \omega^2 \rangle - \langle \omega \rangle^2 = \Omega_s^2 s, \quad (4.56)$$

i.e. the energy straggling parameter Ω_s^2 equals the variance increase per unit path length.

The key point in our argument is that soft interactions involve only comparatively small energy losses. If the number of soft interactions along the path length s is statistically sufficient, it follows from the central limit theorem that the energy loss distribution is Gaussian with mean $S_s s$ and variance $\Omega_s^2 s$, i.e.

$$G(s; \omega) \simeq \frac{1}{(2\pi\Omega_s^2(E)s)^{1/2}} \exp \left[-\frac{(\omega - S_s(E)s)^2}{2\Omega_s^2(E)s} \right]. \quad (4.57)$$

This result is accurate only if 1) the average energy loss $S_s(E)s$ is much smaller than E (so that the DCS $d\sigma_s/dW$ is nearly constant along the step) and 2) its standard

deviation $[\Omega_s^2(E)s]^{1/2}$ is much smaller than its mean $S_s(E)s$ (otherwise there would be a finite probability of negative energy losses), i.e.

$$[\Omega_s^2(E)s]^{1/2} \ll S_s(E)s \ll E. \quad (4.58)$$

Requirement 1) implies that the cutoff energies W_{cc} and W_{cr} for delta ray production and photon emission have to be relatively small. The second requirement holds for path lengths larger than $s_{crit} = \Omega_s^2/S_s^2$.

Now, we address ourselves to the problem of simulating the energy losses due to soft stopping interactions between two consecutive hard events. The distribution (4.57) gives the desired result when conditions (4.58) are satisfied. In fact, the use of a Gaussian distribution to simulate the effect of soft stopping interactions was previously proposed by Andreo and Brahme (1984). Unfortunately, the step lengths found in our simulations are frequently too short for conditions (4.58) to hold (i.e. s is usually less than s_{crit}). To get over this problem, we replace the actual energy loss distribution $G(s; \omega)$ by a simpler “equivalent” distribution $G_a(s; \omega)$ with the same mean and variance, given by eqs. (4.54) and (4.56). Other details of the adopted distribution have no effect on the simulation results, provided that the number of steps along each track is statistically sufficient (say, larger than ~ 20). PENELOPE generates ω from the following distributions

- Case I. If $\langle \omega \rangle^2 > 9 \text{var}(\omega)$, we use a truncated Gaussian distribution,

$$G_{a,I}(s; \omega) = \begin{cases} \exp \left[-\frac{(\omega - \langle \omega \rangle)^2}{2(1.015387\sigma)^2} \right] & \text{if } |\omega - \langle \omega \rangle| < 3\sigma. \\ 0 & \text{otherwise.} \end{cases} \quad (4.59)$$

where $\sigma = [\text{var}(\omega)]^{1/2}$ is the standard deviation and the numerical factor 1.015387 corrects for the effect of the truncation. Notice that the shape of this distribution is very similar to that of the “true” energy-loss distribution, eq. (4.57). Random sampling from (4.59) is performed by means of the Box-Müller method, eq. (1.54), rejecting the generated ω ’s that are outside the interval $\langle \omega \rangle \pm 3\sigma$.

- Case II. When $3 \text{var}(\omega) < \langle \omega \rangle^2 < 9 \text{var}(\omega)$, the energy loss is sampled from the uniform distribution

$$G_{a,II}(s; \omega) = U_{\omega_1, \omega_2}(\omega) \quad (4.60)$$

with

$$\omega_1 = \langle \omega \rangle - \sqrt{3}\sigma, \quad \omega_2 = \langle \omega \rangle + \sqrt{3}\sigma. \quad (4.61)$$

- Case III. Finally, when $\langle \omega \rangle^2 < 3 \text{var}(\omega)$, the adopted distribution is an admixture of a delta and a uniform distribution,

$$G_{a,III}(s; \omega) = a\delta(\omega) + (1 - a)U_{0, \omega_0}(\omega) \quad (4.62)$$

with

$$a = \frac{3\text{var}(\omega) - \langle \omega \rangle^2}{3\text{var}(\omega) + 3\langle \omega \rangle^2} \quad \text{and} \quad \omega_0 = \frac{3\text{var}(\omega) + 3\langle \omega \rangle^2}{2\langle \omega \rangle}. \quad (4.63)$$

It can be easily verified that these distributions have the required mean and variance. It is also worth noticing that they yield ω values that are less than

$$\omega_{\max} = \begin{cases} \langle \omega \rangle + 3\sigma & \text{in case I,} \\ \omega_2 & \text{in case II,} \\ \omega_0 & \text{in case III.} \end{cases} \quad (4.64)$$

ω_{\max} is normally much less than the kinetic energy E of the transported particle. Energy losses larger than E might be generated only when the step length s has a value of the order of the Bethe range, but this never happens in practical simulation (see below). It is worth noticing that, after a moderately large number of steps, this simple simulation scheme effectively yields an energy loss distribution that has the correct first and second moments and is similar in shape to the “true” distribution. Further improvements of the distribution of soft energy losses would mean considering higher order moments of the single scattering inelastic DCS given by eq. (4.49).

In spatial-dose calculations, the energy loss ω due to soft stopping interactions can be considered to be locally deposited at a random position uniformly distributed along the step. This procedure yields dose distributions identical to those obtained by assuming that the energy loss is deposited at a constant rate along the step, but is computationally simpler. According to this, PENELOPE simulates the combined effect of all soft elastic collisions and soft stopping interactions that occur between a pair of successive hard events, separated a distance s , as a single event (a hinge) in which the particle changes its direction of movement according to the distribution $F_a(s; \mu)$, eqs. (4.30)-(4.32), and loses energy ω that is generated from the distribution $G_a(s; \omega)$, eqs. (4.59)-(4.63). The position of the hinge is sampled uniformly along the step, as in the case of purely elastic scattering (section 4.1.2). When the step crosses an interface (see fig. 4.2), the artificial event is simulated only when its position lies in the initial material; otherwise the track is stopped at the interface and restarted in the new material. It can be easily verified that the particle reaches the interface not only with the correct average direction of movement, but also with the correct average energy, $E - S_s t$.

4.2.1 Energy dependence of the soft DCS

The simulation model for soft energy losses described above is based on the assumption that the associated energy-loss DCS does not vary with the energy of the transported particle. To account for the energy dependence of the DCS in a rigorous way, we have to start from the transport equation [cf. eq. (4.48)]

$$\begin{aligned} \frac{\partial G(s; \omega)}{\partial s} &= \mathcal{N} \int_0^\infty G(s; \omega - W) \sigma_s(E_0 - \omega + W; W) dW \\ &\quad - \mathcal{N} \int_0^\infty G(s; \omega) \sigma_s(E_0 - \omega; W) dW, \end{aligned} \quad (4.65)$$

where E_0 denotes the kinetic energy of the particle at the beginning of the step. We desire to obtain expressions for the first and second moments, $\langle \omega \rangle$ and $\langle \omega^2 \rangle$, of the multiple

scattering energy-loss distribution, which define the artificial distribution $G_a(s; \omega)$ as described above. Unfortunately, for a realistic DCS, these moments can only be obtained after arduous numerical calculations and we have to rely on simple approximations that can be easily implemented in the simulation code.

Let us consider that, at least for relatively small fractional energy losses, the DCS varies linearly with the kinetic energy of the particle,

$$\sigma_s(E_0 - \omega; W) \simeq \sigma_s(E_0; W) - \left[\frac{\partial \sigma_s(E; W)}{\partial E} \right]_{E=E_0} \omega. \quad (4.66)$$

We recall that we are considering only soft energy-loss interactions (inelastic collisions and bremsstrahlung emission) for which the cutoff energies, W_{cc} and W_{cr} , do not vary with E . Therefore, the upper limit of the integrals in the right hand side of eq. (4.65) is finite and independent of the energy of the particle. The stopping power $S_s(E_0 - \omega)$ can then be approximated as

$$S_s(E_0 - \omega) \equiv \mathcal{N} \int W \sigma_s(E_0 - \omega; W) dW \simeq S_s(E_0) - S'_s(E_0) \omega, \quad (4.67)$$

where the prime denotes the derivative with respect to E . Similarly, for the straggling parameter $\Omega_s^2(E)$ we have

$$\Omega_s^2(E_0 - \omega) \equiv \mathcal{N} \int W^2 \sigma_s(E_0 - \omega; W) dW \simeq \Omega_s^2(E_0) - \Omega_s^{2'}(E_0) \omega. \quad (4.68)$$

From eq. (4.65) it follows that the moments of the multiple scattering distribution,

$$\langle \omega^n \rangle = \int \omega^n G(s; \omega) d\omega,$$

satisfy the equations

$$\begin{aligned} \frac{d}{ds} \langle \omega^n \rangle &= \mathcal{N} \int d\omega \int dW [(\omega + W)^n G(s; \omega) \sigma_s(E_0 - \omega; W)] \\ &\quad - \mathcal{N} \int d\omega \int dW \omega^n G(s; \omega) \sigma_s(E_0 - \omega; W) \\ &= \mathcal{N} \sum_{k=1}^n \frac{n!}{k!(n-k)!} \int d\omega \int dW \omega^{n-k} W^k G(s; \omega) \sigma_s(E_0 - \omega; W). \end{aligned} \quad (4.69)$$

By inserting the approximation (4.66), we obtain

$$\frac{d}{ds} \langle \omega^n \rangle = \sum_{k=1}^n \frac{n!}{k!(n-k)!} \left(\langle \omega^{n-k} \rangle M_k - \langle \omega^{n-k+1} \rangle M'_k \right), \quad (4.70)$$

where

$$M_k \equiv \mathcal{N} \int W^k \sigma_s(E_0; W) dW \quad (4.71)$$

and

$$M'_k \equiv \mathcal{N} \int W^k \left[\frac{\partial \sigma_s(E; W)}{\partial E} \right]_{E=E_0} dW = \left[\frac{dM_k}{dE} \right]_{E=E_0}. \quad (4.72)$$

The equations (4.70) with the boundary conditions $\langle \omega^n \rangle_{s=0} = 0$ can now be solved sequentially to any order. For $n = 1$ we have

$$\frac{d}{ds} \langle \omega \rangle = S_s(E_0) - S'_s(E_0) \langle \omega \rangle, \quad (4.73)$$

which yields

$$\langle \omega \rangle = \frac{S_s(E_0)}{S'_s(E_0)} \left\{ 1 - \exp[-S'_s(E_0)s] \right\}. \quad (4.74)$$

The equation for $n = 2$ reads,

$$\frac{d}{ds} \langle \omega^2 \rangle = \Omega_s^2(E_0) + [2S_s(E_0) - \Omega_s^{2'}(E_0)] \langle \omega \rangle - 2S'_s(E_0) \langle \omega^2 \rangle, \quad (4.75)$$

and its solution is

$$\begin{aligned} \langle \omega^2 \rangle &= \Omega_s^2(E_0) \frac{1 - \exp[-2S'_s(E_0)s]}{2S'_s(E_0)} \\ &+ s [2S_s(E_0) - \Omega_s^{2'}(E_0)] S_s(E_0) \left[\frac{1 - \exp[-S'_s(E_0)s]}{2S'_s(E_0)} \right]^2. \end{aligned} \quad (4.76)$$

Hence,

$$\begin{aligned} \text{var}(\omega) &= \langle \omega^2 \rangle - \langle \omega \rangle^2 \\ &= \Omega_s^2(E_0) \frac{1 - \exp[-2S'_s(E_0)s]}{2S'_s(E_0)} - 2\Omega_s^{2'}(E_0) S_s(E_0) \left[\frac{1 - \exp[-S'_s(E_0)s]}{2S'_s(E_0)} \right]^2. \end{aligned} \quad (4.77)$$

Since these expressions are derived from the linear approximation, eq. (4.66), it is consistent to evaluate $\langle \omega \rangle$ and $\text{var}(\omega)$ from their Taylor expansions to second order,

$$\begin{aligned} \langle \omega \rangle &= S_s(E_0) s \left[1 - \frac{1}{2} S'_s(E_0) s + \mathcal{O}(s^2) \right] \\ &\simeq S_s(E_0) s \left\{ 1 - \frac{1}{2} \left[\frac{d \ln S_s(E)}{dE} \right]_{E=E_0} S_s(E_0) s \right\} \end{aligned} \quad (4.78)$$

and

$$\begin{aligned} \text{var}(\omega) &= \Omega_s^2(E_0) s - \left[\frac{1}{2} \Omega_s^{2'}(E_0) S_s(E_0) + \Omega_s^2(E_0) S'_s(E_0) \right] s^2 + \mathcal{O}(s^3) \\ &\simeq \Omega_s^2(0) s \left\{ 1 - \left[\frac{1}{2} \frac{d \ln \Omega_s^2(E)}{dE} + \frac{d \ln S_s(E)}{dE} \right]_{E=E_0} S_s(E_0) s \right\}, \end{aligned} \quad (4.79)$$

where the logarithmic derivatives have been introduced for numerical convenience. The factors in curly brackets account for the global effect of the energy dependence of the soft energy-loss DCS (within the linear approximation). To simulate soft energy losses, we sample ω from the artificial distribution $G_a(\omega; s)$, eqs. (4.59) to (4.63), with the “correct” first moment and variance, given by expressions (4.78) and (4.79). In PENELOPE, we use step lengths s such that the fractional energy loss along each step is relatively small (see below) and, consequently, the energy-dependence correction is also small (i.e. the correcting factors are close to unity).

4.3 Combined scattering and energy loss

Up to this point, soft scattering and energy loss have been regarded as essentially independent processes, while in reality they coexist. In this section, we consider their interplay and set the basis of an algorithm that simulates their combined effect.

Ours is a mixed algorithm, where hard interactions are described individually from the associated DCSs (see chapter 3). These interactions are 1) hard elastic collisions, “el”, 2) hard inelastic collisions, “in”, 3) hard bremsstrahlung photon emission, “br”, 4) ionization of inner shells, “si”, and, in the case of positrons, 5) positron annihilation, “an”. The mean free path between consecutive hard events, $\lambda_T^{(h)}$, is given by

$$\left[\lambda_T^{(h)}\right]^{-1} = \mathcal{N}\sigma_T^{(h)} = \mathcal{N}\left[\sigma_{\text{el}}^{(h)} + \sigma_{\text{in}}^{(h)} + \sigma_{\text{br}}^{(h)} + \sigma_{\text{si}} (+\sigma_{\text{an}})\right] \equiv \Sigma_h, \quad (4.80)$$

where $\sigma_T^{(h)}$ is the total atomic cross section for hard interactions. We recall that the inverse mean free path, Σ_h , gives the interaction probability per unit path length. In the absence of soft energy-loss events, the PDF of the step length s between two successive hard events (or from a given point in the track to the next hard event) is

$$p(s) = \Sigma_h \exp(-\Sigma_h s). \quad (4.81)$$

In each hard event, one and only one interaction (i=“el”, “in”, “br”, “si” or “an”) occurs with probability

$$p_i = \sigma_i^{(h)} / \sigma_T^{(h)}. \quad (4.82)$$

When soft energy-losses are considered, the PDF of the distance s travelled by the particle to the following hard interaction is not given by eq. (4.81), because the mean free path $\lambda_T^{(h)}$ varies with energy and may change appreciably along a single step. The simplest way to cope with this problem is to limit the length of the step to make sure that the *average* energy loss is much smaller than the kinetic energy E at the beginning of the step, and consider that $\lambda_T^{(h)}(E)$ remains essentially constant along the step. Then, the mean energy loss in a step is given by

$$\langle \Delta E \rangle = \lambda_T^{(h)} S(E), \quad (4.83)$$

where

$$S(E) = S_{\text{in}}(E) + S_{\text{br}}(E) \quad (4.84)$$

is the total stopping power. Since the mean free path between consecutive hard events of any kind is shorter than the mean free path between hard elastic events, the energy loss per step can be limited by re-defining the hard mean free path. If we wish to tolerate average fractional energy losses $\Delta E/E$ along a step of the order of C_2 (a small value, say, 0.05), we simply take

$$\lambda_{\text{el}}^{(\text{h})}(E) = \max \left\{ \lambda_{\text{el}}(E), \min \left[C_1 \lambda_{\text{el},1}(E), C_2 \frac{E}{S(E)} \right] \right\}. \quad (4.85)$$

This effectively limits the average energy loss per step at the expense of increasing the frequency of hard elastic events. The parameters C_1 and C_2 in eq. (4.85), to be selected by the user, determine the computer time needed to simulate each track. Ideally, they should not have any influence on the *accuracy* of the simulation results. This happens only when their values are sufficiently small (see below).

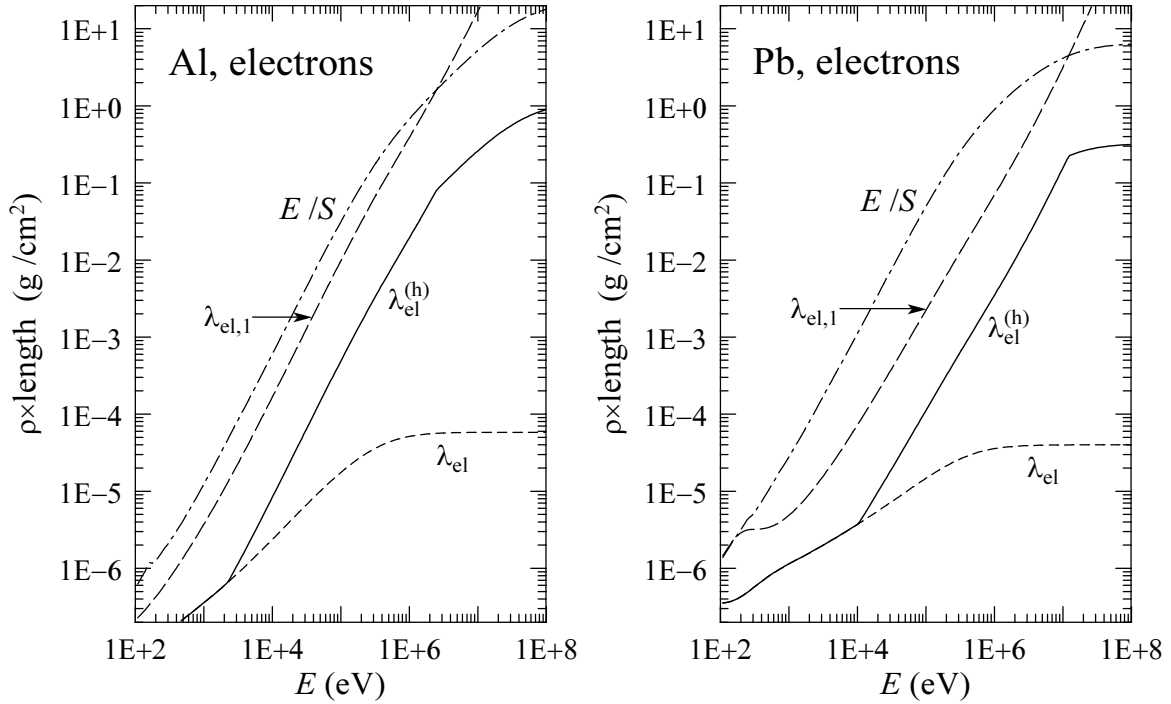


Figure 4.3: Elastic mean free path λ_{el} , first transport mean free path $\lambda_{\text{el},1}$ and $E/S(E)$ for electrons in aluminium and lead. The solid line represents the mean free path between hard elastic events $\lambda_{\text{el}}^{(\text{h})}$ obtained from eq. (4.85) with $C_1 = C_2 = 0.05$.

It should be noted that C_1 and C_2 act on different energy domains. This is illustrated in fig. 4.3, where the lengths λ_{el} , $\lambda_{\text{el},1}$ and E/S for electrons in aluminium and lead are represented as functions of the kinetic energy. The mean free path $\lambda_{\text{el}}^{(\text{h})}$ for hard elastic

events, determined from the prescription (4.85) with $C_1 = C_2 = 0.05$ is also plotted. For low energies, $\lambda_{\text{el}}^{(\text{h})} = \lambda_{\text{el}}$ and the simulation is purely detailed ($\mu_c = 0$). For intermediate energies, $\lambda_{\text{el}}^{(\text{h})} = C_1 \lambda_{\text{el},1}$, whereas $\lambda_{\text{el}}^{(\text{h})} = C_2 E/S(E)$ in the high-energy domain. From fig. 4.3 it is clear that increasing the value of C_2 does not have any effect on the simulation of electron tracks with initial energies that are less than ~ 10 MeV.

4.3.1 Variation of $\lambda_{\text{T}}^{(\text{h})}$ with energy

With the definition (4.85) of the hard elastic mean free path, we only set a limit on the *average* step length. However, since s is sampled from the exponential distribution, its realizations fluctuate amply about the average value. On the other hand, the soft energy loss ω along a step of given length s also fluctuates about the mean value $\langle \omega \rangle$ given by eq. (4.78). This means that the inverse mean free path $\Sigma_{\text{h}}(E)$ varies along the step in an essentially unpredictable way.

Let us consider for a moment that the CSDA is applicable (i.e. that the effect of soft energy straggling is negligible). In this case, there is a one-by-one correspondence between the kinetic energy E of the electron and the travelled path length s ,

$$s = \int_E^{E_0} \frac{dE'}{S_{\text{s}}(E')}, \quad (4.86)$$

where E_0 is the initial energy (at $s = 0$) and $S_{\text{s}}(E)$ is the soft stopping power, eq. (4.46) [we consider that no hard interactions occur along the step]. Equivalently,

$$\frac{ds}{dE} = -\frac{1}{S_{\text{s}}(E)}. \quad (4.87)$$

Thus, the inverse mean free path Σ_{h} can be formally considered as a function of the path length s . The probability $p(s) ds$ of having the first hard interaction when the particle has travelled a length in the interval $(s, s + ds)$ is determined by the equation [cf. eq. (1.87)]

$$p(s) = \Sigma_{\text{h}}(s) \int_s^{\infty} p(s') ds', \quad (4.88)$$

with the normalization condition,

$$\int_0^{\infty} p(s) ds = 1. \quad (4.89)$$

Instead of the path length s , it is convenient to consider the dimensionless variable

$$q \equiv \int_E^{E_0} \frac{\Sigma_{\text{h}}(E')}{S_{\text{s}}(E')} dE' = \int_0^s \Sigma_{\text{h}}(s') ds', \quad (4.90)$$

which varies with energy and

$$\frac{dq}{dE} = -\frac{\Sigma_{\text{h}}(E)}{S_{\text{s}}(E)}. \quad (4.91)$$

The PDF of q is

$$\pi(q) = p(s) \frac{ds}{dq} = p(s) \frac{ds}{dE} \frac{dE}{dq} = p(s) \frac{1}{\Sigma_h(s)}. \quad (4.92)$$

From eq. (4.88) it follows that $\pi(q)$ satisfies the equation

$$\pi(q) = \int_q^\infty \pi(q') dq'. \quad (4.93)$$

Therefore, q is distributed exponentially,

$$\pi(q) = \exp(-q). \quad (4.94)$$

The PDF of the step length s is obtained by inverting the transformation (4.90),

$$p(s) = \Sigma_h(s) \exp\left(-\int_0^s \Sigma_h(s') ds'\right). \quad (4.95)$$

It is not practical to sample s from this complicated PDF. It is much more convenient to sample q [as $-\ln \xi$, cf. eq. (1.36)] and then determine s from (4.90), which can be inverted numerically (for practical details, see Berger, 1998). Although this sampling method effectively accounts for the energy dependence of $\Sigma_s(E)$, it is applicable only to simulations in the CSDA.

A more versatile algorithm for sampling the position of hard events, still within the CSDA, is the following. We let the electron move in steps of maximum length s_{\max} , a value specified by the user. This determines the maximum energy loss along the step,

$$\omega_{\max} = \int_0^{s_{\max}} S_s(s) ds. \quad (4.96)$$

Let $\Sigma_{h,\max}$ denote an upper bound for the inverse mean free path of hard events in the swept energy interval, i.e.

$$\Sigma_{h,\max} > \max\{\Sigma_h(E), E \in (E_0 - \omega_{\max}, E_0)\} \quad (4.97)$$

We now assume that the electron may undergo fictitious events in which the energy and direction remain unaltered (delta interactions). The inverse mean free path of these interactions is defined as

$$\Sigma_\delta(E) = \Sigma_{h,\max} - \Sigma_h(E), \quad (4.98)$$

so that the inverse mean free path of the combined process (delta interactions + hard events) equals $\Sigma_{h,\max}$, a constant. Owing to the Markovian character of the processes, the introduction of delta interactions does not influence the path-length distribution between hard events. Therefore, the occurrence of hard events can be sampled by means of the following simple algorithm,

- (i) Sample a distance s from the exponential distribution with inverse mean free path $\Sigma_{h,\max}$, i.e. $s = (-\ln \xi)/\Sigma_{h,\max}$.

- (ii) If $s > s_{\max}$, move the electron a path length s_{\max} and determine the soft energy loss ω along this path length. Modify the electron energy², $E \leftarrow E - \omega$, and assume that a delta interaction occurs at the end of the step.
- (iii) If $s < s_{\max}$, move the electron a step of length s . Determine the energy loss ω and update the energy, $E \leftarrow E - \omega$. Sample a random number ξ .
 - (1) If $\xi \Sigma_{h,\max} < \Sigma_h(E)$, simulate a hard interaction
 - (2) Otherwise, assume that the particle undergoes a delta interaction.
- (iv) Return to (i).

It is clear that the path-length s to the first hard interaction generated with this algorithm follows the PDF (4.95). The interesting peculiarity of this algorithm is that it makes no explicit reference to the CSDA. Therefore, it can be adopted in mixed simulations with soft-energy-loss straggling, provided only that an upper bound exists for the energy ω lost along the path length s_{\max} .

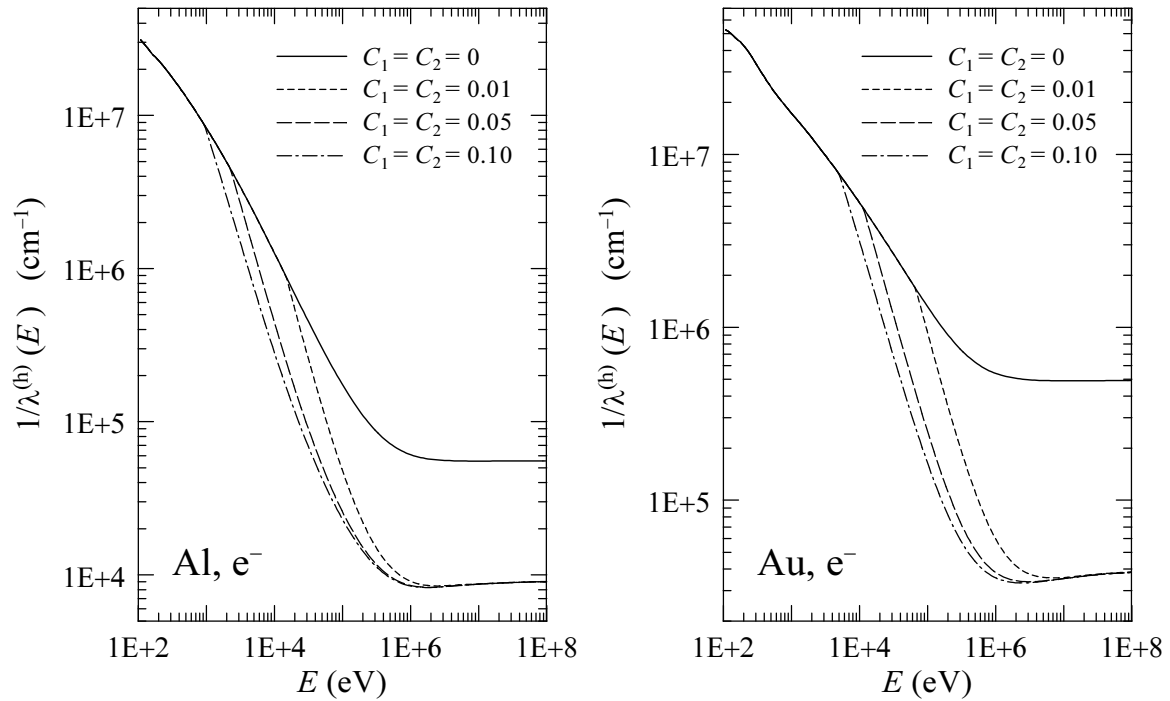


Figure 4.4: Inverse mean free path (interaction probability per unit path length) for hard interactions of electrons in aluminium and gold for the indicated values of the simulation parameters. The plotted curves were calculated with $W_{cc} = W_{cr} = 100$ eV.

Fortunately, the energy loss generated from the artificial distribution $G_a(\omega; s)$, eqs. (4.59)-(4.63), is always less than ω_{\max} , eq. (4.64). Indeed, in case I we use the truncated

²In the description of the algorithms we use the symbol \leftarrow in expressions such as “ $a \leftarrow b$ ” to indicate that the value b replaces the value of a .

Gaussian distribution (4.59) just to enforce this property. In our mixed simulation we shall select a maximum step length s_{\max} , which serves to set an upper bound for the energy that the transported electrons may lose along each step. Since the hard inverse mean free path $\Sigma_h(E)$ has a broad minimum (and no local maxima) in the whole energy interval of interest (see fig. 4.4), the maximum value of Σ_h within a certain energy interval (E_1, E_2) occurs at one of the end points. This makes the practical implementation of the above algorithm very easy.

4.3.2 Scattering by atomic electrons

Most of the existing high-energy simulation codes have difficulties in accounting for the angular deflections of the projectile due to inelastic collisions (see e.g. Jenkins et al., 1988). The inelastic cross section differential in the scattering angle can be calculated approximately in terms of the incoherent scattering function (see e.g. Mott and Massey, 1965). This was the approach followed by Fano (1954) in order to introduce electron scattering effects in the Molière (1948) multiple scattering theory. However, the DCS calculated in this way accounts for all excitations and, hence, it is not adequate for mixed simulations, where the part of electron scattering due to hard collisions is explicitly simulated. Moreover, the calculation of the DCS from the incoherent scattering function involves an average over excitation energies that cannot be performed exactly; instead an effective “minimum momentum transfer” is introduced, which must be estimated empirically. This may cause inconsistencies for low-energy projectiles. A more consistent approach (Baró et al., 1995) is obtained by simply computing the restricted angular DCS, for soft collisions with $W < W_{cc}$, from our inelastic scattering model (see section 3.2), as follows.

We recall that the recoil energy Q is given by (see appendix B)

$$Q(Q + 2m_e c^2) = c^2(p^2 + p'^2 - 2pp' \cos \theta), \quad (4.99)$$

where p and p' are the magnitudes of the momentum of the projectile before and after the collision,

$$(cp)^2 = E(E + 2m_e c^2) \quad \text{and} \quad (cp')^2 = (E - W)(E - W + 2m_e c^2). \quad (4.100)$$

In soft distant interactions, the angular deflection $\mu = (1 - \cos \theta)/2$ and the recoil energy Q are related through

$$Q(Q + 2m_e c^2) = 4cp cp_k \mu + (cp - cp_k)^2, \quad (4.101)$$

where p_k is the momentum of the projectile after the collision,

$$(cp_k)^2 = (E - W_k)(E - W_k + 2m_e c^2). \quad (4.102)$$

The cross section for soft distant interactions³, eq. (3.58), can then be expressed in terms

³Distant transverse interactions do not cause scattering.

of the variable μ as

$$\frac{d\sigma_{\text{dis},l}}{d\mu} = \frac{4\pi e^4}{m_e v^2} \sum_k f_k \frac{1}{W_k} \frac{m_e c^2}{4cp cp_k \mu + (cp - cp_k)^2} \frac{4cp cp_k}{2(Q + m_e c^2)}. \quad (4.103)$$

Considering that $Q \ll m_e c^2$ for the majority of soft distant collisions, we have

$$\frac{d\sigma_{\text{dis},l}}{d\mu} = \frac{2\pi e^4}{m_e v^2} \sum_k f_k \frac{1}{W_k} \frac{1}{R_k + \mu}, \quad 0 < \mu < \mu_k, \quad (4.104)$$

where

$$R_k = \frac{(cp - cp_k)^2}{4cp cp_k} \quad (4.105)$$

and

$$\mu_k = \mu(Q = W_k) = \frac{W_k(W_k + 2m_e c^2) - (cp - cp_k)^2}{4cp cp_k}. \quad (4.106)$$

On the other hand, the DCS per unit oscillator strength for soft ($W < W_{cc}$) close collisions with the i -th oscillator is given by [see eqs. (3.69) and (3.75)]

$$\frac{d\sigma_{\text{clo}}^{(\pm)}}{dW} = \frac{2\pi e^4}{m_e v^2} \sum_k f_k \frac{1}{W^2} F^{(\pm)}(E, W). \quad (4.107)$$

The angular deflection and the energy loss are related by (3.116), which implies that

$$W = \frac{E(E + 2m_e c^2)2(\mu - \mu^2)}{2E(\mu - \mu^2) + m_e c^2} \quad (4.108)$$

and

$$\frac{dW}{d\mu} = \frac{E(E + 2m_e c^2)m_e c^2 2(1 - 2\mu)}{[2E(\mu - \mu^2) + m_e c^2]^2}. \quad (4.109)$$

Therefore,

$$\frac{d\sigma_{\text{clo}}^{(\pm)}}{d\mu} = \frac{2\pi e^4}{m_e v^2} \sum_k f_k \frac{1}{W^2} F^{(\pm)}(E, W) \frac{dW}{d\mu}, \quad \mu_k < \mu < \mu_{cc}, \quad (4.110)$$

where

$$\mu_{cc} = \mu(Q = W_{cc}) = \frac{W_{cc}(W_{cc} + 2m_e c^2) - (cp - cp_{cc})^2}{4cp cp_{cc}} \quad (4.111)$$

with

$$(cp_{cc})^2 = (E - W_{cc})(E - W_{cc} + 2m_e c^2). \quad (4.112)$$

The angular DCS for soft inelastic interactions is then given by

$$\begin{aligned} \frac{d\sigma_s}{d\mu} &= \frac{d\sigma_{\text{dis},l}}{d\mu} + \frac{d\sigma_{\text{clo}}^{(\pm)}}{d\mu} \\ &= \frac{2\pi e^4}{m_e v^2} \sum_k f_k \left\{ \frac{1}{W_k} \frac{1}{R_k + \mu} + \frac{1}{W^2} F^{(\pm)}(E, W) \frac{dW}{d\mu} \right\}, \end{aligned} \quad (4.113)$$

where the summations extend over the oscillators with resonance energy less than W_{cc} and greater than W_{max} , and each term contributes only for the μ -intervals indicated above. The mean free path and the first and second transport mean free paths for soft inelastic scattering are

$$[\lambda_{in}^{(s)}]^{-1} = \mathcal{N} \int_0^{\mu_2} \frac{d\sigma_{in}^{(s)}}{d\mu} d\mu, \quad (4.114)$$

$$[\lambda_{in,1}^{(s)}]^{-1} = \mathcal{N} \int_0^{\mu_2} 2\mu \frac{d\sigma_{in}^{(s)}}{d\mu} d\mu \quad (4.115)$$

and

$$[\lambda_{in,2}^{(s)}]^{-1} = \mathcal{N} \int_0^{\mu_2} 6(\mu - \mu^2) \frac{d\sigma_{in}^{(s)}}{d\mu} d\mu. \quad (4.116)$$

In PENELOPE, soft electronic scattering is simulated together with soft elastic scattering, by means of the artificial distribution (4.30). The combined process is described by the transport mean free paths

$$[\lambda_{comb,1}^{(s)}]^{-1} = [\lambda_{el,1}^{(s)}]^{-1} + [\lambda_{in,1}^{(s)}]^{-1} \quad (4.117)$$

and

$$[\lambda_{comb,2}^{(s)}]^{-1} = [\lambda_{el,2}^{(s)}]^{-1} + [\lambda_{in,2}^{(s)}]^{-1}. \quad (4.118)$$

Thus, to account for soft electronic scattering we only have to replace the soft elastic transport mean free paths by those of the combined process.

4.3.3 Bielajew's alternate random hinge

Angular deflections due to soft interactions along a step of length s are generated from the artificial distribution (4.30) with first and second moments given by eqs. (4.28) and (4.29), which are determined by the transport mean free paths $\lambda_{comb,1}^{(s)}$ and $\lambda_{comb,2}^{(s)}$. To account (at least partially) for the energy dependence of these quantities we use a trick due to Alex Bielajew. The soft energy loss and angular deflection (which occur at the hinge) are considered as independent processes and are simulated in random order. That is, the soft angular deflection is evaluated for the energy at either the beginning or the end of the step, with equal probabilities. This is equivalent to assuming that the transport mean free paths $\lambda_{comb,1}^{(s)}(E)$ and $\lambda_{comb,2}^{(s)}(E)$ vary linearly with energy. The method is fairly accurate and computationally inexpensive provided only that the fractional energy loss along each step (which is of the order of C_2) is sufficiently small.

4.4 Generation of random tracks

Each simulated electron or positron history consists of a chronological succession of events. These can be either hard events, artificial soft events (hinges) or other relevant

stages of the particle history (such as its initial state, the crossing of an interface or the effective absorption after slowing down). The trajectory of the particle between a pair of successive events is straight and will be referred to as a “segment”. We keep the term “step” to designate the portion of a track between two hard events, which consists of two segments and a hinge (when mixed simulation is effective).

Simulation with PENELOPE is controlled by the constants C_1 and C_2 [see eq. (4.85)] and the cutoff energies W_{cc} and W_{cr} . Hereafter, these four quantities will be referred to as simulation parameters. The parameter C_1 , which determines the mean free path $\lambda_{el}^{(h)}$ between hard elastic events, should be small enough to ensure reliable simulation results. PENELOPE admits values of C_1 from 0 (detailed simulation) up to 0.2, which corresponds to a mean angular deflection $\langle\theta\rangle \sim 37$ deg after a steplength $\lambda_{el}^{(h)}$. The simulation parameter C_2 gives the maximum average fractional energy loss in a single step and it is effective only at high energies. From the discussion in section 4.3, it is clear that C_2 should also be small. PENELOPE allows values of C_2 between zero and 0.2. The cutoff energies W_{cc} and W_{cr} mainly influence the simulated energy distributions. The simulation speeds up by using larger cutoff energies, but if these are too large the simulated distributions may be somewhat distorted. In practice, simulated energy distributions are found to be quite insensitive to the adopted values of W_{cc} and W_{cr} when these are less than the bin width used to tally the energy distributions. Thus, the desired energy resolution determines the maximum allowed cutoff energies.

The combined effect of all soft elastic and stopping interactions in a step is simulated as a single artificial event or hinge, in which the particle changes its direction of movement and loses energy. When W_{cc} is less than the lowest oscillator resonance energy, the simulation of inelastic collisions becomes purely detailed, i.e. inelastic collisions do not contribute to the soft stopping power. On the other hand, the simulation of bremsstrahlung emission is only possible by means of a mixed scheme, because of the divergence of the DCS at $W = 0$ [see eq. (3.131)]. To test the accuracy of mixed algorithms, and also in studies of low-energy electron and positron transport (with, say, $E < 100$ keV), it may be convenient to perform strictly detailed simulations (see below). For this purpose, PENELOPE allows the user to switch off the emission of soft bremsstrahlung photons with energy less than 10 eV. This option is activated when the W_{cr} value selected by the user is negative, in which case the program sets $W_{cr} = 10$ eV, disregards soft bremsstrahlung events and simulates hard events (with $W > 10$ eV) in a detailed way. The generation of the angular deflection in artificial events is discontinued when the simulation of elastic and inelastic scattering becomes detailed (i.e. when $\lambda_{el}^{(h)} = \lambda_{el}$, $W_{cc} = 0$).

As indicated above, the length of the steps generated by PENELOPE is always less than s_{max} , an upper bound selected by the user. The simulation code limits the step length by placing delta interactions along the particle track. These are fictitious interactions that do not alter the state of the particle. Their only effect is to interrupt the sequence of simulation operations, which requires altering the values of inner control variables to permit resuming the simulation in a consistent way. The use of bounded step lengths is necessary to account for the energy dependence of the DCSs for soft interactions.

However, this is not the only reason for limiting the step length. Since energy losses and deflections at the hinges are sampled from artificial distributions, the number of hinges per primary track must be “statistically sufficient”, i.e. larger than ~ 10 , to smear off the unphysical details of the adopted artificial distributions. Therefore, when the particle is in a thin region, it is advisable to use a small value of s_{\max} to make sure that the number of hinges within the material is sufficient. In PENELOPE, the parameter s_{\max} can be varied freely during the course of the simulation of a single track. To ensure internal consistency, s_{\max} is required to be less than $3\lambda_T^{(h)}$. When the user-selected value is larger, the code sets $s_{\max} = 3\lambda_T^{(h)}$; in this case, about 5 per cent of the sampled steps have lengths that exceed s_{\max} and are terminated by a delta interaction. This slows down the simulation a little ($\sim 5\%$), but ensures that the energy dependence of $\lambda_T^{(h)}$ is correctly accounted for. Instead of the s_{\max} value set by the user, PENELOPE uses a random maximum step length [from a triangle distribution in the interval $(0, s_{\max})$] that averages to half the user’s value; this is used to eliminate an artifact in the depth-dose distribution from parallel electron/positron beams near the entrance interface. Incidentally, limiting the step length is also necessary to perform simulation of electron/positron transport in external static electromagnetic fields (see appendix C).

The state of the particle immediately after an event is defined by its position coordinates \mathbf{r} , energy E and direction cosines of its direction of movement $\hat{\mathbf{d}}$, as seen from the laboratory reference frame. It is assumed that particles are locally absorbed when their energy becomes smaller than a preselected value E_{abs} ; positrons are considered to annihilate after absorption. The practical generation of random electron and positron tracks in arbitrary material structures, which may consist of several homogeneous regions of different compositions separated by well-defined surfaces (interfaces), proceeds as follows:

- (i) Set the initial position \mathbf{r} , kinetic energy E and direction of movement $\hat{\mathbf{d}}$ of the primary particle.
- (ii) Determine the maximum allowed soft energy loss ω_{\max} along a step and set the value of inverse mean free path for hard events (see section 4.3). The results depend on the adopted s_{\max} , which can vary along the simulated track.
- (iii) Sample the distance s to be travelled to the following hard event (or delta interaction) as

$$s = -\ln \xi / \Sigma_{h,\max}. \quad (4.119)$$

If $s > s_{\max}$, truncate the step by setting $s = s_{\max}$.

- (iv) Generate the length $\tau = s\xi$ of the step to the next hinge. Let the particle advance this distance in the direction $\hat{\mathbf{d}}$: $\mathbf{r} \leftarrow \mathbf{r} + \tau\hat{\mathbf{d}}$.
- (v) If the track has crossed an interface:

Stop it at the crossing point (i.e. redefine \mathbf{r} as equal to the position of this point and set τ equal to the travelled distance).

Go to (ii) to continue the simulation in the new material, or go to (xi) if the new material is the outer vacuum.
- (vi) Simulate the energy loss and deflection at the hinge. This step consists of two actions:

a) Sample the polar angular deflection $\mu = (1 - \cos \theta)/2$ from the distribution $F_a(s; \mu)$, eq. (4.30), corresponding to the current energy E . Sample the azimuthal scattering angle as $\phi = 2\pi\xi$. Perform a rotation $R(\theta, \phi)$ of the vector $\hat{\mathbf{d}}$ according to the sampled polar and azimuthal angular deflections (as described in section 1.4.2) to obtain the new direction: $\hat{\mathbf{d}} \leftarrow R(\theta, \phi)\hat{\mathbf{d}}$.

b) Sample the energy loss ω due to soft stopping interactions along the step s from the distribution $G_a(s; \omega)$, eqs. (4.59)-(4.63), and reduce the kinetic energy: $E \leftarrow E - \omega$.

These two actions are performed in random order to account for the energy dependence of the soft transport mean free paths (see section 4.3.3).

Go to (xi) if $E < E_{\text{abs}}$.

(vii) Let the particle advance the distance $s - \tau$ in the direction $\hat{\mathbf{d}}$: $\mathbf{r} \leftarrow \mathbf{r} + (s - \tau)\hat{\mathbf{d}}$.

(viii) Do as in (v).

(ix) If in step (iii) the step length was truncated, i.e. $s = s_{\text{max}}$, simulate a delta interaction.

Go to (ii).

(x) Simulate the hard event:

Sample the kind of interaction according to the point probabilities,

$$p_{\text{el}} = \frac{\mathcal{N}\sigma_{\text{el}}^{(\text{h})}}{\Sigma_{\text{h,max}}}, \quad p_{\text{in}} = \frac{\mathcal{N}\sigma_{\text{in}}^{(\text{h})}}{\Sigma_{\text{h,max}}}, \quad p_{\text{br}} = \frac{\mathcal{N}\sigma_{\text{br}}^{(\text{h})}}{\Sigma_{\text{h,max}}}, \quad p_{\text{si}} = \frac{\mathcal{N}\sigma_{\text{si}}}{\Sigma_{\text{h,max}}},$$

$$p_{\delta} = \frac{\Sigma_{\delta}}{\Sigma_{\text{h,max}}}, \quad \text{and} \quad p_{\text{an}} = \frac{\mathcal{N}\sigma_{\text{an}}}{\Sigma_{\text{h,max}}} \quad \text{in the case of positrons.} \quad (4.120)$$

If the event is a delta interaction, return to (ii).

If the event is an inner-shell ionization, sample the active shell, simulate the relaxation cascade of the residual ion and return to (ii). Notice that in this case the state of the projectile remains unaltered.

Sample the polar scattering angle θ and the energy loss W from the corresponding DCS. Generate the azimuthal scattering angle as $\phi = 2\pi\xi$. Perform a rotation $R(\theta, \phi)$ of the vector $\hat{\mathbf{d}}$ to obtain the new direction: $\hat{\mathbf{d}} \leftarrow R(\theta, \phi)\hat{\mathbf{d}}$.

Reduce the kinetic energy of the particle: $E \leftarrow E - W$.

If, as a result of the interaction, a secondary particle is emitted in a direction $\hat{\mathbf{d}}_s$, with energy $E_s > E_{\text{abs}}$, store its initial state $(\mathbf{r}, E_s, \hat{\mathbf{d}}_s)$.

Go to (ii) if $E > E_{\text{abs}}$.

(xi) Simulate the tracks of the secondary electrons and photons produced by the primary particle (or by other secondaries previously followed) before starting a new primary track.

4.4.1 Stability of the simulation algorithm

The present simulation scheme for electrons/positrons is relatively stable under variations of the simulation parameters, due mostly to the effectiveness of the energy-loss corrections. This implies that the simulation parameters can be varied amply without

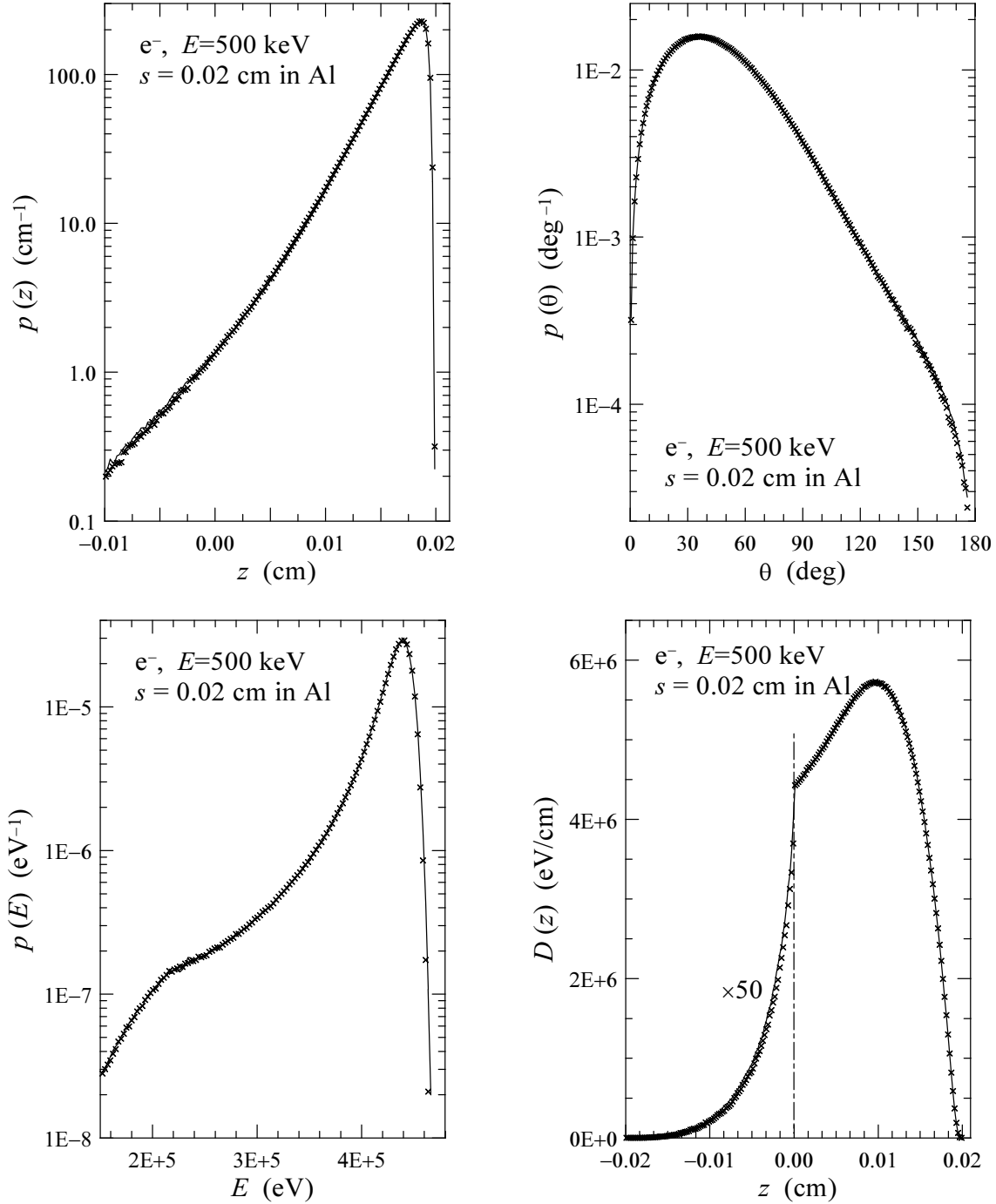


Figure 4.5: Results from the simulations of 500 keV electrons in aluminium described in the text. Crosses, detailed simulation; continuous curves, mixed simulation. $p(z)$ is the PDF of the z -coordinate of the final electron position, after travelling the prescribed $200 \mu\text{m}$. $p(\theta)$ and $p(E)$ are the PDFs of the direction of motion (specified by the polar angle θ) and the kinetic energy E of the electrons at the end of the simulated tracks. The function $D(z)$ represents the “depth-dose” function, i.e. the average energy deposited in the material per unit length along the z -direction (the residual energy at the end of the track is not included in the dose).

practically altering the accuracy of the results. For the important case of low-energy electrons/positrons (with energies of the order of 500 keV or less), the relevant parameters are E_{abs} , C_1 , W_{cc} and s_{max} , because C_2 is not effective (see fig. 4.3) and radiative emission is unimportant (hard bremsstrahlung events occur very seldom and, therefore, W_{cr} has no influence). The value of the parameter s_{max} is important to ensure the reliability of the results; a safe recipe is to set s_{max} equal to one tenth of the “expected track length” or less. Since the values of E_{abs} and W_{cc} are dictated by the characteristics of the considered experiment, it follows that the only “critical” parameter, with a direct influence on the speed of the simulation, is C_1 . As mentioned above, PENELOPE accepts values of C_1 ranging from 0 (detailed simulation of elastic scattering) to 0.2.

In practice, the value of C_1 does not influence the *accuracy* of the simulation results when the other parameters are given “safe” values. This is illustrated in fig. 4.5, which displays results from simulations of 500 keV electrons in aluminium (infinite medium). Electrons started off from the origin of coordinates moving in the direction of the z axis. During the generation of each electron track, we scored the energy deposited at different “depths” (z -coordinate) to get the “depth-dose” distribution. The simulation of a track was discontinued when the electron had travelled a path length s equal to 200 μm , and the PDFs of the final electron energy and position coordinates were tallied. Notice that no secondary radiation was followed and that the kinetic energy of the electrons at $s = 200 \mu\text{m}$ was not included in the dose distribution (i.e. the calculated “dose” does not represent the quantity that would be obtained from a measurement).

The results displayed in fig. 4.5 are from equivalent detailed and mixed simulations with $E_{\text{abs}} = 10 \text{ keV}$ and $s_{\text{max}} = 40 \mu\text{m}$. The detailed simulation was performed by setting $C_1 = C_2 = 0$, $W_{\text{cc}} = 0$ and $W_{\text{cr}} = -100$. Notice that when the user enters a negative value of the cutoff energy loss for radiative events, PENELOPE sets $W_{\text{cr}} = 10 \text{ eV}$, disregards the emission of soft bremsstrahlung photons with $W < 10 \text{ eV}$ (which represents a negligible fraction of the stopping power) and simulates hard bremsstrahlung events as usually, i.e. in a detailed way. The mixed simulation results shown in fig. 4.5 were generated with $C_1 = C_2 = 0.2$, $W_{\text{cc}} = 1 \text{ keV}$ and $W_{\text{cr}} = -100$ (i.e. radiative events were described as in the detailed simulation).

In the detailed simulation, about 15 million electron tracks were generated by running a modified version of the code `PENSLAB.F` (see section 6.2.1) on a 666 MHz PII computer for 85 hours, which corresponds to a simulation speed of 49 tracks/s. The average numbers of elastic, inelastic and bremsstrahlung interactions that had to be simulated to produce each detailed track were 1297, 1222 and 0.03, respectively. On the same computer, the mixed simulation generated 25 million tracks in about 2 hours, which represents a simulation speed of 3421 tracks/s, 71 times faster than that of detailed simulation. The reason is that, on average, there were only 2.4 hard elastic collisions, 6.2 hard inelastic collisions, 0.03 hard bremsstrahlung events and 6.8 delta interactions along each track. From fig. 4.5 we conclude that, in this case, the mixed algorithm is not only stable under variations of the parameter C_1 over the accepted range (0,0.2), but also provides results that are essentially equivalent to those from the detailed simulation. It is worth recalling that detailed simulation is nominally exact, the results are affected

only by statistical uncertainties.

In general, our mixed simulation algorithm yields very accurate results (i.e. agreeing with those from detailed simulation) for electron and positron transport in infinite media, but not necessarily for limited geometries. The existence of interfaces poses considerable problems to condensed (class I) simulation, for which a satisfactory solution/approximation is not yet known. The present mixed (class II) algorithm handles interface crossing in a more accurate, but still approximate way. The rule to ensure accuracy for transport in the vicinity of interfaces is to use a small enough value of s_{\max} .

Chapter 5

Constructive quadric geometry

Practical simulations of radiation transport in material systems involve two different kinds of operations, namely, physical (determination of the path length to the next interaction, random sampling of the different interactions) and geometrical (space displacements, interface crossings, ...). In the case of material systems with complex geometries, geometrical operations can take a large fraction of the simulation time. These operations are normally performed by dedicated subroutine packages, whose characteristics depend on the kind of algorithm used to simulate the interactions. The material system is assumed to consist of a number of homogeneous bodies limited by well-defined surfaces. The evolution of particles within each homogeneous body is dictated by the physical simulation routines, which operate as if particles were moving in an infinite medium with a given composition. Normally, the physical routines can handle a number of different media, whose interaction properties have been previously stored in memory. The job of the geometry routines is to steer the simulation of particle histories in the actual material system. They must determine the active medium, change it when the particle crosses an interface (i.e. a surface that separates two different media) and, for certain simulation algorithms, they must also keep control of the proximity of interfaces.

In this chapter we describe the FORTRAN subroutine package PENGEO, which is adequate for detailed simulation algorithms (i.e. algorithms where all single interactions in the history of a particle are simulated in chronological succession). With these algorithms, the description of interface crossings is very simple: when the particle reaches an interface, its track is stopped just after entering a new material body and restarted again with the new active medium. This method (stopping and restarting a track when it crosses an interface) is applicable even when we have the same medium on both sides of the surface. That is, detailed simulations with a single homogeneous body and with the same body split into two parts by an arbitrary surface yield the same results (apart from statistical uncertainties).

As we have seen, detailed simulation is feasible only for photon transport and low-energy electron transport. For high-energy electrons and positrons, most Monte Carlo codes [e.g. ETRAN (Berger and Seltzer, 1988), ITS3 (Halbleib et al., 1992), EGS4 (Nel-

son et al., 1985), EGSnrc (Kawrakow and Rogers, 2000), GEANT3 (Brun et al., 1986)] have recourse to condensed (class I) or mixed (class II) simulation, where the global effect of multiple interactions along a path segment of a given length is evaluated using available multiple scattering theories. To avoid large step lengths that could place the particle inside a different medium, these condensed procedures require the evaluation of the distance from the current position to the nearest interface, an operation with a high computational cost (see e.g. Bielajew, 1995). The mixed procedure implemented in PENELOPE is, at least computationally, analogous to detailed simulation (it gives a “jump-and-knock” description of particle tracks). In fact, the structure of PENELOPE’s tracking algorithm was designed to minimize the influence of the geometry on the transport physics. This algorithm operates independently of the proximity of interfaces and only requires knowledge of the material at the current position of the particle. As a consequence, the geometry package PENGEO is directly linkable to PENELOPE. However, since PENGEO does not evaluate the distance to the closest interface, it cannot be used with condensed simulation codes, such as those mentioned above.

Let us mention, in passing, that in simulations of high-energy photon transport complex geometries can be handled by means of relatively simple methods, which do not require control of interface crossings (see e.g. Snyder et al., 1969). Unfortunately, similar techniques are not applicable to electron and positron transport, mainly because these particles have much shorter track lengths and, hence, the transport process is strongly influenced by inhomogeneities of the medium. With the analogue simulation scheme adopted in PENELOPE, it is necessary to determine when a particle track crosses an interface, not only for electrons and positrons but also for photons.

PENGEO evolved from a subroutine package of the same name provided with the 1996.02.29 version of the PENELOPE code system. This package was aimed at describing simple structures with a small number of homogeneous bodies limited by quadric surfaces. Although it was robust and very flexible, its speed deteriorated rapidly when the number of surfaces increased. The need for developing a more efficient geometry package became evident when we started to use PENELOPE to simulate radiation transport in accelerator heads (the description of which requires of the order of 100 surfaces) or in studies of total body irradiation (the definition of a realistic anthropomorphic phantom may involve a few hundred surfaces).

With PENGEO we can describe any material system consisting of homogeneous bodies limited by quadric surfaces. To speed up the geometry operations, the bodies of the material system can be grouped into modules (connected volumes, limited by quadric surfaces, that contain one or several bodies); modules can in turn form part of larger modules, and so on. This hierarchic modular structure allows a reduction of the work of the geometry routines, which becomes more effective when the complexity of the system increases.

Except for trivial cases, the correctness of the geometry definition is difficult to check and, moreover, 3D structures with interpenetrating bodies are difficult to visualize. A pair of programs, named GVIEW2D and GVIEW3D, have been written to display

the geometry on the computer screen. These programs use specific computer graphics software and, therefore, they are not portable. The executable files included in the PENELOPE distribution package run on personal computers under Microsoft Windows; they are simple and effective tools for debugging the geometry definition file.

5.1 Rotations and translations

The definition of various parts of the material system (quadric surfaces in reduced form and modules) involves rotations and translations. To describe these transformations, we shall adopt the active point of view: the reference frame remains fixed and only the space points (vectors) are translated or rotated.

In what follows, and in the computer programs, all lengths are in cm. The position and direction of movement of a particle are referred to the laboratory coordinate system, a Cartesian reference frame which is defined by the position of its origin of coordinates and the unit vectors $\hat{\mathbf{x}} = (1, 0, 0)$, $\hat{\mathbf{y}} = (0, 1, 0)$ and $\hat{\mathbf{z}} = (0, 0, 1)$ along the directions of its axes.

A translation $\mathcal{T}(\mathbf{t})$, defined by the displacement vector $\mathbf{t} = (t_x, t_y, t_z)$, transforms the vector $\mathbf{r} = (x, y, z)$ into

$$\mathcal{T}(\mathbf{t})\mathbf{r} = \mathbf{r} + \mathbf{t} = (x + t_x, y + t_y, z + t_z). \quad (5.1)$$

Evidently, the inverse translation $\mathcal{T}^{-1}(\mathbf{t})$ corresponds to the displacement vector $-\mathbf{t}$, i.e. $\mathcal{T}^{-1}(\mathbf{t}) = \mathcal{T}(-\mathbf{t})$.

A rotation \mathcal{R} is defined through the Euler angles ω , θ and ϕ , which specify a sequence of rotations about the coordinate axes¹: first a rotation of angle ω about the z -axis, followed by a rotation of angle θ about the y -axis and, finally, a rotation of angle ϕ about the z -axis. A positive rotation about a given axis would carry a right-handed screw in the positive direction along that axis. Positive (negative) angles define positive (negative) rotations.

The rotation $\mathcal{R}(\omega, \theta, \phi)$ transforms the vector $\mathbf{r} = (x, y, z)$ into a vector

$$\mathbf{r}' = \mathcal{R}(\omega, \theta, \phi)\mathbf{r} = (x', y', z'), \quad (5.2)$$

whose coordinates are given by

$$\begin{pmatrix} x' \\ y' \\ z' \end{pmatrix} = R(\omega, \theta, \phi) \begin{pmatrix} x \\ y \\ z \end{pmatrix}, \quad (5.3)$$

¹This definition of the Euler angles is the one usually adopted in Quantum Mechanics (see e.g. Edmonds, 1960).

where

$$R(\omega, \theta, \phi) = \begin{pmatrix} R_{xx} & R_{xy} & R_{xz} \\ R_{yx} & R_{yy} & R_{yz} \\ R_{zx} & R_{zy} & R_{zz} \end{pmatrix} \quad (5.4)$$

is the rotation matrix. To obtain its explicit form, we recall that the matrices for rotations about the z - and y -axes are

$$R_z(\phi) = \begin{pmatrix} \cos \phi & -\sin \phi & 0 \\ \sin \phi & \cos \phi & 0 \\ 0 & 0 & 1 \end{pmatrix} \quad \text{and} \quad R_y(\theta) = \begin{pmatrix} \cos \theta & 0 & \sin \theta \\ 0 & 1 & 0 \\ -\sin \theta & 0 & \cos \theta \end{pmatrix}, \quad (5.5)$$

respectively. Hence,

$$\begin{aligned} R(\omega, \theta, \phi) &= R_z(\phi) R_y(\theta) R_z(\omega) \\ &= \begin{pmatrix} \cos \phi & -\sin \phi & 0 \\ \sin \phi & \cos \phi & 0 \\ 0 & 0 & 1 \end{pmatrix} \begin{pmatrix} \cos \theta & 0 & \sin \theta \\ 0 & 1 & 0 \\ -\sin \theta & 0 & \cos \theta \end{pmatrix} \begin{pmatrix} \cos \omega & -\sin \omega & 0 \\ \sin \omega & \cos \omega & 0 \\ 0 & 0 & 1 \end{pmatrix} \\ &= \begin{pmatrix} \cos \phi \cos \theta \cos \omega - \sin \phi \sin \omega & -\cos \phi \cos \theta \sin \omega - \sin \phi \cos \omega & \cos \phi \sin \theta \\ \sin \phi \cos \theta \cos \omega + \cos \phi \sin \omega & -\sin \phi \cos \theta \sin \omega + \cos \phi \cos \omega & \sin \phi \sin \theta \\ -\sin \theta \cos \omega & \sin \theta \sin \omega & \cos \theta \end{pmatrix}. \end{aligned} \quad (5.6)$$

The inverse of the rotation $\mathcal{R}(\omega, \theta, \phi)$ is $\mathcal{R}(-\phi, -\theta, -\omega)$ and its matrix is the transpose of $R(\omega, \theta, \phi)$, i.e.

$$R^{-1}(\omega, \theta, \phi) = R(-\phi, -\theta, -\omega) = R_z(-\omega) R_y(-\theta) R_z(-\phi) = R^T(\omega, \theta, \phi). \quad (5.7)$$

Let us now consider transformations $\mathcal{C} = \mathcal{T}(\mathbf{t}) \mathcal{R}(\omega, \theta, \phi)$ that are products of a rotation $\mathcal{R}(\omega, \theta, \phi)$ and a translation $\mathcal{T}(\mathbf{t})$. \mathcal{C} transforms a point \mathbf{r} into

$$\mathbf{r}' = \mathcal{C}(\mathbf{r}) = \mathcal{T}(\mathbf{t}) \mathcal{R}(\omega, \theta, \phi) \mathbf{r} \quad (5.8)$$

or, in matrix form,

$$\begin{pmatrix} x' \\ y' \\ z' \end{pmatrix} = R(\omega, \theta, \phi) \begin{pmatrix} x \\ y \\ z \end{pmatrix} + \begin{pmatrix} t_x \\ t_y \\ t_z \end{pmatrix}. \quad (5.9)$$

Notice that the order of the factors does matter; the product of the same factors in reverse order $\mathcal{D} = \mathcal{R}(\omega, \theta, \phi) \mathcal{T}(\mathbf{t})$ transforms \mathbf{r} into a point $\mathbf{r}' = \mathcal{D}(\mathbf{r})$ with coordinates

$$\begin{pmatrix} x' \\ y' \\ z' \end{pmatrix} = R(\omega, \theta, \phi) \begin{pmatrix} x + t_x \\ y + t_y \\ z + t_z \end{pmatrix}. \quad (5.10)$$

Given a function $F(\mathbf{r})$, the equation $F(\mathbf{r}) = 0$ defines a surface in implicit form. We can generate a new surface by applying a rotation $\mathcal{R}(\omega, \theta, \phi)$ followed by a translation $\mathcal{T}(\mathbf{t})$ (we shall always adopt this order). The implicit equation of the transformed surface is

$$G(\mathbf{r}) = F\left[\mathcal{R}^{-1}(\omega, \theta, \phi) \mathcal{T}^{-1}(\mathbf{t}) \mathbf{r}\right] = 0, \quad (5.11)$$

which simply expresses the fact that $G(\mathbf{r})$ equals the value of the original function at the point $\mathbf{r}' = \mathcal{R}^{-1}(\omega, \theta, \phi) \mathcal{T}^{-1}(\mathbf{t}) \mathbf{r}$ that transforms into \mathbf{r} .

5.2 Quadric surfaces

As already mentioned, the material system consists of a number of homogeneous bodies, defined by their composition (material) and limiting surfaces. For practical reasons, all limiting surfaces are assumed to be quadrics given by the implicit equation

$$\begin{aligned} F(x, y, z) = & A_{xx}x^2 + A_{xy}xy + A_{xz}xz + A_{yy}y^2 + A_{yz}yz + A_{zz}z^2 \\ & + A_x x + A_y y + A_z z + A_0 = 0, \end{aligned} \quad (5.12)$$

which includes planes, pairs of planes, spheres, cylinders, cones, ellipsoids, paraboloids, hyperboloids, etc. In practice, limiting surfaces are frequently known in “graphical” form and it may be very difficult to obtain the corresponding quadric parameters. Try with a simple example: calculate the parameters of a circular cylinder of radius R such that its symmetry axis goes through the origin and is parallel to the vector (1,1,1). To facilitate the definition of the geometry, each quadric surface can be specified either through its implicit equation or by means of its reduced form, which defines the “shape” of the surface (see fig. 5.1), and a few simple geometrical transformations.

A reduced quadric is defined by the expression

$$F_r(x, y, z) = I_1 x^2 + I_2 y^2 + I_3 z^2 + I_4 z + I_5 = 0, \quad (5.13)$$

where the coefficients (indices) I_1 to I_5 can only take the values -1 , 0 or 1 . Notice that reduced quadrics have central symmetry about the z -axis, i.e. $F_r(-x, -y, z) = F_r(x, y, z)$. The possible (real) reduced quadrics are given in table 5.1.

A general quadric is obtained from the corresponding reduced form by applying the following transformations (in the quoted order)².

- (i) An expansion along the directions of the axes, defined by the scaling factors **X-SCALE**= a , **Y-SCALE**= b and **Z-SCALE**= c . The equation of the scaled quadric is

$$F_s(x, y, z) = I_1 \left(\frac{x}{a}\right)^2 + I_2 \left(\frac{y}{b}\right)^2 + I_3 \left(\frac{z}{c}\right)^2 + I_4 \frac{z}{c} + I_5 = 0. \quad (5.14)$$

²Keywords used to denote the various parameters in the geometry definition file are written in typewriter font, e.g. **X-SCALE**). See section 5.4.

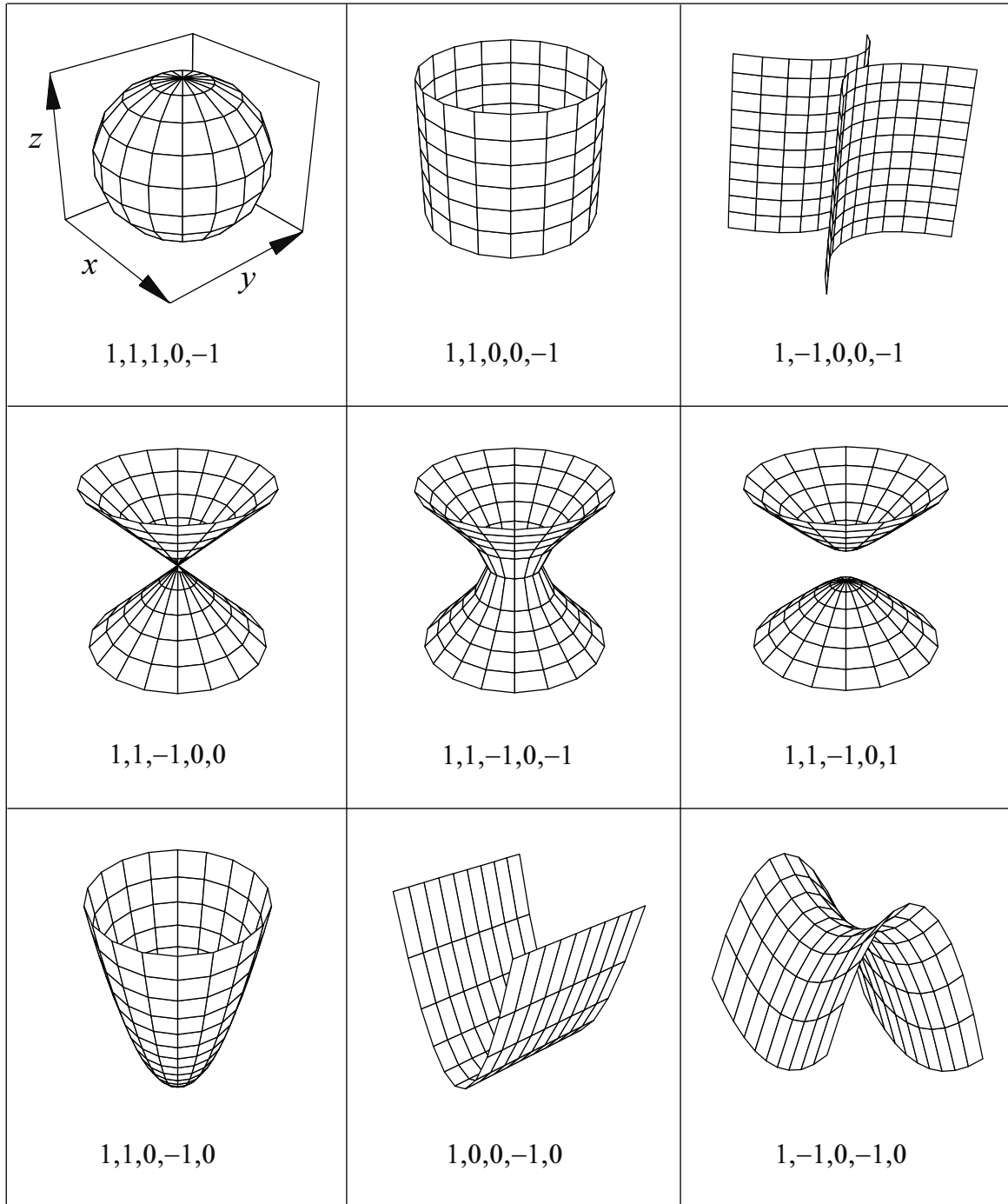


Figure 5.1: Non-planar reduced quadric surfaces and their indices [see eq. (5.13)]. In all cases, the perspective is the same as for the sphere.

Table 5.1: Reduced quadrics.

Reduced form	Indices					Quadric
$z - 1 = 0$	0	0	0	1	-1	plane
$z^2 - 1 = 0$	0	0	1	0	-1	pair of parallel planes
$x^2 + y^2 + z^2 - 1 = 0$	1	1	1	0	-1	sphere
$x^2 + y^2 - 1 = 0$	1	1	0	0	-1	cylinder
$x^2 - y^2 - 1 = 0$	1	-1	0	0	-1	hyperbolic cylinder
$x^2 + y^2 - z^2 = 0$	1	1	-1	0	0	cone
$x^2 + y^2 - z^2 - 1 = 0$	1	1	-1	0	-1	one sheet hyperboloid
$x^2 + y^2 - z^2 + 1 = 0$	1	1	-1	0	1	two sheet hyperboloid
$x^2 + y^2 - z = 0$	1	1	0	-1	0	paraboloid
$x^2 - z = 0$	1	0	0	-1	0	parabolic cylinder
$x^2 - y^2 - z = 0$	1	-1	0	-1	0	hyperbolic paraboloid
... and permutations of x, y and z that preserve the central symmetry with respect to the z -axis.						

For instance, this transforms the reduced sphere into an ellipsoid with semiaxes equal to the scaling factors.

- (ii) A rotation, $\mathcal{R}(\omega, \theta, \phi)$, defined through the Euler angles $\text{OMEGA} = \omega$, $\text{THETA} = \theta$ and $\text{PHI} = \phi$. Notice that the rotation $\mathcal{R}(\omega, \theta, \phi)$ transforms a plane perpendicular to the z -axis into a plane perpendicular to the direction with polar and azimuthal angles THETA and PHI , respectively. The first Euler angle, ω has no effect when the initial (scaled) quadric is symmetric about the z -axis.
- (iii) A translation, defined by the components of the displacement vector \mathbf{t} ($\text{X-SHIFT} = t_x$, $\text{Y-SHIFT} = t_y$, $\text{Z-SHIFT} = t_z$).

A quadric is completely specified by giving the set of indices (I_1, I_2, I_3, I_4, I_5), the scale factors (X-SCALE , Y-SCALE , Z-SCALE), the Euler angles (OMEGA , THETA , PHI) and the displacement vector (X-SHIFT , Y-SHIFT , Z-SHIFT). Any quadric surface can be expressed in this way. The implicit equation of the quadric is obtained as follows. We define the matrix

$$\mathcal{A} = \begin{pmatrix} A_{xx} & \frac{1}{2}A_{xy} & \frac{1}{2}A_{xz} \\ \frac{1}{2}A_{xy} & A_{yy} & \frac{1}{2}A_{yz} \\ \frac{1}{2}A_{xz} & \frac{1}{2}A_{yz} & A_{zz} \end{pmatrix} \quad (5.15)$$

and write the generic quadric equation (5.12) in matrix form

$$\mathbf{r}^T \mathcal{A} \mathbf{r} + \mathbf{A}^T \mathbf{r} + A_0 = 0, \quad (5.16)$$

where \mathbf{r} and $\mathbf{A} \equiv (A_x, A_y, A_z)$ are considered here as one-column matrices. Notice that the matrix \mathcal{A} is symmetric ($\mathcal{A}^T = \mathcal{A}$). Expressing the scaled quadric (5.14) in the form (5.16), the equation for the rotated and shifted quadric is [see eq. (5.11)]

$$(\mathbf{r} - \mathbf{t})^T R \mathcal{A} R^T (\mathbf{r} - \mathbf{t}) + (R\mathbf{A})^T (\mathbf{r} - \mathbf{t}) + A_0 = 0, \quad (5.17)$$

which can be written in the generic form (5.16)

$$\mathbf{r}^T \mathcal{A}' \mathbf{r} + \mathbf{A}'^T \mathbf{r} + A'_0 = 0 \quad (5.18)$$

with

$$\mathcal{A}' = R \mathcal{A} R^T, \quad \mathbf{A}' = R\mathbf{A} - 2\mathcal{A}'\mathbf{t}, \quad A'_0 = A_0 + \mathbf{t}^T (\mathcal{A}'\mathbf{t} - R\mathbf{A}). \quad (5.19)$$

From these relations, the parameters of the implicit equation (5.12) are easily obtained.

A quadric surface $F(x, y, z) = 0$ divides the space into two exclusive regions that are identified by the sign of $F(x, y, z)$, the surface side pointer. A point with coordinates (x_0, y_0, z_0) is said to be inside the surface if $F(x_0, y_0, z_0) \leq 0$ (side pointer = -1), and outside it if $F(x_0, y_0, z_0) > 0$ (side pointer = +1).

5.3 Constructive quadric geometry

A body is defined as a space volume limited by quadric surfaces and filled with a homogeneous material. To specify a body we have to define its limiting quadric surfaces $F(\mathbf{r}) = 0$, with corresponding side pointers (+1 or -1), and its composition (i.e. the integer label used by PENELOPE to identify the material). It is considered that bodies are defined in “ascending”, exclusive order so that previously defined bodies effectively delimit the new ones. This is convenient e.g. to describe bodies with inclusions. The work of the geometry routines is much easier when bodies are completely defined by their limiting surfaces, but this is not always possible or convenient for the user. The example in section 5.7 describes an arrow inside a sphere (fig. 5.2); the arrow is defined first so that it limits the volume filled by the material inside the sphere. It is impossible to define the hollow sphere (as a single body) by means of only its limiting quadric surfaces. It is clear that, by defining a conveniently large number of surfaces and bodies, we can describe any quadric geometry.

The subroutine package PENGEO contains a subroutine, named LOCATE, that “locates” a point \mathbf{r} , i.e. determines the body that contains it, if any. The obvious method is to compute the side pointers [i.e. the sign of $F(\mathbf{r})$] for *all* surfaces and, then, explore the bodies in ascending order looking for the first one that fits the given side pointers. This brute force procedure was used in older versions of PENGEO; it has the advantage of being robust (and easy to program) but becomes too slow for complex systems. A second subroutine, named STEP, “moves” the particle from a given position \mathbf{r}_0 within a body B a certain distance s in a given direction $\hat{\mathbf{d}}$. STEP also checks if the particle leaves the active medium and, when this occurs, stops the particle just after entering

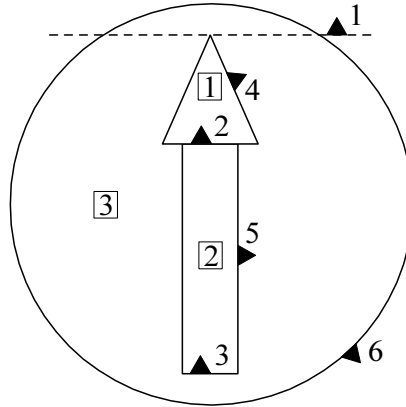


Figure 5.2: Example of simple quadric geometry; an arrow within a sphere (the corresponding definition file is given in section 5.7). The solid triangles indicate the outside of the surfaces (side pointer = +1). Numbers in squares indicate bodies.

the new material. To do this, we must determine the intersections of the track segment $\mathbf{r}_0 + t\hat{\mathbf{d}}$ ($0 < t \leq s$) with *all* the surfaces that limit the body B (including those that limit other bodies that limit B), and check if the final position $\mathbf{r}_0 + s\hat{\mathbf{d}}$ remains in B or not. The reason for using only quadric surfaces is that these intersections are easily calculated by solving a quadratic equation.

Notice that bodies can be concave, i.e., the straight segment joining any two points in a body may not be wholly contained in the body. Hence, even when the final position of the particle lies within the initial body, we must analyze all the intersections of the path segment with the limiting surfaces of B and check if the particle has left the body after any of the intersections. When the particle leaves the initial body, say after travelling a distance $s' (< s)$, we have to locate the point $\mathbf{r}' = \mathbf{r}_0 + s'\hat{\mathbf{d}}$. The easiest method consists of computing the side pointers of *all* surfaces of the system at \mathbf{r}' , and determining the body B' that contains \mathbf{r}' by analyzing the side pointers of the different bodies in ascending order. It is clear that, for complex geometries, this is a very slow process. We can speed it up by simply disregarding those elements of the system that cannot be reached in a single step (e.g. bodies that are “screened” by other bodies). Unfortunately, as a body can be limited by all the other bodies that have been defined previously, the algorithm can be improved only at the expense of providing it with additional information. We shall adopt a simple strategy that consists of lumping groups of bodies together to form modules.

A module is defined as a connected volume³, limited by quadric surfaces, that contains one or several bodies. A module can contain other modules, which will be referred to as submodules of the first. The volume of a module is filled with a homogeneous medium, which automatically fills the cavities of the module (i.e. volumes that do not

³A space volume is said to be connected when any two points in the volume can be joined by an arc of curve that is completely contained within the volume.

correspond to a body or to a submodule); these filled cavities are considered as a single new body. A body that is connected and limited only by surfaces can be declared either as a body or as a module. For the sake of simplicity, modules are required to satisfy the following conditions: 1) the bodies and submodules of a module must be completely contained within the parent module (i.e. it is not allowed to have portions of bodies or submodules that lie outside the module) and 2) a submodule of a module cannot overlap with other submodules and bodies of the same module (this is necessary to make sure that a particle can only enter or leave a module through its limiting surfaces). Notice however, that the bodies of a module are still assumed to be defined in ascending order, i.e. a body is limited by its surfaces and by the previously defined bodies *of the same module*, so that inclusions and interpenetrating bodies can be easily defined. Of course, overlapping bodies must be in the same module.

A module (with its possible submodules) can represent a rigid part (e.g. a radioactive source, an accelerator head, a detector, a phantom, etc.) of a more complex material system. To facilitate the definition of the geometry, it is useful to allow free translations and rotations of the individual modules. The definition of a module (see below) includes the parameters of a rotation $\mathcal{R}(\omega, \theta, \phi)$ and a translation $\mathcal{T}(\mathbf{t})$, which are optional and serve to modify the position and orientation of the module (and its submodules) with respect to the laboratory reference frame. As before, the rotation is applied first. All submodules and bodies of the same module are shifted and rotated together.

In practical simulations, it may be useful to limit the region of space where particles have to be transported. For instance, to simulate the response of a detector with a given photon source, it is advisable to stop the simulation of a particle when it is far enough from the detector. This can be done automatically by considering an “enclosure” of the material system, which is defined as a module that contains the complete system. If such a covering module is not explicitly defined, the subroutines set the enclosure as a sphere of 10^{15} cm radius. It is assumed that there is perfect vacuum outside the enclosure, and in any inner volume that is not a part of a body or of a filled module. Hence, particles that leave the enclosure are lost and will never return to the material system.

For programming purposes, it is useful to imagine each module as the mother of its bodies and submodules, and as the daughter of the module that contains it. We thus have a kind of genealogical tree with various generations of modules and bodies (see fig. 5.3). The first generation reduces to the enclosure (which is the only motherless module). The members of the second generation are bodies and modules that are daughters of the enclosure. The n -th generation consists of modules and bodies whose mothers belong to the $(n - 1)$ -th generation. Each module is defined by its limiting surfaces (which determine the border with the external world) and those of their descendants (which determine the module’s internal structure); this is not true for bodies (childless members of the tree), which can be limited either by surfaces, by other sister bodies or by a combination of both. A body that is limited only by surfaces can be defined as a module, which has the advantage of allowing free rotation and translation.

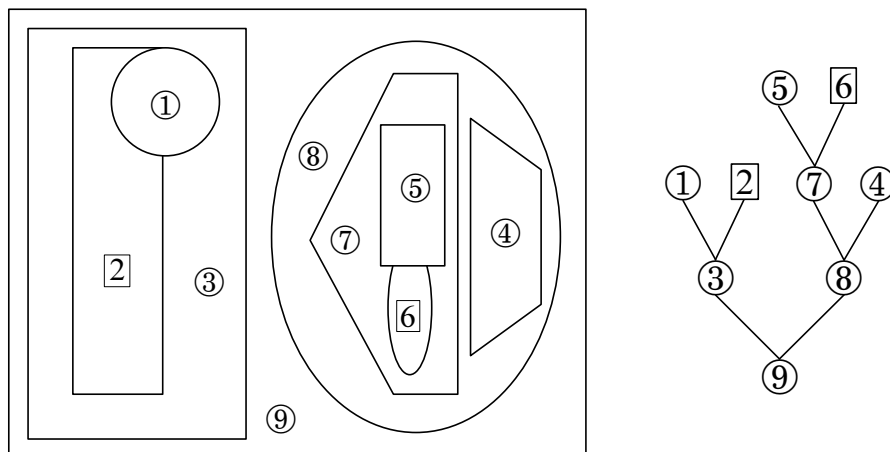


Figure 5.3: Planar cut of a geometry example, showing modules (number labels in circles) and bodies (number labels in squares), and the associated genealogical tree. Notice that a module can always be defined as a body limited by their submodules and daughter bodies, but this affects the structure of the genealogical tree and, therefore, the efficiency (speed) of the geometry operations.

5.4 Geometry definition file

The geometry is defined from the input file (UNIT=IRD). In principle, this permits the simulation of different geometries by using the same main program. The input file consists of a series of data sets, which define the different elements (surfaces, bodies and modules). A data set consists of a number of strictly formatted text lines; it starts and ends with a separation line filled with zeros. The first line after each separation line must start with one of the defining 8-character strings “SURFACE-”, “BODY----”, “MODULE--”, “END-----” or “INCLUDE-” (here, blank characters are denoted by “-”; they are essential!). Informative text (as many lines as desired) can be written at the beginning of the file, before the first separation line. A line starting with the string “END-----” after a separation line discontinues the reading of geometry data. Each element is identified by its type (surface, body or module) and a three-digit integer label. Although the element label can be given an arbitrary value (−99 to 999) in the input file, PENGEOM redefines it so that elements of a given kind are numbered consecutively, according to their input order. Notice that bodies and modules are considered as elements of the same kind (i.e. assigning the same label to a body and to a module will cause an error of the reading routine).

In the input file, numerical quantities must be written within the parentheses in the specified format. All lengths are in cm; angles can be given in either degrees (DEG) or radians (RAD). When angles are in degrees, it is not necessary to specify the unit. The parameters in each data set can be entered in any order. They can even be defined several times, in which case, only the last input value is accepted. This is useful, e.g.

- The format of a body data set is

[illegible]

- The indicator of each material (2nd line) must agree with the convention adopted in PENELOPE. Void inner volumes can be described as material bodies with **MATERIAL** set to 0.
- A line is required to define each limiting surface, with its side pointer, and each limiting body. Limiting surfaces and bodies can be entered in any order.
- Bodies are assumed to be defined in ascending order so that, in principle, it would not be necessary to declare the limiting bodies. However, to speed up the calculations, it is required to declare explicitly all the elements (surfaces and bodies) that actually limit the body that is being defined. Omission of a limiting body will cause inconsistencies unless the materials in the limiting and the limited bodies are the same.

- The format for the definition of a module is the following:

[illegible]

- The material (which must be explicitly declared) fills the cavities of the module. As in the case of bodies, **MATERIAL** = 0 corresponds to vacuum.
- The limiting surfaces must define a connected volume. All inner bodies and modules (submodules) must be declared. Notice that these cannot extend outside the module's volume and that a submodule cannot overlap with the other submodules and bodies.
- Limiting surfaces, inner bodies and submodules can be entered in any order.
- The enclosure of the system can be defined as a module (the last in the geometry file). The enclosure must contain all modules and all bodies that do not belong to modules. Otherwise, the subroutines will define a new enclosure (a sphere with

which is a bit more inconvenient. In any case, the important issue is not how to define the geometry, but the amount of computation needed to follow a particle through the material system.

5.5 The subroutine package PENGEO

The package PENGEO consists of the following subroutines;

- **SUBROUTINE GEOMIN(PARINP, NPINP, NMAT, NBOD, IRD, IWR)**
 Reads geometry data from the input file and initializes the geometry package.
 - Input arguments:
PARINP: Array containing optional parameters, which may replace the ones entered from the input file. This array must be declared in the **MAIN** program, even when **NPINP** = 0.
NPINP: Number of parameters defined in **PARINP** (positive).
IRD: Input file unit (opened in the main program).
IWR: Output file unit (opened in the main program).
 - Output arguments:
NMAT: Number of different materials in full bodies (excluding void regions).
NBOD: Number of defined bodies and modules.

Subroutine **GEOMIN** labels elements of the various kinds (surfaces, bodies and modules) in strictly increasing order; it may also redefine some of the geometry parameters, whose actual values are entered through the array **PARINP**. A copy of the geometry definition file, with the effective parameter values and with the element labels assigned by **GEOMIN**, is printed on the output file (**UNIT IWR**). This part of the output file describes the actual geometry used in the simulation.
- **SUBROUTINE LOCATE**
 Determines the body that contains the point with coordinates (**X**, **Y**, **Z**).
 - Input values (through **COMMON/TRACK/**)⁴ :
X, **Y**, **Z**: Particle position coordinates.
U, **V**, **W**: Direction cosines of the direction of movement.
 - Output values (through **COMMON/TRACK/**):
IBODY: Body where the particle moves.
MAT: Material in **IBODY**. The output **MAT** = 0 indicates that the particle is in a void region.
- **SUBROUTINE STEP(DS, DSEF, NCROSS)**
 Used in conjunction with **PENELOPE**, this subroutine performs the geometrical part of the track simulation. The particle starts from the point (**X**, **Y**, **Z**) and proceeds to travel a length **DS** in the direction (**U**, **V**, **W**) within the material where it moves.

⁴Most of the input/output of the geometry routines is through **COMMON/TRACK/**, which is the common block used by **PENELOPE** to transfer particle state variables.

STEP displaces the particle and stops it at the end of the step, or just after entering a new material. The output value **DSEF** is the distance travelled within the initial material. If the particle enters a void region, **STEP** continues the particle track, as a straight segment, until it penetrates a material body or leaves the system (the path length through inner void regions is not included in **DSEF**). When the particle arrives from a void region (**MAT** = 0), it is stopped after entering the first material body. The output value **MAT** = 0 indicates that the particle has escaped from the system.

◦ Input-output values (through **COMMON/TRACK/**):

X, **Y**, **Z**: Input: coordinates of the initial position.

Output: coordinates of the final position.

U, **V**, **W**: Direction cosines of the displacement. They are kept unaltered.

IBODY Input: initial body, i.e. the one that contains the initial position.

Output: final body.

MAT: Material in body **IBODY** (automatically changed when the particle crosses an interface).

◦ Input argument:

DS: Distance to travel (unaltered).

◦ Output arguments:

DSEF: Travelled path length before leaving the initial material or completing the jump (less than **DS** if the track crosses an interface).

NCROSS: Number of interface crossings (=0 if the particle does not leave the initial material, greater than 0 if the particle enters a new material).

For the handling and storage of geometric information we take advantage of the structure of the genealogical tree. It is assumed that an enclosure has been defined so that it is the only common ancestor for all bodies and modules. To understand the operation of the geometry routines, it is convenient to define a matrix **FLAG(KB,KS)** as follows (the indices **KS** and **KB** indicate the label of a surface and a body or module, respectively),

FLAG(KB,KS) = 1, if **KS** is a limiting surface of **KB** and **KB** is inside **KS** (i.e. side pointer = -1).
 = 2, if **KS** is a limiting surface of **KB** and **KB** is outside **KS** (i.e. side pointer = +1).
 = 3, if **KB** is a body and **KS** does not directly limit **KB**, but appears in the definition of a body that limits **KB**.
 = 4, if **KB** is a module and **KS** limits one of its daughters (bodies and submodules), but does not appear in the definition of **KB**.
 = 5, otherwise.

To locate a point we call subroutine **LOCATE**, where we proceed upwards in the genealogical tree of modules. If the point is outside the enclosure, we set **MAT** = 0 and return to the main program. Otherwise, we look for a module or body of the second generation that contains the point. If it exists, we continue analyzing its descendants

(if any) and so on. The process ends when we have determined the body **IBODY** that contains the point, or as soon as we conclude that the point is outside the material system (i.e. in a void region). Notice that, when we have found that a module **KB** does contain the point, to do the next step we only need to consider the surfaces **KS** such that $\text{FLAG}(\text{KB}, \text{KS}) = 1, 2 \text{ or } 4$.

After the body **IBODY** that contains the initial position of the particle has been identified, we can call subroutine **STEP** to move the particle a certain distance **DS**, dictated by **PENELOPE**, along the direction **(U,V,W)**. We start by checking whether the track segment crosses any of the surfaces that limit **IBODY**. If after travelling the distance **DS** the particle remains within the same body, **DSEF** is set equal to **DS** and control is returned to the main program. It is worth noting that the surfaces **KS** that define the initial body are those with $\text{FLAG}(\text{IBODY}, \text{KS}) = 1$ and 2 (proper limiting surfaces) or $=3$ (limiting surfaces of limiting bodies). Although it may happen that a surface with $\text{FLAG}=3$ does not directly limit the body, subroutine **STEP** cannot know this from the information at hand and, consequently, all surfaces with $\text{FLAG}=3$ are analyzed after each move. It is clear that, to reduce the number of surfaces to be considered, we should minimize the number of bodies used to delimit other bodies.

When the particle leaves **IBODY** and enters a new material, **STEP** stops it just after crossing the interface and determines the new body and material (in this case, the output values of **IBODY** and **MAT** are different from the input ones). To do this, the limiting surfaces of the parent module and of all the sisters of the initial body must be analyzed (if they exist). If the new position is outside the parent module, we must analyze all surfaces that limit the parent's sisters and go downward in the genealogical tree to determine the module that contains the point and, if necessary, go upwards again to find out what the new body is. If the new material is the same as in the initial body, the particle is allowed to move the remaining distance. Void regions (strict vacuum) are crossed freely (i.e. the distance travelled within these regions is not counted). Furthermore, when the particle starts from outside the enclosure, it is allowed to propagate freely until it reaches a material body. The particle is stopped when it penetrates a different material or when it leaves the system (i.e. when, after leaving a material body, its straight trajectory does not intersect a non-void body; in this case, the value $\text{MAT}=0$ is returned). Evidently, the speed of the geometry subroutines depends greatly on the structure of the modules' genealogical tree. The responsibility of optimizing it rests with the user.

When **STEP** moves the particle across an interface, there is a risk that, owing to numerical truncation errors, the particle is placed on the wrong side of the interface (i.e. the track is stopped just before the interface). If this occurs, the program could go into an endless loop in which **STEP** repeatedly tries to move the particle a very small distance (of the order of 10^{-15} cm) towards the interface but does not succeed, i.e. the particle is trapped at the interface. To avoid this collapse of the trajectory, after each interface crossing, **STEP** applies an additional small displacement ($\sim 10^{-8}$ cm) in the direction of movement, which is physically irrelevant and sufficient to compensate for the effect of truncation errors. The same strategy is used in subroutine **LOCATE**: when the particle is too close to an interface, it is moved 10^{-8} cm along the surface gradient direction

or its opposite, depending on whether the particle approaches or leaves the interface. Notice that this strategy requires that the direction of movement ($\mathbf{U}, \mathbf{V}, \mathbf{W}$) be defined before calling `LOCATE`. The extra displacement effectively eliminates the risk of particle trapping at interfaces; but it also sets a limit to the space resolution (geometrical details that are less than ~ 10 Å in size cannot be described).

`PENGEOM` admits up to 250 surfaces and 125 bodies and modules. When the input file contains a larger number of elements, the program stops and a corresponding error message is printed. To describe such complex material systems, it is necessary to edit the source file `PENGEOM.F` and increase the values of the parameters `NS` (maximum number of surfaces) and `NB` (maximum number of bodies) in all subroutines. It is assumed that the number of bodies in a module is less than `NX = 100`, which is also the upper limit for the number of surfaces that can be used to define a body or a module (those with `FLAG < 5`). When `NX` is too small, the module that causes the trouble should be decomposed into several submodules. Although it is possible to increase the parameter `NX`, this would waste a lot of memory. As a consequence, a system with more than 100 surfaces or bodies must be decomposed into modules.

5.6 Debugging and viewing the geometry

A pair of computer programs named `GVIEW2D` and `GVIEW3D` have been written to visualize the geometry and to help the user to debug the definition file. These codes generate two- and three-dimensional 24-bit colour images of the system using specific graphics routines. The executable codes included in the distribution package run on personal computers under Microsoft Windows.

The most characteristic (and useful) feature of `GVIEW2D` is that displayed pictures are generated by using the `PENGEOM` package and, therefore, errors and inconsistencies in the geometry definition file that would affect the results of actual simulations are readily identified. The method to generate the image consists of following a particle that moves on a plane perpendicular to an axis of the reference frame, which is mapped on the window. The particle starts from a position that corresponds to the left-most pixel and moves along a straight trajectory to the right of the window. To do this, we call subroutine `STEP` repeatedly, maintaining the direction of movement and with a large value of `DS` (such that each body is crossed in a single step). A colour code is assigned to each material, and pixels are lit up with the active colour when they are crossed by the particle trajectory. The active colour is changed when the particle enters a new material. The final picture is a map of the bodies and materials intersected by the window plane. The orientation of the window plane, as well as the position and size of the window view, may be changed interactively by entering one of the one-character commands shown in table 5.2, directly from the graphics window (upper- and lower-case letters may work differently). With `GVIEW2D` we can inspect the internal structure of the system with arbitrary magnification (limited only by the intrinsic resolution of the `PENGEOM` routines).

Table 5.2: One-character commands of the GVIEW2D geometry viewer.

```

+++++
+  x --> change window orientation, x-axis,      +
+  y --> change window orientation, y-axis,      +
+  z --> change window orientation, z-axis,      +
+  r,right --> shift right,          l,left --> shift left,  +
+  u,up      --> shift up,           d,down --> shift down,  +
+  f,pgup    --> shift front,        b,pgdn --> shift back,  +
+  i,+       --> zoom in,            o,-      --> zoom out,   +
+  1         --> actual size,        h,?      --> help,      +
+  blank, enter --> repeat last command,      q --> quit.   +
+++++

```

When running the GVIEW2D program, you will be asked to give the path+name of the geometry definition file and the coordinates (XC,YC,ZC) of the centre of the window (relative to the laboratory frame) in cm. The window may appear black (the colour for void regions) if no material bodies are intersected. In this case, use the one-character viewer commands to reach the bodies or, more conveniently, start again and place the window centre near or within a filled body.

GVIEW3D generates three-dimensional pictures of the geometry by using a simple ray-tracing algorithm, with the source light and the camera at the same position. Bodies are displayed with the same colour code used by GVIEW2D and the intensity of each pixel is determined by the angle between the vision line and the normal to the limiting surface. This method does not produce shadows and disregards light diffusion, but makes fairly realistic three-dimensional images. The camera is assumed to be outside the system (placing the camera inside a body would stop the program). To reveal the inner structure of the system, the program can eliminate a wedge (limited by two vertical planes that intersect in the z-axis). The position and size of the system can be modified by means of one-character commands entered from the graphics window. The command keys and actions are similar to those of GVIEW2D. It is worth noting that GVIEW3D generates the image pixel by pixel, whereas GVIEW2D does it by drawing straight lines on the window; as a result, GVIEW2D is much faster.

GVIEW2D and GVIEW3D produce an output file named GEOMETRY.REP (which is generated by subroutine GEOMIN) in the working directory. The programs are stopped either when an input format is incorrect (reading error) or when a clear inconsistency in the definition file is found (e.g. when the element that is being defined and the furnished information do not match). The wrong datum appears in the last printed lines of the GEOMETRY.REP file, usually in the last one. Error messages are also written on that file, so that the identification of inconsistencies is normally very easy. When the structure of the input file is correct, the codes do not stop and the geometry is displayed for further analysis. Most of the possible errors in the input file can only be revealed by direct inspection of the images generated by GVIEW2D and GVIEW3D.

The file GEOMETRY.REP is a duplicate of the input definition file. The only differ-

We have defined the entire system as a single module, so that you may rotate and/or displace it arbitrarily. Notice that the initial arrow points in the positive direction of the z -axis. It is instructive to try various rotations and use `GVIEW2D` or `GVIEW3D` (with a sector excluded to make the inner arrow visible) for visualizing the rotated system.

Writing a geometry file is nothing more than routine work. After a little practice, you can define quite complex systems by using only surfaces and bodies. You will soon realize that the visualization programs (as well as the actual simulations!) slow down when the number of elements in the geometry increases. The only way of speeding up the programs is to group the bodies into modules. The best strategy for improving the calculation speed is to build relatively simple modules and combine them into larger parent modules to obtain a genealogical tree where the number of daughters of each module is not too large (say 4 or 5).

You may save a lot of time by defining each body separately (and checking it carefully) and then inserting it into the progressing module that, once finished, will be added to the file. Notice that the input element labels are arbitrary (as long as they are not repeated for elements of the same kind) and that we can insert new elements anywhere in the file. Once the geometry definition is complete, we can generate an equivalent file, with elements labelled according to their input order, by simply editing the `GEOMETRY.REP` file.

The previous examples of geometry files (`QUADRIC` and `ARROW`) together with several other files of more complex geometries are included in the distribution package. They can be directly visualized by running `GVIEW2D` and `GVIEW3D`. The file `GLASS` (a glass of champagne) shows that common objects can be described quite precisely with only quadric surfaces; in this case, we do not use modules, which are useful only to accelerate the calculations. `WELL` defines a scintillation well detector with much detail; we have set an enclosure for the system, so that you can rotate the entire detector by editing the definition file. Notice that, when the detector is tilted, it is very difficult to get an idea of its geometry from the images generated by `GVIEW2D`. `SATURNE` describes the head of an electron accelerator, quite a complicated geometry with 96 surfaces and 44 bodies. The structure `MALE`, which corresponds to a mathematical anthropomorphic phantom, consists of 174 surfaces and 108 bodies, grouped into 11 modules.

We cannot finish without a word of caution about the use of `PENGEOM`, and other general-purpose geometry packages. For simple geometries, they tend to waste a lot of time. It is always advisable to consider the possibility of handling geometric aspects directly; this may enable substantial reduction of the number of operations by taking full advantage of the peculiarities of the material system.

Chapter 6

Structure and operation of the code system

In this chapter we describe the structure of the PENELOPE code system and its operation. The kernel of the system is the FORTRAN77 subroutine package PENELOPE, which performs “analogue” simulation of electron-photon showers (i.e. the simulated showers are intended to be replicas of actual showers) in infinite (unbounded) media of various compositions. Photon histories are generated by using the detailed simulation method (see section 1.4), i.e. all interaction events are simulated in chronological succession. The generation of electron and positron tracks is performed by using the mixed procedure described in chapter 4. Secondary particles emitted with initial energy larger than the absorption energy –see below– are stored, and simulated after completion of each primary track. Secondary particles are produced in direct interactions (hard inelastic collisions, hard bremsstrahlung emission, positron annihilation, Compton scattering, photoelectric absorption and pair production) and as fluorescent radiation (characteristic x rays and Auger electrons). PENELOPE simulates fluorescent radiation that results from vacancies produced in K shells and L subshells by photoelectric absorption and Compton scattering of photons and by electron/positron impact. The relaxation of these vacancies is followed until the K and L shells are filled up, i.e. until the vacancies have migrated to M and outer shells.

Being a subroutine package, PENELOPE cannot operate by itself. The user must provide a steering MAIN program for her/his particular problem. Nevertheless, this MAIN program is normally fairly simple, since it only has to control the evolution of the tracks simulated by PENELOPE and keep score of relevant quantities. PENELOPE is devised to do the largest part of the simulation work. It allows the user to write her or his own simulation program, with arbitrary geometry and scoring, without previous knowledge of the intricate theoretical aspects of scattering and transport theories. In the case of material systems with quadric geometries, the geometrical operations can be done automatically by using the package PENGEO (see chapter 5). The distribution package also includes various examples of MAIN programs for simple geometries (slab and cylindrical) and for general quadric geometries with limited scoring. Although

they are mostly intended to illustrate the use of the simulation routines, they do allow studying many cases of practical interest. The complete program system is written in FORTRAN77 (ANSI/ISO standard form) and, therefore, it should run on any platform with a FORTRAN77 or FORTRAN90 compiler.

6.1 PENELOPE

PENELOPE simulates coupled electron-photon transport in arbitrary material systems consisting of a number of homogeneous regions (bodies) limited by sharp (and passive) interfaces. Initially, it was devised to simulate the PENetration and Energy LOSS of Positrons and Electrons in matter; photons were introduced later. The adopted interaction models (chapters 2-4), and the associated databases, allow the simulation of electron/positron and photon transport in the energy range from 100 eV to 1 GeV.

It should be borne in mind that our approximate interaction models become less accurate when the energy of the transported radiation decreases. Actually, for energies below ~ 1 keV, the DCSs are not well known, mostly because they are strongly affected by the state of aggregation. On the other hand, for electrons and positrons, the trajectory picture ceases to be applicable (because coherent scattering from multiple centers becomes appreciable) when the de Broglie wavelength, $\lambda_B = (150 \text{ eV}/E)^{1/2} \text{ \AA}$, is similar to or greater than the interatomic spacing ($\sim 1 \text{ \AA}$). Therefore, results from simulations with PENELOPE (or with any other Monte Carlo trajectory code) for energies below 1 keV or so, should be considered to have only a qualitative (or, at most, semi-quantitative) value. We recall also that, for elements with intermediate and high atomic numbers, secondary characteristic photons with energies less than the M-shell absorption edge are not simulated by PENELOPE. This sets a lower limit to the energy range for which the simulation is faithful.

The source file `PENELOPE.F` (about 8000 lines of FORTRAN code) consists of four blocks of subprograms, namely, preparatory calculations and I/O routines, interaction simulation procedures, numerical routines and transport routines. Only the latter are invoked from the `MAIN` program. The interaction simulation routines implement the theory and algorithms described in chapters 2 and 3. Although the interaction routines are not called from the `MAIN` program, there are good reasons to have them properly identified. Firstly, these are the code pieces to be modified to incorporate better physics (when available) and, secondly, some of these subroutines deliver numerical values of the DCSs (which can be useful to apply certain variance reduction techniques). To have these routines organized, we have named them according to the following convention:

- The first letter indicates the particle (**E** for electrons, **P** for positrons, **G** for photons).
- The second and third letters denote the interaction mechanism (**EL** for elastic, **IN** for inelastic, **BR** for bremsstrahlung, **AN** for annihilation, **RA** for Rayleigh, **CO** for Compton, **PH** for photoelectric and **PP** for pair production).
- The random sampling routines have three-letter names. Auxiliary routines, which perform specific calculations, have longer names, with the fourth and subsequent letters

and/or numbers indicating the kind of calculation (TX for total x-section, DX for differential x-section) or action (W for write data on a file, R for read data from a file, I for initialization of simulation algorithm).

Thus, for instance, subroutine **EEL** simulates elastic collisions of electrons while subroutine **EINTX** computes total (integrated) cross sections for inelastic scattering of electrons.

6.1.1 Database and input material data file

PENELOPE reads the required physical information about each material (which includes tables of physical properties, interaction cross sections, relaxation data, etc.) from the input material data file (identified as **UNIT=IRD** in the code source listing). The material data file is created by means of the auxiliary program **MATERIAL**, which extracts atomic interaction data from the database. This program runs interactively and is self-explanatory. Basic information about the considered material is supplied by the user from the keyboard, in response to prompts from the program. The required information is: 1) chemical composition (i.e. elements present and stoichiometric index of each element), 2) mass density, 3) mean excitation energy and 4) energy and oscillator strength of plasmon excitations. Alternatively, for a set of 279 prepared materials, the program **MATERIAL** can read data directly from the **PDCOMPOS.TAB** file (see below).

For compounds and mixtures, the additivity approximation is adopted to define the material's cross sections, i.e. the corresponding "molecular" cross section is set equal to the sum of atomic cross sections weighted with the stoichiometric index of the element. Alloys and mixtures are treated as compounds, with stoichiometric indices equal, or proportional, to the percent number of atoms of the elements.

The PENELOPE database consists of the following 465 ASCII files,

PDATCONF.TAB ... Atomic ground-state configurations, ionization energies (Lederer and Shirley, 1978) and central values, $J_i(p_z = 0)$, of the one-electron shell Compton profiles (Biggs et al., 1975) for the elements, from hydrogen to uranium.

PDCOMPOS.TAB ... This file contains composition data, densities and mean excitation energies for 279 materials, adapted from the database of the **ESTAR** program of Berger (1992). The first 98 entries are the elements $Z = 1 - 98$, ordered by atomic number Z . Materials 99 to 279 are compounds and mixtures, in alphabetical order. Notice that PENELOPE does not work for elements with atomic number $Z > 92$.

PDEFLIST.TAB ... List of materials predefined in file **PDCOMPOS.TAB**, with their identification numbers.

PDRELAX.TAB ... Data on atomic relaxation, extracted from the LLNL Evaluated Atomic Data Library (Perkins et al., 1991). Each line in the file **PDRELAX.TAB** describes an atomic transition. The quantities listed are the atomic number of

the element, the numerical labels of the active electron shells (see table 6.1), the transition probability and the energy of the emitted x-ray or electron, respectively.

Table 6.1: Numerical labels used to designate atomic electron shells. In the case of non-radiative transitions, the label 99 indicates shells beyond the M5 shell.

label	shell	label	shell	label	shell
1	K (1s _{1/2})	11	N2 (4p _{1/2})	21	O5 (5d _{5/2})
2	L1 (2s _{1/2})	12	N3 (4p _{3/2})	22	O6 (5f _{5/2})
3	L2 (2p _{1/2})	13	N4 (4d _{3/2})	23	O7 (5f _{7/2})
4	L3 (2p _{3/2})	14	N5 (4d _{5/2})	24	P1 (6s _{1/2})
5	M1 (3s _{1/2})	15	N6 (4f _{5/2})	25	P2 (6p _{1/2})
6	M2 (3p _{1/2})	16	N7 (4f _{7/2})	26	P3 (6p _{3/2})
7	M3 (3p _{3/2})	17	O1 (5s _{1/2})	27	P4 (6d _{3/2})
8	M4 (3d _{3/2})	18	O2 (5p _{1/2})	28	P5 (6d _{5/2})
9	M5 (3d _{5/2})	19	O3 (5p _{3/2})	29	Q1 (7s _{1/2})
10	N1 (4s _{1/2})	20	O4 (5d _{3/2})	99	outer shells

92 files named PDEELZZ.TAB with ZZ=atomic number (01–92). These files contain integrated cross sections for elastic scattering of electrons and positrons by neutral atoms, calculated by using the partial-wave methods described in section 3.1 (Salvat, 2000). The first line in each file gives the atomic number ZZ; each subsequent line has 7 columns with the following data:

1st column: kinetic energy (eV), in increasing order.

2nd column: total cross section for electrons.

3rd column: first transport cross section for electrons.

4th column: second transport cross section for electrons.

5th column: total cross section for positrons.

6th column: first transport cross section for positrons.

7th column: second transport cross section for positrons.

The grid of energies is approximately logarithmic, with 15 points per decade, and is the same for all elements. All cross sections are in cm².

92 files named PDEBRZZ.TAB with ZZ=atomic number (01–92). They contain the atomic bremsstrahlung scaled cross sections (energy loss spectra) and total integrated radiative cross sections of electrons, for a grid of electron kinetic energies E and reduced photon energies W/E that is dense enough to allow the use of cubic spline log-log interpolation in E and linear interpolation in W/E . The data in these files is from a database, with 32 reduced photon energies, which was provided to the authors by Steve Seltzer (a brief description of the methods used to compute the database and a reduced tabulation is given in Seltzer and Berger,

1986). The format of the bremsstrahlung database files is the following,

1) The first line contains the atomic number ZZ .

2) Each four-lines block contains the electron kinetic energy E , the scaled energy-loss differential cross section at the 32 fixed reduced photon energies and the value of the integrated radiative cross section.

Energies are in eV and the values of the scaled energy-loss cross section are in millibarn (10^{-27} cm^2).

PDBRANG.TAB ... Gives the parameters of the analytical shape function (angular distribution) of bremsstrahlung photons, which is expressed as a statistical mixture of two Lorentz-boosted dipole distributions, eq. (3.151). The distribution parameters were obtained by fitting the benchmark partial-wave shapes tabulated by Kissel et al. (1983).

92 files named PDGPPZZ.TAB with ZZ =atomic number (01–92). Total cross sections for electron-positron pair production by photons with energies up to 100 GeV in the field of neutral atoms. The data were generated by means of the XCOM program of Berger and Hubbell (1987). The first line of each file gives the atomic number ZZ ; each subsequent line gives,

1st column: photon energy, in eV. The same energy grid for all elements.

2nd column: total cross section for pair+triplet production in barn (10^{-24} cm^2).

92 files named PDGPHZZ.TAB with ZZ =atomic number (01–92), containing photoelectric total atomic cross sections and partial cross sections for photoionization of inner shells (K shell and L subshells) for the elements and photon energies in the range from 100 eV to 1 TeV. The data were extracted from the LLNL Evaluated Photon Data Library EPDL97 (Cullen et al., 1997). The format is the following,

1) the first line contains the atomic number ZZ and the number NS of shells for which the partial cross section is tabulated.

2) each of the following lines contains a value of the photon energy (in eV) and the corresponding total cross section and partial cross sections of the shells K, L1, L2 and L3, respectively (all cross sections in barn). For low- Z elements, L-subshells are empty and, therefore, they do not appear in the table.

The grid of energies for each element was obtained by merging a generic grid (the same for all elements, covering the energy range from 100 eV to 100 GeV) with the grid of absorption edges of the element, and adding additional points (where needed) to ensure that linear log-log interpolation will never introduce relative errors larger than 0.02.

92 files named PDEINZZ.TAB with ZZ =atomic number (01–92), containing total (integrated) cross sections for ionization of inner shells (K shell and L subshells) by impact of electrons and positrons with kinetic energies in the range from 100 eV to 1 GeV. These cross sections were evaluated by means of the optical-data model described in section 3.2.6 using photoelectric cross sections read from the files **PDGPHZZ.TAB**. The format is the following,

1) the first line contains the atomic number ZZ .

2) each of the following lines consists of nine columns, with the kinetic energy of the projectile (in eV) in the first one. Columns 2-5 contain the ionization cross sections of the shells K, L1, L2 and L3 for electron impact and columns 6-9 have the corresponding cross sections for ionization by impact of positrons (all cross sections in barn). Cross sections for K and L shells of light elements with ionization energies less than 100 eV are set to zero.

Atomic cross sections for coherent and incoherent scattering of photons, inelastic scattering of electrons and positrons, and positron annihilation are evaluated directly from the analytical DCSs described in chapters 2 and 3 .

In the material definition file generated by the program MATERIAL, mean free paths, transport mean free paths and stopping powers of electrons and positrons are given in mass-thickness units ($1 \text{ mtu} \equiv 1 \text{ g/cm}^2$) and eV/mtu, respectively. Photon mass attenuation coefficients are expressed in cm^2/g . These quantities are practically independent of the material density; the only exception is the collision stopping power for electrons and positrons with kinetic energies larger than about 0.5 MeV, for which the density effect correction may be appreciable.

The energy-dependent quantities tabulated in the input material data file determine the most relevant characteristics of the scattering model. Thus, the MW differential cross section for electron and positron elastic scattering is completely defined by the mean free paths and transport mean free paths. Collision and radiative stopping powers read from the input file are used to renormalize the built-in analytical differential cross sections, i.e. these are multiplied by an energy-dependent factor such that the input stopping powers are exactly reproduced. The mean free paths used in the simulation of photon transport are directly obtained from the input total cross sections. Natural cubic spline log-log interpolation is used to interpolate the tabulated energy-dependent quantities, except for the photoelectric attenuation coefficient, which is obtained by simple linear log-log interpolation in the intervals between consecutive absorption edges.

To simulate geometrical structures with several materials, the corresponding material data files generated by the program MATERIAL must be catenated in a single input file. PENELOPE labels the M-th material in this file with the index **MAT=M**, which is used during the simulation to identify the material where the particle moves. The maximum number of different materials that PENELOPE can handle simultaneously is fixed by the parameter **MAXMAT**, which in the present version is set equal to 10. The required memory storage is roughly proportional to the value of this parameter. The user can increase **MAXMAT** by editing the program source files. Notice that the value of **MAXMAT** *must* be the same in all subprograms.

6.1.2 Structure of the MAIN program

As mentioned above, PENELOPE must be complemented with a steering **MAIN** program, which controls the geometry and the evolution of tracks, keeps score of the relevant quantities and performs the required averages at the end of the simulation.

The connection of PENELOPE and the MAIN program is done via the named common block

→ COMMON/TRACK/E,X,Y,Z,U,V,W,WGHT,KPAR,IBODY,MAT,ILB(5)

that contains the following particle state variables:

KPAR ... kind of particle (1: electron, 2: photon, 3: positron).

E ... current particle energy (eV) (kinetic energy for electrons and positrons).

X, Y, Z ... position coordinates (cm).

U, V, W ... direction cosines of the direction of movement.

WGHT ... in analogue simulations, this is a dummy variable. When using variance reduction methods, the particle weight can be stored here.

IBODY ... this auxiliary flag serves to identify different bodies in complex material structures.

MAT ... material where the particle moves (i.e. the one in the body labelled IBODY).

ILB(5) ... an auxiliary array of 5 labels that describe the origin of secondary particles (see below). It is useful e.g. to study partial contributions from particles originated by a given process.

The position coordinates $\mathbf{r} = (X, Y, Z)$ and the direction cosines $\hat{\mathbf{d}} = (U, V, W)$ of the direction of movement are referred to a fixed rectangular coordinate system, the “laboratory” system, which can be arbitrarily defined. During the simulation, all energies and lengths are expressed in eV and cm, respectively.

The label KPAR identifies the kind of particle: KPAR=1, electron; KPAR=2, photon; KPAR=3, positron. A particle that moves in material M is assumed to be absorbed when its energy becomes less than a value EABS(KPAR,M) (in eV) specified by the user. Positrons are assumed to annihilate, by emission of two photons, when absorbed. In dose calculations, EABS(KPAR,M) should be determined so that the residual range of particles with this energy is smaller than the dimensions of the volume bins used to tally the spatial dose distribution. As the interaction database is limited to energies above 100 eV, absorption energies EABS(KPAR,M) must be larger than this value.

The transport algorithm for electrons and positrons in each material M is controlled by the following simulation parameters,

C1(M) ... Average angular deflection, $C_1 \simeq 1 - \langle \cos \theta \rangle$ [eq. (4.11)], produced by multiple elastic scattering along a path length equal to the mean free path between consecutive hard elastic events [see eq. (4.1)]. C1(M) should be of the order of 0.05; its maximum allowed value is 0.2.

C2(M) ... Maximum average fractional energy loss, C_2 [eq. (4.85)], between consecutive hard elastic events. Usually, a value of the order of 0.05 is adequate. The maximum allowed value of **C2(M)** is 0.2.

WCC(M) ... Cutoff energy loss, W_{cc} (in eV), for hard inelastic collisions in the **Mth** material.

WCR(M) ... Cutoff energy loss, W_{cr} (in eV), for hard bremsstrahlung emission in material **M**.

These parameters determine the accuracy and speed of the simulation. To ensure accuracy, **C1(M)** and **C2(M)** should have small values (of the order of 0.01 or so). With larger values of **C1(M)** and **C2(M)** the simulation gets faster, at the expense of a certain loss in accuracy. The cutoff energies **WCC(M)** and **WCR(M)** mainly influence the simulated energy distributions. The simulation speeds up by using larger cutoff energies, but if these are too large, the simulated energy distributions may be somewhat distorted. In practice, simulated energy distributions are found to be insensitive to the adopted values of **WCC(M)** and **WCR(M)** when these are less than the bin width used to tally the energy distributions. Thus, the desired energy resolution determines the maximum allowed cutoff energies. The reliability of the whole simulation rests on a single condition: the number of steps (or random hinges) per primary track must be “statistically sufficient”, i.e. larger than 10 or so.

The simulation package is initialized from the **MAIN** program with the statement
 \rightarrow **CALL PEINIT(EPMAX,NMAT,IRD,IWR,INFO)**

Subroutine **PEINIT** reads the data files of the different materials, evaluates relevant scattering properties and prepares look-up tables of energy-dependent quantities that are used during the simulation. Its input arguments are:

EPMAX ... Maximum energy (in eV) of the simulated particles. Notice that if the primary particles are positrons with initial kinetic energy **EP**, the maximum energy of annihilation photons may be close to (but less than) $EP_{MAX} = 1.21(EP + m_e c^2)$; in this special case, the maximum energy is larger than the initial kinetic energy.

NMAT ... Number of different materials (less than or equal to **MAXMAT**).

IRD ... Input unit.

IWR ... Output unit.

INFO ... Determines the amount of information that is written on the output unit. Minimal for **INFO=0** and increasingly detailed for **INFO=1, 2**, etc.

For the preliminary computations, **PEINIT** needs to know the absorption energies **EABS(KPAR,M)** and the simulation parameters **C1(M)**, **C2(M)**, **WCC(M)** and **WCR(M)**. This information is introduced through the named common block

\rightarrow **COMMON/CSIMPA/EABS(3,MAXMAT),C1(MAXMAT),C2(MAXMAT),WCC(MAXMAT),**
1 WCR(MAXMAT)

that has to be loaded before invoking subroutine PEINIT. Notice that we can employ different values of the simulation parameters for different materials. This possibility can be used to speed up the simulation in regions of lesser interest.

PENELOPE has been structured in such a way that a particle track is generated as a sequence of track segments (free flights or “jumps”); at the end of each segment, the particle suffers an interaction with the medium (a “knock”) where it loses energy, changes its direction of movement and, in certain cases, produces secondary particles. Electron-photon showers are simulated by successively calling the following subroutines:

SUBROUTINE CLEANS ... Initiates the secondary stack.

SUBROUTINE START ... For electrons and positrons, this subroutine forces the following interaction event to be a soft artificial one. It must be called before starting a new –primary or secondary– track and also when a track crosses an interface. Calling **START** is strictly necessary only for electrons and positrons; for photons this subroutine has no physical effect. However, it is advisable to call **START** for any kind of particle since it checks whether the energy is within the expected range, and can thus help to detect “bugs” in the **MAIN** program.

SUBROUTINE JUMP(DSMAX,DS) ... Determines the length **DS** of the track segment to the following interaction event.

The input parameter **DSMAX** defines the maximum allowed step length for electrons/positrons; for photons, it has no effect. As mentioned above, to limit the step length, PENELOPE places delta interactions along the particle track. These are fictitious interactions that do not alter the physical state of the particle. Their only effect is to interrupt the sequence of simulation operations (which requires altering the values of inner control variables to permit resuming the simulation in a consistent way). The combined effect of the soft interactions that occur along the step preceding the delta interaction is simulated by the usual random hinge method.

As mentioned above, to ensure the reliability of the mixed simulation algorithm, the number of artificial soft events per particle track in each body should be larger than, say, 10. For relatively thick bodies (say, thicker than 10 times the mean free path between hard interactions), this condition is automatically satisfied. In this case we can switch off the step-length control by setting **DSMAX=1.0D35** (or any other very large value). On the other hand, when the particle moves in a thin body, **DSMAX** should be given a value of the order of one tenth of the “thickness” of that body. Limiting the step length is also necessary to simulate particle transport in external electromagnetic fields.

SUBROUTINE KNOCK(DE,ICOL) ... Simulates an interaction event, computes new energy and direction of movement, and stores the initial states of the generated secondary particles, if any. On output, the arguments are:

DE ... deposited energy in the course of the event,

ICOL ... kind of event that has been simulated, according to the following convention,

- Electrons (KPAR=1)
 - ICOL=1, artificial soft event (random hinge).
 - =2, hard elastic collision.
 - =3, hard inelastic collision.
 - =4, hard bremsstrahlung emission.
 - =5, inner-shell ionization by electron impact.
- Photons (KPAR=2)
 - ICOL=1, coherent (Rayleigh) scattering.
 - =2, incoherent (Compton) scattering.
 - =3, photoelectric absorption.
 - =4, electron-positron pair production.
- Positrons (KPAR=3)
 - ICOL=1, artificial soft event (random hinge).
 - =2, hard elastic collision.
 - =3, hard inelastic collision.
 - =4, hard bremsstrahlung emission.
 - =5, inner-shell ionization by positron impact.
 - =6, annihilation.

For electrons and positrons ICOL=7 corresponds to delta interactions. The value ICOL=8 is used for the “auxiliary” interactions (an additional mechanism that may be defined by the user, e.g. to simulate photonuclear interactions, see the source file `PENELOPE.F`).

SUBROUTINE SECPAR(LEFT) ... Sets the initial state of a secondary particle and removes it from the secondary stack. The output value `LEFT` is the number of secondary particles that remained in the stack at the calling time.

SUBROUTINE STORES(E,X,Y,Z,U,V,W,WGHT,KPAR,ILB) ... Stores a particle in the secondary stack. Arguments have the same meaning as in `COMMON/TRACK/`, but refer to the particle that is being stored. The variables `IBODY` and `MAT` are set equal to the current values in `COMMON/TRACK/`.

Calling `STORES` from the `MAIN` program is useful e.g. to store particles produced by splitting, a variance reduction method (see section 1.6.2).

The sequence of calls to generate a random track is independent of the kind of particle that is being simulated. The generation of random showers proceeds as follows (see fig. 6.1):

- (i) Set the initial state of the primary particle, i.e. assign values to the state variables `KPAR`, `E`, position coordinates $\mathbf{r} = (X,Y,Z)$ and direction of movement $\hat{\mathbf{d}} = (U,V,W)$. Specify the body and material where the particle moves by defining the values of `IBODY` and `MAT`, respectively. Optionally, set the values of `WGHT` and `ILB(1:5)`.
- (ii) `CALL CLEANS` to initialize the secondary stack.

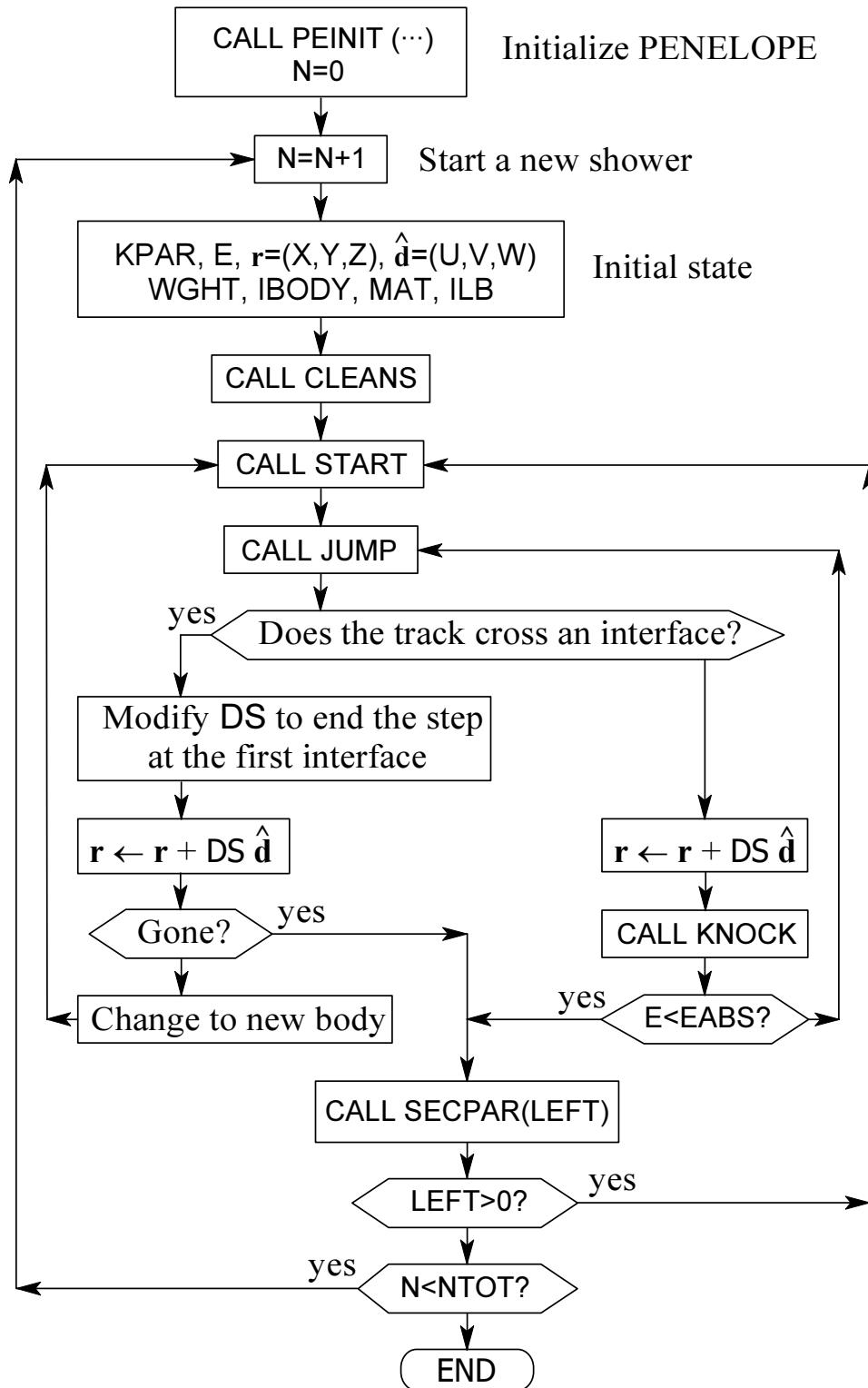


Figure 6.1: Flow diagram of the MAIN program for simulating electron-photon showers with PENELOPE.

- (iii) CALL START to initiate the simulation of the track.
- (iv) CALL JUMP(DSMAX,DS) to determine the length DS of the next track segment (for electrons and positrons, DS will never exceed the input value DSMAX).
- (v) Compute the position of the following event:
 - If the track has crossed an interface, stop the particle at the position where the track intersects the interface, and shorten the step length DS accordingly. Change to the new material (the one behind the interface) by redefining the variables IBODY and MAT.
When the particle escapes from the system, the simulation of the track has been finished; increment counters and go to step (vii).
Go to step (iii).
- (vi) CALL KNOCK(DE,ICOL) to simulate the following event.
 - If the energy is less than EABS(KPAR,MAT), end the track, increment counters and go to step (vii).
 - Go to step (iv).
- (vii) CALL SECPAR(LEFT) to start the track of a particle in the secondary stack (this particle is then automatically removed from the stack).
 - If LEFT>0, go to step (iii). The initial state of a secondary particle has already been set.
 - If LEFT=0, the simulation of the shower produced by the primary particle has been completed. Go to step (i) to generate a new primary particle (or leave the simulation loop after simulating a sufficiently large number of showers).

Notice that subroutines JUMP and KNOCK keep the position coordinates unaltered; the positions of successive events have to be followed by the MAIN program (simply by performing a displacement of length DS along the direction of movement after each call to JUMP). The energy of the particle is automatically reduced by subroutine KNOCK, after generating the energy loss from the relevant probability distribution. KNOCK also modifies the direction of movement according to the scattering angles of the simulated event. Thus, at the output of KNOCK, the values of the energy E , the position $\mathbf{r}=(X,Y,Z)$ and the direction of movement $\hat{\mathbf{d}}=(U,V,W)$ define the particle state immediately after the interaction event.

In order to avoid problems related with possible overflows of the secondary stack, when a secondary particle is produced its energy is temporarily assumed as locally deposited. Hence, the energy E of a secondary must be subtracted from the corresponding dose counter when the secondary track is started. Occasional overflows of the secondary stack are remedied by eliminating the less energetic secondary electron or photon in the stack (positrons are not eliminated since they will eventually produce quite energetic annihilation radiation). As the main effect of secondary particles is to spread out the energy deposited by the primary one, the elimination of the less energetic secondary electrons and photons should not invalidate local dose calculations.

It is the responsibility of the user to avoid calling subroutines `JUMP` and `KNOCK` with energies outside the interval $(EABS(KPAR,M), EMAX)$. This could cause improper interpolation of the cross sections. The simulation is aborted (and an error message is printed in unit 6) if the conditions $EABS(KPAR) < E < EMAX$ are not satisfied when a primary or secondary track is started (whenever subroutine `START` is called at the beginning of the track).

Pseudo-random numbers uniformly distributed in the interval (0,1) are supplied by function `RAND(DUMMY)` that implements a 32-bit generator due to L'Ecuyer (see table 1.1). The seeds of the generator (two integers) are transferred from the `MAIN` program through the named common block `RSEED` (see below). The random number generator can be changed by merely replacing that `FUNCTION` subprogram (the new one has to have a single dummy argument). Some compilers incorporate an intrinsic random number generator with the same name (but with different argument lists). To avoid conflict, `RAND` should be declared as an external function in all subprograms that call it.

Notice that

- (1) In the simulation routines, real and integer variables are declared as `DOUBLE PRECISION` and `INTEGER*4`, respectively. To prevent type mismatches, it is prudent to use the following `IMPLICIT` statement
 \rightarrow `IMPLICIT DOUBLE PRECISION (A-H,O-Z), INTEGER*4 (I-N)`
in the `MAIN` program and other user program units.
- (2) The `MAIN` program *must* include the following three common blocks:
 \rightarrow `COMMON/TRACK/E,X,Y,Z,U,V,W,WGHT,KPAR,IBODY,MAT,ILB(5)`
 \rightarrow `COMMON/CSIMPA/EABS(3,MAXMAT),C1(MAXMAT),C2(MAXMAT),WCC(MAXMAT),`
`1 WCR(MAXMAT) ! Simulation parameters.`
 \rightarrow `COMMON/RSEED/ISEED1,ISEED2 ! Random number generator seeds.`

As mentioned above, `ILB(5)` is an array of labels that describe the origin of secondary particles. It is assumed that the user has set `ILB(1)` equal to 1 (one) when a primary (source) particle history is initiated. Then, `PENELOPE` assigns the following labels to each particle in a shower;

- `ILB(1)`: generation of the particle. 1 for primary particles, 2 for their direct descendants, etc.
- `ILB(2)`: kind `KPAR` of the parent particle, only if `ILB(1) > 1` (secondary particles).
- `ILB(3)`: interaction mechanism `ICOL` (see above) that originated the particle, only when `ILB(1) > 1`.
- `ILB(4)`: a non-zero value identifies particles emitted from atomic relaxation events and describes the atomic transition where the particle was released. The numerical value is $= Z \cdot 10^6 + IS1 \cdot 10^4 + IS2 \cdot 100 + IS3$, where Z is the atomic number of the parent atom and `IS1`, `IS2` and `IS3` are the labels of the active atomic electron shells (see table 6.1).
- `ILB(5)`: this label can be defined by the user; it is transferred to all descendants of the particle.

The ILB label values are delivered by subroutine **SECPAR**, through common **TRACK**, and remain unaltered during the simulation of the track.

Owing to the long execution time, the code will usually be run in batch mode. It is advisable to limit the simulation time rather than the number of tracks to be simulated, since the time required to follow each track is difficult to predict. To this end, one can link a clock routine to the simulation code and stop the computation after exhausting the allotted time; an example of a clock routine (which runs for two different compilers) is included in the **PENELOPE** distribution package.

6.1.3 Variance reduction

The subroutine package **PENELOPE.F** is intended to perform analogue simulation and, therefore, does not include any variance reduction methods. The source file **PENVARED.F** contains subroutines to perform splitting (**VSPLIT**), Russian roulette (**VKILL**) and interaction forcing (**JUMPF**, **KNOCKF**) in an automatic way. Splitting and Russian roulette (see section 1.6.2) do not require changes in **PENELOPE**; the necessary manipulations on the numbers and weights **WGHT** of particles could be done directly in the main program. Particles resulting from splitting are stored in the secondary stack by calling subroutine **STORES**.

Interaction forcing (section 1.6.1) implies changing the mean free paths of the forced interactions and, at the same time, redefining the weights of the generated secondary particles. In principle, it is possible to apply interaction forcing from the **MAIN** program by manipulating the interaction probabilities, that are made available through the named common block **CJUMP0**. These manipulations are performed automatically by calling the subroutines **JUMPF** and **KNOCKF** instead of **JUMP** and **KNOCK**.

Although these subroutines operate like “black boxes”, they should be invoked with care. In general, it is advisable to prevent particle weights from reaching very large or very small values. In the first case, a very “heavy” particle can completely hide the information collected from many lighter particles. Conversely, it is not convenient to spend time simulating particles with very small weights, which contribute insignificant amounts to the scores. Notice also that repeated splitting and interaction forcing may easily lead to saturation of the secondary stack (the default stack size is 1000 particles). Hence, we usually apply interaction forcing only to primary particles.

6.2 Examples of **MAIN** programs

In general, the user must provide the **MAIN** program for each specific geometry. The distribution package of **PENELOPE** includes various examples of **MAIN** programs for simple geometries (slab and cylindrical) and for general quadric geometries with limited scoring. In these examples, we assume that a single kind of particles is emitted from the radiation

source. The programs can be easily generalized to the case of multi-particle sources with continuous (or discrete) energy spectra. For details on the operation of these codes, see section 6.2.4 below and the heading comments in the corresponding source files.

6.2.1 Program PENSLAB

The program PENSLAB simulates electron/photon showers within a material slab (see fig. 6.2). It illustrates the use of the simulation routines for the simplest geometry (as geometry operations are very simple, this program is faster than the ones described below). The slab is limited by the planes $z = 0$ and $z = t$, the thickness. The lateral extension of the slab is assumed to be infinite, i.e. much larger than the maximum range of the particles). Primary particles start with a given energy E_0 from a point source at a given “height” z_0 (positive or negative) on the z -axis, and moving in directions distributed uniformly in a spherical “sector” defined by its limiting polar angles, say θ_1 and θ_2 , which is indicated by the hatched wedge in fig. 6.2. That is, to generate the initial direction, the polar cosine $W = \cos \theta$ is sampled uniformly in the interval from $\cos \theta_1$ to $\cos \theta_2$ and the azimuthal angle ϕ is sampled uniformly in $(0, 2\pi)$. Thus, the case $\theta_1 = 0$ and $\theta_2 = 180$ deg corresponds to an isotropic source, whereas $\theta_1 = \theta_2 = 0$ defines a beam parallel to the z -axis. Notice that the complete arrangement has rotational invariance about the z -axis.

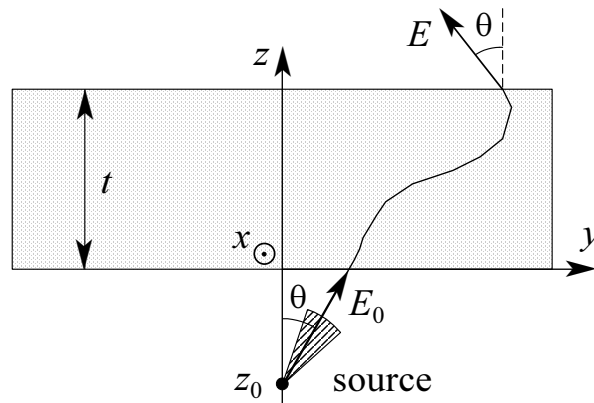


Figure 6.2: General planar geometry considered in PENSLAB.

PENSLAB generates detailed information on many quantities and distributions of physical interest. The output files contain a self-explanatory report of the simulation results, which consist of:

- (i) Fractions of primary particles that are transmitted, backscattered and absorbed and a number of average quantities (track length within the sample; number of events of each kind per particle; energy, direction and lateral displacement of particles that leave the sample, etc.).
- (ii) Energy distributions of transmitted and backscattered primary particles.

- (iii) Angular distributions of transmitted and backscattered particles.
- (iv) Depth-dose distribution (i.e. deposited energy per unit depth).
- (v) Depth-distribution of deposited charge.
- (vi) Distribution of energy deposited into the slab.

Each simulated continuous distribution is printed on a separate file (as a histogram), with a heading describing its content and in a format ready for visualization with a plotting program. The code computes and delivers the statistical uncertainties (3σ) of all evaluated quantities and distributions. Many authors quote these uncertainties as one standard deviation, which means that the probability for the actual value to lie outside the error bar is 0.317. We prefer to be more conservative and stay at the 3σ level, for which the probability of “missing the real value” is only 0.003.

The program **PENSLAB** and its predecessors have been intensively used during the last years to analyze the reliability of **PENELOPE**. They have been applied to a variety of experimental situations, covering a wide energy range. Benchmark comparisons with experimental data have been published elsewhere (Baró et al., 1995; Sempau et al., 1997).

WARNING: In the output files of **PENSLAB** (and also in those of the program **PENCYL** described below), the terms “transmitted” and “backscattered” are used to denote particles that leave the material system moving upwards ($W > 0$) and downwards ($W < 0$), respectively. Notice that this agrees with the usual meaning of these terms only when primary particles impinge on the system coming from below (i.e. with $W > 0$).

6.2.2 Program **PENCYL**

The program **PENCYL** simulates electron and photon transport in multilayered cylindrical structures. The material system consists of one or several layers of given thicknesses. Each layer contains a number of concentric homogeneous rings of given compositions and radii (and thickness equal to that of the layer). The layers are perpendicular to the z -axis and the centre of the rings in each layer is specified by giving its x and y coordinates. When all the centres are on the z -axis, the geometrical structure is symmetrical under rotations about the z -axis (see fig. 6.3).

Primary particles of a given kind, **KPARP**, are emitted from the active volume of the source, either with fixed energy **SE0** or with a specified (histogram-like) energy spectrum. The initial direction of the primary particles is sampled uniformly inside a cone of (semi-) aperture **SALPHA** and with central axis in the direction (**STHETA**, **SPHI**). Thus, **SALPHA** = 0 defines a monodirectional source and **SALPHA** = 180 deg corresponds to an isotropic source.

The program can simulate two different types of sources:

- a) An external point or extense (cylindrical) homogeneous source, defined separately from the geometry of the material system, with its centre at the point (**SX0**, **SY0**, **SZ0**).

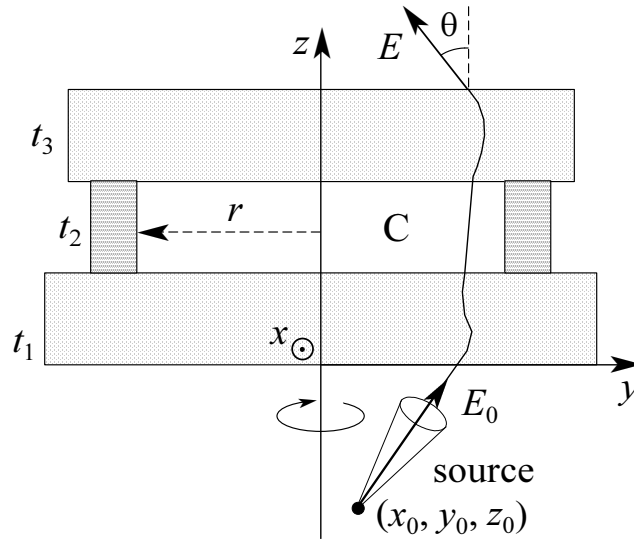


Figure 6.3: An example of cylindrical geometry, a cavity (C) with walls, with a point off-axis source. In this case, the material structure is symmetrical about the z -axis, but the radiation flux and other three-dimensional quantities (e.g. dose and deposited charge distributions) depend on the azimuthal angle ϕ .

The initial position of each primary particle is sampled uniformly within the volume of the source. Notice that when $SX0 = 0$, $SY0 = 0$ and $STHETA = 0$ or 180 deg, the source is axially symmetrical about the z -axis.

b) A set of internal sources spread over specified bodies, each one with uniform activity concentration. The original position of the primary particle is sampled uniformly within the active cylinder or ring, which is selected randomly with probability proportional to the total activity in its volume.

In the distributed form of the program, we assume that both the source and the material structure are symmetrical about the z -axis, because this eliminates the dependence on the azimuthal angle ϕ . The program takes advantage of this symmetry to tally 3D dose distributions. It is possible to consider geometries that are not axially symmetrical, but then the program only delivers values averaged over ϕ . To obtain the dependence of the angular distributions on the azimuthal angle, we need to increase the value of the parameter **NBPHM** (the maximum number of bins for ϕ , which is set equal to 1 in the distributed source file) and, in the input data file, set **NBPH** equal to **NBPHM**.

The source file **PENCYL.F** includes a (self-contained) set of geometry routines for tracking particles through multilayered cylindrical structures. These routines can be used for simulation even when the source is off-axis. Cylindrical geometries can be viewed with the program **GVIEWC** (which is similar to **GVIEW2D** and runs under Microsoft Windows). This program reads the geometry definition list from the input file and displays a two-dimensional map of the materials intersected by the window plane. It is useful for debugging the geometry definition.

PENCYL delivers detailed information on the transport and energy deposition, which includes energy and angular distributions of emerging particles, depth-dose distribution, depth-distribution of deposited charge, distributions of deposited energy in selected materials and 2D (depth-radius) dose and deposited charge distributions in selected bodies (cylinders). PENCYL can be directly used to study radiation transport in a wide variety of practical systems, e.g. planar ionization chambers, cylindrical scintillation detectors, solid-state detectors and multilayered structures.

6.2.3 Program PENDOSES

This MAIN program provides a practical example of simulation with complex material structures (quadric geometry only). It assumes a point source of primary particles at a given position $\mathbf{r}_0 = (X0, Y0, Z0)$ which emits particles in directions uniformly distributed in a cone with (semi)aperture **SALPHA** and central axis in the direction (**STHETA**, **SPHI**) [the same direction distribution assumed in the code PENCYL]. The geometry of the material system is described by means of the package PENGEO (chapter 5).

PENDOSES computes only the average energy deposited in each body per primary particle. With minor modifications, it also provides the probability distribution of the energy deposited in selected bodies or groups of bodies. It is a simple exercise to introduce a spatial grid, and the corresponding counters, and tally spatial dose distributions. Any future user of PENELOPE should become familiar with the programming details of PENDOSES before attempting her/his own application of PENELOPE.

6.2.4 Running the PENCYL program

The programs PENSLAB, PENCYL and PENDOSES operate in a similar way. They all read data from a corresponding input file and output the results in a number of files with fixed names¹. The input files also have similar structures and formats. For concreteness, here we describe that of PENCYL, which is the most versatile of the example programs.

Each line in the input data file of PENCYL consists of a 6-character keyword (columns 1-6) followed either by numerical data (in free format) or by a character string, which start at the 8th column. Keywords are explicitly used/verified by the program (which is case sensitive!). Notice also that the order of the data lines is important. The keyword “-----” (6 blanks, which we have denoted by “-”) indicates comment lines, these can be placed anywhere after the end of the geometry definition list. The program ignores any text following the first blank after the last numerical datum, or after the character string, in each line (thus, in the table given below, the comments in square brackets are ignored by the program). Lines with certain keywords (e.g., “SPECTR”) can appear an arbitrary number of times, limited only by the allocated amount of memory. The program assigns default values to many input variables; lines that declare default values

¹Warning: The programs overwrite older output files that are left in the working directory. You should save all result files on a separate directory before running the program again.

may be removed from the input file. Notice that the default source is a pencil beam that moves upwards along the z -axis.

- Structure of the PENCYL input file (the 72-column rulers are just for visual aid, they do not form part of the input file)

```
.....+.....1.....+.....2.....+.....3.....+.....4.....+.....5.....+.....6.....+.....7..
```

TITLE Title of the job, up to 65 characters.

GSTART >>>>>>> Beginning of the geometry definition list.

LAYER ZLOW,ZHIG [Z_lower and Z_higher]

CENTRE XCEN,YCEN [X_centre and Y_centre]

CYLIND M,RIN,ROUT [Material, R_inner and R_outer]

GEND <<<<<<< End of the geometry definition list.

>>>>>>> Source definition.

SKPAR KPARP [Primary particles: 1=electron, 2=photon, 3=positron]

SENERG SEO [Initial energy (monoenergetic sources only)]

SPECTR Ei,Pi [E bin: lower-end and total probability]

SEXTND KL,KC,RELAC [Extended source in KL,KC and rel. activity conc.]

STHICK STHICK [Source thickness]

SRADII SRIN,SROUT [Source inner and outer radii]

SPOSIT SX0,SY0,SZO [Coordinates of the source centre]

SDIREC STHETA,SPHI [Beam axis direction angles, in deg]

SAPERT SALPHA [Beam aperture, in deg]

>>>>>>> Material data and simulation parameters.

NMAT NMAT [Number of different materials, .le.10]

SIMPAR M,EABS(1:3,M),C1,C2,WCC,WCR [Sim. parameters for material M]

PFNAME filename_0.ext [Material definition file, 18 characters]

>>>>>>> Counter array dimensions and pdf ranges.

NBE NBE,EMIN,EMAX [No. of energy bins, and E-interval]

NBTH NBTH [No. of bins for the polar angle THETA]

NBPH NBPH [No. of bins for the azimuthal angle PHI]

NBZ NBZ [No. of bins for the Z-coordinate]

NBR NBR [No. of radial bins]

NBTL NBTL,TLMIN,TLMAX [No. of track-length bins and TL-interval]

>>>>>>> Additional distributions to be tallied.

ABSEN MAT [Tally the distr. of absorbed E in material MAT]

DOSE2D KL,KC,NZ,NR [Tally 2D dose and charge distribns. in body KL,KC]

>>>>>>> Interaction forcing.

IFORCE KL,KC,KPAR,ICOL,FORCE,WL,WH [Interaction forcing parameters]

```

>>>>>>> Job properties
RESUME filename1.ext          [Resume from this dump file, 18 characters]
DUMPTO filename2.ext          [Generate this dump file, 18 characters]
NSIMSH NTOT                    [Desired number of simulated showers, max=2**31-1]
RSEED ISEED1, ISEED2           [Seeds of the random number generator]
TIME ITIME                     [Allotted simulation time, in sec]
....+....1....+....2....+....3....+....4....+....5....+....6....+....7..

```

The following listing describes the function of each of the keywords, the accompanying data and their default values.

TITLE ... title of the job (up to 65 characters).

-- Default: none (the input file must start with this line)

Geometry definition list ... begins with the line “GSTART” and ends with the line “GEND--” (notice the two blanks). The only allowed keywords in the geometry list are “GSTART”, “LAYER-”, “CENTRE”, “CYLIND” and “GEND--”. The line after “GSTART” must be a “LAYER-” line. Each “LAYER-” line contains the z -coordinates of its lower and upper limiting planes and is followed by a “CENTRE” line (optional) and by one or several “CYLIND” lines, which contain the inner and outer radii of the various concentric rings in the layer; empty layers are disregarded.

Layers must be defined in increasing order of heights, from bottom to top of the structure. If the “CENTRE” line is not entered, cylinders are assumed to be centered on the z -axis ($XCEN = YCEN = 0.0$). Cylinders have to be defined in increasing radial order, from the centre to the periphery. The two lengths in each “LAYER-” and “CYLIND” line must be entered in increasing order. The geometry definition list can be debugged/visualized with the code GVIEWC (operable under Microsoft Windows). Notice that GVIEWC reads the geometry directly from the PENCYL input data file (i.e. the first line in the geometry definition file must be the “TITLE-” line).

SKPAR ... kind of primary particle (1=electrons, 2=photons or 3=positrons).

-- Default: KPARP=1

SENERG ... for monoenergetic sources: initial energy SE0 of primary particles.

-- Default: SE0=1.0E6

SPECTR ... For sources with continuous (stepwise constant) energy spectra. Each “SPECTR” line gives the lower end-point of an energy bin of the source spectrum and the associated relative probability, integrated over the bin. Up to $NSEM = 200$ lines, in arbitrary order. The upper end of the spectrum is defined by entering a line with the upper energy value and null probability.

-- Default: none

SEXTND ... For internal extended sources, this line defines an active body KL, KC (the cylinder KC in layer KL) and its relative activity concentration, RELAC.

-- Default: none

Note: The labels KL, KC that identify each body are defined by the ordering in the input geometry list. These labels are written on the output geometry report.

STHICK ... For an external source, thickness (height) of the active volume of the source (cylinder or ring).

-- Default: STHICK=0.0

SRADII ... inner and outer radii of the active source volume.

-- Defaults: SRIN=0.0, SROUT=0.0

SPOSIT ... coordinates of the centre of the source volume.

-- Defaults: SX0=SY0=0, SZ0=-1.0E15

SDIREC ... polar angle θ and azimuthal angle ϕ of the source beam axis direction, in deg.

-- Defaults: STHETA=0.0, SPHI=0.0

SAPERT ... angular aperture α of the source beam, in deg.

-- Default: SALPHA=0.0

NMAT ... number of different materials (up to 10 with the original program dimensions). Materials are identified by their ordering in PENELOPE's input material data file.

-- Default: NMAT=1

SIMPAR ... set of simulation parameters for the M-th material; absorption energies, EABS(1:3,M), elastic scattering parameters, C1(M) and C2(M), and cutoff energy losses for inelastic collisions and bremsstrahlung emission, WCC(M) and WCR(M). One line for each material.

-- Defaults: EABS(1,M)=EABS(3,M)=0.01*EPMAX, EABS(2,M)=0.001*EPMAX
C1(M)=C2(M)=0.1, WCC=EABS(1,M), WCR=EABS(2,M)

EPMAX is the maximum energy of all particles found in the simulation (depends on the source energies).

PFNAME ... name of PENELOPE's input material data file (18 characters).

-- Default: 'material.mat'

NBE ... number of energy bins and limits of the interval where energy distributions are tallied.

-- Defaults: NBE=100, EMIN=0.0, EMAX=EPMAX

NBTH ... number of bins for the polar angle θ .

-- Default: NBTH=90

NBPH ... number of bins for the azimuthal angle ϕ .

-- Default: NBPH=1 (azimuthal average).

NBZ ... number of bins for the z -coordinate.

-- Default: NBZ=100

NBR ... number of bins for the radial variable, $r = (x^2 + y^2)^{1/2}$.

-- Default: NBR=100

NBTL ... number of bins for track-length distributions of primary particles. Limits of the interval where these distributions are tallied.
 -- Defaults: NBTL=100, TLMIN=0, TLMAX=2.5*RANGE(EPMAX,KPARP,1)

ABSEN ... indicates a material **M** for which we require the code to tally the distribution of absorbed energy (up to three different materials can be selected, a separate line for each).
 -- Default: off

DOSE2D ... the program will tally 2D, depth-radius, dose and deposited charge distributions in the body **KL**, **KC** (i.e. the cylinder **KC** of layer **KL**). The numbers **NZ** and **NR** of *z*- and *r*-bins have to be specified by the user, they must be between 1 and 100. Up to three different bodies can be selected, a **DOSE2D** line for each body.
 -- Default: off
 Note: The labels **KL**, **KC** that identify a given cylinder are defined by the ordering in the input geometry list. These labels are written on the output geometry report.

IFORCE ... activates forcing of interactions of type **ICOL** of particles **KPAR** in cylinder **KC** of layer **KL**. **FORCE** is the forcing factor and **WLOW**, **WHIG** are the limits of the weight window where interaction forcing is active.
 -- Default: no interaction forcing

RESUME ... the program will read the dump file named **filename1.ext** (18 characters) and resume the simulation from the point where it was left. Use this option very, *very* carefully. Make sure that the input data file is fully consistent with the one used to generate the dump file.
 -- Default: off

DUMPTO ... generate a dump file named **filename2.ext** (18 characters) after completing the simulation run. This allows resuming the simulation to improve statistics.
 -- Default: off

NSIMSH ... desired number of simulated showers. Notice that **NTOT** is an **INTEGER*4** value and, hence, it cannot exceed $2^{31} - 1$.
 -- Default: NTOT=2147 million

RSEED ... seeds of the random number generator.
 -- Default: ISEED1=12345; ISEED2=54321

TIME ... allotted simulation time, in sec.
 -- Default: ITIME=100

The program **PENCYL** (as well as the other example **MAIN** programs) is aborted when an incorrect input datum is found. The conflicting quantity usually appears in the last line of the output file. If the trouble is with arrays having dimensions smaller than required, the program indicates how the problem can be solved (this usually requires editing the source file, be careful).

The example of input file given below belongs to the **PENCYL** file set included in the distribution package. It corresponds to the simulation of a narrow photon beam with

$E_0 = 1.25$ MeV (roughly the average energy of gamma rays from ^{60}Co) entering a $3'' \times 3''$ NaI scintillation detector in an Al case, whose inner surface is partially covered by a layer of Al_2O_3 , which diffuses scintillation light back to the crystal and the photomultiplier. In the material data file **NAIAL.MAT**, the order of the materials is NaI (**MAT=1**), Al_2O_3 (**MAT=2**) and Al (**MAT=3**). The incident beam photons move along the z -axis with $\theta = 0$ deg (i.e. upwards) and impinge normally on the surface of the detector. The geometry is shown schematically in the insets of fig. 6.4, which displays two of the distributions generated by **PENCYL**. The plotted distributions were obtained from 5 million random showers; the error bars represent statistical uncertainties (3σ), which are pretty small in this case.

- Example input file of the **PENCYL** code.

```

.....1.....2.....3.....4.....5.....6.....7..
TITLE  Example from the distribution package...
GSTART NaI detector with Al cover and Al2O3 reflecting foil
LAYER      -0.24 -0.16  1
CENTRE      0.00  0.00
CYLIND    3  0.00  4.05
LAYER      -0.16  0.00  2
CYLIND    2  0.00  3.97
CYLIND    3  3.97  4.05
LAYER      0.00  7.72  3
CYLIND    1  0.00  3.81
CYLIND    2  3.81  3.97
CYLIND    3  3.97  4.05
LAYER      7.72  9.72  4
CYLIND    3  0.00  4.05
GEND
SKPAR  2          [Primary particles: 1=electron, 2=photon, 3=positron]
SENERG 1.25E6      [Initial energy (monoenergetic sources only)]
SPOSIT 0.0 0.0 -10.0 [Coordinates of the source centre]
NMAT   3          [Number of different materials, .le.10]
SIMPAR 1 1.0E5 1000 1.0E5 0.1 0.1 1.0E4 1000 [M,EABS,C1,C2,WCC,WCR]
SIMPAR 2 1.0E5 1000 1.0E5 0.1 0.1 1.0E4 1000 [M.EABS,C1,C2,WCC,WCR]
SIMPAR 3 1.0E5 1000 1.0E5 0.1 0.1 1.0E4 1000 [M,EABS,C1,C2,WCC,WCR]
PFNAME naial.mat  [Material definition file, 18 characters]
ABSEN  1          [Tally the distr. of absorbed E in this material]
DOSE2D 3 1 50 50  [Tally 2D dose and charge distr. in this body]
RESUME lastdump.dat [Read from this dump file, 18 characters]
DUMPTO lastdump.dat [Generate this dump file, 18 characters]
NSIMSH 1000       [Desired number of simulated showers, max=2**31-1]
TIME   300        [Allotted simulation time, in sec]
.....1.....2.....3.....4.....5.....6.....7..

```

The upper plot in fig. 6.4 shows the distribution of energy E_d deposited into the NaI crystal volume (per primary photon). The lower figure displays the distribution (per primary photon) of the energy E_b of “backscattered” photons, i.e. photons that emerge from the system pointing “downwards”, with $W = \cos \theta < 0$. These distributions show three conspicuous structures that arise from backscattering of incident photons in the crystal volume or in the Al backing (B), escape of one of the ~ 511 keV x-rays resulting from positron annihilation (A) and escape of ~ 30 keV iodine K x-rays (C). The peak A is so small because pair production is a relatively unlikely process for 1.25 MeV photons (the energy is too close to the threshold).

6.3 Selecting the simulation parameters

The speed and accuracy of the simulation of electrons and positrons is determined by the values of the simulation parameters E_{abs} , C_1 , C_2 , W_{cc} , W_{cr} and s_{max} , which are selected by the user for each material in the simulated structure². Here we summarize the rules for assigning “safe” values to these parameters.

The absorption energies E_{abs} are determined either by the characteristics of the experiment or by the required space resolution. If we want to tally dose or deposited-charge distributions, E_{abs} should be such that the residual range $R(E_{\text{abs}})$ of electrons/positrons is less than the typical dimensions of the volume bins used to tally these distributions³. In other cases, it is advisable to run short simulations (for the considered body alone) with increasing values of E_{abs} (starting from 100 eV) to study the effect of this parameter on the results.

The allowed values of the elastic scattering parameters C_1 and C_2 are limited to the interval (0,0.2). For the present version of PENELOPE, these parameters have a very weak influence on the results, weaker than for previous versions of the code. As discussed in section 4.4.1, this is mostly due to the improved modelling of soft energy losses and to the consideration of the energy dependence of the hard mean free paths (see sections 4.2 and 4.3). Our recommended practice is to set $C_1 = C_2 = 0.05$, which is fairly conservative, as shown by the example given below. Before increasing the value of any of these parameters, it is advisable to perform short test simulations to verify that with the augmented parameter value the results remain essentially unaltered (and that the simulation runs faster; if there is no gain in speed, keep the conservative values).

We have already indicated that the cutoff energies W_{cc} and W_{cr} have a very weak influence on the accuracy of the results provided only that they are both smaller than the width of the bins used to tally energy distributions. When energy distributions are of no interest, our recommendation is setting these cutoff energies equal to one hundredth of the typical energy of primary particles.

²To specify simulation parameters for a single body we can simply assign a specific material to this body, different from that of other bodies of the same composition.

³PENELOPE prints tables of electron and positron ranges if subroutine PEINIT is invoked with INFO=3 or larger.

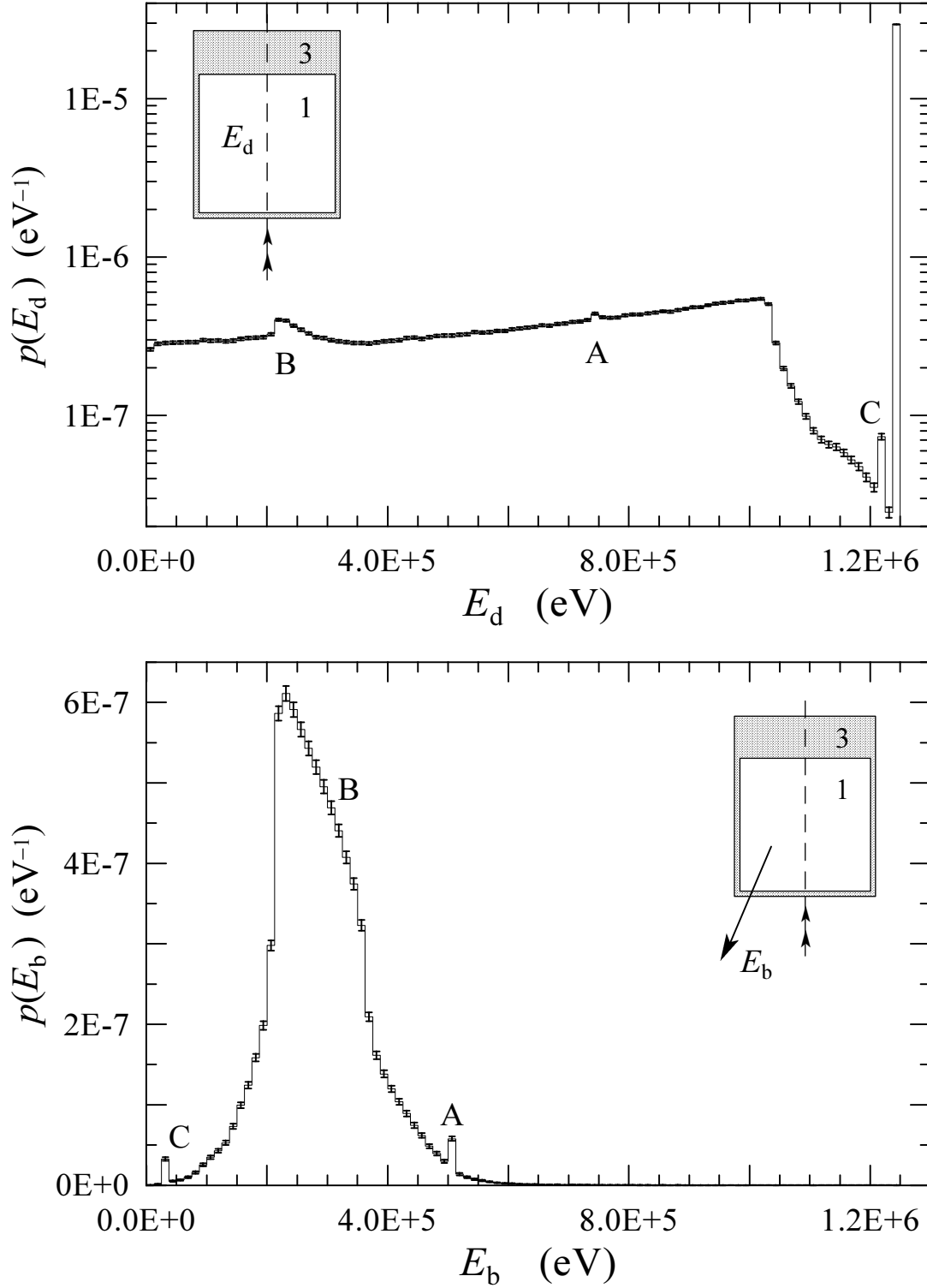


Figure 6.4: Partial results from PENCYL for the NaI photon detector described in the text. Top: distribution of energy deposited in the NaI crystal (MAT=1). Bottom: energy distribution of backscattered photons.

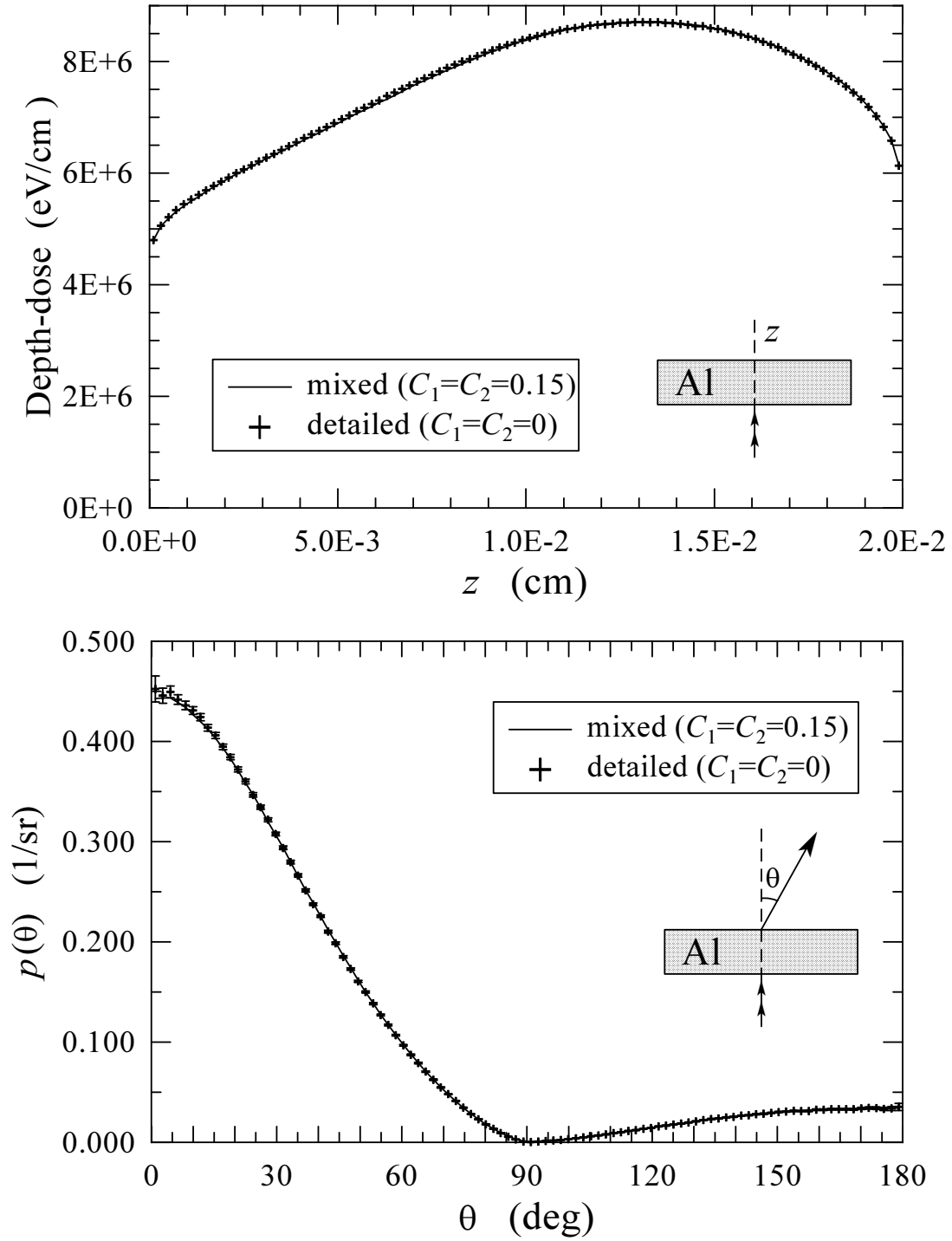


Figure 6.5: Results from PENSLAB for a 500 keV electron beam impinging normally on the surface of a 200- μ m-thick aluminium slab (further details are given in the text). Top: depth-dose distribution within the slab. Bottom: angular distribution of emerging (transmitted and backscattered) electrons (primary and secondary).

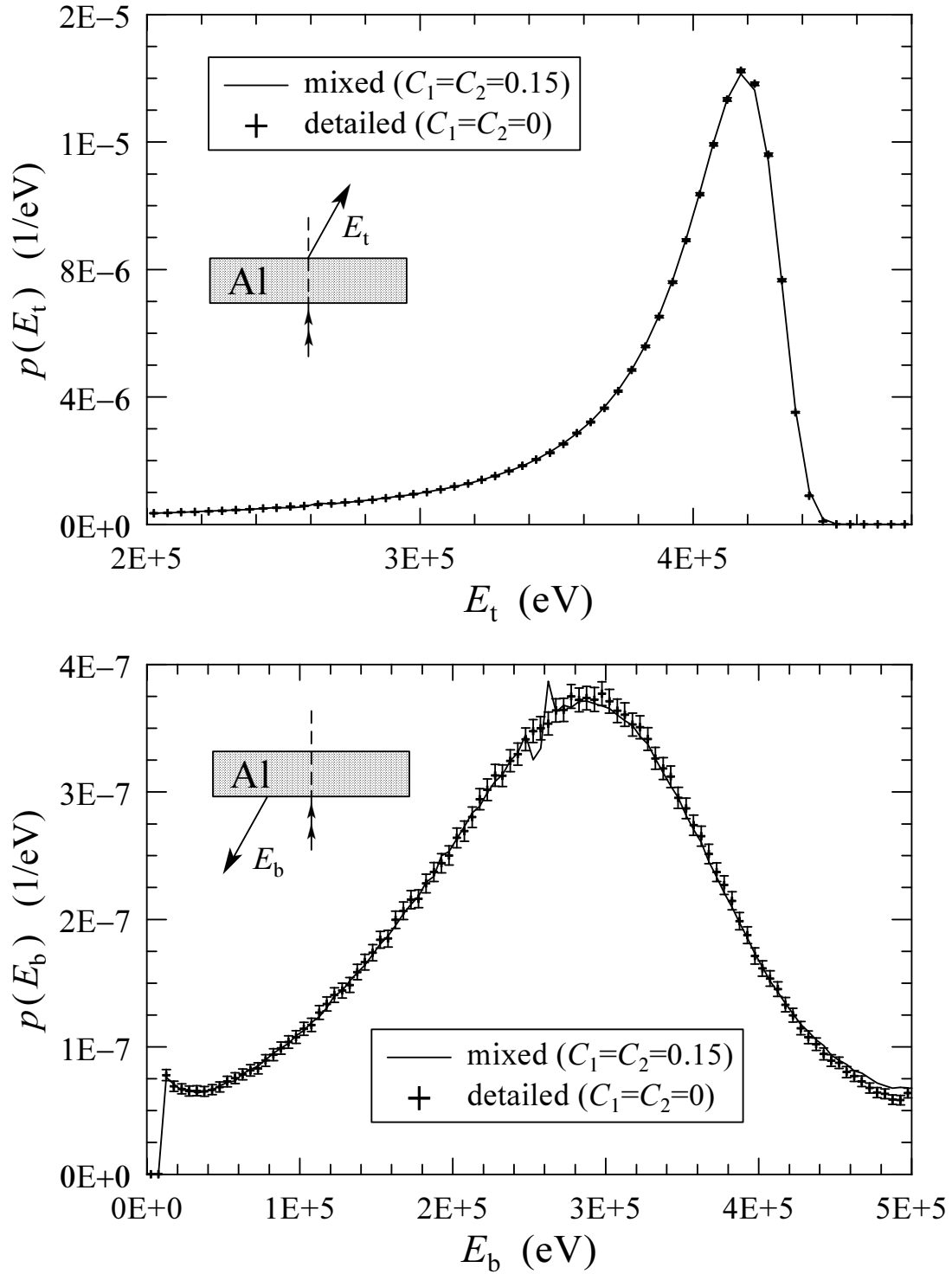


Figure 6.6: Results from PENSLAB for a 500 keV electron beam impinging normally on the surface of a 200- μm -thick aluminium slab (further details are given in the text). Top: energy distribution of transmitted electrons. Bottom: energy distribution of backscattered electrons. Secondary electrons are included in both cases.

The maximum allowed step length s_{\max} (denoted by **DSMAX** in the FORTRAN source files) should be less than one tenth of the characteristic thickness of the body where the particle moves. This ensures that, on average, there will be more than 20 soft events⁴ (hinges) along a typical electron/positron track within that body, which is enough to “wash out” the details of the artificial distributions used to sample these events. Notice however that PENELOPE internally forces the step length to be less than $\sim 3\lambda_T^{(h)}$ (see section 4.4). Therefore, for thick bodies (thicker than $\sim 20\lambda_T^{(h)}$), we can set $s_{\max} = 10^{35}$, or some other very large value, to switch off the external step-length control.

The **MAIN** program **PENSLAB** can be readily used to study the effect of the simulation parameters for a material body of a given characteristic thickness. As an example, figs. 6.5 and 6.6 display partial results from a **PENSLAB** simulation for a parallel electron beam of 500 keV impinging normally on the surface of a 200- μm -thick aluminium slab. The absorption energies were set equal to 10 keV (for all kinds of particles) and W_{cr} was given a negative value, which compels PENELOPE to set $W_{\text{cr}} = 10$ eV and to disregard emission of soft bremsstrahlung (with $W < 10$ eV). We ran **PENSLAB** using $W_{\text{cc}} = 0$ and $C_1 = C_2 = 0$; in this case, PENELOPE performs purely detailed, collision by collision, simulation and, therefore, it provides exact results (affected only by statistical uncertainties and by inaccuracies of the physical interaction model). Differences between these results and those from mixed simulation are then completely attributable to the approximations in our mixed transport algorithm. To our knowledge, no other high-energy transport code allows detailed simulation and this kind of direct validation of the electron/positron transport mechanics.

In figs. 6.5 and 6.6 we compare results from the detailed simulation (7.5 million showers) with those from a mixed simulation using $W_{\text{cc}} = 1$ keV and $C_1 = C_2 = 0.15$ (20 million simulated showers); the error bars indicate statistical uncertainties (3σ). With these relatively high values of C_1 and C_2 , mixed simulation is quite fast, the speed (generated showers per second) being about 45 times higher than that of the detailed simulation. As shown in the plots, mixed simulation results are practically equivalent to those from detailed simulation. It should be noted that backscattering, fig. 6.6b, is one of the most difficult cases to study, because it involves transport near and across an interface that is far from electronic equilibrium. The only visible artifact is a kind of singularity in the energy distribution of backscattered electrons at ~ 250 keV (which averages to the correct value and, therefore, would not be seen in a coarser energy grid). This artifact is also present in the energy distribution of transmitted electrons, but hardly visible in the scale of fig. 6.6a.

6.4 The code SHOWER

Monte Carlo simulation has proven to be a very valuable tool for education. In the past, radiation physics used to be considered as a tough subject, mostly because high-energy

⁴PENELOPE randomizes s_{\max} in such a way that the actual step lengths never exceeds the value s_{\max} set by the user and, on average, is equal to $s_{\max}/2$.

radiation is well outside the realm of daily experience. Nowadays, by simply running a transport simulation code on a personal computer we can learn more than from tens of obscure empirical formulas and numerical tables, and eventually “understand” many aspects of radiation transport (those for which we have run the simulation code and “digested” the results).

The PENELOPE distribution package includes a binary file named `SHOWER` that generates electron-photon showers within a slab (of one of the 279 materials defined in `PDCOMPOS.TAB`) and displays them (projected) on the computer screen plane. The current version operates only under Microsoft Windows. The program is self-explanatory, and requires only a small amount of information from the user, which is entered from the keyboard, in response to prompts from the program. Electron, photon and positron tracks are displayed in different colors and intensities that vary with the energy of the particle. It is worth mentioning that the maximum number of showers that can be plotted in a single shot is limited to 50, because the screen may become too messy. Generating this small number of showers takes a short time, of the order of a few seconds, even on modest personal computers (provided only that the absorption energies are sensibly chosen).

Once on the graphical screen, the view plane can be rotated about the horizontal screen axis by typing “r” and the rotation angle in degrees; the screen plane can also be rotated progressively, by 15 deg steps, by pressing the “enter” key repeatedly. Entering the single-character command “n” erases the screen and displays a new shower. Observation of single showers projected on a revolving plane gives a truly three-dimensional perspective of the transport process.

6.5 Installation

The FORTRAN77 source files of PENELOPE, the examples and auxiliary programs and the database are distributed as a single ZIP compressed file named `PENELOPE.ZIP`. To extract the files, keeping the directory structure, create the directory `PENELOPE` in your hard disk, copy the distribution file `PENELOPE.ZIP` into this directory and, from there, inflate (unzip) it. The directory structure and contents of the PENELOPE code system are the following (see fig. 6.7):

- Subdirectory `FSOURCE`. It contains the following 6 files:

`MANUAL.TXT` . . . abridged manual with general information.

`PENELOPE.F` . . . simulation subroutine package.

`PENGEOM.F` . . . modular quadric geometry subroutine package (handles systems with up to 250 surfaces and 125 bodies).

`PENVARED.F` . . . variance-reduction subroutines (splitting, Russian roulette and interaction forcing).

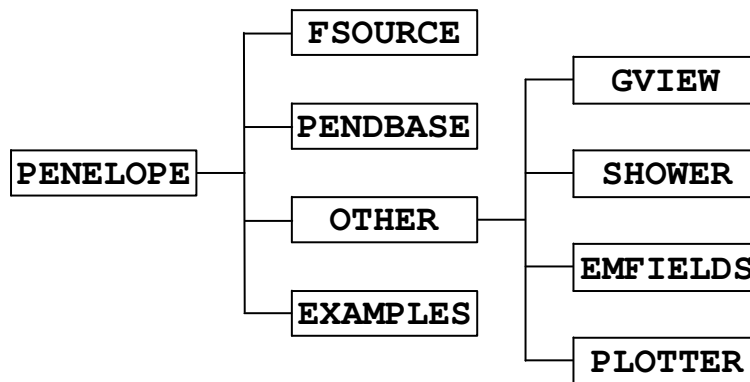


Figure 6.7: Directory tree of the PENELOPE code system.

MATERIAL.F ... main program to generate material data files.

TABLES.F ... main program to tabulate interaction data (mean free paths, ranges, stopping powers, ...) of particles in a given material. It also determines interpolated values.

- Subdirectory **EXAMPLES**. It contains the following 11 files:

PENSLAB.F ... main program for particle transport in a slab.

PENSLAB.IN ... sample input data file of **PENSLAB**.

AL.MAT ... Material data file for **PENSLAB**.

PENCYL.F ... main program for multilayered cylindrical geometries and axially symmetric beams.

PENCYL.IN ... sample input data file of **PENCYL**. Describes the same geometry as **PENDOSSES.GEO**.

PENDOSSES.F ... main program for arbitrary quadric geometries.

PENDOSSES.IN ... sample input data file of **PENDOSSES**.

PENDOSSES.GEO ... geometry definition file for **PENDOSSES**.

NAIAL.MAT ... material data file for **PENCYL** and **PENDOSSES**. Illustrates the use of multiple materials.

TIMER.F ... generic clock subroutine. It gives the execution time in seconds.

TIMER works with the Compaq Visual Fortran 6.5 compiler and with the g77 Fortran compiler of the Free Software Foundation.

The compact G77 for Win32 (Windows 9x/NT/2000/XP) package can be downloaded from <http://www.geocities.com/Athens/Olympus/5564>.

g77 is the default FORTRAN compiler in most Linux distributions.

NOTIMER.F ... fake clock subroutine. To be used with “unfamiliar” compilers for which a proper timing routine is not known/available. It gives a constant time (1 sec).

To get the executable file of MATERIAL, compile and link the files MATERIAL.F and PENELOPE.F. This executable file must be placed and run in the same subdirectory as the database files (PENDBASE).

The executable files of PENSLAB, PENCYL and PENDOSES are obtained by compiling and linking the following groups of source files:

```
PENSLAB :  PENSLAB.F, PENELOPE.F, TIMER.F
PENCYL  :  PENCYL.F, PENELOPE.F, PENVARED.F, TIMER.F
PENDOSES:  PENDOSES.F, PENELOPE.F,  PENGEO.M.F, TIMER.F
```

The simulation programs are written in standard FORTRAN77 language, so that they should run on any computer. The only exception is the clock subroutine TIMER.F, which must be adapted to your computer's compiler.

- Subdirectory PENDBASE. PENELOPE's database. 465 files with the extension ".TAB" and names beginning with the letters "PD" (for details, see section 6.1.1).
- Subdirectory OTHER. Consists of the following subdirectories,

GVIEW ... Contains the geometry viewers GVIEW2D, GVIEW3D and GVIEWC, that are operable under Microsoft Windows, and several examples of geometry definition files.

EMFIELDS ... Contains the subroutine package PENFIELD.F, which does simulation of electron/positron transport under external static magnetic and electric fields (see appendix C), and examples of programs that use it.

SHOWER ... Contains a single binary file named SHOWER.EXE, which operates only under Microsoft Windows. This code generates electron-photon showers within a slab and displays them projected on the screen. To use the SHOWER viewer, just copy the file SHOWER.EXE into the directory PENDBASE and run it from there. This little tool is particularly useful for teaching purposes, it makes radiation physics "visible".

PLOTTER ... The programs PENSLAB and PENCYL generate multiple files with simulated probability distribution functions. Each output file has a heading describing its content, which is in a format ready for visualization with a plotting program. We use GNUPLOT, which is small in size, available for various platforms (including Linux and Microsoft Windows) and free (distribution sites are listed at the Gnuplot Central site, <http://www.gnuplot.info>). The directory PLOTTER contains GNUPLOT scripts that plot the probability distributions evaluated by the simulation codes on your terminal. For instance, after running PENSLAB you can visualize the results by simply 1) copying the file PENSLAB.GNU from the directory PLOTTER to the directory that contains the results and 2) entering the command "GNUPLOT PENSLAB.GNU" (or clicking the icon).

Appendix A

Collision kinematics

To cover the complete energy range of interest in radiation transport studies we use relativistic kinematics. Let \tilde{P} denote the energy-momentum 4-vector of a particle, i.e.

$$\tilde{P} = (\mathcal{W}c^{-1}, \mathbf{p}), \quad (\text{A.1})$$

where \mathcal{W} and \mathbf{p} are the total energy (including the rest energy) and momentum respectively and c is the velocity of light in vacuum. The product of 4-vectors, defined by

$$(\tilde{P}\tilde{P}') = \mathcal{W}\mathcal{W}'c^{-2} - \mathbf{p}\cdot\mathbf{p}', \quad (\text{A.2})$$

is invariant under Lorentz transformations. The rest mass m of a particle determines the invariant length of its energy-momentum,

$$(\tilde{P}\tilde{P}) = \mathcal{W}^2c^{-2} - \mathbf{p}^2 = (mc)^2. \quad (\text{A.3})$$

The kinetic energy E of a massive particle ($m \neq 0$) is defined as

$$E = \mathcal{W} - mc^2, \quad (\text{A.4})$$

where mc^2 is the rest energy. The magnitude of the momentum is given by

$$(cp)^2 = E(E + 2mc^2). \quad (\text{A.5})$$

In terms of the velocity \mathbf{v} of the particle, we have

$$E = (\gamma - 1)mc^2 \quad \text{and} \quad \mathbf{p} = \beta\gamma mc\hat{\mathbf{v}}, \quad (\text{A.6})$$

where

$$\beta \equiv \frac{v}{c} = \sqrt{\frac{\gamma^2 - 1}{\gamma^2}} = \sqrt{\frac{E(E + 2mc^2)}{(E + mc^2)^2}} \quad (\text{A.7})$$

is the velocity of the particle in units of c and

$$\gamma \equiv \sqrt{\frac{1}{1 - \beta^2}} = \frac{E + mc^2}{mc^2} \quad (\text{A.8})$$

is the total energy in units of the rest energy. From the relation (A.5), it follows that

$$E = \sqrt{(cp)^2 + m^2c^4} - mc^2 \quad (\text{A.9})$$

and

$$\frac{dp}{dE} = \frac{1}{v} = \frac{1}{c\beta}. \quad (\text{A.10})$$

For a photon (and any other particle with $m = 0$), the energy and momentum are related by

$$E = cp. \quad (\text{A.11})$$

A.1 Two-body reactions

Consider a reaction in which a projectile “1” collides with a target “2” initially at rest in the laboratory frame of reference. We limit our study to the important case of two-body reactions in which the final products are two particles, “3” and “4”. The kinematics of such reactions is governed by energy and momentum conservation.

We take the direction of movement of the projectile to be the z -axis, and set the x -axis in such a way that the reaction plane (i.e. the plane determined by the momenta of particles “1”, “3” and “4”) is the x - z plane. The energy-momentum 4-vectors of the projectile, the target and the reaction products are then (see fig. A.1)

$$\tilde{P}_1 = (\mathcal{W}_1c^{-1}, 0, 0, p_1) \quad (\text{A.12a})$$

$$\tilde{P}_2 = (m_2c, 0, 0, 0) \quad (\text{A.12b})$$

$$\tilde{P}_3 = (\mathcal{W}_3c^{-1}, p_3 \sin \theta_3, 0, p_3 \cos \theta_3) \quad (\text{A.12c})$$

$$\tilde{P}_4 = (\mathcal{W}_4c^{-1}, -p_4 \sin \theta_4, 0, p_4 \cos \theta_4) \quad (\text{A.12d})$$

Energy and momentum conservation is expressed by the 4-vector equation

$$\tilde{P}_1 + \tilde{P}_2 = \tilde{P}_3 + \tilde{P}_4. \quad (\text{A.13})$$

From this equation, the angles of emergence of the final particles, θ_3 and θ_4 , are uniquely determined by their energies, \mathcal{W}_3 and \mathcal{W}_4 . Thus,

$$\begin{aligned} m_4^2c^2 &= (\tilde{P}_4\tilde{P}_4) = (\tilde{P}_1 + \tilde{P}_2 - \tilde{P}_3)(\tilde{P}_1 + \tilde{P}_2 - \tilde{P}_3) \\ &= (\tilde{P}_1\tilde{P}_1) + (\tilde{P}_2\tilde{P}_2) + (\tilde{P}_3\tilde{P}_3) + 2(\tilde{P}_1\tilde{P}_2) - 2(\tilde{P}_1\tilde{P}_3) - 2(\tilde{P}_2\tilde{P}_3) \\ &= m_1^2c^2 + m_2^2c^2 + m_3^2c^2 + 2\mathcal{W}_1\mathcal{W}_2c^{-2} \\ &\quad - 2(\mathcal{W}_1\mathcal{W}_3c^{-2} - p_1p_3 \cos \theta_3) - 2\mathcal{W}_2\mathcal{W}_3c^{-2}, \end{aligned} \quad (\text{A.14})$$

and it follows that

$$\cos \theta_3 = \frac{m_4^2c^4 - m_1^2c^4 - m_2^2c^4 - m_3^2c^4 + 2\mathcal{W}_1(\mathcal{W}_3 - \mathcal{W}_2) + 2\mathcal{W}_2\mathcal{W}_3}{2(\mathcal{W}_1^2 - m_1^2c^4)^{1/2}(\mathcal{W}_3^2 - m_3^2c^4)^{1/2}}. \quad (\text{A.15})$$

Clearly, by symmetry, we can obtain a corresponding expression for $\cos \theta_4$ by interchanging the indices 3 and 4

$$\cos \theta_4 = \frac{m_3^2 c^4 - m_1^2 c^4 - m_2^2 c^4 - m_4^2 c^4 + 2\mathcal{W}_1(\mathcal{W}_4 - \mathcal{W}_2) + 2\mathcal{W}_2\mathcal{W}_4}{2(\mathcal{W}_1^2 - m_1^2 c^4)^{1/2}(\mathcal{W}_4^2 - m_4^2 c^4)^{1/2}}. \quad (\text{A.16})$$

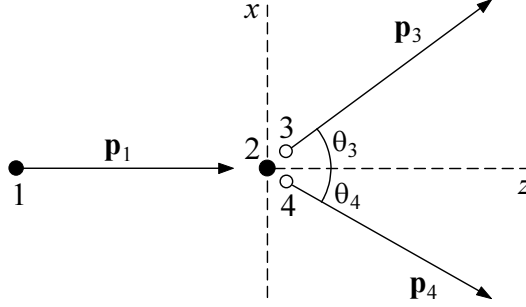


Figure A.1: Kinematics of two-body reactions.

The different two-body reactions found in Monte Carlo simulation of coupled electron-photon transport can be characterized by a single parameter, namely the energy of one of the particles that result from the reaction. The energy of the second particle is determined by energy conservation. Eqs. (A.15) and (A.16) then fix the polar angles, θ_3 and θ_4 , of the final directions. Explicitly, we have

- Binary collisions of electrons and positrons with free electrons at rest.

Projectile: Electron or positron $m_1 = m_e, \quad \mathcal{W}_1 = E + m_e c^2.$

Target: Electron $m_2 = m_e, \quad \mathcal{W}_2 = m_e c^2.$

Scattered particle: $m_3 = m_e, \quad \mathcal{W}_3 = E - W + m_e c^2.$

Recoil electron: $m_4 = m_e, \quad \mathcal{W}_4 = W + m_e c^2.$

$$\cos \theta_3 = \left(\frac{E - W}{E} \frac{E + 2m_e c^2}{E - W + 2m_e c^2} \right)^{1/2}, \quad (\text{A.17})$$

$$\cos \theta_4 = \left(\frac{W}{E} \frac{E + 2m_e c^2}{W + 2m_e c^2} \right)^{1/2}. \quad (\text{A.18})$$

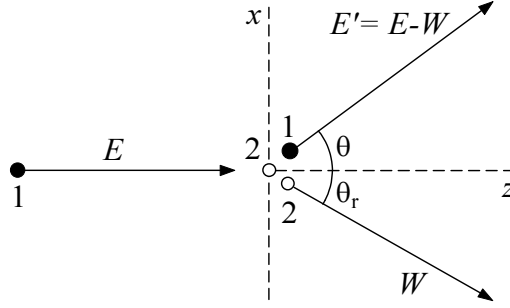
- Compton scattering of photons by free electrons at rest.

Projectile: Photon $m_1 = 0, \quad \mathcal{W}_1 = E \equiv \kappa m_e c^2.$

Target: Electron $m_2 = m_e, \quad \mathcal{W}_2 = m_e c^2.$

Scattered photon: $m_3 = 0, \quad \mathcal{W}_3 \equiv \tau E.$

Recoil electron: $m_4 = m_e, \quad \mathcal{W}_4 = m_e c^2 + (1 - \tau)E.$

**Figure A.2:** Kinematics of elastic collisions.

In the case of collisions of particles with equal mass, $m = M$, this expression simplifies to

$$W = \frac{E(E + 2mc^2) \sin^2 \theta}{E \sin^2 \theta + 2mc^2} \quad \text{if } M = m. \quad (\text{A.26})$$

In this case, θ can only take values less than 90 deg. For $\theta = 90$ deg, we have $W = E$ (i.e. the full energy and momentum of the projectile are transferred to the target). Notice that for binary collisions of electrons and positrons ($m = m_e$), the relation (A.26) becomes identical to (A.17).

For elastic collisions of electrons by atoms and ions, the mass of the target is much larger than that of the projectile and eq. (A.25) becomes

$$W = \frac{[(E + mc^2) \sin^2 \theta + Mc^2(1 - \cos \theta)] E(E + 2mc^2)}{(E + Mc^2)^2 - E(E + 2mc^2) \cos^2 \theta} \quad \text{if } M \gg m. \quad (\text{A.27})$$

The non-relativistic limit ($c \rightarrow \infty$) of this expression is

$$W = \frac{2m}{M}(1 - \cos \theta)E \quad \text{if } M \gg m \text{ and } E \ll mc^2. \quad (\text{A.28})$$

A.2 Inelastic collisions of charged particles

We consider here the kinematics of inelastic collisions of charged particles of mass m and velocity \mathbf{v} as seen from a frame of reference where the stopping medium is at rest (laboratory frame). Let \mathbf{p} and E be the momentum and the kinetic energy of the projectile just before an inelastic collision, the corresponding quantities after the collision are denoted by \mathbf{p}' and $E' = E - W$, respectively. Evidently, for positrons the maximum energy loss is $W_{\max} = E$. In the case of ionization by electron impact, owing to the indistinguishability between the projectile and the ejected electron, the maximum energy loss is $W_{\max} \simeq E/2$ (see section 3.2). The momentum transfer in the collision is $\mathbf{q} \equiv \mathbf{p} - \mathbf{p}'$. It is customary to introduce the recoil energy Q defined by

$$Q(Q + 2m_e c^2) = (cq)^2 = c^2 (p^2 + p'^2 - 2pp' \cos \theta), \quad (\text{A.29})$$

where m_e is the electron rest mass and $\theta = \arccos(\hat{\mathbf{p}} \cdot \hat{\mathbf{p}}')$ is the scattering angle. Equivalently, we can write

$$Q = \sqrt{(cq)^2 + m_e^2 c^4} - m_e c^2. \quad (\text{A.30})$$

Notice that, when the collision is with a free electron at rest, the energy loss is completely transformed into kinetic energy of the recoiling electron, i.e. $Q = W$. For collisions with bound electrons, the relation $Q \simeq W$ still holds for hard ionizing collisions (that is, when the energy transfer W is much larger than the ionization energy of the target electron so that binding effects are negligible).

The kinematically allowed recoil energies lie in the interval $Q_- < Q < Q_+$, with end points given by eq. (A.29) with $\cos \theta = +1$ and -1 , respectively. That is

$$\begin{aligned} Q_{\pm} &= \sqrt{(cp \pm cp')^2 + m_e^2 c^4} - m_e c^2 \\ &= \sqrt{\left[\sqrt{E(E + 2mc^2)} \pm \sqrt{(E - W)(E - W + 2mc^2)} \right]^2 + m_e^2 c^4} - m_e c^2. \end{aligned} \quad (\text{A.31})$$

Notice that, for $W < E$, Q_+ is larger than W and $Q_- < W$. When $W \ll E$, expression (A.31) is not suitable for evaluating Q_- since it involves the subtraction of two similar quantities. In this case, it is more convenient to use the approximate relation

$$cp - cp' \simeq c \left(\frac{dp}{dE} W - \frac{1}{2} \frac{d^2 p}{dE^2} W^2 \right) = \frac{W}{\beta} \left(1 + \frac{1}{2\gamma(\gamma + 1)} \frac{W}{E} \right) \quad (\text{A.32})$$

and calculate Q_- as

$$Q_- \simeq \sqrt{(cp - cp')^2 + m_e^2 c^4} - m_e c^2 \quad (\text{A.33})$$

or, if $cp - cp' \ll m_e c^2$,

$$Q_- \simeq \frac{1}{2} \frac{(cp - cp')^2}{m_e c^2} - \frac{1}{8} \frac{(cp - cp')^4}{(m_e c^2)^3}. \quad (\text{A.34})$$

Thus, for $E \gg W$,

$$Q_-(Q_- + 2m_e c^2) \simeq W^2 / \beta^2. \quad (\text{A.35})$$

In the non-relativistic limit,

$$Q \equiv q^2 / 2m_e, \quad Q_{\pm} = \left[E^{1/2} \pm (E - W)^{1/2} \right]^2. \quad (\text{A.36})$$

From (A.31), it is clear that the curves $Q = Q_-(W)$ and $Q = Q_+(W)$ vary monotonously with W and intersect at $W = E$. Thus, they define a single continuous function $W = W_m(Q)$ in the interval $0 < Q < Q_+(0)$. By solving the eqs. $Q = Q_{\pm}(W_m)$ we obtain

$$W_m(Q) = E + mc^2 - \sqrt{\left[\sqrt{E(E + 2mc^2)} - \sqrt{Q(Q + 2m_e c^2)} \right]^2 + m^2 c^4}, \quad (\text{A.37})$$

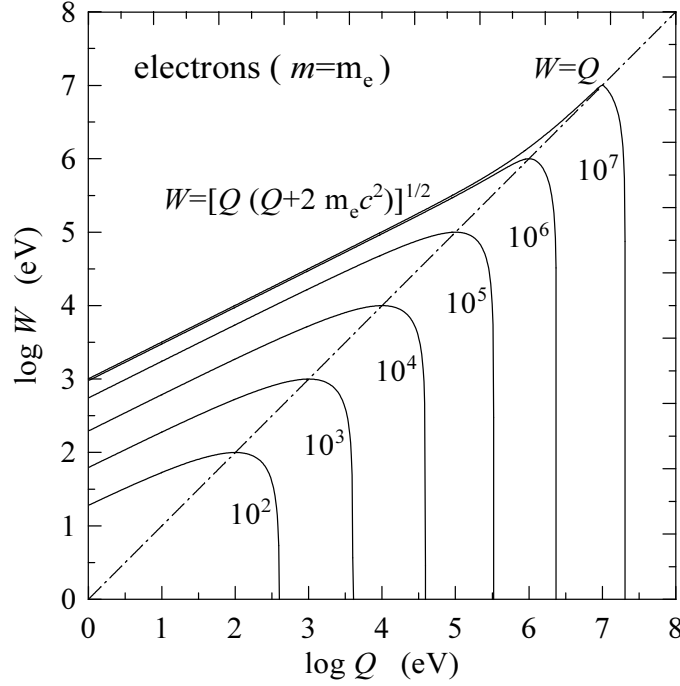


Figure A.3: Domains of kinematically allowed transitions in the (Q, W) plane for electrons/positrons. The curves represent the maximum allowed energy loss $W_m(Q)$, given by eq. (A.37), for electrons with the indicated kinetic energies (in eV). When E increases, $W_m(Q)$ approaches the vacuum photon line, $W = [Q(Q + 2m_e c^2)]^{1/2}$, which is an absolute upper bound for the allowed energy losses.

which, when $W \ll E$, reduces to

$$W_m(Q) \simeq \beta \sqrt{Q(Q + 2m_e c^2)}. \quad (\text{A.38})$$

Now it follows that, for given values of E and Q [$< Q_+(0)$], the only kinematically allowed values of the energy loss are those in the interval $0 < W < W_m(Q)$ (see fig. A.3).

For a given energy loss W , the quantity

$$q_{\min} \equiv c^{-1} \sqrt{Q_-(Q_- + 2m_e c^2)}, \quad (\text{A.39})$$

is the minimum value of the momentum transfer in an inelastic collision, which occurs when $\theta = 0$. q_{\min} is always larger than W/c . When the energy of the projectile increases, $\beta \rightarrow 1$ and q_{\min} decreases approaching (but never reaching) the value W/c . It is worth recalling that a photon of energy W in vacuum has a linear momentum $q = W/c$ and, hence, interactions consisting of emission of bare photons would be located on the line $Q(Q + 2m_e c^2) = W^2$ of the (Q, W) plane, the so-called vacuum photon line. This line, lies outside the kinematically allowed region, i.e. the “recoil” energy of the photon is less than Q_- (see fig. A.3). Therefore, when the target is a single atom, the emission of

photons by the projectile is not possible¹. When the energy E of the projectile increases, Q_- decreases and tends to the photon line when β tends to unity. Hence, emission of photons by ultrarelativistic projectiles in low-density media is barely prevented by energy and momentum conservation. Generally speaking, as the interaction involves the exchange of a virtual photon, the DCS increases as the photon becomes more real, that is as we approach the photon line. For a dilute gas, this causes a gradual increase of the cross section with the projectile energy when $\beta \rightarrow 1$.

The scattering angle θ is related to the energy loss through

$$\cos \theta = \frac{(cp)^2 + (cp')^2 - Q(Q + 2m_e c^2)}{2(cp)(cp)}. \quad (\text{A.40})$$

The recoil angle θ_r between \mathbf{p} and \mathbf{q} is given by

$$\cos \theta_r = \frac{(cp)^2 - (cp')^2 + (cq)^2}{2(cp)(cq)}, \quad (\text{A.41})$$

which can also be written in the form

$$\cos^2 \theta_r = \frac{W^2/\beta^2}{Q(Q + 2m_e c^2)} \left(1 + \frac{Q(Q + 2m_e c^2) - W^2}{2W(E + mc^2)} \right)^2. \quad (\text{A.42})$$

For heavy ($m \gg m_e$) high-energy projectiles and collisions such that $Q \ll E$ and $W \ll E$,

$$\cos^2 \theta_r \simeq \frac{W^2/\beta^2}{Q(Q + 2m_e c^2)} \simeq \frac{Q_-(Q_- + 2m_e c^2)}{Q(Q + 2m_e c^2)}. \quad (\text{A.43})$$

¹In a condensed medium, ultrarelativistic projectiles can emit real photons (Cerenkov radiation) under certain, quite restricting circumstances (see e.g. Jackson, 1975).

Appendix B

Numerical tools

B.1 Cubic spline interpolation

In this section we follow the presentation of Maron (1982). Suppose that a function $f(x)$ is given in numerical form, i.e. as a table of values

$$f_i = f(x_i) \quad (i = 1, \dots, N). \quad (\text{B.1})$$

The points (knots) x_i do not need to be equispaced, but we assume that they are in (strictly) increasing order

$$x_1 < x_2 < \dots < x_N. \quad (\text{B.2})$$

A function $\varphi(x)$ is said to be an interpolating cubic spline if

- 1) It reduces to a cubic polynomial within each interval $[x_i, x_{i+1}]$, i.e. if $x_i \leq x \leq x_{i+1}$

$$\varphi(x) = a_i + b_i x + c_i x^2 + d_i x^3 \equiv p_i(x) \quad (i = 1, \dots, N-1). \quad (\text{B.3})$$

- 2) The polynomial $p_i(x)$ matches the values of $f(x)$ at the endpoints of the i -th interval,

$$p_i(x_i) = f_i, \quad p_i(x_{i+1}) = f_{i+1} \quad (i = 1, \dots, N-1), \quad (\text{B.4})$$

so that $\varphi(x)$ is continuous in $[x_1, x_N]$.

- 3) The first and second derivatives of $\varphi(x)$ are continuous in $[x_1, x_N]$

$$p'_i(x_{i+1}) = p'_{i+1}(x_{i+1}) \quad (i = 1, \dots, N-2), \quad (\text{B.5})$$

$$p''_i(x_{i+1}) = p''_{i+1}(x_{i+1}) \quad (i = 1, \dots, N-2). \quad (\text{B.6})$$

Consequently, the curve $y = \varphi(x)$ interpolates the table (B.1) and has a continuously turning tangent.

To obtain the spline coefficients a_i, b_i, c_i, d_i ($i = 1, \dots, N-1$) we start from the fact that $\varphi''(x)$ is linear in $[x_i, x_{i+1}]$. Introducing the quantities

$$h_i \equiv x_{i+1} - x_i \quad (i = 1, \dots, N-1) \quad (\text{B.7})$$

and

$$\sigma_i \equiv \varphi''(x_i) \quad (i = 1, \dots, N), \quad (\text{B.8})$$

we can write the obvious identity

$$p_i''(x) = \sigma_i \frac{x_{i+1} - x}{h_i} + \sigma_{i+1} \frac{x - x_i}{h_i} \quad (i = 1, \dots, N-1). \quad (\text{B.9})$$

Notice that x_{i+1} must be larger than x_i in order to have $h_i > 0$. Integrating eq. (B.9) twice with respect to x , gives for $i = 1, \dots, N-1$

$$p_i(x) = \sigma_i \frac{(x_{i+1} - x)^3}{6h_i} + \sigma_{i+1} \frac{(x - x_i)^3}{6h_i} + A_i(x - x_i) + B_i(x_{i+1} - x), \quad (\text{B.10})$$

where A_i and B_i are constants. These can be determined by introducing the expression (B.10) into eqs. (B.4), this gives the pair of eqs.

$$\sigma_i \frac{h_i^2}{6} + B_i h_i = f_i \quad \text{and} \quad \sigma_{i+1} \frac{h_i^2}{6} + A_i h_i = f_{i+1}. \quad (\text{B.11})$$

Finally, solving for A_i and B_i and substituting the result in (B.10), we obtain

$$\begin{aligned} p_i(x) = & \frac{\sigma_i}{6} \left[\frac{(x_{i+1} - x)^3}{h_i} - h_i(x_{i+1} - x) \right] + f_i \frac{x_{i+1} - x}{h_i} \\ & + \frac{\sigma_{i+1}}{6} \left[\frac{(x - x_i)^3}{h_i} - h_i(x - x_i) \right] + f_{i+1} \frac{x - x_i}{h_i}. \end{aligned} \quad (\text{B.12})$$

To be able to use $\varphi(x)$ to approximate $f(x)$, we must find the second derivatives σ_i ($i = 1, \dots, N$). To this end, we impose the conditions (B.5). Differentiating (B.12) gives

$$p_i'(x) = \frac{\sigma_i}{6} \left[-\frac{3(x_{i+1} - x)^2}{h_i} + h_i \right] + \frac{\sigma_{i+1}}{6} \left[\frac{3(x - x_i)^2}{h_i} - h_i \right] + \delta_i, \quad (\text{B.13})$$

where

$$\delta_i = \frac{y_{i+1} - y_i}{h_i}. \quad (\text{B.14})$$

Hence,

$$p_i'(x_{i+1}) = \sigma_i \frac{h_i}{6} + \sigma_{i+1} \frac{h_i}{3} + \delta_i, \quad (\text{B.15a})$$

$$p_i'(x_i) = -\sigma_i \frac{h_i}{3} - \sigma_{i+1} \frac{h_i}{6} + \delta_i \quad (\text{B.15b})$$

and, similarly,

$$p'_{i+1}(x_{i+1}) = -\sigma_{i+1}\frac{h_{i+1}}{3} - \sigma_{i+2}\frac{h_{i+1}}{6} + \delta_{i+1}. \quad (\text{B.15c})$$

Replacing (B.15a) and (B.15c) in (B.5), we obtain

$$h_i\sigma_i + 2(h_i + h_{i+1})\sigma_{i+1} + h_{i+1}\sigma_{i+2} = 6(\delta_{i+1} - \delta_i) \quad (i = 1, \dots, N-2). \quad (\text{B.16})$$

The system (B.16) is linear in the N unknowns σ_i ($i = 1, \dots, N$). However, since it contains only $N - 2$ equations, it is underdetermined. This means that we need either to add two additional (independent) equations or to fix arbitrarily two of the N unknowns. The usual practice is to adopt *endpoint strategies* that introduce constraints on the behaviour of $\varphi(x)$ near x_1 and x_N . An endpoint strategy fixes the values of σ_1 and σ_N , yielding an $(N - 2) \times (N - 2)$ system in the variables σ_i ($i = 2, \dots, N - 1$). The resulting system is, in matrix form,

$$\begin{pmatrix} H_2 & h_2 & 0 & \cdots & 0 & 0 & 0 \\ h_2 & H_3 & h_3 & \cdots & 0 & 0 & 0 \\ 0 & h_3 & H_4 & \cdots & 0 & 0 & 0 \\ \vdots & \vdots & \vdots & \ddots & \vdots & \vdots & \vdots \\ 0 & 0 & 0 & \cdots & H_{N-3} & h_{N-3} & 0 \\ 0 & 0 & 0 & \cdots & h_{N-3} & H_{N-2} & h_{N-2} \\ 0 & 0 & 0 & \cdots & 0 & h_{N-2} & H_{N-1} \end{pmatrix} \begin{pmatrix} \sigma_2 \\ \sigma_3 \\ \sigma_4 \\ \vdots \\ \sigma_{N-3} \\ \sigma_{N-2} \\ \sigma_{N-1} \end{pmatrix} = \begin{pmatrix} D_2 \\ D_3 \\ D_4 \\ \vdots \\ D_{N-3} \\ D_{N-2} \\ D_{N-1} \end{pmatrix}, \quad (\text{B.17})$$

where

$$H_i = 2(h_{i-1} + h_i) \quad (i = 2, \dots, N-1) \quad (\text{B.18})$$

and

$$\begin{aligned} D_2 &= 6(\delta_2 - \delta_1) - h_1\sigma_1 \\ D_i &= 6(\delta_i - \delta_{i-1}) \quad (i = 3, \dots, N-2) \\ D_{N-1} &= 6(\delta_{N-1} - \delta_{N-2}) - h_{N-1}\sigma_N. \end{aligned} \quad (\text{B.19})$$

(σ_1 and σ_N are removed from the first and last equations, respectively). The matrix of coefficients is symmetric, tridiagonal and diagonally dominant (the larger coefficients are in the diagonal), so that the system (B.17) can be easily (and accurately) solved by Gauss elimination. The spline coefficients a_i , b_i , c_i , d_i ($i = 1, \dots, N - 1$)—see eq. (B.3)—can then be obtained by expanding the expressions (B.12):

$$\begin{aligned} a_i &= \frac{1}{6h_i} [\sigma_i x_{i+1}^3 - \sigma_{i+1} x_i^3 + 6(f_i x_{i+1} - f_{i+1} x_i)] + \frac{h_i}{6} (\sigma_{i+1} x_i - \sigma_i x_{i+1}), \\ b_i &= \frac{1}{2h_i} [\sigma_{i+1} x_i^2 - \sigma_i x_{i+1}^2 + 2(f_{i+1} - f_i)] + \frac{h_i}{6} (\sigma_i - \sigma_{i+1}), \\ c_i &= \frac{1}{2h_i} (\sigma_i x_{i+1} - \sigma_{i+1} x_i), \\ d_i &= \frac{1}{6h_i} (\sigma_{i+1} - \sigma_i). \end{aligned} \quad (\text{B.20})$$

When accurate values of $f''(x)$ are known, the best strategy is to set $\sigma_1 = f''(x_1)$ and $\sigma_N = f''(x_N)$, since this will minimize the spline interpolation errors near the endpoints x_1 and x_N . Unfortunately, the exact values $f''(x_1)$ and $f''(x_N)$ are not always available.

The so-called *natural spline* corresponds to taking $\sigma_1 = \sigma_N = 0$. It results in a $y = \varphi(x)$ curve with the shape that would be taken by a flexible rod (such as a draughtman's spline) if it were bent around pegs at the knots but allowed to maintain its natural (straight) shape outside the interval $[x_1, x_N]$. Since $\sigma_1 = \sigma_N = 0$, extrapolation of $\varphi(x)$ outside the interval $[x_1, x_N]$ by straight segments gives a continuous function with continuous first and second derivatives [i.e. a cubic spline in $(-\infty, \infty)$].

The accuracy of the spline interpolation is mainly determined by the density of knots in the regions where $f(x)$ has strong variations. For constant, linear, quadratic and cubic functions the interpolation errors can be reduced to zero by using the exact values of σ_1 and σ_N (in these cases, however, the natural spline may introduce appreciable errors near the endpoints). It is important to keep in mind that a cubic polynomial has, at most, one inflexion point. As a consequence, we should have at least a knot between each pair of inflexion points of $f(x)$ to ensure proper interpolation. Special care must be taken when interpolating functions that have a practically constant value in a partial interval, since the spline tends to wiggle instead of staying constant. In this particular case, it may be more convenient to use linear interpolation.

Obviously, the interpolating cubic spline $\varphi(x)$ can be used not only to obtain interpolated values of $f(x)$ between the knots, but also to calculate integrals such as

$$\int_a^b f(x) dx \simeq \int_a^b \varphi(x) dx, \quad x_1 \leq a \quad \text{and} \quad b \leq x_N, \quad (\text{B.21})$$

analytically. It is worth noting that derivatives of $\varphi(x)$ other than the first one may differ significantly from those of $f(x)$.

To obtain the interpolated value $\varphi(x_c)$ —see eq. (B.3)—of $f(x)$ at the point x_c , we must first determine the interval $(x_i, x_{i+1}]$ that contains the point x_c . To reduce the effort to locate the point, we use the following binary search algorithm:

- (i) Set $i = 1$ and $j = N$.
- (ii) Set $k = [(i + j)/2]$.
- (iii) If $x_k < x_c$, set $i = k$; otherwise set $j = k$.
- (iv) If $j - i > 1$, go to step (ii).
- (v) Deliver i .

Notice that the maximum delivered value of i is $N - 1$.

B.2 Numerical quadrature

In many cases, we need to calculate integrals of the form

$$\int_A^B f(z) dz, \quad (\text{B.22})$$

where the integrand is coded as an external function subprogram, which gives nominally exact values. These integrals are evaluated by using the FORTRAN77 external function **SUMGA**, which implements the twenty-point Gauss method with an adaptive bipartition scheme to allow for error control. This procedure is comparatively fast and is able to deal even with functions that have integrable singularities located at the endpoints of the interval $[A, B]$, a quite exceptional feature.

B.2.1 Gauss integration

We use the twenty-point Gauss formula (see e.g. Abramowitz and Stegun, 1974), given by

$$\int_a^b f(z) dz = \frac{b-a}{2} \sum_{i=1}^{20} w_i f(z_i) \quad (\text{B.23})$$

with

$$z_i = \frac{b-a}{2} x_i + \frac{b+a}{2}. \quad (\text{B.24})$$

The abscissa x_i ($-1 < x_i < 1$) is the i -th zero of the Legendre polynomial $P_{20}(x)$, the weights w_i are defined as

$$w_i = \frac{2}{(1-x_i^2) [P'_{20}(x_i)]^2}. \quad (\text{B.25})$$

The numerical values of the abscissas and weights are given in table B.1. The difference between the exact value of the integral and the right-hand side of eq. (B.23) is

$$\Delta_{20} = \frac{(b-a)^{41} (20!)^4}{41 (40!)^3} f^{(40)}(\xi), \quad (\text{B.26})$$

where ξ is a point in the interval $[a, b]$.

The Gauss method gives an estimate of the integral of $f(z)$ over the interval $[a, b]$, which is obtained as a weighted sum of function values at fixed points inside the interval. We point out that (B.23) is an open formula, i.e. the value of the function at the endpoints of the interval is never required. Owing to this fact, function **SUMGA** can integrate functions that are singular at the endpoints. As an example, the integral of $f(x) = x^{-1/2}$ over the interval $[0, 1]$ is correctly evaluated. This would not be possible with a method based on a closed formula (i.e. one that uses the values of the integrand at the interval endpoints).

Table B.1: Abscissas and weights for twenty-point Gauss integration.

$\pm x_i$	w_i
7.6526521133497334D-02	1.5275338713072585D-01
2.2778585114164508D-01	1.4917298647260375D-01
3.7370608871541956D-01	1.4209610931838205D-01
5.1086700195082710D-01	1.3168863844917663D-01
6.3605368072651503D-01	1.1819453196151842D-01
7.4633190646015079D-01	1.0193011981724044D-01
8.3911697182221882D-01	8.3276741576704749D-02
9.1223442825132591D-01	6.2672048334109064D-02
9.6397192727791379D-01	4.0601429800386941D-02
9.9312859918509492D-01	1.7614007139152118D-02

B.2.2 Adaptive bipartition

Function **SUMGA** exploits the fact that the error Δ_{20} , eq. (B.26), of the calculated integral decreases when the interval length is reduced. Thus, halving the interval and applying the Gauss method to each of the two subintervals gives a much better estimate of the integral, provided only that the function $f(x)$ is smooth enough over the initial interval. Notice that the error decreases by a factor of about 2^{-40} (!).

The algorithm implemented in **SUMGA** is as follows. The integration interval (A, B) is successively halved so that each iteration gives a doubly finer partition of the initial interval. We use the term “ n -subinterval” to denote the subintervals obtained in the n -th iteration. In each iteration, the integrals over the different n -subintervals are evaluated by the Gauss method, eq. (B.23). Consider that the integral over a given n -subinterval is S_1 . In the following iteration, this n -subinterval is halved and the integrals over each of the two resulting $(n + 1)$ -subintervals are evaluated, giving values S_{1a} and S_{1b} . If $S'_1 = S_{1a} + S_{1b}$ differs from S_1 in less than the selected tolerance, S'_1 is the sought value of the integral in the considered n -subinterval; the value S'_1 is then accumulated and this n -subinterval is no longer considered in subsequent iterations. Each iteration is likely to produce new holes (eliminated subintervals) in the regions where the function is smoother and, hence, the numerical effort progressively concentrates in the regions where $f(x)$ has stronger variations. The calculation terminates when the exploration of the interval (A, B) has been successfully completed or when a clear indication of an anomalous behaviour of $f(x)$ is found (e.g. when there is a persistent increase of the number of remaining n -subintervals in each iteration). In the second case a warning message is printed in unit 6 and the control is returned to the calling program.

Appendix C

Electron/positron transport in electromagnetic fields

In this appendix, we consider the transport of electrons/positrons in static external electromagnetic (EM) fields, in vacuum and in condensed media. We assume that, in the region where particles move, there is an electric field \mathcal{E} and a magnetic field \mathcal{B} , which are set up by external sources and do not vary with time. For practical purposes, we also consider that both \mathcal{E} and \mathcal{B} are continuous functions of the position vector \mathbf{r} .

The interactions with the medium will be described by means of PENELOPE. In each individual interaction event, the electron/positron loses a discrete amount of kinetic energy and changes its direction of motion. In the absence of EM fields, the electron travels freely between consecutive interaction events, i.e. following a straight trajectory segment at constant speed. To simulate electron transport with static external EM fields, we assume that the interaction properties of electrons with the medium are not substantially affected by the field. Consequently, to account for the effect of the EM field, we only need to consider that along each “free flight” the electron is driven by the EM force. With a proper selection of the simulation parameters (i.e. the energy loss and angular cutoff values), trajectory segments may have macroscopic lengths. Therefore, in material media it is appropriate to consider the macroscopic EM fields \mathbf{D} and \mathbf{H} rather than the microscopic fields \mathcal{E} and \mathcal{B} .

It should be noted that, under the action of an electric field, the kinetic energy of the electron can vary substantially along a single trajectory segment. This conflicts with one of the basic assumptions in PENELOPE, namely that the energy of the particle stays practically constant along the segment. In practice, however, we can always limit the maximum segment length by means of the parameter s_{max} . Then, the effect of the EM field can be treated independently of that of the interactions with the medium. In other words, for simulation purposes, we only need an efficient method to generate particle trajectories in the EM field *in vacuum*. It is also important to recall that strong electric fields in material media accelerate unbound charged particles, even when they are at rest (i.e. electrons are never absorbed, simulated tracks can only terminate when they

leave the field volume). Injection of a single electron in the medium may give rise to a complex cascade of delta rays, that accelerate in the direction opposite to the electric field. To describe these cascades we need accurate cross sections for ionization of outer atomic shells by impact of low-energy electrons, much more accurate than the simple ones implemented in PENELOPE. Therefore, PENELOPE *is not* expected to yield a reliable description of this process. The simulation algorithm described here is applicable only to magnetic fields and, cautiously, to weak electric fields. Notice also that we disregard the emission of radiation by the charged particle when it is accelerated by the external EM field (see e.g. Jackson, 1975); this approximation is not valid for very strong magnetic and electric fields.

C.1 Tracking particles in vacuum.

Let us begin by describing a “brute force” method to calculate trajectories of charged particles in arbitrary static electric and magnetic fields in vacuum. We start from the Lorentz force equation¹ for an electron ($Z_0 = -1$) or positron ($Z_0 = +1$),

$$\frac{d\mathbf{p}}{dt} = Z_0 e \left(\boldsymbol{\mathcal{E}} + \frac{\mathbf{v}}{c} \times \boldsymbol{\mathcal{B}} \right), \quad (\text{C.1})$$

which we write as

$$\frac{d(\gamma\beta\hat{\mathbf{v}})}{dt} = \frac{Z_0 e}{m_e c} (\boldsymbol{\mathcal{E}} + \beta\hat{\mathbf{v}} \times \boldsymbol{\mathcal{B}}), \quad (\text{C.2})$$

with $\hat{\mathbf{v}} = \mathbf{v}/v$, $\beta = v/c$ and $\gamma = (1 - \beta^2)^{-1/2}$. We note that

$$\frac{d(\gamma\beta\hat{\mathbf{v}})}{dt} = \gamma^3 \frac{d\beta}{dt} \hat{\mathbf{v}} + \gamma\beta \frac{d\hat{\mathbf{v}}}{dt} \quad (\text{C.3})$$

where the vectors $\hat{\mathbf{v}}$ and $d\hat{\mathbf{v}}/dt$ are orthogonal. Then, projecting eq. (C.2) into the directions of these two vectors, we obtain

$$\frac{d\beta}{dt} = \frac{Z_0 e}{m_e c \gamma} (1 - \beta^2) (\boldsymbol{\mathcal{E}} \cdot \hat{\mathbf{v}}) \quad (\text{C.4})$$

and

$$\frac{d\hat{\mathbf{v}}}{dt} = \frac{Z_0 e}{m_e c \beta \gamma} [\boldsymbol{\mathcal{E}} - (\boldsymbol{\mathcal{E}} \cdot \hat{\mathbf{v}}) \hat{\mathbf{v}} + \beta \hat{\mathbf{v}} \times \boldsymbol{\mathcal{B}}]. \quad (\text{C.5})$$

It then follows that

$$\begin{aligned} \frac{d\beta\hat{\mathbf{v}}}{dt} &= \frac{d\beta}{dt} \hat{\mathbf{v}} + \beta \frac{d\hat{\mathbf{v}}}{dt} \\ &= \frac{Z_0 e}{m_e c \gamma} [\boldsymbol{\mathcal{E}} - \beta^2 (\boldsymbol{\mathcal{E}} \cdot \hat{\mathbf{v}}) \hat{\mathbf{v}} + \beta \hat{\mathbf{v}} \times \boldsymbol{\mathcal{B}}], \end{aligned} \quad (\text{C.6})$$

¹In this appendix, electromagnetic quantities are expressed in the Gaussian system of units.

which we cast in the form

$$\frac{d\mathbf{v}}{dt} = \mathbf{A}, \quad \mathbf{A} \equiv \frac{Z_0 e}{m_e \gamma} [\boldsymbol{\mathcal{E}} - \beta^2 (\boldsymbol{\mathcal{E}} \cdot \hat{\mathbf{v}}) \hat{\mathbf{v}} + \beta \hat{\mathbf{v}} \times \boldsymbol{\mathcal{B}}]. \quad (\text{C.7})$$

Notice that, for arbitrary fields $\boldsymbol{\mathcal{E}}$ and $\boldsymbol{\mathcal{B}}$, the “acceleration” \mathbf{A} is a function of the particle’s position \mathbf{r} , energy E and direction of motion $\hat{\mathbf{v}}$.

Implicit integration of eq. (C.7) gives the equations of motion

$$\mathbf{v}(t) = \mathbf{v}_0 + \int_0^t \mathbf{A}(\mathbf{r}(t'), E(t'), \hat{\mathbf{v}}(t')) dt', \quad (\text{C.8})$$

$$\mathbf{r}(t) = \mathbf{r}_0 + \int_0^t \mathbf{v}(t') dt'. \quad (\text{C.9})$$

Evidently, these equations are too complex for straight application in a simulation code and we must have recourse to approximate solution methods. We shall adopt the approach proposed by Bielajew (1988), which is well suited to transport simulations. The basic idea is to split the trajectory into a number of conveniently short steps such that *the acceleration \mathbf{A} does not change much over the course of a step*. Along each step, we then have

$$\mathbf{v}(t) = \mathbf{v}_0 + t \mathbf{A}(\mathbf{r}_0, E_0, \hat{\mathbf{v}}_0) \quad (\text{C.10})$$

$$\mathbf{r}(t) = \mathbf{r}_0 + t \mathbf{v}_0 + t^2 \frac{1}{2} \mathbf{A}(\mathbf{r}_0, E_0, \hat{\mathbf{v}}_0), \quad (\text{C.11})$$

where the subscript “0” indicates values of the various quantities at the starting point ($t = 0$). The traveled path length s and the flying time t are related by

$$t = \int_0^s \frac{ds'}{v}, \quad (\text{C.12})$$

which to first order becomes

$$t = s/v_0. \quad (\text{C.13})$$

Then, to first order in the electromagnetic force,

$$\begin{aligned} \mathbf{v}(s) &= \mathbf{v}_0 + s \frac{\mathbf{A}(\mathbf{r}_0, E_0, \hat{\mathbf{v}}_0)}{c\beta_0} \\ \mathbf{r}(s) &= \mathbf{r}_0 + s \hat{\mathbf{v}}_0 + s^2 \frac{1}{2} \frac{\mathbf{A}(\mathbf{r}_0, E_0, \hat{\mathbf{v}}_0)}{c^2 \beta_0^2}. \end{aligned}$$

That is,

$$\mathbf{r}(s) = \mathbf{r}_0 + s \hat{\mathbf{v}}_0 + s^2 \frac{1}{2} \frac{Z_0 e [\boldsymbol{\mathcal{E}}_0 - \beta_0^2 (\boldsymbol{\mathcal{E}}_0 \cdot \hat{\mathbf{v}}_0) \hat{\mathbf{v}}_0 + \beta_0 \hat{\mathbf{v}}_0 \times \boldsymbol{\mathcal{B}}_0]}{m_e c^2 \gamma_0 \beta_0^2}. \quad (\text{C.14})$$

The particle’s velocity can be calculated directly from eq. (C.10), which to first order gives

$$\mathbf{v}(s) = \mathbf{v}_0 + \Delta \mathbf{v} \quad (\text{C.15})$$

with

$$\Delta \mathbf{v} = s \frac{Z_0 e [\boldsymbol{\mathcal{E}}_0 - \beta_0^2 (\boldsymbol{\mathcal{E}}_0 \cdot \hat{\mathbf{v}}_0) \hat{\mathbf{v}}_0 + \beta_0 \hat{\mathbf{v}}_0 \times \boldsymbol{\mathcal{B}}_0]}{m_e c \gamma_0 \beta_0}. \quad (\text{C.16})$$

In the tracking algorithm, the velocity is used to determine the direction vector at the end of the step,

$$\hat{\mathbf{v}}(s) = \frac{\mathbf{v}_0 + \Delta \mathbf{v}}{|\mathbf{v}_0 + \Delta \mathbf{v}|}. \quad (\text{C.17})$$

Owing to the action of the electromagnetic force, the kinetic energy E of the particle varies along the step. As the trajectory is accurate only to first order, it is not advisable to compute the kinetic energy from the velocity of the particle. It is preferable to calculate $E(t)$ as

$$E(s) = E_0 + Z_0 e [\varphi(\mathbf{r}_0) - \varphi(\mathbf{r}(s))] \quad (\text{C.18})$$

where $\varphi(\mathbf{r})$ is the electrostatic potential, $\boldsymbol{\mathcal{E}} = -\nabla \varphi$. Notice that this ensures energy conservation, i.e. it gives the exact energy variation in going from the initial to the final position.

This tracking method is valid only if

1) the fields do not change too much along the step

$$\frac{|\boldsymbol{\mathcal{E}}(\mathbf{r}(s)) - \boldsymbol{\mathcal{E}}(\mathbf{r}_0)|}{|\boldsymbol{\mathcal{E}}(\mathbf{r}_0)|} < \delta_{\boldsymbol{\mathcal{E}}} \ll 1, \quad \frac{|\boldsymbol{\mathcal{B}}(\mathbf{r}(s)) - \boldsymbol{\mathcal{B}}(\mathbf{r}_0)|}{|\boldsymbol{\mathcal{B}}(\mathbf{r}_0)|} < \delta_{\boldsymbol{\mathcal{B}}} \ll 1 \quad (\text{C.19})$$

and

2) the relative changes in kinetic energy and velocity (or direction of motion) are small

$$\left| \frac{E(s) - E_0}{E_0} \right| < \delta_E \ll 1, \quad \frac{|\Delta \mathbf{v}|}{v_0} < \delta_v \ll 1. \quad (\text{C.20})$$

These conditions set an upper limit on the allowed step length, s_{\max} , which depends on the local fields *and* on the energy and direction of the particle. The method is robust, in the sense that it converges to the exact trajectory when the maximum allowed step length tends to zero. In practical calculations, we shall specify the values of the δ -parameters (which should be of the order of 0.05 or less) and consider step lengths consistent with the above conditions. Thus, the smallness of the δ -parameters determines the accuracy of the generated trajectories.

To test the accuracy of a tracking algorithm, it is useful to consider the special cases of a uniform electric field (with $\boldsymbol{\mathcal{B}} = 0$) and a uniform magnetic field (with $\boldsymbol{\mathcal{E}} = 0$), which admit relatively simple analytical solutions of the equations of motion.

C.1.1 Uniform electric fields

Let us study first the case of a uniform electric field $\boldsymbol{\mathcal{E}}$. The equation of the trajectory of an electron/positron that starts at $t = 0$ from the point \mathbf{r}_0 with velocity \mathbf{v}_0 can be

expressed in the form (adapted from Bielajew, 1988)

$$\mathbf{r}(t) = \mathbf{r}_0 + t\mathbf{v}_{0\perp} + \frac{1}{a} \left[\cosh(act) - 1 + \frac{v_{0\parallel}}{c} \sinh(act) \right] \hat{\mathcal{E}}, \quad (\text{C.21})$$

where $\mathbf{v}_{0\parallel}$ and $\mathbf{v}_{0\perp}$ are the components of \mathbf{v}_0 parallel and perpendicular to the direction of the field,

$$\mathbf{v}_{0\parallel} = (\mathbf{v}_0 \cdot \hat{\mathcal{E}}) \hat{\mathcal{E}}, \quad \mathbf{v}_{0\perp} = \mathbf{v}_0 - (\mathbf{v}_0 \cdot \hat{\mathcal{E}}) \hat{\mathcal{E}} \quad (\text{C.22})$$

and

$$a \equiv \frac{Z_0 e \mathcal{E}}{m_e c^2 \gamma_0} = \frac{Z_0 e \mathcal{E}}{E_0}. \quad (\text{C.23})$$

The velocity of the particle is

$$\begin{aligned} \mathbf{v}(t) &= \mathbf{v}_{0\perp} + \left[c \sinh(act) + v_{0\parallel} \cosh(act) \right] \hat{\mathcal{E}} \\ &= \mathbf{v}_0 + \left\{ c \sinh(act) + v_{0\parallel} [\cosh(act) - 1] \right\} \hat{\mathcal{E}}. \end{aligned} \quad (\text{C.24})$$

Since the scalar potential for the constant field is $\varphi(\mathbf{r}) = -\mathcal{E} \cdot \mathbf{r}$, the kinetic energy of the particle varies with time and is given by

$$E(t) = E_0 - Z_0 e \mathcal{E} \cdot [\mathbf{r}_0 - \mathbf{r}(t)]. \quad (\text{C.25})$$

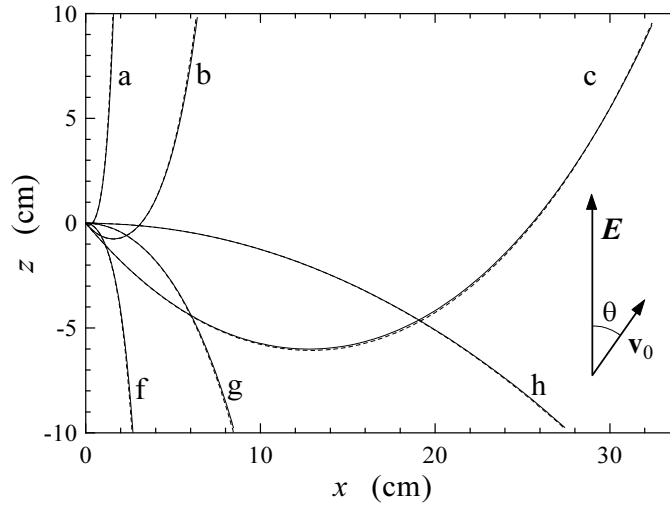


Figure C.1: Trajectories of electrons and positrons in a uniform electric field of 511 kV/cm. Continuous curves represent exact trajectories obtained from eq. (C.21). The dashed lines are obtained by using the first-order numerical tracking method described by eqs. (C.14)-(C.20) with $\delta \mathcal{E} = \delta E = \delta v = 0.02$. The displayed trajectories correspond to the following cases. a: positrons, $E_0 = 0.1$ MeV, $\theta = 135$ deg. b: positrons, $E_0 = 1$ MeV, $\theta = 135$ deg. c: positrons, $E_0 = 10$ MeV, $\theta = 135$ deg. f: electrons, $E_0 = 0.2$ MeV, $\theta = 90$ deg. g: electrons, $E_0 = 2$ MeV, $\theta = 90$ deg. h: electrons, $E_0 = 20$ MeV, $\theta = 90$ deg.

Fig. C.1 displays trajectories of electrons and positrons with various initial energies and directions of motion in a uniform electric field of 511 kV/cm directed along the positive z -axis. Particles start from the origin ($\mathbf{r}_0 = 0$), with initial velocity in the xz -plane forming an angle θ with the field, i.e. $\mathbf{v}_0 = (\sin \theta, 0, \cos \theta)$, so that the whole trajectories lie in the xz -plane. Continuous curves represent exact trajectories obtained from the analytical formula (C.21). The dashed curves are the results from the first-order tracking algorithm described above [eqs. (C.14)-(C.20)] with $\delta_{\mathcal{E}} = \delta_E = \delta_v = 0.02$. We show three positron trajectories with initial energies of 0.1, 1 and 10 MeV, initially moving in the direction $\theta = 135$ deg. Three trajectories of electrons that initially move perpendicularly to the field ($\theta = 90$ deg) with energies of 0.2, 2 and 20 MeV are also depicted. We see that the tracking algorithm gives quite accurate results. The error can be further reduced, if required, by using shorter steps, i.e. smaller δ -values.

C.1.2 Uniform magnetic fields

We now consider the motion of an electron/positron, with initial position \mathbf{r}_0 and velocity \mathbf{v}_0 , in a uniform magnetic field \mathcal{B} . Since the magnetic force is perpendicular to the velocity, the field does not alter the energy of the particle and the speed $v(t) = v_0$ is a constant of the motion. It is convenient to introduce the precession frequency vector $\boldsymbol{\omega}$, defined by (notice the sign)

$$\boldsymbol{\omega} \equiv -\frac{Z_0 e \mathcal{B}}{m_e \gamma c} = -\frac{Z_0 e c \mathcal{B}}{E_0}, \quad (\text{C.26})$$

and split the velocity \mathbf{v} into its components parallel and perpendicular to $\boldsymbol{\omega}$,

$$\mathbf{v}_{\parallel} = (\mathbf{v} \cdot \hat{\boldsymbol{\omega}}) \hat{\boldsymbol{\omega}}, \quad \mathbf{v}_{\perp} = \mathbf{v} - (\mathbf{v} \cdot \hat{\boldsymbol{\omega}}) \hat{\boldsymbol{\omega}}. \quad (\text{C.27})$$

Then, the equation of motion (C.7) becomes

$$\frac{d\mathbf{v}_{\parallel}}{dt} = 0, \quad \frac{d\mathbf{v}_{\perp}}{dt} = \boldsymbol{\omega} \times \mathbf{v}_{\perp}. \quad (\text{C.28})$$

The first of these eqs. says that the particle moves with constant velocity $\mathbf{v}_{0\parallel}$ along the direction of the magnetic field. From the second eq. we see that, in the plane perpendicular to \mathcal{B} , the particle describes a circle with angular frequency ω and speed $v_{0\perp}$ (which is a constant of the motion). The radius of the circle is $R = v_{0\perp}/\omega$. That is, the trajectory is an helix with central axis along the \mathcal{B} direction, radius R and pitch angle $\alpha = \arctan(v_{0\parallel}/v_{0\perp})$. The helix is right-handed for electrons and left-handed for positrons (see fig. C.2).

In terms of the path length $s = tv_0$, the equation of motion takes the form

$$\mathbf{r}(s) = \mathbf{r}_0 + \frac{s}{v_0} \mathbf{v}_{0\parallel} + R [1 - \cos(s_{\perp}/R)] (\hat{\boldsymbol{\omega}} \times \hat{\mathbf{v}}_{0\perp}) + R \sin(s_{\perp}/R) \hat{\mathbf{v}}_{0\perp}, \quad (\text{C.29})$$

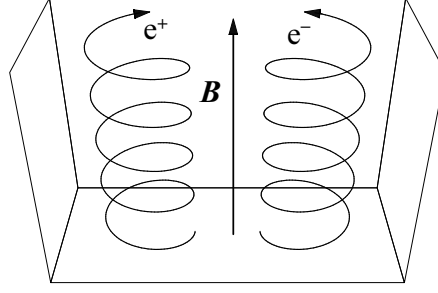


Figure C.2: Trajectories of electrons and positrons in a uniform magnetic field. The two particles start from the base plane with equal initial velocities.

where $\hat{\mathbf{v}}_{0\perp} \equiv \mathbf{v}_{0\perp}/v_{0\perp}$ and $s_{\perp} = sv_{0\perp}/v_0$. Equivalently,

$$\mathbf{r}(s) = \mathbf{r}_0 + s\hat{\mathbf{v}}_0 - \frac{s}{v_0}\mathbf{v}_{0\perp} + \frac{1}{\omega}[1 - \cos(s\omega/v_0)](\hat{\boldsymbol{\omega}} \times \mathbf{v}_{0\perp}) + \frac{1}{\omega}\sin(s\omega/v_0)\mathbf{v}_{0\perp}. \quad (\text{C.30})$$

After the path length s , the particle velocity is

$$\mathbf{v}(s) = v_0 \frac{d\mathbf{r}}{ds} = \mathbf{v}_0 + [\cos(s\omega/v_0) - 1]\mathbf{v}_{0\perp} + \sin(s\omega/v_0)(\hat{\boldsymbol{\omega}} \times \mathbf{v}_{0\perp}). \quad (\text{C.31})$$

In fig. C.3 we compare exact trajectories of electrons and positrons in a uniform magnetic field obtained from the analytical formula (C.30) with results from the first-order tracking algorithm [eqs. (C.14)-(C.20)] with $\delta_{\mathcal{B}} = \delta_E = \delta_v = 0.02$. The field strength is 0.2 tesla. The depicted trajectories correspond to 0.5 MeV electrons (a) and 3 MeV positrons (b) that initially move in a direction forming an angle of 45 deg with the field. We see that the numerical algorithm is quite accurate for small path lengths, but it deteriorates rapidly for increasing s . In principle, the accuracy of the algorithm can be improved by reducing the value of δ_v , i.e. the length of the step length. In practice, however, this is not convenient because it implies a considerable increase of numerical work, which can be easily avoided.

C.2 Exact tracking in homogeneous magnetic fields

In our first-order tracking algorithm [see eqs. (C.14) and (C.16)], the effects of the electric and magnetic fields are uncoupled, i.e. they can be evaluated separately. For uniform electric fields, the algorithm offers a satisfactory solution since it usually admits relatively large step lengths. In the case of uniform magnetic fields (with $\boldsymbol{\mathcal{E}} = 0$), the kinetic energy is a constant of the motion and the only effective constraint on the step length is that the change in direction $|\Delta\mathbf{v}|/v_0$ has to be small. Since the particle trajectories on the plane perpendicular to the field \mathbf{B} are circles and the first-order algorithm generates each step as a parabolic segment, we need to move in sub-steps of length much less than the radius R (i.e. δ_v must be given a very small value) and this

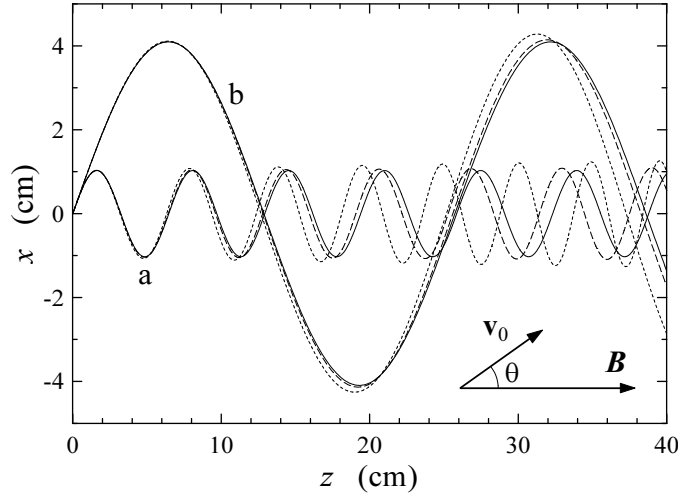


Figure C.3: Trajectories of electrons and positrons in a uniform magnetic field of 0.2 tesla. Continuous curves are exact trajectories calculated from eq. (C.30). The short-dashed lines are obtained by using the numerical tracking method described in the text with $\delta_v = 0.02$. Long-dashed curves are the results from the tracking algorithm with $\delta_v = 0.005$. a: electrons, $E_0 = 0.5$ MeV, $\theta = 45$ deg. b: positrons, $E_0 = 3$ MeV, $\theta = 45$ deg.

makes the calculation slow. On the other hand, the action of the uniform magnetic field is described by simple analytical expressions [eqs. (C.30) and (C.31)], that are amenable for direct use in the simulation code. These arguments suggest the following obvious modification of the tracking algorithm.

As before, we assume that the fields are essentially constant along each trajectory step and write

$$\mathbf{r}(s) = \mathbf{r}_0 + s\hat{\mathbf{v}}_0 + (\Delta\mathbf{r})_{\mathcal{E}} + (\Delta\mathbf{r})_{\mathcal{B}}, \quad (\text{C.32})$$

where $(\Delta\mathbf{r})_{\mathcal{E}}$ and $(\Delta\mathbf{r})_{\mathcal{B}}$ are the displacements caused by the electric and magnetic fields, respectively. For $(\Delta\mathbf{r})_{\mathcal{E}}$ we use the first-order approximation [see eq. (C.14)],

$$(\Delta\mathbf{r})_{\mathcal{E}} = s^2 \frac{1}{2} \frac{Z_0 e [\mathcal{E}_0 - \beta_0^2 (\mathcal{E}_0 \cdot \hat{\mathbf{v}}_0) \hat{\mathbf{v}}_0]}{m_e c^2 \gamma_0 \beta_0^2}. \quad (\text{C.33})$$

The displacement caused by the magnetic field is evaluated using the result (C.30), i.e.

$$(\Delta\mathbf{r})_{\mathcal{B}} = -\frac{s}{v_0} \mathbf{v}_{0\perp} + \frac{1}{\omega} [1 - \cos(s\omega/v_0)] (\hat{\omega} \times \mathbf{v}_{0\perp}) + \frac{1}{\omega} \sin(s\omega/v_0) \mathbf{v}_{0\perp} \quad (\text{C.34})$$

with

$$\omega \equiv -\frac{Z_0 e c \mathcal{B}_0}{E_0}, \quad \text{and} \quad \mathbf{v}_{0\perp} = \mathbf{v}_0 - (\mathbf{v}_0 \cdot \hat{\omega}) \hat{\omega}. \quad (\text{C.35})$$

Similarly, the particle velocity along the step is expressed as

$$\mathbf{v}(s) = \mathbf{v}_0 + (\Delta\mathbf{v})_{\mathcal{E}} + (\Delta\mathbf{v})_{\mathcal{B}} \quad (\text{C.36})$$

with [see eqs. (C.16) and (C.31)]

$$(\Delta \mathbf{v})_{\mathcal{E}} = s \frac{Z_0 e [\mathcal{E}_0 - \beta_0^2 (\mathcal{E}_0 \cdot \hat{\mathbf{v}}_0) \hat{\mathbf{v}}_0]}{m_e c \gamma_0 \beta_0} \quad (\text{C.37})$$

and

$$(\Delta \mathbf{v})_{\mathcal{B}} = [\cos(s\omega/v_0) - 1] \mathbf{v}_{0\perp} + \sin(s\omega/v_0) (\hat{\boldsymbol{\omega}} \times \mathbf{v}_{0\perp}). \quad (\text{C.38})$$

In our implementation of this tracking algorithm, the allowed step lengths s are limited by the following constraints [see eqs. (C.19) and (C.20)]

$$\frac{|\mathcal{E}(\mathbf{r}(s)) - \mathcal{E}(\mathbf{r}_0)|}{|\mathcal{E}(\mathbf{r}_0)|} < \delta_{\mathcal{E}} \ll 1, \quad \frac{|\mathcal{B}(\mathbf{r}(s)) - \mathcal{B}(\mathbf{r}_0)|}{|\mathcal{B}(\mathbf{r}_0)|} < \delta_{\mathcal{B}} \ll 1 \quad (\text{C.39})$$

and

$$\left| \frac{E(s) - E_0}{E_0} \right| < \delta_E \ll 1, \quad \frac{|(\Delta \mathbf{v})_{\mathcal{E}} + (\Delta \mathbf{v})_{\mathcal{B}}|}{v_0} < \delta_v \ll 1. \quad (\text{C.40})$$

The algorithm is robust, i.e. the accuracy of the generated trajectories increases when the δ -parameters are reduced. In many practical cases, a good compromise between accuracy and simulation speed is obtained by setting $\delta_{\mathcal{E}} = \delta_{\mathcal{B}} = \delta_E = \delta_v = 0.02$. Notice that, in the case of a uniform magnetic field, the tracking algorithm is now exact, irrespective of the step length.

This tracking algorithm has been implemented in the subroutine package `PENFIELD`, which is devised to work linked to `PENELOPE` and `PENGEO`. To simulate radiation transport in a given field/material configuration, the user must provide the steering main program as well as specific routines that define the EM field (see the examples and comments in the source file `PENFIELD.F`).

Bibliography

- Abramowitz M. and I.A. Stegun (1974), eds., *Handbook of Mathematical Functions* (Dover, New York).
- Acosta E., X. Llovet, E. Coleoni, J.A. Riveros and F. Salvat (1998), “Monte Carlo simulation of x-ray emission by kilovolt electron bombardment”, *J. Appl. Phys.* **83**, 6038–6049.
- Andreo P. (1991), “Monte Carlo techniques in medical radiation physics”, *Phys. Med. Biol.* **36**, 861–920.
- Andreo P. and A. Brahme (1984), “Restricted energy-loss straggling and multiple scattering of electrons in mixed Monte Carlo procedures”, *Rad. Res.* **100**, 16–29.
- Baró J., M. Roteta, J.M. Fernández-Varea and F. Salvat (1994a), “Analytical cross sections for Monte Carlo simulation of photon transport”, *Radiat. Phys. Chem.* **44**, 531–552.
- Baró J., J. Sempau, J.M. Fernández-Varea and F. Salvat (1994b), “Simplified Monte Carlo simulation of elastic electron scattering in limited media”, *Nucl. Instrum. Meth. B* **84**, 465–483.
- Baró J., J. Sempau, J.M. Fernández-Varea and F. Salvat (1995), “PENELOPE: an algorithm for Monte Carlo simulation of the penetration and energy loss of electrons and positrons in matter”, *Nucl. Instrum. Meth. B* **100**, 31–46.
- Bearden J.A. (1967), “X-ray wavelengths”, *Rev. Mod. Phys.* **39**, 78–124.
- Benedito E., J.M. Fernández-Varea and F. Salvat (2001), “Mixed simulation of the multiple elastic scattering of electrons and positrons using partial-wave differential cross sections”, *Nucl. Instrum. Meth. B* **174**, 91–110.
- Berger M.J. (1963), “Monte Carlo calculation of the penetration and diffusion of fast charged particles”, in *Methods in Computational Physics*, vol. 1, eds. B. Alder, S. Fernbach and M. Rotenberg (Academic Press, New York) pp. 135–215.
- Berger M.J. (1992), “ESTAR, PSTAR and ASTAR: computer programs for calculating stopping-power and range tables for electrons, protons and helium ions”, *Report NISTIR 4999* (National Institute of Standards and Technology, Gaithersburg, MD).
- Berger M.J. (1998), “Applicability of the condensed-random-walk Monte Carlo method at low energies in high-*Z* materials”, *Radiat. Phys. Chem.* **53**, 191–203.

- Berger M.J. and J.H. Hubbell (1987), “XCOM: Photon Cross Sections on a Personal Computer”, *Report NBSIR 87-3597* (National Bureau of Standards, Gaithersburg, MD).
- Berger M.J. and S.M. Seltzer (1972), “Response functions for sodium iodide scintillation detectors”, *Nucl. Instrum. Meth.* **104**, 317–332.
- Berger M.J. and S.M. Seltzer (1982), “Stopping Power of Electrons and Positrons”, *Report NBSIR 82-2550* (National Bureau of Standards, Gaithersburg, MD).
- Berger M.J. and S.M. Seltzer (1988), chapters 7, 8 and 9, in *Monte Carlo Transport of Electrons and Photons*, eds. T.M. Jenkins, W.R. Nelson and A. Rindi (Plenum, New York).
- Bethe, H.A. (1930), “Zur Theorie des Durchgangs schneller Korpuskularstrahlen durch Materie”, *Ann. Physik* **5**, 325–400.
- Bethe, H.A. (1932), “Bremsformel für Elektronen relativistischer Geschwindigkeit”, *Z. Physik* **76**, 293–299.
- Bethe H.A. and W. Heitler (1934), “On the stopping of fast particles and on the creation of positive electrons”, *Proc. R. Soc. (London) A* **146**, 83–112.
- Bhabha H.J. (1936), “The scattering of positrons by electrons with exchange on Dirac’s theory of the positron”, *Proc. R. Soc. (London) A* **154**, 195–206.
- Bielajew A.F. (1988), “Electron transport in \vec{E} and \vec{B} fields”, in *Monte Carlo Transport of Electrons and Photons*, eds. T.M. Jenkins, W.R. Nelson and A. Rindi (Plenum, New York) pp. 421–434.
- Bielajew A.F. (1995), “HOWFAR and HOWNEAR: Geometry Modeling for Monte Carlo Particle Transport”, *Report PIRS-0341* (National Research Council of Canada, Ottawa).
- Bielajew A.F. and D.W.O. Rogers (1987), “PRESTA: The parameter reduced electron-step transport algorithm for electron Monte Carlo transport”, *Nucl. Instrum. Meth. B* **18**, 165–181.
- Bielajew A.F. and D.W.O. Rogers (1988), “Variance-reduction techniques”, in *Monte Carlo Transport of Electrons and Photons*, eds. T.M. Jenkins, W.R. Nelson and A. Rindi (Plenum, New York) pp. 407–419.
- Bielajew A.F. and F. Salvat (2001), “Improved electron transport mechanics in the PENELOPE Monte-Carlo model”, *Nucl. Instrum. Meth. B* **173**, 332–343.
- Biggs F., L.B. Mendelsohn and J.B. Mann (1975), “Hartree-Fock Compton profiles for the elements”, *At. Data Nucl. Data Tables* **16**, 201–309.
- Blunck O. and S. Leisegang (1950), “Zum Energieverlust schneller Elektronen in dünnen Schichten”, *Z. Physik* **128**, 500–505.
- Born M. (1969), *Atomic Physics* (Blackie and Son, London).
- Bransden B.H. and C.J. Joachain (1983), *Physics of Atoms and Molecules* (Longman, Essex, England).

- Briesmeister J.F. (1997), “MCNP—A general Monte Carlo N-particle transport code”, *Report LA-12625-M Version 4B* (Los Alamos National Laboratory, Los Alamos, NM).
- Brun R., F. Bruyant, M. Maire, A.C. McPherson and P. Zanarini (1986), “GEANT3”, *Report DD/EE/84-1* (CERN, Geneva).
- Brusa D., G. Stutz, J.A. Riveros, J.M. Fernández-Varea and F. Salvat (1996), “Fast sampling algorithm for the simulation of photon Compton scattering”, *Nucl. Instrum. Meth. A* **379**, 167–175.
- Chan H.-P. and K. Doi (1983), “The validity of Monte Carlo simulation in studies of scattered radiation in diagnostic radiology”, *Phys. Med. Biol.* **28**, 109–129.
- Cooper M. (1971), “Compton scattering and electron momentum distributions”, *Adv. Phys.* **20**, 453–491.
- Cullen D.E., M.H. Chen, J.H. Hubbell, S.T. Perkins, E.F. Plechaty, J.A. Rathkopf and J.H. Scofield (1989), “Tables and graphs of photon-interaction cross sections from 10 eV to 100 GeV derived from the LLNL evaluated photon data library (EPDL)”, *Report UCRL-50400* vol. 6, rev. 4, parts A and B. (Lawrence Livermore National Laboratory, Livermore, CA).
- Cullen D.E., J.H. Hubbell and L. Kissel (1997), “EPDL97 The evaluated data library, '97 version”, *Report UCRL-50400* vol. 6, rev. 5 (Lawrence Livermore National Laboratory, Livermore, CA).
- Davies H., H.A. Bethe and L.C. Maximon (1954), “Theory of bremsstrahlung and pair production. II. Integral cross section for pair production” *Phys. Rev.* **93**, 788–795.
- Desclaux J.P. (1975), “A multiconfiguration relativistic Dirac-Fock program”, *Comput. Phys. Commun.* **9**, 31–45. Erratum: *ibid.* **13** (1977) 71.
- Doyle P.A. and P.S. Turner (1968), “Relativistic Hartree-Fock X-ray and electron scattering factors”, *Acta Cryst. A* **24**, 390–397.
- Edmonds A.R. (1960), *Angular Momentum in Quantum Mechanics*, 2nd edition (Princeton University Press, Princeton, NJ).
- Fano U. (1954), “Inelastic collisions and the Molière theory of multiple scattering”, *Phys. Rev.* **93**, 117–120.
- Fano U. (1963), “Penetration of protons, alpha particles and mesons”, *Ann. Rev. Nucl. Sci.* **13**, 1–66.
- Fernández-Varea J.M., R. Mayol, D. Liljequist and F. Salvat (1993a) “Inelastic scattering of electrons in solids from a generalized oscillator strength model using optical and photoelectric data”, *J. Phys: Condens. Matter* **5**, 3593–3610.
- Fernández-Varea J.M., R. Mayol, J. Baró and F. Salvat (1993b), “On the theory and simulation of multiple elastic scattering of electrons”, *Nucl. Instrum. Meth. B* **73**, 447–473.
- Goudsmit S. and J.L. Saunderson (1940a), “Multiple scattering of electrons”, *Phys. Rev.* **57**, 24–29.

- Goudsmit S. and J.L. Saunderson (1940b), "Multiple scattering of electrons. II", *Phys. Rev.* **58**, 36–42.
- Habib J.A., R.P. Kensek, T.A. Mehlhorn, G.D. Valdez, S.M. Seltzer and M.J. Berger (1992), "ITS version 3.0: the integrated TIGER series of coupled electron/photon Monte Carlo transport codes", *Report SAND91-1634* (Sandia National Laboratories, Albuquerque, NM).
- Haug E. (1975), "Bremsstrahlung and pair production in the field of free electrons", *Z. Naturforsch.* **30a**, 1099–1113.
- Hayward E. and J. Hubbell (1954), "The albedo of various materials for 1-Mev photons", *Phys. Rev.* **93**, 955–956.
- Heinrich K.F.J. and D.E. Newbury (1991), eds., *Electron Probe Quantitation* (Plenum Press, New York).
- Heitler W. (1954), *The Quantum Theory of Radiation* (Oxford Univ. Press, London).
- Hippler R. (1990), "Plane wave Born calculations of K-shell ionization at low velocities", *Phys. Lett.* **A144**, 81–85.
- Hubbell J.H. (1989), "Bibliography and current status of K, L, and higher shells fluorescence yields for computations of photon energy-absorption coefficients", *Report NISTIR 89-4144* (National Institute of Standards and Technology, Gaithersburg, MD).
- Hubbell J.H., H.A. Gimm and I. Øverbø (1980), "Pair, triplet, and total atomic cross sections (and mass attenuation coefficients) for 1 MeV–100 GeV photons in elements $Z = 1$ to 100", *J. Phys. Chem. Ref. Data* **9**, 1023–1147.
- Hubbell J.H., Wm.J. Veigele, E.A. Briggs, R.T. Brown, D.T. Cromer and R.J. Howerton (1975), "Atomic form factors, incoherent scattering functions, and photon scattering cross sections", *J. Phys. Chem. Ref. Data* **4**, 471–538. Erratum: *ibid.* **6** (1977) 615–616.
- ICRU 37 (1984), *Stopping Powers for Electrons and Positrons* (ICRU, Bethesda, MD).
- Inokuti M. (1971), "Inelastic collisions of fast charged particles with atoms and molecules—the Bethe theory revisited", *Rev. Mod. Phys.* **43**, 297–347.
- Inokuti M., Y. Itikawa and J.E. Turner (1978), "Addenda: inelastic collisions of fast charged particles with atoms and molecules—the Bethe theory revisited", *Rev. Mod. Phys.* **50**, 23–35.
- Inokuti M. and D.Y. Smith (1982), "Fermi density effect on the stopping power of metallic aluminum", *Phys. Rev. B* **25**, 61–66.
- Jablonski A. (1987), "Effects of Auger electron elastic scattering in quantitative AES", *Surf. Science* **188**, 164–180.
- Jackson J.D. (1975), *Classical Electrodynamics* (John Wiley and Sons, New York).
- James F. (1980), "Monte Carlo theory and practice", *Rep. Prog. Phys.* **43**, 1145–1189.

- James F. (1990), “A review of pseudorandom number generators”, *Comput. Phys. Commun.* **60**, 329–344.
- Jenkins T.M., W.R. Nelson and A. Rindi (1988), eds., *Monte Carlo Transport of Electrons and Photons* (Plenum, New York).
- Kalos M.H. and P.A. Whitlock (1986), *Monte Carlo Methods*, vol. 1 (Wiley, New York).
- Kane P.P., L. Kissel, R.H. Pratt and S.C. Roy (1986), “Elastic scattering of γ -rays and X-rays by atoms”, *Phys. Rep.* **140**, 75–159.
- Kawrakow I. and D.W.O. Rogers (2000), “The EGSnrc code system: Monte Carlo simulation of electron and photon transport”, *Report PIRS-701* (National Research Council of Canada, Ottawa).
- Kim L., R.H. Pratt, S.M. Seltzer and M.J. Berger (1986), “Ratio of positron to electron bremsstrahlung energy loss: an approximate scaling law”, *Phys. Rev. A* **33**, 3002–3009.
- Kirkpatrick P. and L. Wiedmann (1945), “Theoretical continuous X-ray energy and polarization”, *Phys. Rev.* **67**, 321–339.
- Kissel L., C.A. Quarles and R.H. Pratt (1983), “Shape functions for atomic-field bremsstrahlung from electrons of kinetic energy 1–500 keV on selected neutral atoms $1 \leq Z \leq 92$ ”, *At. Data Nucl. Data Tables* **28**, 381–460.
- Kittel C. (1976), *Introduction to Solid State Physics* (John Wiley and Sons, New York).
- Koch H.W. and J.W. Motz (1959), “Bremsstrahlung cross-section formulas and related data”, *Rev. Mod. Phys.* **31**, 920–955.
- Landau L. (1944), “On the energy loss of fast particles by ionisation”, *J. Phys. U.S.S.R.* **8**, 201–207.
- L’Ecuyer P. (1988), “Efficient and portable combined random number generators”, *Commun. ACM* **31**, 742–749.
- Lederer C.M. and V.S. Shirley (1978), eds., *Table of Isotopes*, 7th edition (Wiley, New York) appendix III.
- Lewis H.W. (1950), “Multiple scattering in an infinite medium”, *Phys. Rev.* **78**, 526–529.
- Lewis H.W. (1952), “Range straggling of a nonrelativistic charged particle”, *Phys. Rev.* **85**, 20–24.
- Liljequist D. (1983), “A simple calculation of inelastic mean free path and stopping power for 50 eV–50 keV electrons in solids”, *J. Phys. D: Appl. Phys.* **16**, 1567–1582.
- Liljequist D. (1987), “Critical path length for the similarity of elastic multiple scattering processes”, *J. Appl. Phys.* **62**, 333–341.
- Lindhard J. and A. Winther (1964), “Stopping power of electron gas and equipartition rule”, *Mat. Fys. Medd. Dan. Vid. Selsk.* **34**, 1–22.

- Ljungberg M. and S.-E. Strand (1989), “A Monte Carlo program for the simulation of scintillation camera characteristics”, *Comput. Meth. Programs Biomed.* **29**, 257–272.
- Manson S.T. (1972), “Theoretical study of generalized oscillator strengths in atoms: comparison with experiment and other calculations”, *Phys. Rev. A* **5**, 668–677.
- Maron M.J. (1982), *Numerical Analysis: A Practical Approach* (Macmillan, New York).
- Mayol R. and F. Salvat (1990), “Cross sections for K-shell ionisation by electron impact”, *J. Phys. B: At. Mol. Opt. Phys.* **23**, 2117–2130.
- Mohr P.J. and B.N. Taylor (2000), “CODATA recommended values of the fundamental physical constants: 1998”, *Rev. Mod. Phys.* **72**, 351–495.
- Molière G. (1947), “Theorie der Streuung schneller geladener Teilchen I. Einzelstreuung am abgeschirmten Coulomb-Feld”, *Z. Naturforsch.* **2a**, 133–145.
- Molière G. (1948), “Theorie der Streuung schneller geladener Teilchen II. Mehrfach- und Vielfachstreuung”, *Z. Naturforsch.* **3a**, 78–97.
- Møller C. (1932), “Zur Theorie des Durchgangs schneller Elektronen durch Materie”, *Ann. Physik* **14**, 531–585.
- Mott N.F. and H.S.W. Massey (1965), *The Theory of Atomic Collisions*, 3rd edition (Oxford Univ. Press, London).
- Motz J.W., H.A. Olsen and H.W. Koch (1969), “Pair production by photons”, *Rev. Mod. Phys.* **41**, 581–639.
- Namito Y., S. Ban and H. Hirayama (1994), “Implementation of the Doppler broadening of a Compton-scattered photon into the EGS4 code”, *Nucl. Instrum. Meth. A* **349**, 489–494.
- Nelson W.R., H. Hirayama and D.W.O. Rogers (1985), “The EGS4 Code System”, *Report SLAC-265* (Stanford Linear Accelerator Center, Stanford, CA).
- Perkins S.T., D.E. Cullen, M.H. Chen, J.H. Hubbell, J. Rathkopf and J. Scofield (1991), “Tables and graphs of atomic subshell and relaxation data derived from the LLNL evaluated atomic data library (EADL), $Z = 1$ –100”, *Report UCRL-50400* vol. 30 (Lawrence Livermore National Laboratory, Livermore, CA).
- Pratt R.H., A. Ron and H.K. Tseng (1973), “Atomic photoelectric effect above 10 keV”, *Rev. Mod. Phys.* **45**, 273–325. Erratum: *ibid.* **45** (1973) 663–664.
- Pratt R.H., H.K. Tseng, C.M. Lee and L. Kissel (1977), “Bremsstrahlung energy spectra from electrons of kinetic energy $1 \text{ keV} \leq T_1 \leq 2000 \text{ keV}$ incident on neutral atoms $2 \leq Z \leq 92$ ”, *At. Data Nucl. Data Tables* **20**, 175–209. Erratum: *ibid.* **26** (1981) 477–481.
- Press W.H. and S.A. Teukolsky (1992), “Portable random number generators”, *Computers in Physics* **6**, 522–524.
- Reimer L. (1985), *Scanning Electron Microscopy* (Springer, Berlin).

- Reimer L. and E.R. Krefting (1976), “The effect of scattering models on the results of Monte Carlo calculations”, *National Bureau of Standards Special Publication 460* (US Government Printing Office, Washington DC) pp. 45–60.
- Reimer L., U. Zepke, J. Moesch, St. Schulze-Hillert, M. Ross-Messemer, W. Probst and E. Weimer (1992), *EEL Spectroscopy* (Carl Zeiss, Oberkochen).
- Ribberfors R. (1983), “X-ray incoherent scattering total cross sections and energy-absorption cross sections by means of simple calculation routines”, *Phys. Rev. A* **27**, 3061–3070.
- Ribberfors R. and K.-F. Berggren (1982), “Incoherent-x-ray-scattering functions and cross section $(d\sigma/d\Omega')_{\text{incoh}}$ by means of a pocket calculator”, *Phys. Rev. A* **26**, 3325–3333.
- Rubinstein R.Y. (1981), *Simulation and the Monte Carlo Method* (Wiley, New York).
- Sakurai J.J. (1967), *Advanced Quantum Mechanics* (Addison and Wesley, New York).
- Saloman E.B., J.H. Hubbell and J.H. Scofield (1988), “X-ray attenuation cross sections for energies 100 eV to 100 keV and elements $Z = 1$ to $Z = 92$ ”, *At. Data Nucl. Data Tables* **38**, 1–197.
- Salvat F. (1987), “Algorithms for random sampling from single-variate distributions”, *Comput. Phys. Commun.* **46**, 427–436.
- Salvat F. (1998), “Simulation of electron multiple elastic scattering”, *Radiat. Phys. Chem.* **53**, 247–256.
- Salvat F. (2000), Private communication.
- Salvat F. and J.M. Fernández-Varea (1992), “Semiempirical cross sections for the simulation of the energy loss of electrons and positrons in matter”, *Nucl. Instrum. Meth. B* **63**, 255–269.
- Sauter F. (1931), “Über den atomaren Photoeffekt in der K-Schale nach der relativistischen Wellenmechanik Diracs”, *Ann. Phys.* **11**, 454–488.
- Schiff L.I. (1968), *Quantum Mechanics*, 3rd edition (McGraw-Hill Kogakusha Ltd., Tokyo).
- Schneider H., I. Tobehn, F. Ebel and R. Hippler (1993), “Absolute cross sections for inner shell ionization by lepton impact”, *Phys. Rev. Lett.* **71**, 2707–2709.
- Schultz P.J. and K.G. Lynn (1988), “Interaction of positron beams with surfaces, thin films, and interfaces”, *Rev. Mod. Phys.* **60**, 701–770.
- Scofield J.H. (1978) “K- and L-shell ionization of atoms by relativistic electrons”, *Phys. Rev. A* **18**, 963–970.
- Seltzer S.M. and M.J. Berger (1985), “Bremsstrahlung spectra from electron interactions with screened atomic nuclei and orbital electrons”, *Nucl. Instrum. Meth. B* **12**, 95–134.

- Seltzer S.M. and M.J. Berger (1986), “Bremsstrahlung energy spectra from electrons with kinetic energy 1 keV–10 GeV incident on screened nuclei and orbital electrons of neutral atoms with $Z = 1$ –100”, *At. Data Nucl. Data Tables* **35**, 345–418.
- Sempau J., E. Acosta, J. Baró, J.M. Fernández-Varea and F. Salvat (1997), “An algorithm for Monte Carlo simulation of coupled electron-photon transport”, *Nucl. Instrum. Meth. B* **132**, 377–390.
- Sempau J., J.M. Fernández-Varea, E. Acosta and F. Salvat (2003), “Experimental benchmarks of the Monte Carlo code PENELOPE”, *Nucl. Instrum. Meth. B* **207**, 107–123.
- Sevier K.D. (1972), *Low Energy Electron Spectrometry* (Wiley Interscience, New York).
- Shiles E., T. Sasaki, M. Inokuti and D.Y. Smith (1980), “Self-consistency and sum-rule tests in the Kramers-Kronig analysis of optical data: applications to aluminum”, *Phys. Rev. B* **22**, 1612–1628.
- Snyder W.S., M.R. Ford, G.G. Warner and H.L. Fisher Jr. (1969), “Estimates of absorbed fractions for monoenergetic photon sources uniformly distributed in various organs of a heterogeneous phantom”, MIRD Pamphlet No. 5, *J. Nucl. Med.* **10**, suppl. No. 3, 5–52.
- Statham P.J. (1976), “The generation, absorption and anisotropy of thick-target bremsstrahlung and the implications for quantitative energy dispersive analysis”, *X-Ray Spectrom.* **5**, 154–168.
- Sternheimer R.M. (1952), “The density effect for the ionization loss in various materials”, *Phys. Rev.* **88**, 851–859.
- Sternheimer R.M., S.M. Seltzer and M.J. Berger (1982), “Density effect for the ionization loss of charged particles in various substances”, *Phys. Rev. B* **26**, 6067–6076. Erratum: *ibid.* **27** (1983) 6971.
- Titus F. (1970), “Measurements of the energy response functions of scintillators for monoenergetic electrons”, *Nucl. Instrum. Meth.* **89**, 93–100.
- Tofterup A.L. (1986), “Theory of elastic and inelastic scattering of electrons emitted from solids: energy spectra and depth profiling in XPS/AES”, *Surf. Science* **167**, 70–100.
- Tsai Y.S. (1974), “Pair production and bremsstrahlung of charged leptons”, *Rev. Mod. Phys.* **46**, 815–851.
- Walker A.J. (1977), “An efficient method for generating discrete random variables with general distributions”, *ACM Trans. Math. Software* **3**, 253–256.
- Walker D.W. (1968), “Spin polarization in electron scattering from molecules”, *Phys. Rev. Lett.* **20**, 827–828.
- Walker D.W. (1971), “Relativistic effects in low energy electron scattering from atoms”, *Adv. Phys.* **20**, 257–323.
- Wentzel G. (1927), “Zwei Bemerkungen über die Zerstreuung korpuskularer Strahlen als Beugungserscheinung”, *Z. Phys.* **40**, 590–593.

- Yates A.C. (1968), “Calculations of electron spin polarization for electron-molecule collisions”, *Phys. Rev. Lett.* **20**, 829–831.
- Zerby C.D. (1963), “A Monte Carlo calculation of the response of gamma-ray scintillation counters”, in *Methods in Computational Physics*, vol. 1, eds. B. Alder, S. Fernbach and M. Rotenberg (Academic Press, New York) pp. 89–134.
- Zheng-Ming L. and A. Brahme (1993), “An overview of the transport theory of charged particles”, *Radiat. Phys. Chem.* **41**, 673–703.
-